Summer 7-13-2022

Halogen and Non-traditional Isotope Geochemistry of Planetary and Terrestrial Materials

Anthony Gargano
University of New Mexico - Main Campus

Zachary Sharp
University of New Mexico - Main Campus

Justin Simon
NASA Johnson Space Center

Charles Shearer
University of New Mexico - Main Campus

Adrian Brearley
University of New Mexico - Main Campus

See next page for additional authors

Anthony Michael Gargano

Candidate

Earth and Planetary Sciences

Department

This dissertation is approved, and it is acceptable in quality and form for publication:

Approved by the Dissertation Committee:

Zachary Sharp, Chairperson

Justin Simon

Charles Shearer

Adrian Brearley

James Day

HALOGEN AND NON-TRADITIONAL ISOTOPE GEOCHEMISTRY OF PLANETARY AND TERRESTRIAL MATERIALS

by

ANTHONY MICHAEL GARGANO

B.S., Geology, University of North Carolina at Charlotte, 2016

DISSERTATION

Submitted in Partial Fulfillment of the

Requirements for the Degree of

Doctor of Philosophy

Earth and Planetary Sciences

The University of New Mexico

Albuquerque, New Mexico

July 2022

ACKNOWLEDGEMENTS

To New Mexico – the community, native peoples, and culture of this land will continue to captivate me for the rest of my life. I am filled with gratitude having experienced it. To the staff of UNM Earth and Planetary Sciences and the Center for Stable Isotopes – Cindy, Paula, Faith, Laura, Viorel, you all made some of the most difficult parts of graduate school easier. To the students, Jordan, Erick, Jess, Zoltan, Marina, and others, thank you for the comradery throughout these years. I must especially thank the Elliott-Smith family for their support, and Emma for listening to my ceaseless geochemical stream of consciousness. I was not prepared for the kindness and acceptance you all brought to my life during the final & most difficult stages of my Ph. D.

To my mentors – the knowledge and experience you have imparted in me will be carried on and I am grateful for the opportunity to have learned from each of you. Justin – the curiosity and humility you bring to science is an example I strive to follow. I could not have done this broad exploratory work without you and Wayne, and I am eternally grateful for the opportunities your help has provided me the past couple years. To Chip, you are a beacon of light in this field, and I hope to help carry on the legacy that you and your mentors brought to planetary science.

Zach, five years later and I still cannot envision a better fit for a mentor. I came to UNM a lot of enthusiasm, but very little knowledge or experience. You enabled my growth by making me comfortable with breaking stuff, making mistakes, and being wrong. You allowed me to explore any system or process which sparked my curiosity and showed me the value in a community of like-minded people with genuine curiosities in understanding the

poorly understood. While our journey was far from linear, I wouldn't have had it any other way.

Lastly, none of this would have been possible without the support of my parents and the Huffman family all these years. My path to this point was anything but expected and traditional…thank you for making it possible in whichever way you could. This dissertation is dedicated to Melvin Simpson (1938-2020) and Ruth Gargano (1933-2021). Your hard work and persistence gave me these opportunities to get to where I am today.

HALOGEN AND NON-TRADITIONAL ISOTOPE GEOCHEMISTRY OF PLANETARY AND TERRESTRIAL MATERIALS

by

ANTHONY MICHAEL GARGANO

B.S., Geology, University of North Carolina at Charlotte, 2016

Ph.D., Earth and Planetary Sciences, University of New Mexico, 2022

ABSTRACT

This dissertation presents the advances in non-traditional isotope geochemistry of planetary and terrestrial materials encompassing chlorine, sulfur, and zinc isotopes, as well as halogen geochemistry. A wide breadth of materials was studied throughout the completion of this work including iron meteorites, achondrites, chondrites, Apollo lunar samples, as well ancient marine chert, and carbonate sediments. Much of the focus involved the development of a method capable of simultaneously measuring the halogen contents and chlorine isotope compositions of geological materials. Here, I present these data sets to broadly characterize the process of devolatilization of planetary materials, and specifically the problem of 'halogen-poisoning' during planetary evolution wherein an overabundance of halogen elements would lead to highly saline planetary water reservoirs. The characterization of this problem encompasses several representative materials at different periods during the solar system's evolution beginning with chondrites and achondrites, followed by lunar samples, and lastly, marine sediments.

TABLE OF CONTENTS

LIST OF FIGURES

LIST OF TABLES

PREFACE

This preface acknowledges the funding sources and outlines the roles that co-authors, and collaborators performed in each chapter pursuant to the requirements of the University of New Mexico and the Department of Earth and Planetary Sciences. Anthony M. Gargano is the primary author and conducted greater than or equal to 51% of the work presented in each chapter of this dissertation. Two National Aeronautics and Space Agency (NASA) grants funded the research. Support provided by NASA grants 17-AS&ASTAR17-0026 and 13-MFRP13-0022.

Chapter 1 has been published in the journal *Meteoritics and Planetary Sciences* with co-authors Zachary Sharp. Anthony M. Gargano generated and analyzed the data and wrote the manuscript alongside Zachary Sharp.

Chapter 2 has been published in the journal, *Proceedings to the National Academy of Sciences*, with co-authors Zachary Sharp, Charles Shearer, Justin Simon, Alex Halliday, and Wayne Buckley. Anthony M. Gargano wrote the manuscript, consolidated and interpreted all data, and analyzed all samples for halogen contents and chlorine isotope compositions. Zachary Sharp, Charles Shearer, and Alex Halliday managed the research and provided guidance and edits on the manuscript. Justin Simon and Wayne Buckley provided guidance during method development.

Chapter 3 has been published in the journal, *American Mineralogist*, with co-authors James Dottin, Sean Hopkins, Zachary Sharp, Charles Shearer, Alex Halliday, James Farquhar, Fiona Larner, and Justin Simon. Anthony M. Gargano wrote the manuscript, consolidated, and interpreted all data. James Dottin, James Farquhar, Sean Hopkins, Alex Halliday and Fiona Larner performed the sulfur and zinc isotope analyses.

Chapter 4 will be submitted to the journal, *Science* with co-authors Zachary Sharp, and Justin Simon. Anthony M. Gargano wrote the manuscript, consolidated and interpreted all data, created all samples, and performed the chlorine isotope and analyses. Zachary Sharp and Justin Simon provided edits and advice on the manuscript.

Chapter 5 is unpublished work involving the biogeochemical cycle of halogens applied to deep time and paleosalinity, and extensive method developments in halogen geochemical techniques and stable chlorine isotope analyses.

1. THE CHLORINE ISOTOPE COMPOSITION OF IRON METEORITES: EVIDENCE FOR THE CL ISOTOPE COMPOSITION OF THE SOLAR NEBULA AND IMPLICATIONS FOR EXTENSIVE DEVOLATILIZATION DURING PLANET FORMATION

Abstract

The bulk chlorine concentrations and isotopic compositions of a suite of NC and CC iron meteorites were measured using gas source mass spectrometry. The $\delta^{37}Cl$ values of magmatic irons range from -7.2 to 18.0 ‰ vs. SMOC and are only loosely related to chlorine concentrations, which range from 0.3 to 161 ppm. Non-magmatic IAB irons are comparatively Cl-rich containing >161 ppm with $\delta^{37}Cl$ values ranging from -6.1 to -3.2 ‰.. The anomalously high and low $\delta^{37}Cl$ values are inconsistent with a terrestrial source, and as Cl contents in magmatic irons are largely consistent with derivation from a chondrite-like silicate compliment, we suggest that Cl is indigenous to iron meteorites. Two NC irons, Cape York and Gibeon have high cooling rates with anomalously high $\delta^{37}Cl$ values of 13.4 and 18.0 ‰. We interpret these high isotopic compositions to result from Cl degassing during the disruption of their parent bodies, consistent with their low volatile contents (Ge, Ag, Ga). As no relevant mechanisms are known to decrease $\delta^{37}Cl$ values, whereas volatilization is known to increase $\delta^{37}Cl$ values by the preferential loss of light isotopes, we interpret the low isotope

values of <-5‰ and down to -7.2 ‰ to most-closely represent the primordial isotopic composition of Cl in the solar nebula. Similar conclusions have been derived from low δ^{37}Cl values down to -6, and -3.8 ‰ measured in Martian and Vestan meteorites, respectively. These low δ^{37}Cl values are in contrast to those of chondrites which average around 0 ‰ previously explained by the incorporation of isotopically heavy HCl-clathrate into chondrite parent bodies. The poor retention of low δ^{37}Cl values in many differentiated planetary materials suggest that extensive devolatilization occurred during planet formation which can explain Earth's high δ^{37}Cl value by the loss of approximately 60% of the initial Cl content.

Introduction

The building blocks for the terrestrial planets are thought to be early-formed planetesimals, the remnant metallic cores of which are sampled by iron meteorites (Morbidelli et al., 2012). Iron meteorites are a diverse group of planetary materials that represent the first generations of differentiated bodies formed <1Ma after CAI's (Burkhardt et al., 2008; Kleine et al., 2005; Markowski et al., 2006; Qin et al., 2008). They are broadly categorized into magmatic or non-magmatic, where the magmatic irons are thought to represent fractionally-crystallized metallic cores, whereas the non-magmatic iron meteorites, with relatively younger ages, suggest that impacts played an important role in their formation (Haack and McCoy, 2003; Scott, 1972). Iron meteorites are grouped according to their trace element compositions (i.e. Ga, Ge, Au) (Goldstein et al., 2009; Wasson et al., 1980). The primary chemical distinction between the iron meteorite groups are an increasing depletion of volatile elements such as Ga and Ge from type I to IV irons (Scott and Wasson 1975). Each

iron meteorite group, or 'irons' are thought to be derived from distinct parent bodies as cooling rates are relatively similar within each group (Goldstein et al., 2009).

Iron Meteorite Groups

An introduction to the meteorite groups in which samples are measured in this work are discussed in brief; a more in-depth discussion can be found in Scott and Wasson (1975) and Goldstein et al. (2009).

Ungrouped Iron Meteorites

Ungrouped iron meteorites have different structures and chemical compositions from grouped irons and represent approximately 14-15 % of all iron meteorites (Scott, 1979; Wasson, 1990). The formation mechanisms for the ungrouped irons vary, although they are commonly thought to have experienced similar chemical processing to the grouped irons and represent many different parent bodies (Scott and Wasson, 1975). Despite this diversity, the Ga and Ge concentrations in the ungrouped irons generally fall within the range from groups I to IV (Haack and McCoy, 2003).

Group IAB

Type IAB iron meteorites are non-magmatic and are thought to have experienced a distinctly different formation history compared to the magmatic irons, as their trace element trends are inconsistent with simple fractional crystallization (Goldstein et al., 2009). They are the second largest group of iron meteorites and contain the highest concentrations of volatiles such as Ga and Ge (Haack and McCoy, 2003). The proposed formation mechanisms for this group include impact induced metallic melt generation and crystal segregation (Wasson and Kallemeyn, 2002), and the reassembly of a dismembered partially differentiated asteroid (Benedix et al., 2000).

Group IIAB

Type IIAB iron meteorites are magmatic irons with the lowest Ni and highest S contents of any iron meteorite group and are thought to have formed largely by fractional crystallization (Wasson et al., 2007). The precursor materials for this group of iron meteorites are highly reduced based on their low Ni contents, as well of the presence of graphite (Haack and McCoy, 2003). Wasson et al. (2007) propose that all IIAB irons contain trapped melt of varying compositions depending on where the sample crystallized in the core of the parent asteroid which consisted of two immiscible P and S-rich liquids.

Group IID

Type IID iron meteorites are magmatic irons which contain high volatile contents (i.e. Ga and Ge) with low S which is suggested by Wasson and Huber (2006) to be the result of formation and segregation of S-rich melts as opposed to loss by devolatilization. The meteorites in this group are suspected to largely sample the inner portion of the parent asteroidal core that was P-rich (Wasson and Huber, 2006).

Group IIIAB

Type IIIAB magmatic iron meteorites are the largest group of irons consisting of >200 members, and as a result it is thought that all depths of the asteroidal core from which this group was derived is well sampled. This group is prominently clustered with cosmic ray exposure (CRE) ages of 650 ± 100 Ma which is interpreted to be the age of the IIIAB parent body breakup (Keil et al., 1994; Voshage and Feldmann, 1979). The majority of IIIAB irons show evidence for shock in the appearance of shock-hatched structures (Buchwald, 1975). Highly variable cooling rates are also measured in this group, varying by around a factor of

6, interpreted to result from the exposure of the metallic core to space during cooling (Yang and Goldstein, 2006).

Group IVA

Type IVA magmatic iron meteorites are the third largest group of irons and are notably depleted in volatile elements relative to the other iron meteorite groups (Wasson et al., 2006). Akin to type IIIAB irons, the IVA irons cluster with CRE ages around 400 ± 100 Ma, which represents the time of parent body breakup (Keil et al., 1994; Voshage and Feldmann, 1979). Approximately 20% of them show shock-hatched structures (Buchwald, 1975). More dramatically, however, the type IVA irons have cooling rate estimates that vary by an order of magnitude more than IIIABs, which is thought to result from the complete stripping of the insulating mantle around the IVA parent body from a hit-and-run collision (Yang et al., 2007).

Group IVB

Type IVBs are a small group of magmatic irons, and the most volatile depleted iron meteorite group. This group has high Ni contents suggestive of devolatilization following large impacts and loss of moderately siderophile elements by oxidation (Campbell and Humayun, 2005; Rasmussen et al., 1984; Yang et al., 2010). The extent of volatile depletion in this group is generally considered to be too large to result solely from devolatilization, and is more consistent with nebular volatile depletion (i.e. from high temperature condensation)(Campbell and Humayun, 2005; Kelly and Larimer, 1977). Kelly and Larimer (1977) suggest the composition and volatile depletion of this group of irons can be explained by their formation from rapidly accreted high-temperature condensates in the IVB parent body.

Carbonaceous and Non-Carbonaceous Precursors

Warren (2011) first proposed that carbonaceous (CC) and non-carbonaceous (NC) chondrites formed in isotopically distinct regions of the nebula based on Cr, Ni, and O isotope compositions. Furthermore, this author suggested that the CCs were formed in the outer solar system, whereas the NCs formed inward of the asteroid belt (~ 3 AU), potentially separated by Jupiter. From this, it has been proposed that iron meteorites formed from the differentiation of CC and NC asteroids (e.g. Rubin, 2018) can be distinguished based on Mo and W isotope anomalies (Budde et al., 2016; Kruijer et al., 2017; Poole et al., 2017). Although astrophysical models suggest that most differentiated planetesimals formed close to the Sun where accretion rates were high (Bottke et al., 2006), isotopic anomalies show that iron meteorite parent bodies may have also formed in the outer solar system (Budde et al., 2016; Burkhardt et al., 2011; Kruijer et al., 2017; Warren, 2011). NC iron meteorites include groups IAB, IC, IIE, IIAB, IIIAB, IIIE, IIG, and IVA, with the CC irons including groups IIC, IID, IIF, IIIF, and IVB (Budde et al., 2016; Kruijer et al., 2017).

In total, these observations have significant implications. Chondrites are known to be younger by >1 Ma relative to the iron meteorite parent bodies (Amelin and Krot, 2007; Asphaug et al., 2011; Wadhwa et al., 2007), which Rubin (2018) states, suggests that chondrites in the meteorite collections do not necessarily represent the precursor materials to iron meteorites. Therefore, iron meteorites may retain primordial geochemical signatures prior to the accretion of chondrite parent bodies from both the inner (NC irons), and outer solar system (CC irons). With this in mind, although iron meteorites represent evolved planetary materials, if they retain indigenous chlorine from their parent bodies, then their isotopic compositions may contain critical information regarding the isotopic composition of

their precursor materials. Iron meteorites may also record the history of devolatilization that is thought to occur throughout planetary evolution and potentially reveal secondary processing (i.e. aqueous alteration) that took place on the relatively later formed chondrite parent bodies.

Carbonaceous and Non-Carbonaceous Precursors

Iron meteorites have long been recognized to contain chlorine, although whether the source was indigenous or derived from terrestrial alteration has been extensively debated (Buchwald, 1975; Buchwald and Clarke, 1989). Many authors have described occurrences of Cl-bearing minerals in iron meteorites, including chlorapatite (Marshall and Keil, 1965), djerfisherite (Fuchs, 1966), and lawrencite (Farrington, 1915; Mason, 1962). Despite the presence of these minerals, a terrestrial origin was presented by Buchwald and Clarke (1989), who argued that chlorine in iron meteorites is mostly derived from terrestrial alteration and the formation of akaganéite due to electrochemical corrosion of Fe-Ni alloys. We propose that the source of chlorine in iron meteorites could be definitively determined by chlorine isotope measurements. If Cl in iron meteorites is terrestrial, it should be isotopically similar to terrestrial materials, which cluster around 0 ‰ (Barnes and Sharp, 2017). Instead, if Cl in iron meteorites is indigenous, the extensive devolatilization thought to have taken place in some iron meteorite parent bodies should result in anomalously high $\delta^{37}Cl$ values and therefore would convincingly support an extraterrestrial origin.

The motivation for this study is in that the chlorine isotope compositions of chondrites are markedly different to those of Martian and Vestan meteorites, the latter of which are interpreted to resemble more primitive nebular isotopic compositions (Sarafian et al., 2017; Sharp et al., 2016). The chlorine isotope compositions of primitive Martian

meteorites and eucrites reach values as low as -6 (Shearer et al., 2017) and -3.8 ‰ respectively (Sarafian et al., 2017), whereas chondrites cluster around 0 ‰. The higher $\delta^{37}Cl$ values of most chondrites have been interpreted to result from the incorporation of isotopically heavy HCl clathrate into chondrite parent bodies (Sharp et al., 2016), whereas in this interpretation, the low $\delta^{37}Cl$ values measured in samples from Mars and 4Vesta preserve the value of the solar nebula. If iron meteorites can be shown to have Cl derived from their parent bodies, it should also be isotopically light in samples which are not extensively devolatilized. We test the idea that the solar nebula was isotopically light, and that chondrites no longer retain isotopically primitive chlorine isotope compositions by measuring the $\delta^{37}Cl$ values of iron meteorites.

Methods

The chlorine isotope composition and concentration of magmatic and non-magmatic iron meteorites from both CC and NC irons were measured. Care was taken to avoid altered samples via visual inspection and physical removal of surface material when present. This was only performed on IAB iron meteorites. All other samples were interior chips that were free of rust or any signs of alteration. Samples were cleaned with acetone and deionized H_2O to remove surface contamination and Cl was liberated by acid digestion with 50% HNO_3. After cleaning, the water-soluble Cl on two IAB irons (Table 1) were collected by soaking overnight in DI water, before an accompanying acid digestion to release structurally-bound Cl. Cl-bearing solutions were then reacted with 0.4 M $AgNO_3$ overnight to precipitate AgCl which was filtered and flame-sealed in 8mm evacuated Pyrex tubes with 10μL CH_3I at 80°C for 48 hours to produce CH_3Cl as an analyte. CH_3Cl was separated from excess CH_3I using a

gas chromatography (GC) column (Eggenkamp, 2014). The $\delta^{37}Cl$ values of the CH_3Cl were measured on a Delta^{Plus}XL gas source mass spectrometer at the University of New Mexico in continuous flow mode. Measurements were standardized to Standard Mean Ocean Chloride (SMOC) (Kaufmann et al., 1984) using seawater standards which vary by <0.1 ‰ (Godon et al., 2004). The reproducibility of this method in our laboratory been shown to be <±0.25 ‰ (Barnes and Sharp, 2006; Selverstone and Sharp, 2011; Sharp et al., 2010). Chlorine isotope values are reported in delta notation in per mil relative to SMOC where $\delta^{37}Cl = \left(\frac{\frac{^{37}Cl}{^{35}Cl}_{Sample}}{\frac{^{37}Cl}{^{35}Cl}_{SMOC}} - 1\right) * 1000.$

Results

The chlorine isotope compositions of non-magmatic IAB iron meteorites range from -6.1 to -3.2 ‰ with Cl contents from 244 to >4000 ppm. The Cl and Ge concentrations are far higher than for any other group of iron meteorites (Figs. 1.2, 1.3). The $\delta^{37}Cl$ values of magmatic iron meteorites are highly variable from -7.2 to 18.0 ‰ and are not related to chlorine concentrations, which range from 0.3 to 161 ppm (Figs. 1.2, 1.3). The type IVB iron meteorite Hoba has the lowest chlorine isotope composition measured in planetary materials to date at -7.2 ‰. Cape York (IIIAB) and Gibeon (IVA) have anomalously high $\delta^{37}Cl$ values of +13.2 and +18.0 ‰, respectively. Three samples we have measured fall within the CC group of iron meteorites (Carbo IID, Hoba IVB, and Chinga ungrouped)(Rubin, 2018). These CC irons have low $\delta^{37}Cl$ values ranging from -7.2 ‰ in Hoba to -4.8 ‰ in Carbo, whereas NC irons measured have highly variable $\delta^{37}Cl$ values ranging from -6.1 ‰ in Cranbourne to 18.0 ‰ in Gibeon.

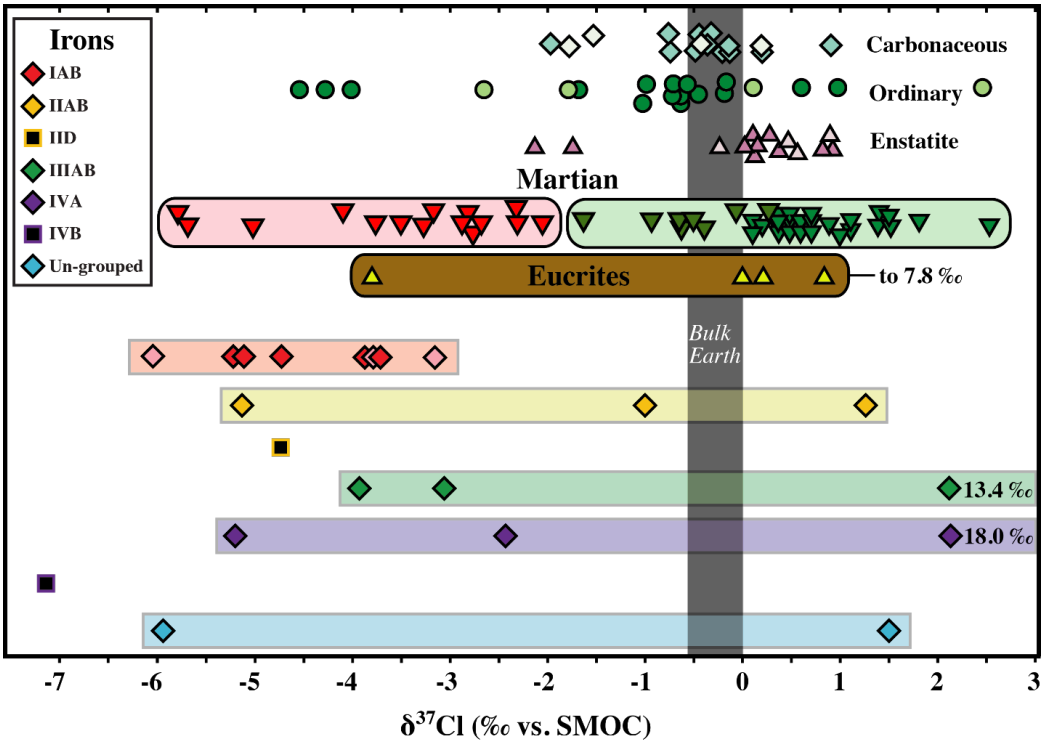

Figure 1.1: Chlorine isotope composition of iron meteorites and selected planetary materials (Sarafian et al., 2017; Shearer et al., 2017). Water-soluble chloride fractions are represented by faded symbols in their respective groups. Martian Samples attributed to representing the chlorine isotope composition of the primitive Martian mantle are enclosed in pink field, whereas those attributed to mixing with the crust are enclosed in the green field. The bulk Earth value is shown by the vertical grey field at approximately 0 ‰. Samples with $\delta^{37}Cl$ values larger than 3 ‰ are indicated, but not shown. The uncertainty in iron meteorite $\delta^{37}Cl$ values are smaller than symbol size.

Table 1.1: Chlorine isotope compositions & chlorine concentrations of iron meteorites. All samples are finds. Sub-splits labeled by (a), (b). All measurements are from structurally-bound chloride prepared by acid digestions unless sample is noted as a water-soluble fraction (WSF). [*]Sample obtained by the Division of Meteorites and Department of Mineral Sciences at the Smithsonian. [†]Sample obtained by Larry Taylor at University of Tennessee. [‡]Sample obtained by UNM Institute for Meteoritics.

Sample	Group	$\delta^{37}Cl$ (‰ vs. SMOC)	[Cl] (ppm)	Mass (g)
Campo Del Cielo (a)[†]	IAB	-3.98	244	8.2
Campo Del Cielo (WSF) (a)[†]	IAB	-3.16	483	N/A
Canyon Diablo[‡]	IAB	-3.79	957	5.3
Cranbourne (a)[†]	IAB	-5.15	3848	0.5
Cranbourne (b)[†]	IAB	-5.23	>4000	1.4
Cranbourne (WSF) (a)[†]	IAB	-3.89	2173	N/A
Cranbourne (WSF) (b)[†]	IAB	-6.07	3577	N/A
Odessa[‡]	IAB	-4.72	1131	14.1
Coahuila[*]	IIAB	-1.00	5	3.7
Old Woman[*]	IIAB	-5.14	0.3	7.3
Sikhote Alin[‡]	IIAB	1.30	23	6.8
Carbo[‡]	IID	-4.75	33	4.3
Cape York[*]	IIIAB	13.37	0.2	4.5
Grants[‡]	IIIAB	-3.07	161	11.1
Grants[‡]	IIIAB	-3.91	153	7.5
Gibeon[*]	IVA	17.96	9	3.0
Muonionalusta[*]	IVA	-2.42	17	3.2
Muonionalusta[‡]	IVA	-5.21	2	7.1
Hoba[*]	IVB	-7.19	0.3	3.7
Chinga[‡]	Un-grouped	-5.95	103	4.4
Gebel Kamil[‡]	Un-grouped	1.60	18	8.1

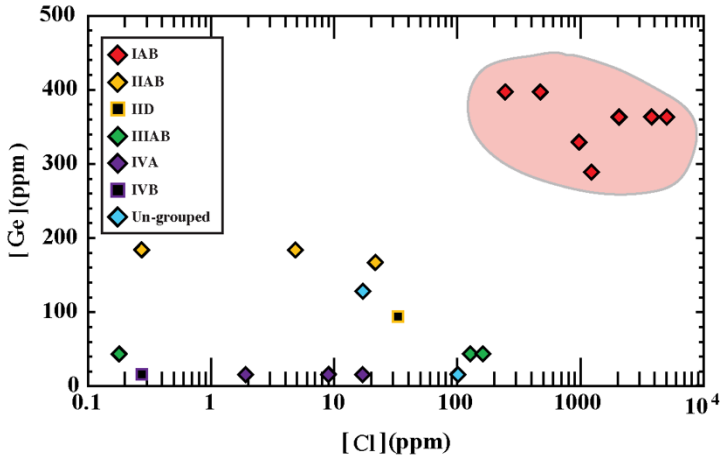

Figure 1.2: Cl vs. Ge concentrations in iron meteorites. Ge data are from (Goldstein et al., 2009) and references therein. Group IAB iron meteorites are distinctly separated from other iron meteorites seen in the pink field. Other iron meteorite groups do not show less distinct grouping. As Cl and Ge are thought to be similarly volatile, these groupings suggest that the IAB parent body was distinctly enriched in volatile elements.

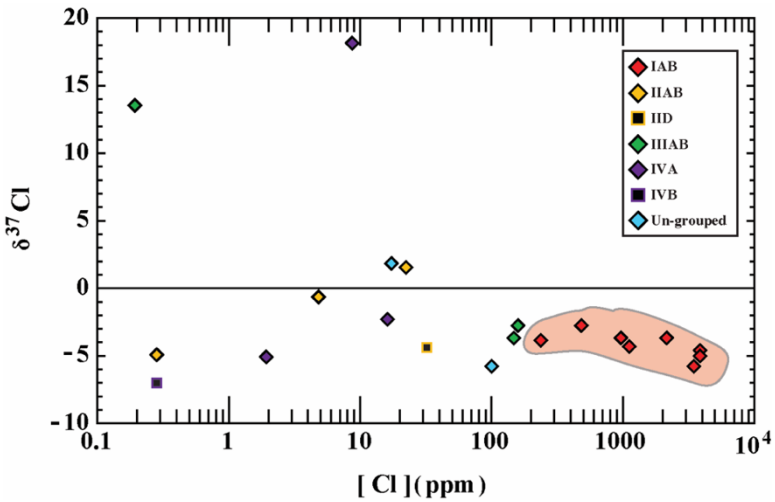

Figure 1.3: Chlorine concentrations (ppm) vs. δ37Cl values of iron meteorites. The uncertainty in δ37Cl and [Cl] are smaller than symbol size. Type IAB non-magmatic iron meteorites moderately trend with Cl concentration and δ37Cl value (R2 = 0.66). Magmatic iron meteorites do not show significant trends within individual groups.

Discussion

The Chlorine Content of Iron Meteorites

The Cl contents of magmatic iron meteorites range from <1 to 161 ppm (Table 1) with no significant relationship between [Cl] and δ^{37}Cl value (Fig. 1.3). We attempted to find the Cl-bearing phase in magmatic irons and observed a Cl-rich mineral in Uruachic (IIIAB, Fig. 1.4), and Carbo (IID, Fig. 1.5) using the JEOL 8200 electron microprobe at the University of New Mexico (see figure captions for details). The Cl contents of the non-magmatic IAB irons are significantly higher than magmatic irons (244 to >4000 ppm) and also correlate with [Ge] (Fig. 1.2) suggesting that the IABs are distinctly enriched in volatile elements. In partitioning experiments, Kuwahara et al. (2017) showed that the Cl metal-silicate partition coefficient ranges from 0.15 in S-free, to 0.3 in S-bearing experiments. Of the 13 magmatic irons measured in this work, 10 have Cl contents <45 ppm. These Cl contents can be explained with an accompanying silicate portion of the iron meteorite parent bodies with Cl concentrations similar to ordinary (up to 150 ppm [Cl]) or enstatite (up to 800 ppm [Cl]) chondrites (Fig. 1.6)(Kuwahara et al., 2017). The chlorine contents of IAB irons are largely unexplainable by metal-silicate partitioning and may represent the presence of Cl-bearing immiscible phases formed in metallic liquids (i.e. Kuwahara et al. 2017).

The anomalously high and low δ^{37}Cl values of the iron meteorites are inconsistent with a terrestrial source. The bulk silicate Earth has a chlorine isotope composition of approximately 0 ‰, and with the exception of sedimentary pore fluids with δ^{37}Cl values down to -7.8 ‰, and volcanic fumaroles with δ^{37}Cl values up to 18.8 ‰, the range of δ^{37}Cl values found in iron meteorites cannot be explained by terrestrial chlorine (Barnes and Sharp, 2017). If the chlorine was a product of terrestrial contamination, we would expect the δ^{37}Cl

values to cover a narrow range and cluster around 0±1 ‰ and not be correlated with the type of iron meteorite. Instead, the $\delta^{37}Cl$ values span almost the entire known range of terrestrial materials and we therefore expect this reflects an extraterrestrial source. Additionally, water-soluble chloride measured in IAB irons has similarly low $\delta^{37}Cl$ values to that of the structurally-bound chloride (within ~ 1 ‰) suggesting that 1) low $\delta^{37}Cl$ values are not from terrestrial contamination, and 2) the same Cl-bearing phase in irons is being measured in the water-soluble and structurally-bound chloride fractions. Lastly, the chlorine isotope measurement on Carbo (-4.75 ‰) was performed on a mirrored chip of the prepared mount where a Cl-rich phase is seen in Figure 1.5. This low isotope value, in addition to Cl contents within this phase up to 26 wt%, which we speculate is lawrencite ($FeCl_2$) argues against a terrestrial source for the low $\delta^{37}Cl$ values.

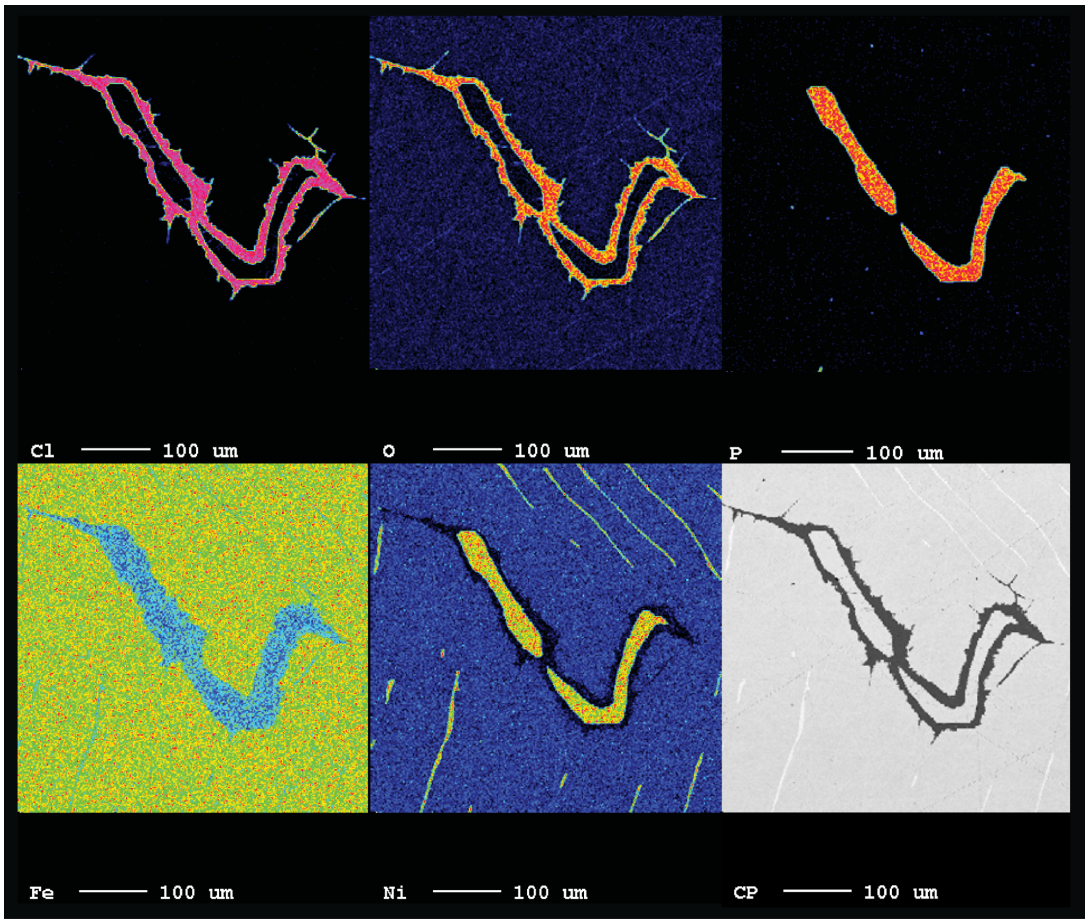

Figure 1.4: X-ray maps of Uruachic (IIIAB) collected with an JEOL 8200 electron microprobe at the University of New Mexico operated at an accelerating voltage of 15 kV and beam current of 20 nA. Chlorine contents of the Cl-bearing phase ranges from between 17-17.25 wt% Cl. The Cl-rich phase occurs bounding a schreibersite inclusion between grain boundaries of kamacite and taenite.

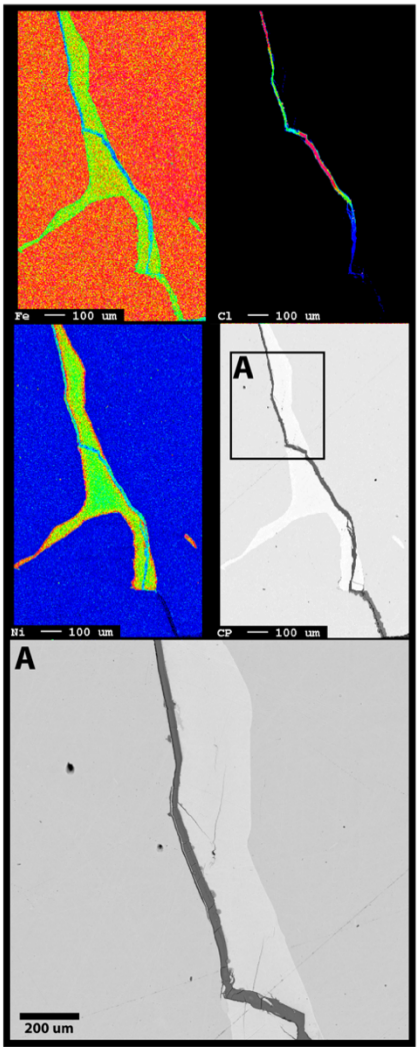

Figure 1.5: X-ray maps of Carbo (IID) collected with an JEOL 8200 electron microprobe at the University of New Mexico operated at an accelerating voltage of 15 kV and beam current of 20 nA. Image A is a magnified back-scattered electron image of the Cl-rich phase outlined in black. Chlorine contents of the Cl-bearing phase is heterogenous and ranges from between 3 to 26 wt% Cl. The Cl-rich phase occurs between a grain boundary between kamacite and taenite. A mirrored chip of this sample was measured with a $\delta^{37}Cl$ value of -4.75 ‰, suggestive of extraterrestrial origin.

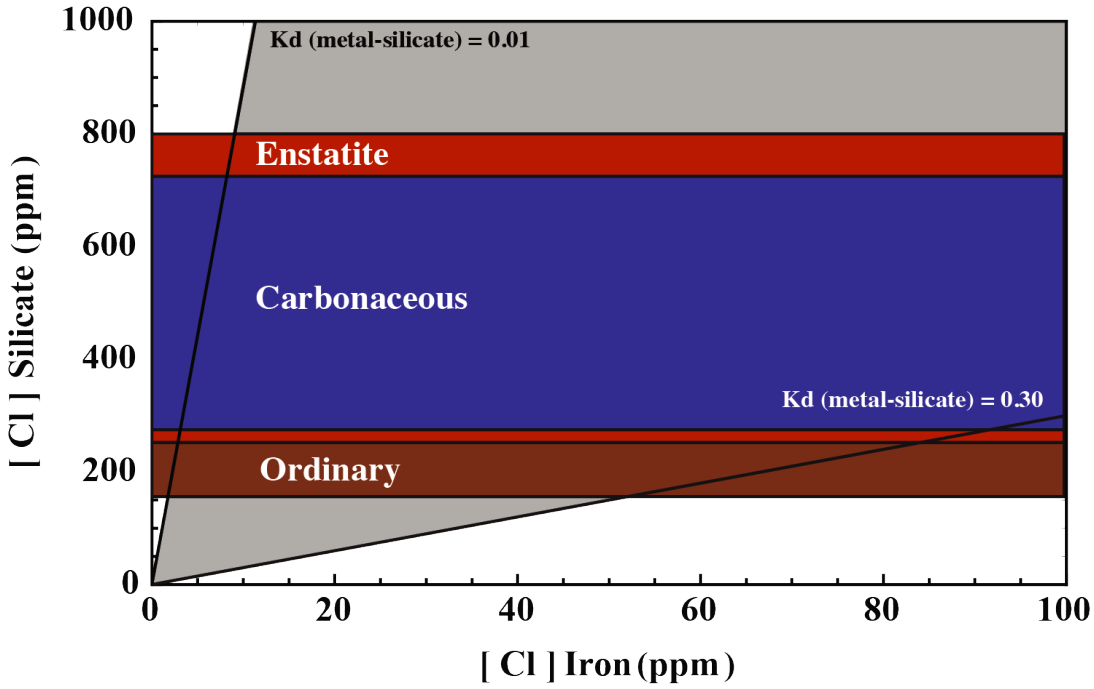

Figure 1.6: Range of chlorine partition coefficients between metal and silicate (Kuwahara et al., 2017; Sharp and Draper, 2013).The solution field of partitioning is in grey. In this field, experimental partition coefficients relate the chlorine concentration of an iron meteorite to an accompanying chondrite-like silicate compliment. The range of chlorine concentrations in chondrite groups is from Fegley & Lewis (1980), and Sharp et al., (2013). An enstatite or carbonaceous chondrite-like silicate compliment for the iron meteorite parent bodies can explain the Cl concentrations of magmatic iron meteorites which range up to 161 ppm.

Iron meteorites are extensively processed planetary materials. The processes that could have affected the volatile components within them are numerous and the effects on the chlorine isotope compositions are largely unknown with the exception of devolatilization. Equilibrium isotope fractionation between silicate and metal in a differentiating parent body should be negligible as the isotopic fractionation factor (α) is proportional to $1/T^2$ and approaches near-zero values at magmatic temperatures. Other processes such as the formation of immiscible S or P-rich melts likely can be similarly assumed to produce negligible isotope fractionation. We do not know of any mechanisms for significantly decreasing $\delta^{37}Cl$ values in iron meteorite parent bodies, in contrast to processes such as degassing that increases chlorine isotope compositions (Sharp et al., 2010). Devolatilization could then be expected to be the dominant control on changing the chlorine isotope composition of iron meteorite parent bodies. It is for this reason that we interpret the lowest $\delta^{37}Cl$ value to represent the initial isotopic composition of an iron meteorite parent body most closely, and the region of the protoplanetary disk in which their precursor materials were derived.

Further evidence for devolatilization being the dominant process responsible for raising the $\delta^{37}Cl$ values of iron meteorites are the high $\delta^{37}Cl$ values of Cape York & Gibeon. These two irons have the highest $\delta^{37}Cl$ values at 13.2 and 18.0 ‰, and have low chlorine concentrations of 0.2 and 9 ppm, respectively. Extensive devolatilization is thought to have occurred due to depletion of Ga, Ge, and Ag, in addition to high cooling rates thought to result from partial to complete loss of their insulating silicate mantles (Asphaug et al., 2006; Kleine et al., 2018; Yang and Goldstein, 2006). Degassing of Cl from the exposed metallic core should result in a preferential loss of light Cl isotopes to space, similar to observations

in most lunar samples with high $\delta^{37}Cl$ values (Sharp et al., 2010). The low [Cl] and high $\delta^{37}Cl$ values in these two meteorites are consistent with chlorine volatilization following disruption of their parent bodies.

The Chlorine Isotope Compositions of CC and NC Iron Meteorites

CC and NC iron meteorites are thought to have formed in distinct regions of the protoplanetary disk. If the CC reservoir is in fact beyond the orbit of Jupiter as suggested by Warren (2011), then comparing the Cl isotope compositions of these two groups of iron meteorites may elucidate potential heterogeneities in the Cl isotope composition of the solar nebula. The similarly lowest $\delta^{37}Cl$ values of NC (-6.1 ‰) and CC (-7.2 ‰) iron meteorites suggests that the protoplanetary disk was not significantly heterogeneous with respect to chlorine isotopes.

Both CC IVB, and NC IVA irons are volatile depleted, yet are starkly different in chlorine isotope compositions. Gibeon IVA contains 9 ppm [Cl] with a $\delta^{37}Cl$ value of 18.0 ‰, whereas Hoba IVB contains 0.3 ppm [Cl] with a $\delta^{37}Cl$ value of -7.2 ‰. This discrepancy may result from different mechanisms of volatile depletion. Scott (1979) suggests that iron meteorites have experienced volatile depletion by both primary (i.e. nebular condensation) and secondary processing (i.e. vaporization). Although both processes are capable of producing volatile element depletions, they may result in distinctly different isotopic compositions. Humayun and Clayton (1995) argue that evaporation and condensation can be distinguished as evaporation should result in large mass dependent kinetic isotope fractionation (i.e. preferential loss of light isotopes), whereas isotope fractionation from high temperature condensation should be small. The low [Cl] and $\delta^{37}Cl$ value in Hoba could

thereby explained by high-temperature condensation which is consistent with formation models of IVB irons and their volatile depletion (Kelly and Larimer, 1977).

The Chlorine Isotope Composition of the Solar Nebula & Chondrites

Sharp et al. (2016) originally proposed that the low $\delta^{37}Cl$ values measured in Martian meteorites suggested that the solar nebula was isotopically light. As CC and NC irons have comparably low $\delta^{37}Cl$ values, and presumably formed in distinct regions of the nebula, we interpret the lowest $\delta^{37}Cl$ value of -7.2 ‰ to most closely represent the primitive chlorine isotopic composition of the solar nebula. The discrepancy between light 'solar' Cl isotope values to those of chondrites (around 0 ‰) has been explained by incorporation of HCl clathrate with a $\delta^{37}Cl$ value around 0 ‰, as the HCl clathrate - HCl gas isotopic fractionation ranges from 3 to 6 ‰ at ~150 K (Schauble et al., 2003; Sharp et al., 2016). HCl clathrate is stable only below ~150K (Zolotov and Mironenko, 2007). If this heavy HCl clathrate component is then mixed into chondrite parent bodies, it would provide a heavy Cl isotope component relative to isotopically primitive HCl gas. HCl clathrate has also been proposed to be the primary source of acidic fluids in chondrite parent bodies, and many chondrites are thought to have experienced alteration by Cl-bearing fluids which is consistent with the Cl isotope data (Brearley and Krot, 2013; Lewis and Jones, 2016; Zolotov and Mironenko, 2007). The distinctly higher $\delta^{37}Cl$ values of most chondrites relative to our proposed initial solar $\delta^{37}Cl$ value at ~-7 ‰ suggests that HCl clathrate was widely incorporated in chondrite parent bodies.

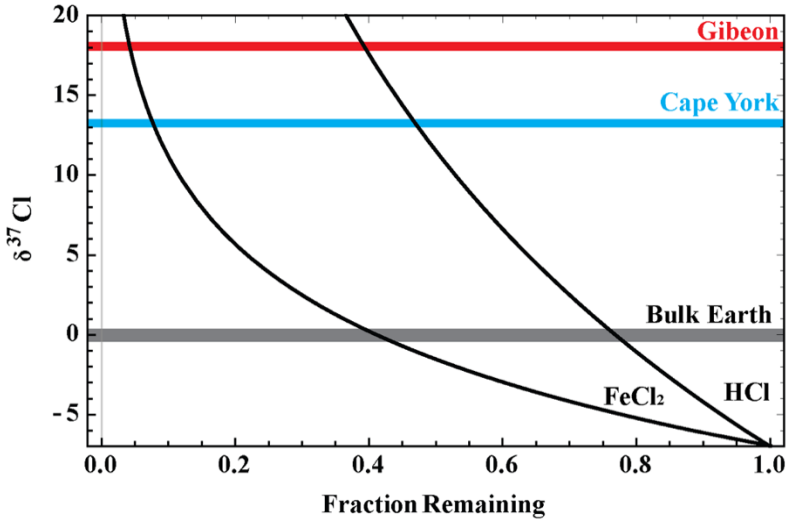

Figure 1.7: Rayleigh distillation curve following Eq. 1. Two potential isotopologues ($FeCl_2$ and HCl) are chosen with fractionation assumed to follow Graham's Law diffusion. The initial isotopic value of the parent body is assumed to be solar at -7‰. The grey band represents the chlorine isotope composition of the bulk Earth and can be explained by the degassing of approximately 20-60% of its initial chlorine. We expect that $FeCl_2$ is a more appropriate isotopologue for iron meteorites, and the isotopic compositions of Cape York and Gibeon can be accounted for by the degassing of >90% of their initial chlorine contents.

Differentiated bodies – Earth, Mars, and Moon

The chlorine isotope compositions of terrestrial, lunar, and most Martian meteorite samples are similar to or higher than the average chondritic value at around 0 ‰ (Barnes and Sharp, 2017). If we assume the initial isotopic value of the nebula to be approximately -7 ‰, then significant secondary processing must account for these higher values. Here we propose two processes capable of explaining the heavy chlorine isotope compositions of these differentiated bodies: 1) a chlorine 'overprint' by the addition of isotopically heavy chondritic material, and/or 2) ^{37}Cl enrichment associated with chlorine volatilization and preferential light isotope loss (i.e. degassing). We focus this application to Earth, as it is the best sampled planetary body that no longer retains an isotopically light solar Cl component.

Chondritic Overprinting

Addition of chondritic material to the Earth would cause an enrichment in chlorine with an isotopic composition close to 0 ‰ and add highly siderophile elements (HSEs) to the mantle. If the addition occurred prior to core formation, subsequent incorporation of HSE by metal would sequester the late-added HSEs to the core (Chou et al., 1983; Morgan et al., 2001; Walker et al., 2004) and erase any evidence for the early addition of HSEs. Instead, if the chondritic addition occurred post-core formation, then the HSE abundance would necessarily increase. Chondritic addition after core formation explains the similarity of Earth's chlorine isotope composition with chondrites and the isotopic composition of HSEs in the primitive upper mantle; however, as shown below, in order to achieve a sufficiently high δ^{37}Cl value, the HSE abundance of the mantle would be unreasonably high.

If we assume the chlorine that was initially incorporated into the Earth from the proto-planetary disk had a δ^{37}Cl value of -7 ‰, an additional 85 % chondritic Cl input is necessary to increase the δ^{37}Cl value to -1 ‰. A simple model can be constructed to test the idea of late accretion of Cl. We assume a modern-day bulk silicate Earth with 17 ppm [Cl] (Sharp and Draper, 2013) and an enstatite chondrite (EC) component containing up to 800 ppm [Cl] (Sharp et al., 2013). To account for 85 % of Earth's chlorine by ECs requires 3.6 % enstatite chondrite addition when using the highest range of chlorine concentrations. The necessary chondritic component is increased further if lower chlorine contents are used (i.e. (Clay et al., 2017)). Additionally, an independent estimate that satisfies other isotopic constraints using some amount of ordinary chondrites would require an even larger chondritic component. This estimate is well above that of Chou et al. (1983), who first proposed that Earth's HSEs could be explained by a chondritic component comprising <1 %

of Earth. A 1 ‰ chondritic addition satisfying mantle HSE concentrations by any chondrite type, would only explain 8-50 % of Earth's total chlorine, and raise the $\delta^{37}Cl$ value of the mantle up to -3.5 ‰. Earth's chlorine isotope composition therefore cannot be explained by simply overprinting the initial Cl content with chondrites unless this addition occurred before and/or was contemporaneous with core formation. The amount of chondrites required to account for Earth's high chlorine isotope composition by overprinting would be less if some degassing of the initial isotopically light chlorine occurred (thereby increasing the $\delta^{37}Cl$ value of the Earth). If a significant fraction of Earth's primordial chlorine was lost by degassing, a chondritic overprint of Earth could explain the high $\delta^{37}Cl$ value of Earth without resorting to a chondritic component that exceeds HSE constraints.

Chlorine Devolatilization During Planet Formation

The Earth and other differentiated bodies are depleted in chlorine relative to solar abundances following their respective planetary volatility trends (Fig. 1 in Sharp and Draper (2013)). If devolatilization occurred, the $\delta^{37}Cl$ values could be raised from a nebular value of -7 ‰ to a near-zero value seen on Earth. Chlorine degassing has been shown to produce significant heavy isotope enrichments resulting in high $\delta^{37}Cl$ values >35 ‰ measured in lunar samples (Barnes et al., 2016b; Boyce et al., 2015; Potts et al., 2018; Sharp et al., 2010). Isotopic fractionation from degassing assuming Graham's Law diffusion and Rayleigh Distillation can be modeled such that

$$\delta_{Final} = \delta_{Initial} + (1000 + \delta_{Initial}) * \left(F_{Remaining}^{(\alpha - 1)} - 1\right) \quad (1)$$

where

$$\alpha = \sqrt{\frac{M_1}{M_2}} \quad (2)$$

and M_1 is the mass of the light isotopologue (i.e. $Fe^{35}Cl_2$), and M_2 is the mass of the heavy isotopologue (i.e. $Fe^{35}Cl^{37}Cl$). If we consider a simple model with a primordial Earth having an initial $\delta^{37}Cl$ value of -7 ‰ following the aforementioned conditions, approximately 60 % Cl loss as $FeCl_2$ is required to increase the isotopic composition from -7 ‰ to 0 ‰ (Fig. 1.7). This estimate places Earth's initial conditions closer to the estimates for the Cl concentration of Mars at ~35 ppm [Cl], and is consistent with primitive Martian meteorites retaining a primordial Cl isotope composition (Sharp and Draper, 2013; Sharp et al., 2016; Shearer et al., 2017). A similar calculation can be made to account for the high isotopic compositions of Cape York and Gibeon. The high $\delta^{37}Cl$ values of these samples corresponds to the degassing of >90 % of their initial chlorine contents from an initial $\delta^{37}Cl$ value of -7 ‰. Assuming that differentiated bodies formed from a relatively homogenous Cl isotope reservoir as indicated from the lowest $\delta^{37}Cl$ values of CC and NC iron meteorites of -7 to -6 ‰, and that the terrestrial planets formed from the accretion of such bodies, extensive volatile loss during planet formation could explain the near-zero $\delta^{37}Cl$ value of Earth.

Conclusion

The following conclusions can be derived from the chlorine isotope compositions of iron meteorites.

1. The extreme low and high $\delta^{37}Cl$ values are inconsistent with expected terrestrial contamination sources and suggest that much of the Cl is indigenous from the parent body, partitioned into the metal during planetary differentiation. The wide ranges in Cl content and $\delta^{37}Cl$ values of individual

iron meteorite groups suggest that Cl was potentially devolatilized throughout parent body processing.

2. As no relevant processes are known to decrease chlorine isotope values in a planetary body, and the $\delta^{37}Cl$ values of both CC and NC iron meteorites are similarly low, we suggest the solar nebula was not significantly stratified with respect to chlorine isotopes and the lowest $\delta^{37}Cl$ value of -7.2 ‰ in Hoba IVB most closely represents the isotopic composition of the solar nebula.
3. The high $\delta^{37}Cl$ values found in Cape York and Gibeon, both of which have evidence for extreme volatile loss and shock, suggest that devolatilization occurred during planet building in the early solar system. These samples have presumably lost >90% of their primordial Cl by degassing following dismemberment of their parent bodies.
4. On the basis of experimental data for metal-silicate Cl partitioning, the average bulk Cl content is consistent with a complimentary silicate source having similar concentrations as chondrites.

2. THE Cl ISOTOPE COMPOSITION AND HALOGEN CONTENTS OF APOLLO-RETURN SAMPLES

Introduction

Over the 50 years since the Apollo missions, chemical and isotopic compositions of lunar materials have revolutionized our collective scientific understanding of planetary materials. A major finding is the recognition that lunar materials are strongly depleted in volatiles relative to Earth and that they exhibit a range of volatile-element stable isotope anomalies (Barnes et al., 2016a; Barnes et al., 2016b; Boyce et al., 2015; Day and Moynier, 2014; Day et al., 2017b; Kato and Moynier, 2017; Kato et al., 2015; Potts et al., 2018; Pringle and Moynier, 2017; Robinson et al., 2016; Saal et al., 2013; Sharp et al., 2010; Wing and Farquhar, 2015). Studying these isotopic systems allows us to better understand volatile sources and mechanisms by which volatile elements are lost throughout planetary evolution. The chlorine isotope system is of particular interest because the Cl isotope values of the Moon are uniquely high. The high values, and increases in the Cl isotope composition of a planetary body from the nebular baseline (around -5 to -7 ‰ as compared to Earth) are related to the amount of Cl that was lost throughout its accretionary and differentiation history (Gargano and Sharp, 2019; Williams et al., 2016).

Lunar materials have extremely elevated δ^{37}Cl values relative to the bulk Earth value of ~0 ‰ (Sharp et al., 2013; Sharp et al., 2010). Sharp et al. (2010) measured the bulk and in-situ Cl isotope compositions of a variety of lunar lithologies and observed a range in δ^{37}Cl values from -0.7 to 24.5 ‰. These authors interpreted these results to suggest that anhydrous degassing of lunar magmas resulted in significant Cl isotope fractionation. Many workers have since focused on in-situ measurements of late-crystallizing apatite due to the relative

ease of this analysis by ion microprobe methods (i.e. SIMS or NanoSIMS). As a result, bulk-rock Cl isotope measurements are few, with limited comparison to the *in situ* analyses. The δ^{37}Cl values of lunar apatite have been shown to span a large range from 2.2 up to 81.1 ‰ (Jolliff et al., 2018; Wang et al., 2019). Typically, the highest δ^{37}Cl values in lunar apatite are observed within lithologies such as the Mg-suite (McCubbin and Barnes, 2020a), KREEP-rich basalts and impact lithologies (Potts et al., 2018) which have largely been explained in terms of a urKREEP component (residual melt of lunar magma ocean, Warren and Wasson, 1979) with a characteristically high δ^{37}Cl value (Barnes et al., 2016b; Boyce et al., 2015). This conclusion was initially supported by trends in bulk-rock REE content and average apatite δ^{37}Cl value (Barnes et al., 2016b; Boyce et al., 2015), although this trend is not seen in some lithologies (Potts et al., 2018; Treiman et al., 2014).

There are two relevant underlying issues that have not been adequately addressed. The first is that for the limited samples in which both bulk and in situ apatite data are available, the apatite invariable has a higher δ^{37}Cl value. The second is that the range of isotope values in apatite measured within a single thin section can exceed 10 ‰ (e.g., Barnes et al., 2016b). If the high δ^{37}Cl values of some lunar samples is explained by wide-scale incorporation of a urKREEP component, then the variation at the thin-section scale should be minimal. A logical explanation for the range of apatite δ^{37}Cl values at a small scale is that local degassing, at least in-part, controls the chlorine isotope composition of apatite. Extensive degassing of halogens is seen on Earth in volcanic systems (Balcone-Boissard et al., 2010; Noble et al., 1967) and is expected in lunar basalts as well. This explanation, however, opens the possibility that the chlorine isotope compositions of late-formed apatite may not be representative of the bulk rock, and instead preserve the composition of the last

melt following extensive degassing. To test this hypothesis and to also address the mechanisms of planetary halogen-loss, we analyzed a suite of lunar lithologies for their bulk Cl isotope compositions and mare basalts for halogen (F, Cl, Br, I) contents.

Methods

Cl isotope compositions of a suite of lunar materials were measured following the methodology of Sharp et al. (2010) at the University of New Mexico. Water-soluble chloride (WSC) was collected by leaching powders with de-ionized water overnight. Structurally-bound chloride (SBC) was extracted by pyrohydrolysis on the residual powders following WSC leaching. Leached powders were rinsed an additional 3 times before drying to remove any residual WSC component, dried and then loaded into quartz tubes. Samples were then subsequently pyrolyzed by melting with an oxy-propane torch in a stream of water vapor within a distillation apparatus (Barnes et al., 2016b). An aliquot of parent solutions were measured at NASA JSC for Cl, Br and I contents by ICPMS following the methodology of (Noble et al., 1967). Average 1σ deviation on Cl, Br and I contents were 2.2, 11.4, and 1.14 %, respectively. Additional information regarding halogen measurements can be found in the appendix. Fluorine contents were measured at UNM using Ion Chromatography.

A split of the sample solutions were reacted with 5 mL of 50 % HNO_3 overnight in order to remove sulfur, followed by an addition of 1 mL of 0.4 M $AgNO_3$ overnight in a light-free environment in order to precipitate AgCl. AgCl was then filtered, dried, and loaded into 8 mm pyrex tubes. Sample tubes were then evacuated, 10 μL of CH_3I was added and subsequently flame sealed. Sealed tubes were then reacted at 80 °C for 48 hours to produce CH_3Cl as an analyte. Introduction of CH_3Cl into the mass spectrometer took place by

cracking sealed sample tubes in a stream of He and collecting the CH_3Cl in a liquid N_2 trap. This trap was subsequently warmed, and the sample gas was passed through a GC column held at 80 °C to separate excess CH_3I from the CH_3Cl analyte. A small 'sniffer' capillary was used to detect when CH_3Cl had completely left the column and was trapped in a second liquid N_2 trap. Flow direction was then reversed prior to the incorporation of CH_3I, which resulted in a pure CH_3Cl sample. Trapped CH_3Cl was then released by warming the LN2 trap and introduced via an open split into the mass spectrometer. Chlorine isotope compositions were measured in continuous flow on a Delta^{PLUS}XL. Measurements were standardized relative to SMOC with a long-term reproducibility of this method being $<\pm 0.25$ ‰ in our laboratory.

Results

Halogen Contents

Cl concentrations were measured on both water-soluble chloride (WSC) and insoluble or structurally-bound chloride (SBC) (Table 2.1). Concentrations of the other halogens (F, Br, I) were measured only on previously leached samples, such that the water-soluble fraction was removed prior to analysis. Previous halogen measurements of lunar samples show that the water-soluble F fraction is minimal (Reed and Jovanovic, 1973) and that the Cl/Br ratios are similar between the water-soluble and structural components (Reed and Jovanovic, 1970). We therefore assume that our F analyses are a reasonable approximation for the total F in the rock, and that Cl/Br ratios of the insoluble fraction are similar to that of the bulk-rock.

For mare basalts, WSC contents range from 1.9 to 12.3 ppm while SBC contents are more restricted, ranging from 1.1 to 5.8 ppm (Table 2.1). For all mare samples, 65±10 % of total Cl resides in the water-soluble fraction. If the WSC is derived from vapor exsolution and deposition, then a significant fraction of the degassed component appears to be retained in the lunar samples. This large fraction of WSC is consistent with studies of terrestrial igneous rocks in which up to 90 % of Cl is lost by degassing (Balcone-Boissard et al., 2010; Noble et al., 1967; Wang et al., 2014). The mare basalts also have more variable Br concentrations relative to Cl (Table 1) and overall have distinctly lower Cl/Br ratios compared to MORB (Jambon et al., 1995; Kendrick et al., 2012). The three anorthosite samples average 9 ppm total Cl with variable, but roughly equal proportions in the SBC and WSC.

The F contents of lunar materials range from 4.7 to 38.1 ppm, with highlands lithologies exhibiting a marked depletion relative to mare basalts (Fig. 2.1). F contents appear to be in-part related to Ti contents, with high-Ti basalts being the most F-rich from 20.0 to 38.1 ppm. A best fit to the mare samples is a Cl/F = 0.32 (R^2=0.62). The bulk Cl/F ratios are higher than the average Cl/F ratios of lunar apatite, consistent with the result that the majority of Cl resides in the water-soluble fraction (Table 2.1). The Cl/F ratios of the insoluble fraction (rinsed samples) overlap the average Cl/F ratio of lunar apatite, further supporting this conclusion. Lastly, the F and Cl concentration of lunar samples are depleted by an order-of-magnitude relative to Earth.

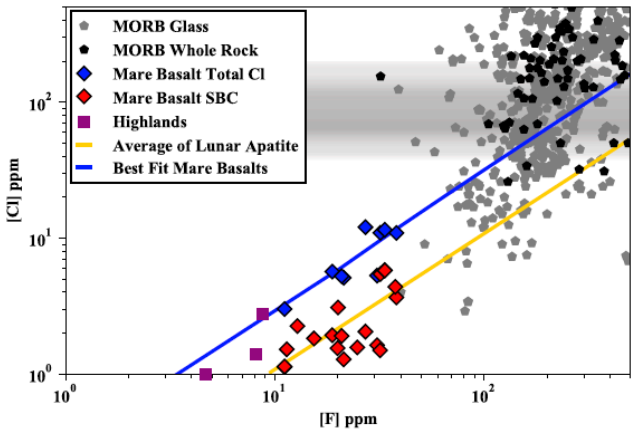

Figure 2.1: F vs. Cl contents (ppm) of terrestrial mid-ocean ridge basalts (MORB) (whole-rock – black pentagons and glasses – grey pentagons) and lunar materials. Blue diamonds are the total bulk Cl contents of mare basalts (WSC + SBC). Red diamonds are the structurally-bound Cl contents. Highlands Cl and F abundances are from the SBC fraction only. Data of MORB collected from the PETDB database. Apatite F and Cl data gathered from (Barnes et al., 2019; Barnes et al., 2016b; McCubbin et al., 2015) and are seen in the red line. Blue line represents the best-fit for mare basalts. Faded grey horizontal bar is the accepted range of Cl abundances in MORB (Jambon et al., 1995; Wörndle et al., 2019). Higher Cl values are likely contamination. Cl and F error are smaller than symbol size.

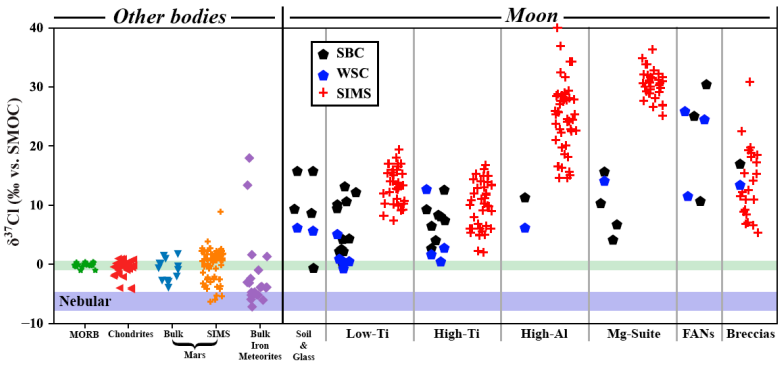

Figure 2.2: Chlorine isotope values of planetary and terrestrial materials. MORB data from (Sharp et al., 2013a). Bulk lunar data from (Sharp et al., 2010; Shearer et al., 2014). SIMS data: low-Ti and high-Ti basalts from (Barnes et al., 2019; Boyce et al., 2015

Table 2.1: Halogen contents and chlorine isotope compositions of lunar materials.

Sample	Lithology	Structural Cl		Water-Soluble Cl		Structural-halogens			Fraction WSC	Bulk δ^{37}Cl
		[Cl] (ppm)	δ^{37}Cl	[Cl] (ppm)	δ^{37}Cl	[I] (ppb)	[Br] (ppb)	[F] (ppm)		
12002	Low-Ti	2.25	9.4			42.65	138.47	12.81		
10017–405 (int)	High-Ti-K	4.37	12.53			206.12	55.26	37.63		
10017–400 (ext)	High-Ti-K	3.66	9.23	7.25	12.63	28.94	20.16	38.11	0.66	11.49
10020–255	High-Ti	1.9	8.03	3.34	0.39	16.09	14.67	20.84	0.64	3.16
10044–566	High-Ti	1.63	1.63	3.67	3.67	90.77	56.43	30.78	0.69	3.04
12018–277	Low-Ti	1.93	10.05	3.74	5.03	45.50	29.09	18.80	0.66	6.74
12054–146	Low-Ti	2.05	2.14	9.99	-0.78	31.77	6.45	27.08	0.83	-0.28
12054–150	Low-Ti	5.43	4.29	5.51	0.43	60.74	32.96	31.91	0.50	2.35
12063–343	Low-Ti	1.28	4.19	3.83	0.48	30.27	2.69	21.32	0.75	1.41
14053–305	High-Al	5.80	11.24	5.71	6.11	20.11	14.90	33.49	0.50	8.70
15016–240	Low-Ti	1.12	2.14	1.88	0.84	22.26	12.98	11.12	0.63	1.33
15535–165	Low-Ti	1.52	12.12			27.51	162.36	11.39		
15556–258	Low-Ti	1.83	10.57			38.45	153.85	15.37		
70215–389	High-Ti	1.49	6.42			15.09	6.53	31.83		
70255–56	High-Ti	1.57	7.37			24.13	20.87	24.75		
71135–34	High-Ti	3.08	4.01			554.00	34.39	20.02		
74275–355	High-Ti	1.55	8.28			20.80	10.16	19.92		
76335	Troctolite	1.00	4.07			41.45	9.82	4.66		
77215	Cataclastic Norite	2.76	10.26			42.80	15.84	8.77		
78235	Shocked Norite	1.4	6.67			267.8	11.43	8.07		
60015	Cataclastic Anorthosite	0.52	10.5	1.71	11.37				0.77	11.17
60025	Ferroan Anorthosite	12.1	30.2	3.60	24.45				0.23	28.88
62255	Anorthosite	4.69	25.21	3.44	25.69				0.42	25.41

Chlorine Isotope Compositions

Chlorine isotope values are reported in per mil notation (‰) relative to standard mean ocean chloride (SMOC)(Kaufmann et al., 1984). The average δ^{37}Cl value for total Cl in mare basalts (sum of WSC + SBC) is 4.2±3.9 ‰ (*n*=9). The structural component averages 7.3±3.6 ‰ (*n*=17), while the water-soluble fraction averages 2.1±2.4 ‰ (*n*=9) (excluding an anomalous WSC value at 12.6 ‰, 10017-405) (Fig. 2.2). There is no statistically significant difference between the δ^{37}Cl values of the structurally-bound component for high-Ti basalts (7.2±3.3 ‰, *n*=8) and low-Ti basalts (6.9±4.1‰, *n*=8) (Two tailed T-test: t(14) = 0.175, p-value = 0.86). Figure 2.2 clearly indicates that the water-soluble fraction for most of the samples is significantly lower than that of the structurally-bound Cl. Excluding WSC in sample 10017-405, the isotopic compositions of the WSC and SBC are distinctly different in mare basalts (Two tailed T-test: t(24) = 3.881, p-value = 0.0007). The three ferroan anorthosites (FANs) samples have much higher δ^{37}Cl values than the mare basalts of 10.5, 30.2, and 25.2 in the SBC, and 11.4, 24.5, and 25.7 ‰ in the WSC in samples 60015, 60025, and 62255, respectively. The three non-FAN highlands samples (two norites and a troctolite – 76335, 78235, and 77215) have SBC δ^{37}Cl values of 4.07, 6.67 and 10.3 ‰, respectively, similar to the mare basalts.

The δ^{37}Cl values of published SIMS analyses of apatite grains from high-Ti and low-Ti mare basalts averages 9.4±4.1 ‰ (Barnes et al., 2019; Boyce et al., 2015), a value that is higher and significantly statistically different from the bulk data of 3.3±3.0 ‰ excluding the WSC of 10017-405 (Two tailed T-test: t(78) = 4.078, p-value = 0.0001), but similar to the structurally bound values of 7.3±3.6 ‰ (Two tailed T-test: t(87) = 1.940, p-value = 0.0555).

The discrepancy between bulk and *in situ* $\delta^{37}Cl$ values is even more striking for the high-Al and three highlands samples where apatite has $\delta^{37}Cl$ values clustering from 20 to 30 ‰ compared to the SBC average of 8.1 ‰. Clearly, the $\delta^{37}Cl$ values of apatite in these samples are not representative of the bulk-rock. Lastly, no trend is observed between Cl concentration and $\delta^{37}Cl$ values (except for FANs, see Fig. 2.4), whereas a poor correlation is observed between F contents and bulk total $\delta^{37}Cl$ values.

Discussion

Halogen Degassing

The Cl/F ratios of mare basalts are similar to those of the least altered MORB basalts, but their concentrations are an order-of-magnitude lower (Fig. 2.1). As F is thought to be less volatile than Cl, this result suggests that ~90 % of halogens were lost during an extremely energetic process, such as the Giant Impact, assuming that the lunar protolith was similar to Earth. Although we anticipated that Cl/Br and Cl/F ratios would correlate with $\delta^{37}Cl$ values given the fact that Br is significantly heavier than Cl, and F is less volatile, no trends are observed. There is also no apparent relationship in the Cl abundance and $\delta^{37}Cl$ values, and only a weak relationship between F abundance and $\delta^{37}Cl$ value, which we interpret as a manifestation of the high $\delta^{37}Cl$ values from F-rich apatite grains. Lastly, Br contents are more variable than Cl, which may be related to differing degrees of retention as the non-soluble 'structurally-bound' component. Unfortunately, we were unable to measure water-soluble bromide in any sample as they had already been processed prior to this work, leaving our Br/Cl relationship ambiguous at present.

Chlorine Isotope Composition of Mare Basalts

The majority of Cl in mare basalts is hosted in the water-soluble fraction (Table 1). The water-soluble and structurally-bound fractions average 5.0 and 2.5 ppm Cl, respectively. The $\delta^{37}Cl$ values of the WSC average 2.0±2.5 ‰ (excluding 10017-405) and are far lower than those of the SBC (7.3±3.6 ‰) (Fig. 2.3). Similar differences have been seen in $\delta^{66}Zn$ values of water-soluble and structural Zn in Rusty Rock (66095), although the effect is far less pronounced (Day et al., 2017b) and importantly, the $\delta^{66}Zn$ values are anomalously low compared to Earth, while the $\delta^{37}Cl$ values are high. If the WSC and SBC were in isotopic equilibrium, we would expect their $\delta^{37}Cl$ values to be almost identical, as the fractionation between all chloride-bearing phases is very small at high temperatures (Schauble et al., 2003). Instead, the isotopically light WSC component is most readily explained by preferential local degassing of ^{35}Cl and subsequent deposition of the light vapor as a water-soluble salt during the waning stages of crystallization. The degassing may occur along fractures or into fluid inclusions and/or vesicles (Fortin et al., 2017). Documentation of visible water-soluble Cl-bearing phases, however, is scarce due to their deliquescent nature and resulting poor preservation. Cl-bearing phases such as akaganéite, lawrencite, and Cl-bearing sulfates have been described in Rusty Rock 66095 (El Goresy et al., 1973), and over 60 % of Apollo 16 rocks contain a chlorine-bearing 'rust' such as akagenéite which is thought to the be hydrated byproduct of $FeCl_2$ (Hunter and Taylor, 1982). Pyroclastic glasses have also been observed to be coated in NaCl (McKay and Wentworth, 1993). In general, the trace amounts of Cl-bearing water-soluble phases have simply not been described in lunar materials due to either a lack of attention or trace deliquescent occurrences being erased by sample preparation/storage procedures.

Arguably the most striking observation in this work is the fact that in no samples measured to date do the bulk $\delta^{37}Cl$ values match those of apatite. While the higher Cl/F ratio of the bulk-rock compared to lunar apatite supports the observation that significant Cl resides outside of the apatite in the mare basalts (Fig. 2.1); the poor relationship with $\delta^{37}Cl$ values and F contents, suggests that other F-bearing phases are also present. As K-rich mesostasis glass is commonly cited in the literature to occur alongside apatite (Potts et al., 2016) we measured the Cl and F contents of trapped immiscible melts in sample 10050 (low-K, high-Ti basalt) by electron microprobe. Both the K-rich and Fe-rich melts contained significant amounts of F and Cl (1480, 160 and 5450, 230 ppm F and Cl, respectively). Although no Cl isotope analyses of these Cl-rich glasses have been made – these phases clearly represent another source of Cl and F

in lunar materials and partly explain the poor relationship with F contents and $\delta^{37}Cl$ values.

In terms of the individual components, lunar apatite has the highest $\delta^{37}Cl$ values in mare basalts, averaging 12.6±4.8 ‰ (high-Ti) and 9.9±4.1 ‰ (low-Ti). Apatite crystallizes after most of the Cl has been lost to the vapor phase or sequestered in other minerals or glass. The $\delta^{37}Cl$ values of the apatite are therefore not representative of the bulk-rock or lunar lithologies in general, but rather record the $\delta^{37}Cl$ values of the last stages of crystallization. The loss of a light Cl-bearing vapor raises the $\delta^{37}Cl$ value of the residual Cl which is ultimately incorporated in late-forming apatite and glass. The large spread in $\delta^{37}Cl$ values in apatite measured within individual thin sections or even single grains is consistent with apatite forming during the waning stages of crystallization and the final phases of local vaporization.

The overall calculated bulk $\delta^{37}Cl$ value of the mare basalts averages 4.2 ‰, higher than the Earth value, but far lower than the apatite values (Fig. 2.2). This higher $\delta^{37}Cl$ value of the bulk-Moon relative to Earth, alongside the poor relationship with F/Cl and $\delta^{37}Cl$ values despite the fact the F is less volatile, suggests that lunar halogen depletion and ^{37}Cl-enrichment likely resulted from a planet-wide event, presumably the Giant Impact.

Chlorine Isotope Compositions of the Highlands Lithologies

The SBC $\delta^{37}Cl$ values from troctolite 76335 (4.1 ‰) and two norites 77215, 78235 (10.3 ‰, 6.7 ‰) measured are similar to the mare basalts. In contrast, the $\delta^{37}Cl$ values of apatite grains from the highlands lithologies (30.6±2.3 ‰) and the Al-rich basalts (24.9±6.0 ‰) are far higher than those of the mare basalts (Fig. 2.2). The low bulk SBC $\delta^{37}Cl$ values of highlands troctolites and norites compared to their apatite requires, from mass balance constraints, that the majority of the SBC has a low $\delta^{37}Cl$ value and, like the mare basalts, mainly resides somewhere besides the apatite. This conclusion is supported by the fact that the highlands lithologies have far less F, but the same amount of Cl, relative to basalts. Assuming that the majority of F resides in apatite, then the amount of apatite in these rocks is low compared to the mare basalts. Only the ferroan anorthosites have anomalously high bulk chlorine isotope values, similar to those found in highlands apatite. The $\delta^{37}Cl$ values of the SBC and WSC components from the three FANs are similar to each other and exceptionally high (10.5 to 30.2 ‰) compared to all other lithologies.

It has been suggested that the high $\delta^{37}Cl$ values of the highland rocks apatite is due to the incorporation of a high $\delta^{37}Cl$-bearing urKREEP component (Barnes et al., 2016b; Boyce et al., 2015). urKREEP is the hypothetical reservoir representing the final residue of LMO

crystallization (Warren and Wasson, 1979) and is therefore exceptionally enriched in incompatible trace elements. It has been proposed that urKREEP magma(s) underwent significant degassing and preferentially lost ^{35}Cl to space (Boyce et al., 2015). These high $^{37}Cl/^{35}Cl$ melts were then subsequently incorporated into the highlands lithologies raising their $\delta^{37}Cl$ values. The correlation between the REE abundances and the $\delta^{37}Cl$ values of apatite have been used in support of this argument (Barnes et al., 2016b; Boyce et al., 2015). The causal relationship between urKREEP incorporation and high $\delta^{37}Cl$ values, however, has not been established. One would expect that if the addition of the isotopically heavy and Cl-rich urKREEP occurred, then the Cl content of the rocks would also increase. In other words, in order to raise the $\delta^{37}Cl$ values of the urKREEP-contaminated lithologies, it is necessary to introduce additional heavy Cl. However, the Cl contents of the highlands lithologies are lower, not higher than the mare basalts. Additionally, the FANs are the only lithology to record the high bulk $\delta^{37}Cl$ values characteristic of urKREEP, yet they do not contain apatite, nor do they have clear evidence of a urKREEP component.

An alternative explanation for the high $\delta^{37}Cl$ values of the highland lithologies is their markedly different cooling history compared to mare basalts. The norites, troctolites and anorthosites all cooled very slowly as part of a planet-wide cooling event on the order of 10 °C/Ma (Marks et al., 2019). In contrast, the mare basalts cooled on the order of ~1 to 20 °C/hr (Shearer et al., 1989). The slowly cooled highlands lithologies can therefore be expected to have lost far more Cl during degassing, compared to rapidly cooled mare basalts. Conversely, the high $\delta^{37}Cl$ values of high-Al basalt apatite may also be in-part explained by vapor phase metasomatism (Potts et al., 2018). As described below, the effect on the Cl

isotope composition of the different rock types can be evaluated using the concept of Rayleigh distillation.

Add partial Cl-Retention section

If, instead, the system is open to vapor loss during the early, high-temperature phase of cooling, then different isotope values will be achieved compared to the closed-system case above. This is what we expect for the slowly cooled highlands rocks. During the initial stages of degassing, temperatures would be too high for the vapor phase to condense (Day et al., 2017b), and the light vapor component would not be retained. Given the extremely slow cooling rates, the vapor would migrate out of the system and be lost from the system with the $\delta^{37}Cl$ value of the rock progressively increasing. Loss of a significant fraction of the light vapor, as expected in the slowly-cooled highlands rocks, results in high $^{37}Cl/^{35}Cl$ in the residue, and thus explains the elevated bulk values and the very high $\delta^{37}Cl$ values of their late-formed apatite grains.

Anomalous Cl and Zn isotope compositions of the ferroan anorthosites

The FANs are thought to represent the primordial lunar crust that formed by the accumulation of buoyant plagioclase over the lunar magma ocean (LMO) (Snyder et al., 1992; Wood et al., 1970). Standard LMO crystallization models state that the primitive lunar crust would have formed a thermally insulating 'lid' on the crystallizing magma ocean, potentially limiting volatile loss to space (Barnes et al., 2016b; Day and Moynier, 2014; Elkins-Tanton and Grove, 2011). However, volatiles could have continually percolated through the crust post-crystallization (Hunter and Taylor, 1982), possibly during a global mode of volcanic "heat-pipes" transporting melt to the surface (Moore et al., 2017), or be lost by crust-breaching impacts (Barnes et al., 2016b). The bulk $\delta^{37}Cl$ values of FANs are the

highest measured in planetary materials to date and positively correlate with Cl contents, opposite from what would be expected from a simple open system degassing trend (Fig. 2.4). Instead, the data suggest incorporation and deposition of a heavy Cl-bearing vapor into the FANs. This is consistent with Cl being incorporated in the FANs only after most had passed through the lithology as a gas phase. Zn isotope compositions on the other hand, have a negative correlation with concentration suggesting that the FANs incorporated an early degassed light Zn-bearing phase.

Exotic sources of Cl and Zn to the FANs such as chondrites or regolith can be discounted on the basis that both Cl and Zn isotope values, as well as elemental concentrations, are a poor match. A heavy urKREEP source could also be invoked to explain the FANs high δ^{37}Cl values. Some KREEPy lithologies (i.e. Mg-suite) are thought to represent plutonic emplacements into the lunar crust and therefore the proximity of the FANs and urKREEP is certainly feasible. McCubbin et al. (2015) estimates KREEP melts likely contained 1.4 wt % Cl when apatite began to crystallize which record the characteristically high Cl isotope compositions. Mixing with 0.1 % KREEP with a δ^{37}Cl value of +30 ‰ could explain the highest [Cl] and δ^{37}Cl reported here, however, this mixing component is not seen in elevated REE patterns or any other geochemical system to our knowledge. Additionally, the FANs were likely emplaced prior to urKREEP formation (Shearer and Papike, 2005), and their Zn isotope compositions are also distinct from KREEPy samples, with comparable [Zn] but with significantly lower δ^{66}Zn values (Kato et al., 2015). In total, assimilation of urKREEP is inconsistent with both Cl and Zn isotope data (Shearer et al., 2015). We instead propose that the Cl and Zn isotope compositions resulted from vapor deposition from the degassing of underlying magma(s).

While it has generally been assumed that Zn and Cl both degas as chlorides (and ZnS), the isotopic compositions of the FANs require that these two elements are decoupled (see also, Day et al., 2017). Assuming that Zn and Cl had similar volatilities, they would vaporize and condense over roughly the same temperature interval. If this were the case, low δ^{66}Zn values would occur alongside low δ^{37}Cl values, which is clearly not seen in the data for the FANs or other samples such as Rusty Rock. Furthermore, it is difficult to explain the very low δ^{66}Zn values of -13.7 ‰ found in Rusty Rock, or -11.4 ‰ in 65315 using a simple Rayleigh fractionation model if $ZnCl_2$ is assumed to be the degassing species and the initial δ^{66}Zn value of the source was close to 0 ‰. This is because the maximum $1000ln\alpha$ value for $ZnCl_2$ is only -7.4 ‰, far less than the ~13-14 ‰ fractionation for Rusty Rock (Day et al., 2017b). The trends seen in Figure 2.4 make coupled degassing equally unlikely for the FANs.

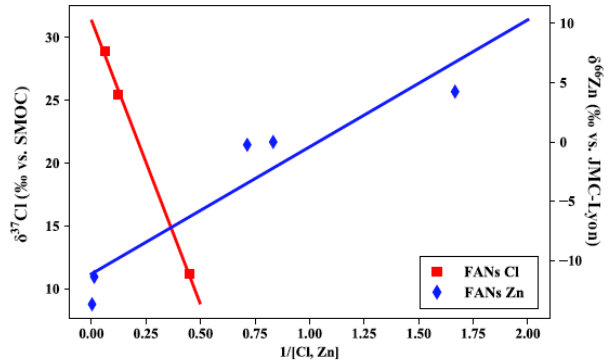

Figure 2.1: Plot of 1/[Cl, Zn] (ppm) vs δ^{37}Cl and δ^{66}Zn value for FANs. The y intercept gives the δ^{37}Cl value of the infiltrating gas at 31 ‰. An initial concentration of 1.5 ppm (before infiltration of Cl vapor) gives a δ^{37}Cl value of pristine FAN of 4 ‰. Zn data from (Kato et al., 2015). Red line is the best for the Cl data with an R^2 = 0.9982. Blue line is the best fit for the Zn data with an R^2 = 0.8847.

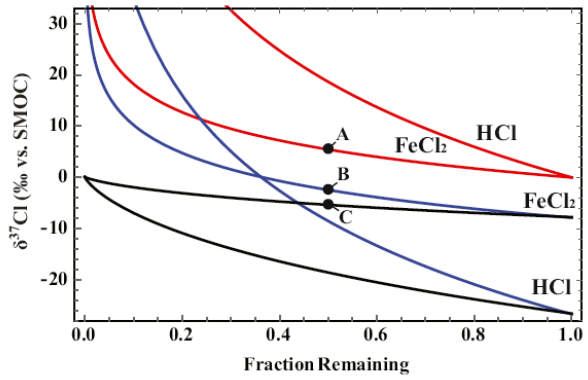

Figure 2.2: Rayleigh Distillation models of chlorine degassing into a vacuum assuming α values following Graham's Law and Eq. 1. Red lines show the isotopic composition of the residual fraction (i.e. the degassing reservoir). Blue line shows the instantaneous isotopic composition of vapor derived from the residual melt. Black lines show the isotopic composition of the cumulative vapor component. The isotopic compositions of lunar materials are readily achieved by the degassing of $FeCl_2$ or HCl.

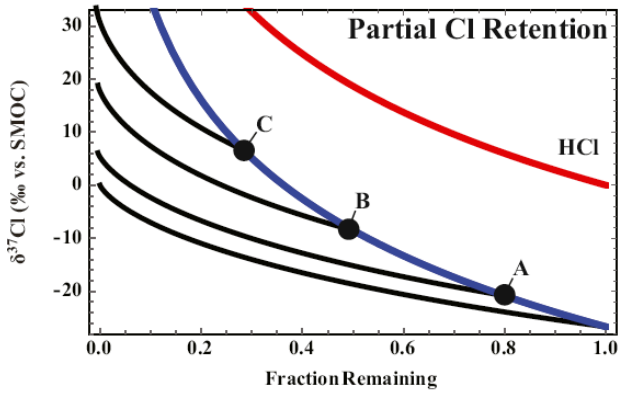

Figure 2.3: Modified Rayleigh Distillation model showing partial chlorine retention. Line legend is the same as in Fig. 2.3. In this model, we choose to use HCl as an isotopologue capable of reaching the largest range of $\delta^{37}Cl$ values. Three different arbitrary points are chosen for schematic purposes (A, B, C) in which to vapor derived from an underlying melt is retained. If vapor begins to be retained at point A and is completely incorporated it will have a $\delta^{37}Cl$ value of +6 ‰ with 80 % of initial [Cl]. Likewise, for B with a $\delta^{37}Cl$ of +20 ‰ and 50 % of initial [Cl], and lastly C with a $\delta^{37}Cl$ of +34 ‰ and 30 % initial [Cl]. The partial retention of chlorine following this model will show increasing $\delta^{37}Cl$ with [Cl].

We instead propose that the low $\delta^{66}Zn$ values are better explained by the degassing of Zn^o from the underlying magma and subsequent deposition in the FANs at relatively high temperatures, as suggested by recent thermodynamic modeling (Renggli et al., 2017). Importantly, the $1000ln\alpha$ value of Zn^o degassing is -15.4 ‰, compared to only -7.4 ‰ for $ZnCl_2$ (assuming Grahams law applies). In contrast to Zn^o gas, which condenses at around 700 °C, metal chloride species are volatile above 500 °C (Renggli et al., 2017; Renggli and Klemme, 2020). In the most extreme case where Cl is transported as HCl, Cl would never condense. It would only become incorporated in a rock when it reacts to form a solid chloride phase (e.g., $FeCl_2$). Zn^o gas derived from the underlying magma ocean would degas through the FANs where the high condensation temperatures of ZnS or Zn^o would lead to only a small amount of Zn migrating to the higher and colder levels of the FANs. As the FANs cool, the migration distance of the Zn decreases from the underlying magma, such that only the early, light Zn would be found in the upper level of the FANs, which is presumably what is sampled in the Apollo collection. Cl differs from Zn because it has a lower condensation temperature. As long as the anorthositic lid remained hot, Cl would not condense, but rather pass through the FANs. Retention of this vapor percolating through the FANs would only have occurred when temperatures dropped sufficiently for Cl-bearing vapors to condense (e.g., Day et al., 2017b). If most of the Cl had already been lost from the underlying magma before it could condense in the FANs, then the $\delta^{37}Cl$ value of the vapor that was ultimately incorporated would be isotopically heavy (Fig. 2.5). In the case of HCl degassing, loss of 90 % of the total Cl would raise the vapor value to over 30 ‰. For $FeCl_2$, the amount lost would

be closer to 99 %. Addition of the heavy vapor would have increased both the Cl concentration and the δ^{37}Cl value, and indeed, a negative linear mixing trend of 1/[Cl] vs. δ^{37}Cl is seen in the limited data for the FANs, supporting this hypothesis (Fig. 2.4). In total, the partial Cl-retention model in the FANs suggests they were only partially effective in limiting volatile-loss to the surface and future modeling of LMO volatile-loss should account for the continued loss of volatiles after FAN crystallization (Dhaliwal et al., 2018).

Conclusion

There are several important findings in this work. First, the bulk Cl isotope compositions of lunar mare basalts is 3-4 ‰ higher than the bulk Earth and the halogen concentration of lunar lithologies is an order of magnitude lower than MORB. We propose that these differences are the result of an early planetary-wide halogen depletion and isotope fractionation associated with the Giant Impact, similar to what is seen for other volatile elements (Vollstaedt et al., 2020).

Second, we find a large isotope fractionation between the water-soluble and structurally-bound chloride within individual samples. Approximately 65 % of Cl in the mare basalts is hosted in a water-soluble with an average δ^{37}Cl value of 2.0±2.5 ‰ (excluding 10017-405). The remaining insoluble or structurally-bound chloride averages δ^{37}Cl values of 7.3±3.6 ‰.The large difference in the isotopic composition of these two coexisting Cl reservoirs cannot be explained in terms of equilibrium, high-temperature isotope fractionation (Schauble et al., 2003). Instead, the low δ^{37}Cl values of the vapor component are explained by kinetic isotope fractionation during local degassing. The δ^{37}Cl values of apatite grains are significantly higher than the bulk δ^{37}Cl values in all lithologies. Rather than being representative of the bulk-rock, apatite δ^{37}Cl values record information about the final

stages of crystallization. Local degassing during late-stage crystallization explains the wide range of δ^{37}Cl values seen in apatite grains within individual thin sections.

Third, the highlands rocks have extremely elevated δ^{37}Cl values in apatite, but only moderately elevated bulk δ^{37}Cl values (Fig. 2.2). We explain the high δ^{37}Cl values of the late-formed apatite as being a result of the slow cooling rate for these plutonic lithologies resulting in extensive Cl degassing prior to apatite formation. Compared to the mare basalts, cooling of the magma ocean and overlying solid lithologies was many orders of magnitude slower. The very slow cooling would result in a larger fraction of Cl to be lost to the vapor phase, thereby causing the residual melt to have increasingly high δ^{37}Cl values. This effect is especially notable for the late-formed apatite which records the highest δ^{37}Cl values (Fig. 2.4).

Finally, the FANs uniquely have extremely high δ^{37}Cl values for both the WSC and SBC (Fig. 2.2), although they have no urKREEP component, nor apatite grains. This result is at odds with the hypothesis that the high δ^{37}Cl values of highlands rocks is related to incorporation of urKREEP. Instead, we suggest that their extremely high δ^{37}Cl values are explained as the product of condensation of a heavy Cl-bearing vapor. The anorthosite layer above the crystallizing magma ocean would have been extremely hot post crystallization. The Cl-bearing vapor derived from the underlying magma would therefore pass through the anorthositic lid without condensing. Only after extensive degassing would the anorthosite layer cool sufficiently for the Cl-bearing vapor to condense. By the time this occurred, the vapor would have evolved to a very high δ^{37}Cl value (>30 ‰) which is supported in the positive correlation between Cl content and δ^{37}Cl values. In contrast, Zn has a much higher condensation temperature (over 700 °C for ZnS). Only the earliest, and thereby the

isotopically lightest Zn^o vapor would penetrate to the upper layers of the FANs resulting in the incorporation of Zn with exceptionally low $\delta^{66}Zn$ values. Once the FANs cooled below 700 °C, Zn migration distances would be severely curtailed. The very low $\delta^{66}Zn$ values of FANs (and Rusty Rock) are thereby best explained by degassing of Zn^o where the $1000\ln\alpha$ value is significantly higher than for higher mass Zn-bearing compounds.

3. THE Zn, S, AND Cl ISOTOPE COMPOSITIONS OF MARE BASALTS: IMPLICATIONS FOR THE EFFECTS OF ERUPTION STYLE AND PRESSURE ON VOLATILE ELEMENT STABLE ISOTOPE FRACTIONATION ON THE MOON

Abstract

We compare the stable isotope compositions of Zn, S, and Cl for Apollo mare basalts to better constrain the sources and timescales of lunar volatile loss. Mare basalts have broadly elevated, yet limited, ranges in $\delta^{66}Zn$, $\delta^{34}S$, and $\delta^{37}Cl_{SBC+WSC}$ values of 1.27 ± 0.71, 0.55 ± 0.18, and 4.1 ± 4.0‰, respectively compared to the silicate Earth at 0.15, -1.28‰, and 0‰, respectively. We find that the Zn, S, and Cl isotope compositions are similar between the low and high-Ti mare basalts, providing evidence of a geochemical signature in the mare basalt source region that is inherited from lunar formation and magma ocean crystallization. The uniformity of these compositions implies mixing following mantle overturn, as well as minimal changes associated with subsequent mare magmatism. Degassing of mare magmas and lavas did not contribute to the large variations in Zn, S, and Cl isotope compositions found in some lunar materials (i.e., 15‰ in $\delta^{66}Zn$, 60‰ in $\delta^{34}S$, and 30‰ in $\delta^{37}Cl$). This reflects magma sources that experienced minimal volatile loss due to high confining pressures that generally exceeded their equilibrium saturation pressures. Alternatively, these data indicate effective isotopic fractionation factors were near unity.

Our observations of S isotope compositions in mare basalts contrast to those for picritic glasses (Saal & Hauri 2021) which vary widely in S isotope compositions from -14.0

to 1.3‰ explained by extensive degassing of picritic magmas under high P/P_{Sat} values (> 0.9) during pyroclastic eruptions. The difference in the isotope compositions of picritic glass beads and mare basalts may result from differences in effusive (mare) and explosive (picritic) eruption styles wherein the high gas contents necessary for magma fragmentation would result in large effective isotopic fractionation factors during degassing of picritic magmas. Additionally, in highly vesiculated basalts, the $\delta^{34}S$ and $\delta^{37}Cl$ values of apatite grains are higher and more variable than the corresponding bulk-rock values. The large isotopic range in the vesiculated samples is explained by late-stage low-pressure 'vacuum' degassing (P/P_{Sat} ~ 0) of mare lavas wherein vesicle formation and apatite crystallization took place post-eruption. Bulk-rock mare basalts were seemingly unaffected by vacuum degassing. Degassing of mare lavas only became important in the final stages of crystallization recorded in apatite - potentially facilitated by cracks/fractures in the crystallizing flow. We conclude that samples with wide-ranging volatile element isotope compositions are likely explained by localized processes which do not represent the bulk-Moon.

Introduction

Compared to the Earth, the Moon is extensively depleted in volatile elements and preserves a wide range of volatile-element stable isotope compositions such as for H, Cl, Zn, and S (Barnes et al., 2014; Faircloth et al., 2020; Moynier et al., 2006; Rees and Thode, 1974; Saal and Hauri, 2021). These distinct chemical features are largely consistent with lunar formation from a Giant Impact (Charnoz et al., 2021; Paniello et al., 2012; Wing and Farquhar, 2015), in which a Mars-sized impactor collided with the proto-Earth forming a silicate-vapor disk which would later condense to form the Moon (Canup et al., 2015). Partial condensation of the proto-lunar disk (**PLD**) is consistent with volatile depletion (Canup et al.,

2015; Lock et al., 2018), and many isotopic anomalies in moderately volatile stable isotope systems can be explained by vapor-drainage of the PLD to the proto-Earth (Nie and Dauphas, 2019). The explanation for the larger ranges in the isotopic compositions of highly volatile elements, however, remains elusive. This difficulty stems from the fact that the Moon underwent multiple events capable of causing isotopic fractionation of highly volatile elements such as the Giant Impact (Paniello et al., 2012), tidally-assisted hydrodynamic escape (Charnoz et al., 2021), degassing from the Lunar Magma Ocean (**LMO**)(Tang and Young, 2020), and later mare volcanism, which covered ~17% of the lunar surface in basaltic lava flows and pyroclastics (Head and Wilson, 2017; Shearer et al., 2006).

Mechanisms to explain highly volatile element stable isotope anomalies include degassing from the LMO (Boyce et al., 2018), degassing facilitated by crust-breaching impacts (Barnes et al., 2016b; McCubbin and Barnes, 2020b), volcanic degassing (Sharp et al., 2010) and devolatilization associated with the Giant Impact (Gargano et al., 2020). The importance of early, global degassing must take into account the rapid solidification of the LMO surface layer 'lid' which would presumably reduce vapor-loss (Barnes et al., 2016b; Gargano et al., 2020), and occurred rapidly within thousands of years (Elkins-Tanton et al., 2011a). In addition, recent isotopic modeling has shown that the silicate-vapor above the LMO would be in isotopic equilibrium with the magma ocean, resulting in limited isotopic fractionation (Tang and Young, 2020). Subsequent mare magmatism was comparatively prolonged, occurring from 3.9 to 3.1 Ga (Hiesinger et al., 2011), which would feasibly result in further extents of degassing.

The degree to which these individual volatile-loss mechanisms contribute to lunar volatile element stable isotope anomalies is poorly constrained. Are they inherited from the

Giant Impact, the LMO, or are they a direct result from degassing during mare volcanism? Addressing the origin of volatile element stable isotope anomalies has been hampered by the lack of a resolvable relationship between a given volatile element's concentration and its isotopic composition (i.e. [Cl] and δ^{37}Cl). In this work we address this problem by combining three volatile element stable isotope systems which differ in volatility and geochemical affinity. Our intent in the combination of these measurement techniques is to interrogate the relationships between volatile element stable isotope compositions and better understand the sources thereof. We thus measured the Zn, S, and Cl in the same lunar mare basalts, taking into account the well-recognized intra- and intersample isotopic variability in lunar materials (Lock et al., 2020). If the isotopic anomalies for these elements relative to the Earth are a product of early, global processes during lunar formation (Giant Impact and/or subsequent degassing of the LMO), then their isotopic compositions should not change during subsequent magmatic processes such as fractional crystallization within the LMO and localized volcanic degassing. In contrast, if mare volcanism significantly contributed to lunar volatile loss and isotope fractionation, then the mare basalt suite should have a range of isotopic compositions associated with differing volatile contents and other volatile element stable isotope compositions.

Results

We measured a suite of mare basalts for Zn, S and Cl isotope analyses. Quadruple S isotope measurements were made using gas source mass spectrometry at the University of Maryland (Fig. 3.1), and Zn concentration and isotopic compositions were measured using double-spiking and MC-ICPMS at Oxford University (Fig. 3.2) (see Methods for details of analysis). The halogen contents and δ^{37}Cl values of these samples were measured at the

Center for Isotope Cosmochemistry and Geochronology at NASA JSC and the University of New Mexico and have been previously presented (Fig. 3.3) (Gargano et al. 2020). Chlorine analyses are separated into water-soluble chloride (**WSC**) and structurally-bound chloride (**SBC**) fractions.

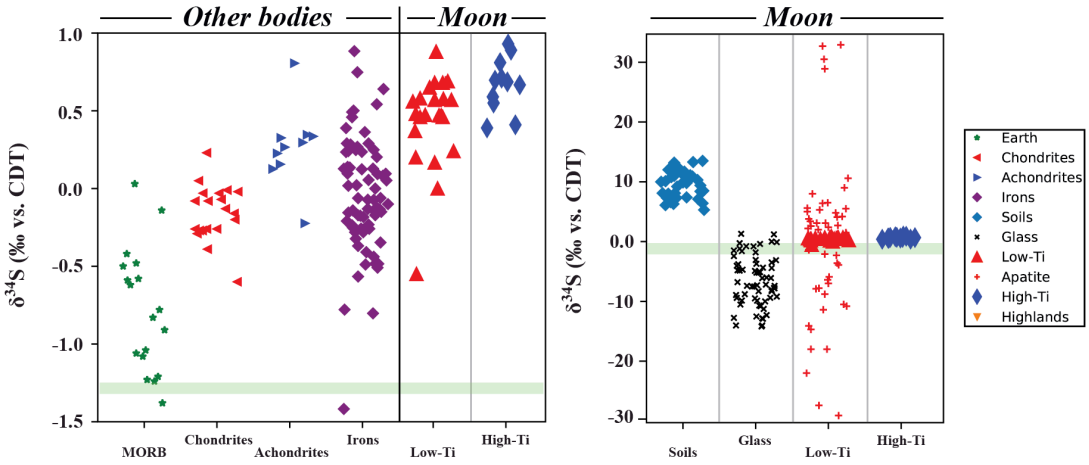

Figure 3.1: $\delta^{34}S$ (‰ vs. Canyon Diablo Troilite (CDT)) values of terrestrial and planetary materials. Data from (Antonelli et al., 2014; Faircloth et al., 2020; Gao and Thiemens, 1991; Gao and Thiemens, 1993a; Gao and Thiemens, 1993b; Herzog et al., 2009; Labidi et al., 2013; Rees and Thode, 1974; Saal and Hauri, 2021; Wing and Farquhar, 2015; Wu et al., 2018). Green bar represents the estimated $\delta^{34}S$ value of the silicate Earth (Labidi et al., 2013).

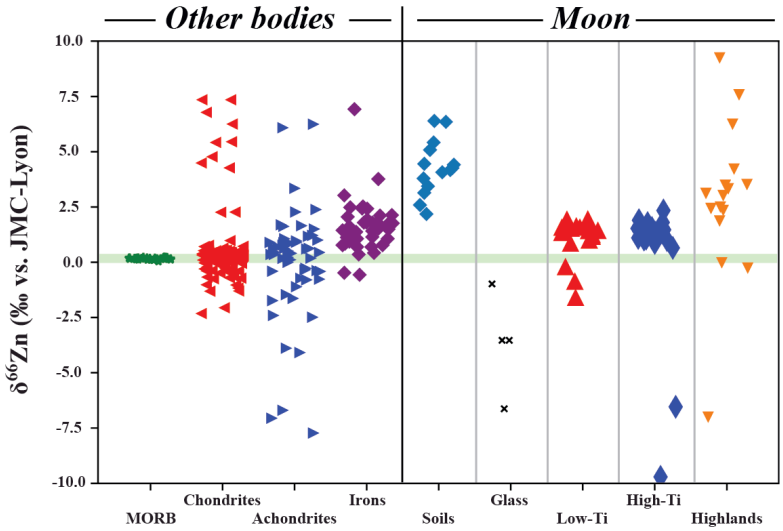

Figure 3.2: δ^{66}Zn (‰ vs. JMC-Lyon) values of terrestrial and planetary materials. Data from (Creech and Moynier, 2019; Day et al., 2020b; Herzog et al., 2009; Moynier et al., 2006; Moynier et al., 2010; Moynier et al., 2007b; Paniello et al., 2012; Sossi et al., 2018). Legend is same as Fig. 3.1. Green bar represents the estimated δ^{66}Zn value of the silicate Earth (Sossi et al., 2018).

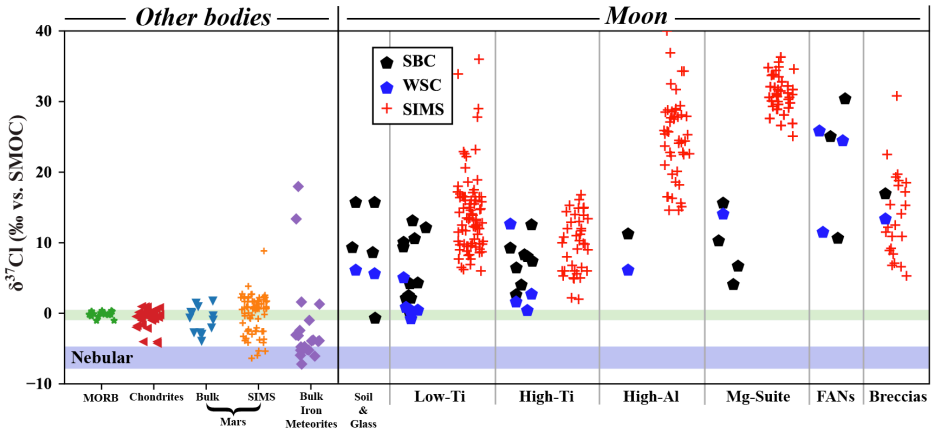

Figure 3.3: δ^{37}Cl (‰ vs. SMOC) of terrestrial and planetary materials. Figure adapted from Gargano et al., (2020). References can be found therein, in addition to Faircloth et al., (2020). Green bar represents the estimated δ^{37}Cl value of the silicate Earth (Sharp et al., 2013). Purple bar represents the estimated nebular value from Gargano & Sharp (2019) and Sharp et al., (2016).

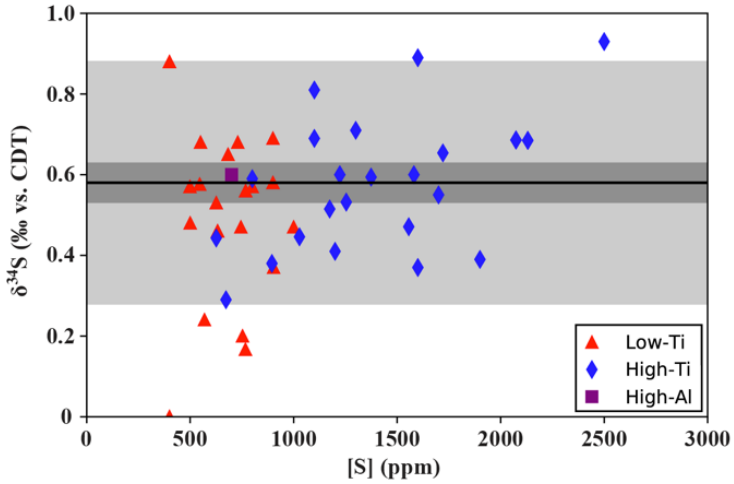

Figure 3.4: [S] (ppm) vs. $\delta^{34}S$ (‰ vs. CDT) of mare basalts. Light grey bar represents the 0.3‰ uncertainty in $\delta^{34}S$ values. Grey bar represents the 1 sigma standard deviation of the average $\delta^{34}S$ value of the mare basalt suite. Data sources: Rees & Thode (1972) and Wing & Farquhar (2015).

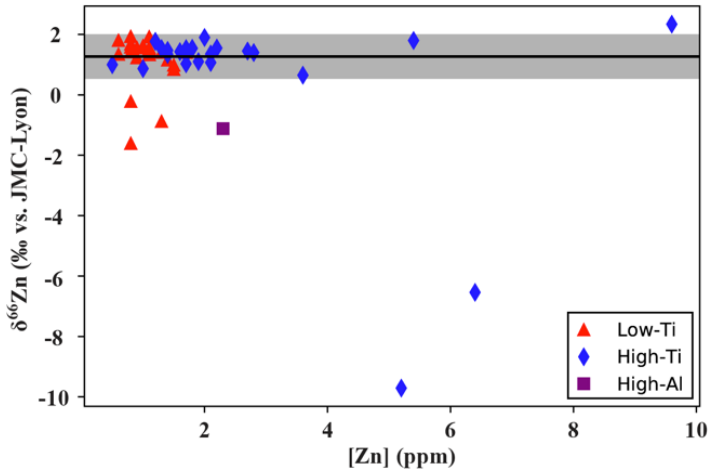

Figure 3.5: [Zn] (ppm) vs. $\delta^{66}Zn$ (‰ vs. JMC-Lyon) of mare basalts. Grey bar represents the 1 sigma standard deviation of the average $\delta^{66}Zn$ value of the mare basalt suite. Error is smaller than symbol size. Data sources: Day et al., (2020), Paniello et al., (2012) & Moynier et al., (2006).

Table 3.1: Zn and S contents and isotope compositions of mare basalts. Halogen contents and $\delta^{37}Cl$ values of this sample suite can be found in Gargano et al., (2020).

Sample	Lithology	[Zn] (ppm)	$\delta^{66}Zn$	2s	[S] (ppm)	$\delta^{34}S$	$\Delta^{33}S$	$\Delta^{36}S$
10017–405	High-Ti	6.7	-6.42	0.15	1900	0.39	-0.01	0.028
10017–400	High-Ti	5.5	-9.59	0.23	2500	0.93	0.013	-0.147
10020–255	High-Ti	1.3	1.55	0.06	1300	0.71	0.016	-0.119
10044–566	High-Ti	2.1	1.19	0.18	1100	0.81	-0.009	-0.191
12018–277	Low-Ti	1.5	-0.76	0.06	500	0.48	0.015	0.49
12054–13	Low-Ti	1.5	1.1	0.14				
12054–146	Low-Ti	0.8	1.92	0.13	900	0.58	0.005	-0.056
12054–150	Low-Ti	0.8	1.8	0.18	1000	0.47	0.001	-0.027
12063–343	Low-Ti	0.8	1.8	0.13	900	0.69	-0.009	0.076
14053–305	High-Al	1.6	-1	0.08	700	0.6	-0.01	-0.106
15016–240	Low-Ti	1	-1.49	0.12	400	0.88	-0.008	0.02
15535–165	Low-Ti	1	1.53	0.21	400	0	0.016	0.03
15556–258	Low-Ti	0.9	1.54	0.07	800	0.57	0.012	-0.017
70215–389	High-Ti	2.1	1.46	0.09	1700	0.55	0.007	0.26
70255–56	High-Ti	1.6	1.22	0.17	1600	0.89	-0.005	-0.086
71135–34	High-Ti	1.5	1.65	0.11	800	0.59	-0.011	-0.035
71546–22	High-Ti	1.8	1.54	0.27	1100	0.69	-0.008	-0.066
74275–355	High-Ti	1.2	1.64	0.17	1200	0.41	0.001	0.31
75035–249	High-Ti	1	0.87	0.75	1600	0.37	-0.006	0.23

Of the samples measured in this work, the $\delta^{66}Zn$ values (‰ vs. JMC-Lyon) range from -9.6 to +1.9‰ with concentrations from 0.8 to 6.7 ppm, and $\delta^{34}S$ values (‰ vs. CDT) range from 0.07 to 0.93‰ with concentrations from 500 to 2500 ppm (Table 3.1). The Zn contents of high and low-Ti basalts average 2.48 ± 1.96 and 1.04 ± 0.30 ppm, respectively and $\delta^{66}Zn$ values average -0.49 ± 4.0 and 0.93 ± 1.3‰, respectively (± indicates 1σ standard deviation). Sulfur contents of high and low-Ti basalts average 1480 ± 490 and 700 ± 258 ppm with $\delta^{34}S$ values of 0.63 ± 0.21 and 0.52 ± 0.27‰, respectively. High and low-Ti basalts have $\Delta^{33}S$ and $\Delta^{36}S$ values of -0.0012 ± 0.01, 0.0046 ± 0.01, and 0.0184 ± 0.182, 0.0737 ± 0.189‰, respectively. The slight differences in the $\Delta^{33}S$ and $\Delta^{36}S$ values between the low and high-Ti mare basalts are not significant relative to the estimated uncertainties of 0.008 and 0.3‰, respectively.

The differences for the $\delta^{66}Zn$ and $\delta^{34}S$ values between low and high-Ti mare basalts measured in this work are not statistically significant (unpaired *t* test results: $\delta^{66}Zn$ $t_{(18)}$ = 2.047, P = 0.0575; $\delta^{34}S$ $t_{(18)}$ = 0.9820, P = 0.3407). Previous results for mare basalts average $\delta^{66}Zn$ = 1.27 ± 0.71‰ (Moynier et al., 2006; Paniello et al., 2012), which is indistinguishable from our average of 1.31 ± 0.44 (excluding 10017) and $\delta^{34}S$ values of 0.55 ± 0.18‰ (Rees and Thode, 1974; Wing and Farquhar, 2015), compared to our values of 0.59 ± 0.22‰ (Figs. 3.4 & 3.5). The $\delta^{37}Cl_{SBC}$ and $\delta^{37}Cl_{WSC}$ values are similarly indistinguishable between the low and high-Ti basalts and range from 7.3 ± 3.5 and 1.8 ± 2.5‰, respectively with concentrations from 1.1 to 5.8, and 1.9 to 10 ppm, respectively (Fig. 3.6). No clear correlation is present in the $\delta^{66}Zn$, $\delta^{34}S$, and $\delta^{37}Cl_{SBC, WSC}$ values of mare basalts (Fig. 3.7).

In contrast to the isotope data, there are clear differences in the S and Zn contents of low and high-Ti basalts. High-Ti basalts contain an average of 1542 ± 462 ppm S relative to the 678 ± 180 in low-Ti basalts ($t_{(41)} = 8.6730$, $P = 0.0001$). A similar statistically significant difference holds for Zn contents, with high and low-Ti mare basalts containing an average of 2.55 ± 1.75 and 1.02 ± 0.31 ppm Zn, respectively ($t_{(38)} = 3.5550$, $P = 0.0015$). There is also a positive correlation between the F and S concentrations for the full suite of mare basalts (Fig. 3.8). Lastly, while the Zn, S, and Cl isotope compositions of mare basalts are generally independent of Zn, S, and halogen contents, sample 10017 with the lowest δ^{66}Zn values has far higher Zn contents than the average mare basalt.

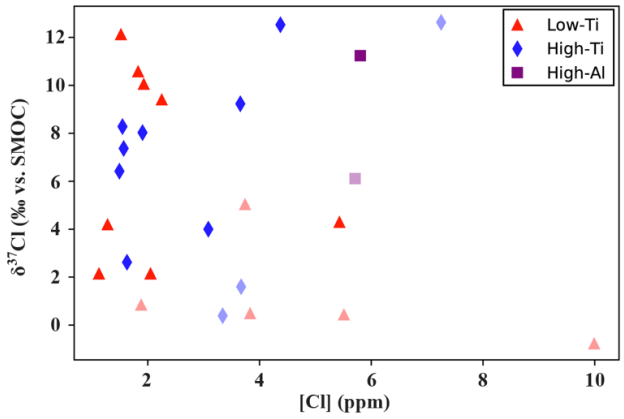

Figure 3.6: [Cl] (ppm) vs. δ^{37}Cl (‰ vs. SMOC) of mare basalts. SBC and WSC are plotted as solid and feint symbols respectively. Data from Gargano et al., (2020) and Sharp et al., (2010).

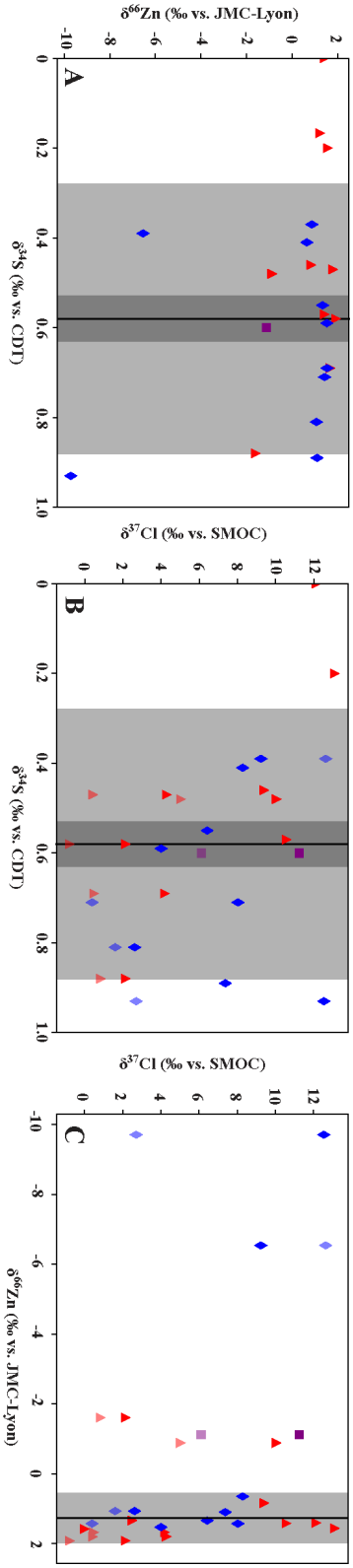

Figure 3.7: $\delta^{34}S$ vs. $\delta^{66}Zn$ (A), $\delta^{34}S$ vs. $\delta^{37}Cl$ (B), and $\delta^{66}Zn$ vs. $\delta^{37}Cl$ (C).

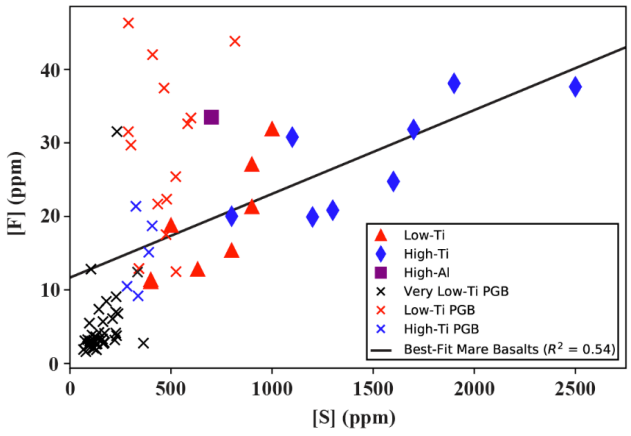

Figure 3.8: [S] (ppm) vs. [F] (ppm) of mare basalts and PGBs. Data from Gargano et al., (2020) and Saal & Hauri (2021).

Discussion

The Zn, S, Cl, and F contents of mare basalts:

We begin our discussion with the Zn, S, Cl and F contents and isotope compositions of mare basalts within the context of lunar mantle differentiation. Following lunar accretion, the LMO quickly solidified with 80% crystallization taking place within 1000 years (Elkins-Tanton et al., 2011a). The initial ~70% of crystallization formed olivine and orthopyroxene-rich cumulates, and later plagioclase, which was positively buoyant in the LMO and produced the ferroan anorthosite (FANs) crust (Snyder et al., 1992).

Further crystallization continued for 10-100 million years, forming olivine, orthopyroxene and clinopyroxene-bearing cumulates as well as ilmenite-rich cumulates at >90% crystallization (Elkins-Tanton et al., 2011a; Snyder et al., 1992). Prior to complete solidification, the lunar mantle overturned due to the crystallization of dense ilmenite-rich

cumulates above comparatively less-dense olivine and pyroxene-rich cumulates, mixing the lunar mantle (Elkins-Tanton et al., 2011a; Shearer et al., 2006). Mare basalts represent partial melts derived from such cumulates and are generally separated into the low-Ti and high-Ti subgroupings, with the high-Ti basalts likely represent mixing between early-stage olivine & pyroxene-bearing cumulates and late-stage ilmenite-bearing cumulates respectively (Hess and Parmentier, 1995; van Kan Parker et al., 2011). Multiple saturation pressures of mare basalts range between 1-1.5 GPa, relating to source region depths of 200-300 km (Ding et al., 2018; Green et al., 1975; Kesson, 1975; Longhi, 1992; Longhi et al., 1972; Snyder et al., 1992; Walker et al., 1976; Walker et al., 1972). Mare basalts consist of numerous lava flows erupted over a period of ~300 Ma (Snyder et al., 2000). Differences, or lack thereof, in the Zn, S, and Cl contents and isotopic compositions of the mare basalt suite are expected to be related to the temporal variation between the crystallization of the cumulate source regions, subsequent magmatic processes such as differentiation and degassing, and crystallization of individual lava flows.

The magmatic compatibilities of the elements of interest are Zn > F > Cl > S. If the high-Ti basalts were sourcing a late-crystallizing component rich in incompatible elements, then we would expect to see the relative concentrations of these elements related to their magmatic compatibility. Instead, we find that the high-Ti basalts contain higher Zn (2.55 ± 1.75 and 1.02 ± 0.31) and F (28.0 ± 7.6 vs. 18.7 ± 7.6 ppm) abundances, yet similar Cl_{SBC} (2.4 ± 1.1 vs. 2.2 ± 1.4 ppm) and far higher S contents (1542 ± 462 ppm vs. 678 ± 180) compared to low-Ti basalts. As Zn is lithophile under relevant P-T and fO_2 conditions of the lunar mantle, the increased Zn content of the high-Ti basalts is likely due to Zn incorporation in the chromite component within the source region (Snyder et al., 1992) and high Zn-

partitioning thereof (Davis et al., 2013). Recent work has shown F partitioning in pyroxene and olivine to be dependent on Ti contents (Potts et al., 2021), and olivine within Apollo 11 rocks is in fact Ti-rich (Brett et al., 1971), likely explaining the F vs. Ti trend observed in the mare basalt suite (Gargano et al., 2020).

Concentrations of volatiles in mare basalts may also be lowered by degassing. Renggli et al. (2017) showed with lunar gas phase modeling that at 1200 ºC, 10^{-6} bar and at IW-2, the predominant gas species are S_2, CO, and H_2 – with Zn, Cl, and F speciation of $Zn^{o}_{(g)}$, HCl, and HF, respectively (Renggli et al., 2017; Renggli and Klemme, 2021). At higher pressures (1 bar) the dominant S-speciation changes to S_2 becoming subordinate relative to H_2S and COS. As such, the amount of degassing expected from our elements of interest is S > Cl > F > Zn, in agreement with the trend of Ustunisik et al. (2015). Sulfur is likely the most readily degassed volatile followed by Cl where the vapor-melt partition coefficient (2.2 to 13-85) is influenced by the abundance of H_2O and S in the melt whereas F is unaffected (1.8) (Sigmarsson et al., 2020). Sulfur in particular is recognized to efficiently degas from basaltic melts, with some terrestrial lavas having lost up to 94% of their initial sulfur following exhumation and solidification (Bali et al., 2018; Gauthier et al., 2016). In contrast, F and Cl are minimally lost owing to their high solubilities (several wt%) in H_2O-poor basaltic melts (Webster et al., 1999). Low Cl vapor-melt partition coefficients may also reflect the decreased role of carrier gas phases such as H_2O and SO_2 which facilitate the formation of HCl and S-Cl ligands (Sigmarsson et al., 2020; Zolotov and Matsui, 2002). The affinity for Zn in the vapor phase is more difficult to constrain, although the high Zn abundance on the coatings of volcanic glass beads is necessarily explained by Zn vaporization during lunar

volcanism (Hauri et al., 2015; Ma and Liu, 2019). Lastly, the extent of degassing of these volatiles should also be reflected in their isotopic compositions.

The S, Zn, and Cl isotope compositions of mare basalts

Most bulk-rock mare basalts have generally elevated, yet limited, ranges in $\delta^{66}Zn$, $\delta^{34}S$, and $\delta^{37}Cl_{SBC+WSC}$ values (averages 1.31 ± 0.44, 0.59 ± 0.22, and 4.1 ± 4.0‰, respectively) compared to the silicate Earth (0.15, -1.28, and 0‰)(Labidi et al., 2013; Sossi et al., 2018). There are several anomalous samples that have low $\delta^{66}Zn$ values (10017, 12018, 15016, and 14053) explained by degassing and subsequent vapor deposition (Day et al., 2017a; Day et al., 2020b). This idea is also seen in Cl, with the particularly high $\delta^{37}Cl_{SBC, WSC}$ values in 10017-405 (9.2 and 12.6‰), 12018 (10.1 and 5.0‰), and 14053 (11.2 and 6.1‰) (Gargano et al., 2020). In the case of "Rusty Rock" 66095, which represents the 'end-member' of low $\delta^{66}Zn$ (-15‰) and high $\delta^{37}Cl_{SBC}$ and $\delta^{37}Cl_{WSC}$ values (~15‰) resulting from vapor condensation (Day et al., 2017a; Shearer et al., 2014), these isotope values may reflect specific conditions such as orders of magnitude higher fCl_2 values when compared to pyroclastic gases (Renggli and Klemme, 2021). As such, these anomalous samples are unlikely to reflect primary isotopic signatures of the Moon, and instead represent secondary processes resulting from vapor condensation.

The more restricted main population of bulk-rock $\delta^{66}Zn$ and $\delta^{34}S$ values of mare basalts reflects conditions that produced limited isotope fractionation throughout LMO crystallization and degassing, as well as during later exhumation and crystallization as lava flows. If there had been isotope fractionation during LMO crystallization, then we would expect to see variable isotopic compositions between low-Ti and high-Ti basalts due to differing extents of degassing and incorporation of late-stage melts. The lack of isotopic

variability between the two basalt types is consistent with the fact that $\delta^{34}S$ and $\delta^{66}Zn$ are insensitive to partial melting (Labidi and Cartigny, 2016; Wang et al., 2017), and $\delta^{66}Zn$ is minimally affected by magmatic differentiation (i.e. $\Delta^{66}Zn_{Spl\text{-}Ol} = 0.12 \pm 0.07‰$) (Chen et al., 2013; Wang et al., 2017). Sulfur isotope values are more sensitive to differentiation; at sulfide saturation $\Delta^{34}S_{FeS\text{-}melt}$ ranges from 1-2‰ at 1450 ºC (de Moor et al., 2013; Marini et al., 2011), which would leave residual silicates with low $\delta^{34}S$ values. This fractionation mechanism, however, is inconsistent with the high $\delta^{34}S$ values of mare basalts.

The effect of differentiation on Cl isotope fractionation has not been studied experimentally, although is generally assumed to be minimal given the small isotopic fractionations at high temperatures (Gargano and Sharp, 2019; Schauble et al., 2003) and the absence of multiple Cl oxidation states in magmatic systems. Instead, the low $\delta^{37}Cl_{WSC}$ (1.8 ± 2.5‰) relative to the high $\delta^{37}Cl_{SBC}$ (7.3 ± 3.5) values is interpreted to reflect kinetic isotope fractionation of Cl via degassing, followed by subsequent deposition of isotopically light Cl-bearing vapor (Gargano et al., 2020). It is important to note that samples with anomalously high $\delta^{37}Cl_{WSC}$ values (i.e., FANs, 66095, 10017) are necessarily sourced from a high $\delta^{37}Cl$-bearing melt in order to off-set the light isotope enrichment in the vapor phase (Gargano et al., 2020).

In total, while the concentrations of S, Zn, and Cl can change during fractional crystallization and assimilation, the only effective way to significantly modify their isotopic compositions is through extraction of the vapor phase. The variable S and Z concentrations, but effectively constant isotopic compositions for most samples suggest either that degassing of mare basalts was minimal for these elements, or that the integrated effective isotopic fractionation factor associated with degassing was near unity.

Implications for the $\Delta^{33}S$ values of mare basalts

An important observation from our work and that presented in Wing and Farquhar (2015) is that the $\Delta^{33}S$ values of mare basalts is no different than that of the silicate Earth (where $\Delta^{33}S$ = 0‰, Labidi et al. 2013). Recent work has shown that various primitive and differentiated meteoritic materials have distinct $\Delta^{33}S$ compositions that are linked to specific parent bodies where the differences in $\Delta^{33}S$ among the parent bodies may be due to processing of sulfur in different nebular environments (Antonelli et al., 2014; Dottin III et al., 2018; Labidi et al., 2017; Rai et al., 2005; Wu et al., 2018). Furthermore, similarity in $\Delta^{33}S$ between various planetary materials (e.g. Main Group Pallasites and IIIAB iron meteorites) can be used to link the two materials to a single parent body (Dottin III et al., 2018). Although the silicate Earth and Moon have differences in $\delta^{34}S$ values, the similarity in $\Delta^{33}S$ simply suggests that they are related. Their relationship may reflect formation from materials in the same nebular environment and/or derivation from the same parent body.

Isotopic systematics of lunar volcanism

Degassing of mare basalts occurred in the subsurface from gas exsolution during exhumation (Head and Wilson, 2017), and during second-boiling upon eruption (Wilson and Head, 2017a). If degassing occurred under vacuum conditions at the surface via a fracture network, then the preferential loss of light isotopes (i.e., ^{64}Zn, ^{35}Cl, and ^{32}S) could dominate other isotopic fractionation mechanisms (i.e., equilibrium fractionation between mineral phases at high temperatures) and leave the residue enriched in the heavy isotope.

Evaporative loss under vacuum conditions is approximated by the kinetic isotope fractionation factor (α_{Kin}) defined as where $M_{1,2}$ are the masses of the light and heavy isotopologues, respectively. For lunar gas compositions, COS and H_2S are the expected

dominant phases for S (Renggli et al., 2017; Renggli and Klemme, 2021). Under ideal degassing into a vacuum, the fractionation of these S-bearing isotopologues yields $1000ln\alpha_{\text{Melt-H2S, Melt-COS}}$ = 28 and 16‰, respectively, enriching the melt in ^{34}S. In contrast, equilibrium fractionation between these vapor species and silicate melt has the opposite effect, with COS and H_2S being ^{34}S-rich relative to the melt, depleting the melt in ^{34}S (Marini et al., 2011; Richet et al., 1977). This means that the gas phase will vary from strongly incorporating the light isotope during vacuum degassing to incorporating the heavy isotope under gas saturated, equilibrium conditions (van Kooten et al., 2020). Even minimal volatile-loss under vacuum conditions should lead to wide-ranging and heavy isotopic compositions regardless of which S-bearing species is dominant at any given condition (i.e., P, T, fH_2, fO_2). For example, 20% S-loss as H_2S under vacuum would produce a $\delta^{34}S$ change of +7‰ in the residual magma, whereas the measured range of $\delta^{34}S$ values for the entire mare basalt suite is less than 2‰ (Wing and Farquhar, 2015). A similar argument also holds for Zn. As such, the lack of large variations in the $\delta^{34}S$ and $\delta^{66}Zn$ values of mare basalts suggests that either the integrated effective fractionation factors during degassing were near unity or alternatively, that the amount of degassing itself was minimal.

In contrast to the mare basalts, some lunar lithologies have been shown to have extreme variations in the Zn, S and Cl isotope compositions (15‰ in $\delta^{66}Zn$, 60‰ in $\delta^{34}S$, and 30‰ in $\delta^{37}Cl$). These isotope values are likely explained by kinetic isotope fractionation during degassing into a near-vacuum with large effective α values. The magnitude of this effect will be increased if the escaping gas involve low-mass species, such as Zn^o and HCl, which lead to larger fractionations than for relatively higher-mass isotopologues, such as ZnS, FeS_2 and $FeCl_2$. Low molecular mass degassing is required to explain the exceptionally

low Zn and high Cl isotope values seen in 66095 (Rusty Rock) and some FAN samples (Gargano et al., 2020; Kato et al., 2015). Interestingly, while bulk-rock mare basalts do not retain such anomalous Zn, S, or Cl isotope compositions, the $\delta^{34}S$ values of picritic glass beads (**PGBs**) range from -14.0 to 1.3‰ (Saal and Hauri, 2021) despite the fact that they are generally petrogenetically related to the more evolved mare basalts (Hauri et al., 2015). Picritic magmas are expected to have experienced limited differentiation, whereas mare basalts were produced following 20-30% fractional crystallization (Shearer and Papike, 1993). As such, the starkly different $\delta^{34}S$ values of the PGBs when compared to mare basalts is likely explained by differences in eruption styles.

Isotopic consequences of pyroclastic vs. effusive mare volcanism

The initial stages of lunar volcanism are characterized by high ascent rate explosive volcanic eruptions via rapid dike propagation driven by the exsolution of CO (Wilson and Head, 2018) and H_2 (Newcombe et al., 2019; Newcombe et al., 2017). Explosive mare volcanism resulted in widespread pyroclastic deposits such as picritic glasses which were fragmented during exhumation due to high gas phase volumes (~>70%) (Rutherford et al., 2017). Wilson and Head (2018) describe this phase as short-lived, with a zone of pure gas extending within the dike from depths from 100-200 m, above a highly vesicular foam extending to around 10 km. It is important to note that such dike systems are expected to be vertically extensive ranging from 50-90 km, penetrating the ~30 km thick lunar crust (Wieczorek et al., 2013) and upper lunar mantle (Wilson and Head, 2017b). In contrast, mare basalt volcanism consisted of more prolonged events (10-100 days) with relatively slower ascent rates and fluxes (Wilson and Head, 2018). We suggest these two styles or phases of volcanism represent starkly different degassing regimes. The former, sampled in PGBs is

extensively degassed – as evidenced by marked differences in volatile contents when compared to melt inclusions (Chen et al., 2015; Hauri et al., 2011; Ni et al., 2019) and exceptionally low $\delta^{34}S$ values (Saal and Hauri, 2021). The subsequently-emplaced mare basalts are comparatively less degassed – seen by limited ranges in Zn, S and Cl isotope values, comparatively higher Zn, S, and Cl concentrations, and the vesicular nature of several samples such as 15556 and 15016.

Pyroclastic: Picritic Magmas

Saal & Hauri (2021) interpret the wide range of S contents and $\delta^{34}S$ values in PGBs to result from extensive degassing under high P/P_{Sat} values. These authors propose a degassing regime with an effective isotope fractionation factor of $\alpha\alpha$, where P/P_{Sat} is equal to the effective vapor pressure of a given element relative to the saturation vapor pressure (Saal and Hauri, 2021). In this scenario, a crossover at $P/P_{Sat} \sim 0.86$ results in the α value deviating from <1 to >1, resulting in heavy-isotope loss when degassing occurs in a near-saturated medium with $P/P_{Sat} > 0.86$ and a light-isotope loss when degassing occurs under low vapor pressure conditions. The crossover P/P_{Sat} value depends on the appropriate proportions of degassing S-species (S_2, H_2S and COS) ranging from 0.8 assuming S_2 degassing, and 0.9 with H_2S.

Saal & Hauri (2021) conclude that the low $\delta^{34}S$ values of PGBs requires degassing to take place into a medium with $P/P_{Sat} > 0.9$. This condition is feasible within the upper levels of the volcanic conduit given the high-gas phase volumes necessary for magma formation and PGB formation (Newcombe et al., 2017; Rutherford et al., 2017). Rutherford et al. (2017) propose that picritic magmas were rapidly exhumed from ~500 m depth to the lunar surface within 50-100s. These authors further describe the evolution of picritic magmas with

8-15% gas phase volumes at 500 m depth, rapidly increasing to 93-94% at 25 m. The high gas pressures in the upper levels of the conduit (approaching equilibrium with the melt) can explain the necessary high $\alpha'_{Kin(vapor\text{-}melt)}$ values (>1).

Importantly, the exceptionally low $\delta^{34}S$ values in PGBs requires that >80% of their initial S content was lost during degassing and it was done at a near-saturation confining pressure. This condition is feasible in pyroclastic eruption styles as exsolved volatiles remain coupled to the melt in a closed-system degassing regime (Cassidy et al., 2018). When gas and melt are coupled with low melt volumes relative to the gas as expected for the picritic magmas, then extensive volatile-loss (i.e. $F_{Remaining} < 0.2$) would readily lead to wide ranges in $\delta^{34}S$ values of the residual melt measured in PGBs. This mechanism may be further facilitated by high surface-area/volume ratios of PGBs. Additionally, given that the volume of magma released during a single eruptive event was small (a few %) relative to the total source volume (Head and Wilson, 2017), it is further consistent that PGBs degassed with comparatively little isotopic effect on the residual magma chamber if it were to mix with other reservoirs.

It is also feasible that during exhumation of picritic magmas, bubble nucleation and subsequent volatile partitioning into the gas-phase was relatively more efficient compared to mare basalt melts. At shallow depths (~120 m), H_2 followed by H_2O and CO become volumetrically dominant in H-rich picritic melts (Newcombe et al., 2017). The presence of H_2-H_2O-CO-rich vapors in picritic magmas would result in an increasingly efficient volatile partitioning into the gas-phase for Cl (Sigmarsson et al., 2020), and S as COS (Sato, 1976), and H_2S (Rutherford et al., 2017). The efficient partitioning of S and Cl in the H-rich high gas-phase volumes required to fragment the picritic magmas, alongside the high P/P_{Sat} values and associated $\alpha'_{Kin(vapor\text{-}melt)}$ values >1 can readily explain the exceptionally low $\delta^{34}S$ values of PGBs.

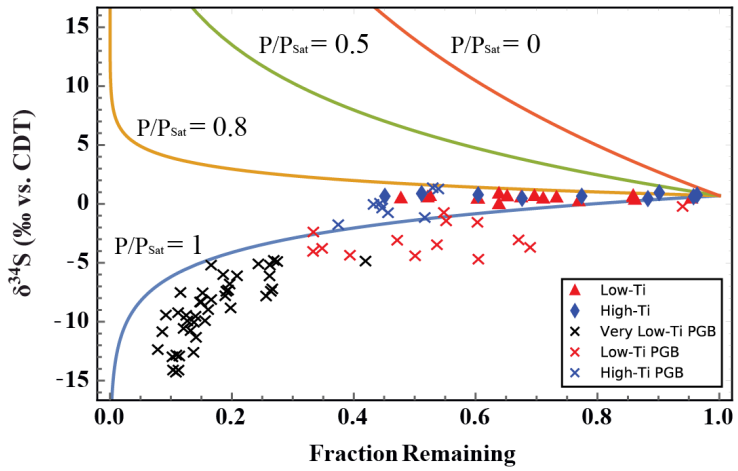

Figure 3.9: Rayleigh degassing regime of mare materials with initial $\delta^{34}S$ estimated at 0.7‰ with α'_{Kin} values from (Cheng et al., 2020; Saal and Hauri, 2021; Wu et al., 2018). Fraction S remaining is calculated by estimates of initial S contents in source regions. Picritic glass beads are estimated relative to melt inclusions (74220 and 15016)(Chen et al., 2015; Ni et al., 2019). Mare basalts are relative to source region estimates (Bombardieri et al., 2005; Steenstra et al., 2018). A number of A15 basalts are excluded due to $F_{Remaining} > 1$ (15058, 15499, 15555, and 15556).

Effusive: Mare Magmas

In comparison to PGBs, mare basalts show little variation in $\delta^{34}S$ values which suggests that they did not undergo extensive S-loss, and/or that the integrated effective α values during degassing were close to 1 (i.e., minimal fractionation with $P/P_{sat} \sim 0.86$)(Fig. 3.9). When the $\delta^{34}S$ values of PGBs are examined together with mare basalts in terms of S, F, and Cl contents, the differing extents of degassing can be readily observed relative to the ranges measured in melt inclusions (Fig. 3.10). Enigmatically, the mare basalts cooled much more slowly than the quenched PGBs (1-20 ºC/h vs. 1-3 K/s (Saal et al., 2008; Zhang et al., 2019)). The slow cooling rate of the mare basalts could feasibly result in further extents of degassing; however, this idea is inconsistent with the limited ranges of Zn, S and Cl isotope compositions, as well as comparably higher volatile contents (with exception to H) to volcanic glasses (Fig. 3.10).

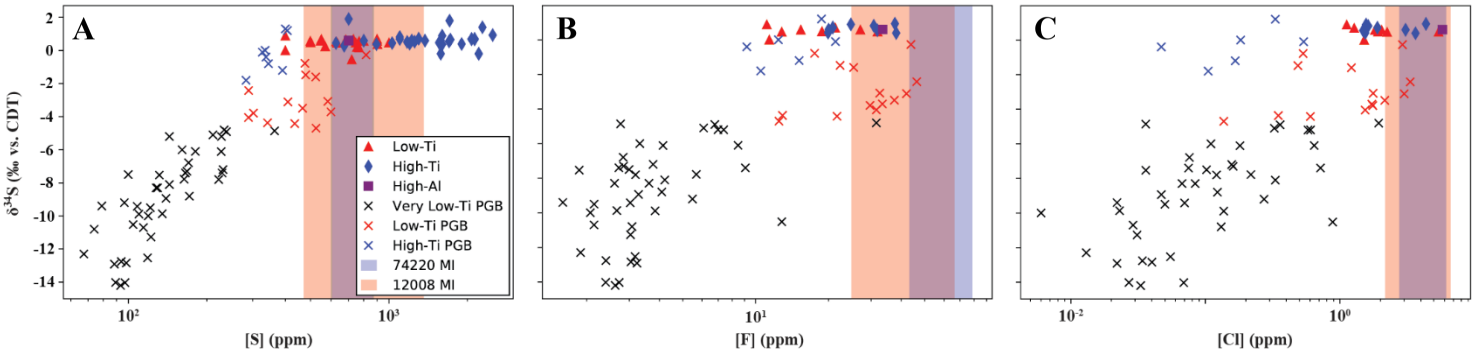

Figure 3.10: [S] (A), [F] (B), and $[Cl]_{SBC}$ (C)(ppm) vs $\delta^{34}S$ (‰ vs. CDT) of lunar mare basalts and PBGs. Vertical blue (74220) and red (12008) bars represent the ranges of S, F, and Cl contents in melt inclusions from Ni et al., (2019) and Chen et al., (2015).

Instead, the effusive eruption style which produced the mare basalts was seemingly inefficient in the loss of volatile elements as mare magmas did not undergo the extensive low P volatile separation within the volcanic conduit in the case for the picritic magmas. The thick mare lava flows would form quench crusts serving to further limit volatile loss, such that there would be minimal isotopic effects during degassing despite low pressure conditions on the lunar surface. This idea is consistent with the fact that at low P/P_{Sat} values, even minimal extents of S-loss would produce high $\delta^{34}S$ values which is not observed in the mare basalt data (Fig. 3.9). These observations are also broadly consistent with bulk Cl and Zn isotope compositions which also exclude the possibility of ideal vacuum degassing ($P/P_{Sat} \sim 0$) in bulk-rock mare basalts given the limited ranges in isotope values relative to the large kinetic isotope fractionation factors ($1000\ln\alpha_{Kinetic(gas\text{-}melt)} = -23$ and -15‰ for HCl and Zn^{o}, respectively)(Gargano et al., 2020).

Despite the limited range of bulk-rock Zn, S and Cl isotope compositions relative to the large kinetic isotope fractionation factors, there is evidence for near-kinetic (vacuum or near-vacuum) degassing in late-forming and/or secondary phases contained in mare basalts. The $\delta^{37}Cl$ values of WSC in bulk-rock mare basalts are generally lighter than the corresponding SBC by 4.3 ‰ (Sharp et al., 2010; Gargano et al. 2020) which is explained by degassing and deposition of HCl or other Cl-bearing volatile phase into a near-vacuum, presumably along cracks in a mostly solidified basalt. The magnitude of this effect is even larger in the late-formed apatite grains where the degassing extent necessarily becomes very large to explain their high and wide-ranging $\delta^{37}Cl$ values (i.e., $F_{Remaining}$ approaches 0). For example, the $\delta^{37}Cl$ values of apatite in samples 15016 and 15556 (highly vesiculated low-Ti basalts) range from 6.5-19.1 and 28.9-36.4‰, respectively (Barnes et al., 2019; Faircloth et

al., 2020). The $\delta^{34}S$ values of apatite are similarly wide-ranging in 15016 and 15556 from 14.6-29.5 and 2.7-10.6‰, respectively (Faircloth et al., 2020). These $\delta^{37}Cl$ and $\delta^{34}S$ values of apatite in 15016 and 15556 are in stark contrast to the bulk-rock $\delta^{37}Cl_{SBC}$ values of 2.14 and 10.57, and $\delta^{34}S$ values of 0.88 and 0.57‰, respectively. These discrepancies are best explained by kinetic isotope fractionation of S and Cl from the mare lavas under low P/P_{Sat} values along an open network of fractures in a nearly completely crystallized basalt. Similar ideas have been proposed in the formation of foam mounds in late-stage lava lakes where vesicles in the upper part of the mound 'pop' in vacuum (Wilson and Head, 2017a). Under these conditions and given the relatively small melt volumes retained in mesostasis regions where apatite crystallizes it is feasible that the differences between the bulk-rock and apatite result from vacuum degassing of apatite leading to their far higher and wide ranging $\delta^{34}S$ and $\delta^{37}Cl$ values.

Implications

The long-standing difficulty in addressing the sources of volatile-element stable isotope anomalies in lunar materials resulted from ambiguous relationships between isotopic compositions and volatile contents (i.e. $\delta^{37}Cl$ and [Cl]). At present, however, a wealth of data has been generated from numerous lithologies with different isotope systems, as well as target phases which further elucidate this problem. While bulk-rock mare basalt measurements show limited variation in Zn, S and Cl isotope compositions, *in situ* measurements of late-formed apatite show significantly more variability (i.e., apatite, Figs. 3.1, 3.3). Additionally, a number of other lithologies such as Rusty Rock (Day et al., 2019; Shearer et al., 2014), and lunar FANs (Gargano et al., 2020; Kato et al., 2015) show

significant variability and ranges of isotope values that are not seen in the bulk-rock mare basalt suite.

These data suggest localized surface-related processes that produced anomalously low or high isotope values for Zn, S, and Cl consistent with vacuum degassing. Bulk-rock low and high-Ti mare basalts have elevated, yet restricted ranges of Zn, S, and Cl isotope compositions (relative to the silicate Earth) that have been interpreted to reflect devolatilization during the Giant Impact (Day et al., 2020b; Gargano et al., 2020; Moynier et al., 2006; Paniello et al., 2012; Wing and Farquhar, 2015). In contrast, the wide ranges in H, Cl, and S isotope compositions of lunar apatite are interpreted to reflect isotope fractionation during magmatic degassing (Barnes et al., 2014; Barnes et al., 2016b; Faircloth et al., 2020).

The similarity in bulk-rock $\delta^{66}Zn$, $\delta^{34}S$, and $\delta^{37}Cl$ values of low and high-Ti mare basalts, and generally high isotope values relative to Earth suggest that the Giant Impact and/or LMO degassing resulted in the heavy-isotope enrichment of Zn, S, and Cl in the mare source region. The restricted range of isotope values suggests that most mare basalts did not experience extensive post-eruptive volatile-loss, and/or that the integrated effective α during degassing was ~ 1. While we cannot define the degree of isotope fractionation resulting solely from LMO degassing due to effective mantle mixing following mantle overturn, our data show that bulk-rock Zn, S, and Cl isotope compositions are identical between the low and high-Ti mare basalt suite such that no evidence exists to support this argument. Instead, the slightly elevated Zn, S and Cl isotope compositions of mare basalts suggest that the lunar mantle inherited a heavy-isotope enriched signature resulting from lunar formation (during the Giant Impact event) and remained largely unchanged throughout mare volcanism.

Conclusion

In this work we show that the high Zn, S and Cl isotope values of the effusively erupted mare basalts are inherited from lunar formation and/or in addition to lunar magma ocean degassing. The bulk-rock Zn, S and Cl isotope compositions are not correlated, nor are they correlated with their respective volatile contents (i.e., δ^{37}Cl and [Cl]). This suggests that mare magmatism did not cause the heavy isotope enrichments relative to Earth. In contrast, the explosively erupted picritic glass beads exhibit a wide range of low δ^{34}S values inversely related to their S contents resulting from extensive degassing with high $P/P_{Sat} > 0.9$ and $\alpha > 1$. The restricted range of δ^{34}S values of the mare basalts suggests that they were, in general, minimally degassed, and/or that their effective integrated isotope fractionation factor was near unity.

We are able to exclude the possibility of vacuum degassing affecting bulk-rock mare basalts given the limited range of Zn, S and Cl isotope values in lieu of the large kinetic isotope fractionation that would occur by this process. Mare lavas likely formed quench crusts and crystallized before significant volatile loss could occur in the bulk-rock under low P/P_{Sat} conditions on the lunar surface. In contrast, apatite in highly vesiculated basalts exhibit marked differences in δ^{34}S and δ^{37}Cl values when compared to the bulk-rock which suggests that apatite records extensive post-eruptive degassing under relatively lower P/P_{Sat} conditions. In total, these data provide further evidence for the idea that lunar volatile loss and volatile-element stable isotope fractionation largely occurred during lunar formation and that exceptionally high or low isotopic compositions likely resulted from localized phenomena influenced by reservoir effects.

Supplemental Information

Notable Sample Description

10017**:** Sample 10017 is a fine-grained vesicular high-Ti-K mare basalt with high modal mesostasis and vesicularity up to 20% (Beaty and Albee, 1978) and consisted of an exterior (10017-405) and interior chip (10017-400). The interior of this sample was measured to have a δ^{66}Zn value of -9.6‰ with 5.5 ppm Zn, with an exterior value of -6.42‰ and 6.7 ppm Zn. The $\delta^{37}Cl_{SBC}$ of the interior and exterior was 9.23‰ and 12.53, respectively. Compared to other samples, the WSC isotope composition of the interior is anomalously high at 12.63‰. The interior of the sample contained 2500 ppm S with a δ^{34}S value of 0.93‰, with an exterior value of 0.39‰ and 1900 ppm S. The interior of this sample contains both lower Zn and Cl isotope values, yet higher S isotope values from the exterior. The abundances of S, Zn, and Cl are comparable in both the exterior and interior sections, and both are enriched in these elements relative to other high-Ti basalts. Lastly, we find it important to note that troilite within high-Ti-K basalts commonly occurs as spherules suggested to reflect sulfide immiscibility, and also occurs as globules within vesicles (Beaty and Albee, 1978).

15016 & 15556: Samples 15016 and 15556 are medium-grained olivine basalts with 1-5 mm vesicles which comprise up to 50% of the samples. The δ^{34}S values are comparable at 0.88 and 0.57‰, respectively with differing S contents of 400 and 800 ppm, respectively. In contrast, the δ^{66}Zn and $\delta^{37}Cl_{SBC}$ values are -1.49 and 1.54, and 2.14 and 10.6‰, respectively. The Cl_{SBC} and F contents of these samples are different at 1.12 and 1.83 ppm, and 11.1 and 15.4 ppm respectively. Goldberg et al. 1976 find F-rich coatings within the vesicles of these samples with 15016 containing 2x more F in the intervesicular region when

compared to the vesicles, whereas 15556 is measured to contain similar F contents in both regions.

Samples

In this work we chose to analyze 19 mare basalts with sample aliquots designated from partnering chips for Cl, Zn and S isotope compositions. Our chosen samples encompass the low-Ti, and high-Ti mare basalt sub-groupings (Neal and Taylor, 1992). We also measured the interiors and exteriors of some notable samples such as 10017 and 12054 to address sample heterogeneity and surface-relate isotopic anomalies. Two Apollo 15 basalts 15016 and 15556 were also measured due to high vesicularity.

Methods

Zn isotope measurements were performed at the University of Oxford by S. Hopkins and A. Halliday. Samples were transferred to metal-free centrifuge tubes and cleaned with DI water for 2 hours. Samples were then dried and powdered in an agate mortar. Powder aliquots were then measured to obtain approximately 0.25 ug Zn (around 20-140 mg of sample). Hotplate dissolution was then performed using HF-HNO_3 and HCl over multiple days. Sample dissolution was complete when no undissolved components remained. Small aliquots of each sample dissolution was then weighed and mixed with a ^{64}Zn-^{67}Zn double spike (5.10025 ppm, (Arnold et al., 2010)) and equilibrated over 48 hours at 60°C. Solutions were then passed through an anion-exchange column before analysis by MC-ICPMS to determine the Zn concentrations. These concentrations were then used to calculate the appropriate mass ratios of spike/sample solution. Appropriated spiked samples were then passed through the anion-exchange column twice to purify Zn from interfering elements. Zn isotope compositions were then measured using a *Nu instruments* Plasma HR mass

spectrometer. Masses 62, 64, 66, 67, 67.5, and 68 were measured simultaneously. Masses 62 and 67.5 were used for $^{64}Ni^{+}$ and Ba^{2+} corrections. Exterior sample washes typically had negligible Zn contents (<0.2 ng). USGS reference materials BCR2, BHVO2, and BIR1a were prepared in the same manner as the lunar samples. The isotopic composition of Zn is reported relative to JMC-Lyon.

Sulfur isotopes were measured at the University of Maryland by J. Dottin and J. Farquhar. Samples were firstly coarsely crushed in a steel mortar and pestle and subsequently powdered in an agate mortar using <5mL ethanol to reduce dust loss. Ethanol-powder slurry was then quantitatively transferred to reactions vessels. Flasks were filled with 20mL 5M HCl and 20mL of Cr(II) Chloride solution and heated to sub boiling temperatures with a continuous flow of N_2 (Canfield et al., 1986). The reaction proceeds for ~3 hours as the release of H_2S that is first carried through a water trap to capture acid vapors and second through an $AgNO_3$ trap where S is precipitated as Ag_2S. Precipitated Ag_2S was then centrifuged and transferred to 1.5ml Eppendorf tubes and rinsed 6 times with Milli-Q.

After rinsing, samples were dried for ~ 2 hours at 70 degrees C and weighed for extraction yields to estimate S concentrations. The Ag_2S was then transferred into clean aluminum foil, loaded into Ni reaction vessels and reacted with approximately 10x stoichiometric excess of F_2 at 250°C overnight yielding SF_6 as an analyte. Analyte gas was separated from non-condensable gases by liquid-N_2 traps. HF was then separated from SF_6 by an ethanol-liquid N_2 trap. SF_6 was then purified by passing through a 12.5 A Hasep Q gas chromatography column. Purified SF6 was lastly analyzed in dual inlet mode on a MAT 253 mass spectrometer. The isotopic composition of sulfur is normalized using the same method as Antonelli et al. (2014) and Dottin et al. (2018) where samples are first normalized to

bracketed analyses of IAEA-S1 from each analytical session and subsequently normalized to the value IAEA-S1 relative to Canyon Diablo Troilite (CDT) reported in Antonelli et al. (2014) which places IAEA-S1 at $\delta^{33}S = -0.091$, $\delta^{34}S = -0.401$, $\delta^{36}S = -1.558$, $\Delta^{33}S = 0.116$, $\Delta^{36}S = -0.796$ (Dottin et al. 2020).

4. HALOGEN GEOCHEMISTRY OF NON-CARBONACEOUS CHONDRITES AND THE SOURCE OF SALT TO EARTH

Preface

The halogen contents of chondrites have been a long-standing problem in planetary science. A review of these historical difficulties can be found in the supplements. As this work will show, the halogen contents and chlorine isotope compositions of chondrites are related to the extent of metamorphism on the asteroidal parent bodies. These relationships were previously not recognized due to the idea that all terrestrial falls were irreconcilably contaminated with halogens, and an inadvertent sampling bias of high petrologic type falls. The large variability in halogen contents, whilst previously suggested to reflect contamination, is more easily explained by the widespread incorporation of halogen-rich vapors sourced from the thermal/impact induced decomposition of halogen-rich phases which are most apparent in samples associated with impact melt and high Br contents. These demonstrably primary geochemical characteristics are likely a larger source of ambiguity than the weathering features themselves.

Although this work was unable to identify a quantitative criterion for terrestrial contamination of falls, careful consideration is necessarily made in terms of weathering features relative to the state of the material (i.e., petrologic type, parent mass, lithology, weathering grade, etc.). It is evident that a primary water-soluble halogen component exists in chondrites (Sharp et al., 2013), confounding attempts to relate leachable chemistry to the extent of weathering (Lee and Bland, 2004). The primary soluble components are the result

of fluid and/or vapor deposition on the parent body, however, further work is required to understand the citing of the water-soluble and vapor deposited phases in chondrites. I suspect that the water-soluble iodide is unreliable, however, of the several samples that evidently contain high water-soluble iodine contents reflective of contamination, this contaminant has not affected the insoluble halogens.

Despite these numerous complexities, the high fluorine retention in the anhydrous enstatite chondrites contrasts with the stark fluorine depletion in the hydrous ordinary chondrites and is informative to volatile processing of labile elements during metamorphism, as well as the precursor materials to the Earth. Recent discussion on the bulk-silicate Earth's fluorine contents indicate that up to 59 ppm fluorine could be explained by the transition zone (Roberge et al., 2015). Thus, relative to <10 ppm fluorine which is retained in type 6 ordinary chondrites, these materials are unlikely to comprise a majority of Earth's mass, thereby providing additional constraint pointing towards an enstatite-chondrite-like Earth (Javoy et al., 2010).

As follows after a brief background discussion, I present a short format manuscript to be submitted to *Science Advances* which presents these halogen data for the non-carbonaceous chondrites and achondrites. Although the relationships between chondrite and achondrites remain tenuous, I treat these materials as representing a continuum of volatile processing that would have taken place on early solar system bodies (Elkins-Tanton et al., 2011b). I draw no delineations between NC chondrites and achondrites, and instead, assume them to be representative of NC chondrite materials experiencing progressive metamorphism from an initial chondrite-like chemistry. An abundance of supplementary material is provided for additional context.

This manuscript conveys the importance of halogen processing throughout planetary evolution whereby the accretion and processing of chondritic material results in the progressive loss of halogens. We construct a simple model utilizing the measured data as inputs and create a Monte Carlo simulation showing the effects of crustal erosion on the halogen contents of asteroidal materials in concluding that the Earth's salt is derived from enstatite chondrites.

Background

Early solar system bodies

Chondrites are chemically primitive planetary materials comprised of aggregates of dust, chondrules and refractory inclusions formed in the first few million years of the solar system (Halliday and Kleine, 2006). Chondritic meteorites are divided between more than a dozen sub-groups based on unique chemical, mineralogic, and isotopic compositions (Krot et al., 2014), with variations largely thought to represent sampling different regions of material in the protoplanetary disk (Wood, 2005). The abundances of volatile elements differ from the individual chondrite groups caused by the thermal stratification in the protoplanetary disk in which they formed; which was hot in the inner solar system (~ <3AU, 500-1500K), and cold in the outer solar system (<150K) (Boss, 1998). Thus, while the outer solar system was cold and thereby condensed volatile-rich materials, the inner solar system is thought to have been hot and subsequently volatile-poor (Ebel, 2006; Lodders, 2003; Sossi and Fegley Jr, 2018).

To a first order, chondrites can be delineated as belonging to the outer-solar system carbonaceous (CC) or inner solar system non-carbonaceous chondrite groups (NC). The NC vs. CC 'dichotomy' results from nucleosynthetic isotopic anomalies in O, Cr, Ni and Ti isotopes, potentially resulting from the physical separation of these reservoirs (Kruijer et al.,

2020; Warren, 2011). The non-carbonaceous chondrites include the ordinary (OC) and enstatite (EC) chondrites, and unequivocally comprise a majority of Earth's mass (Dauphas et al., 2014; Warren, 2011).

Early volatile processing of early solar system bodies

The temporal and cosmochemical context of chondrites in the early solar system is enigmatic. Chondrites are chemically primitive solar system materials yet are millions of years younger than the first generations of differentiated asteroids (Hellmann et al., 2019; Kleine et al., 2009; Spitzer et al., 2020). While the chondrites were spared from processing to the extent of melting, the comparatively ancient material retained in iron meteorites and achondrites were derived from bodies which rapidly accreted with abundant short-lived radionuclides (i.e., ^{26}Al) resulting in melting and differentiation (Elkins-Tanton, 2012; McCoy et al., 2006).

Following the accretion of chondrites into asteroidal bodies, a continuum of processes including thermal metamorphism, shock metamorphism and aqueous alteration modified their initial chemistries. The qualitative scheme used to depict these processes is petrologic type – whereby types 3-6 reflect increasing degrees of thermal metamorphism (Huss et al., 2006; Van Schmus and Wood, 1967), and types 3-1 indicate increasing degrees of aqueous alteration (Brearley, 2006). Unique to the OCs – types 3.0 to 3.9 are further subdivided from well-characterized changes in olivine Cr_2O_3 content (Grossman and Brearley, 2005). It is not possible to similarly delineate the ECs from complex thermal and shock histories (Zhang et al., 1995). Although the exact temperatures, cooling rates, and durations of metamorphism are debated, it generally follows that highly metamorphosed samples are derived from hot

asteroidal interiors, whereas unequilibrated materials are derived from cold, asteroidal crusts (Kimura et al., 2005; Lucas et al., 2020; Zhang et al., 1995).

Although it is a simple framework to view chondrites as being derived from primitive bodies which were spared from significant processing, Elkins-Tanton et al. (2011) instead argues for the idea that chondrites may instead represent the preserved crusts of early solar system bodies which often overlayed and insulated internal magma oceans (Ghosh and McSween Jr, 1998; Ghosh et al., 2006). This arrangement also places melted, and potentially degassing material under a cold crust where the transfer of volatiles can be expected to occur. As the largest control on the extent of metamorphism is the time in which bodies accrete (McCoy et al., 2006; Scheinberg et al., 2015), bodies of tens of km-radii which accrete <1.5 Myrs after CAIs will readily melt, retaining a thin crusts and an internal magma ocean (Elkins-Tanton, 2012; Elkins-Tanton et al., 2011b). The continual accretion of increasingly young chondritic material would function to grow the body, with younger bodies preserving a higher proportion of their chondritic crusts (Elkins-Tanton, 2012).

A notable difference in the thermal histories of bodies derived from OC-like vs. EC-like chondritic materials is the presence of water (Brearley and Krot, 2013). OCs accreted water-ice in their matrix which was released during the earliest stages of metamorphism (Lewis et al., 2022) resulting in aqueously metasomatized mineral assemblages (Brearley, 2006; Dobrică and Brearley, 2020; Grossman and Brearley, 2005). In contrast, the ECs were anhydrous, although vapors derived from their volatile-rich precursor materials may have instead manifested by exotic mineral assemblages reflective of high F-Cl-S fugacities (El Goresy et al., 2017; Lin and Kimura, 1998). Despite the numerous complexities in relating vapors/fluids derived from the metamorphism of these chemically distinct materials, some

continuum of hydrous, briney, sulfidic, and carbon-rich mediums will be released during metamorphism, locally react with the rock, and perhaps be lost to space (Elkins-Tanton, 2012; Elkins-Tanton et al., 2011b; Scheinberg et al., 2015), resulting in volatile depletions.

Due to the low confining pressure of asteroidal interiors, hydrated minerals were never stable and thus continually released fluids throughout low grade metamorphism (Elkins-Tanton, 2012). The marked density difference between these heated fluids and the surrounding materials likely resulted in significant fluid mobility (Britt and Consolmagno, 2003) and is expected to have exceeding the tensile strength of chondritic materials resulting in fracturing (Grimm and McSween Jr, 1989). On small (<100 km) permeable OC and CC parent bodies, fluids are thought to have been capable of migrating throughout the entire parent body in around 1 Myrs (Scheinberg et al., 2015). It is feasible that these fluids could become trapped in cold crustal regions, resulting in additional alteration and/or loss to space (Elkins-Tanton et al., 2011b; Young et al., 2003). In contrast, it is generally thought that ECs are less permeable, although fracturing could serve to increase the efficiency of fluid/vapor flow (Clauser, 1992).

EARTH'S SALT IS DERIVED FROM ENSTATITE CHONDRITES

Abstract

The chemical processing of chondrite parent bodies in the early solar system dictated the chemistry inherited by the planets. The concentrations and isotopic compositions of bio-essential and highly volatile elements (H, C, N, Cl) depict prolific vaporization throughout asteroidal accretion and thermal metamorphism; however, an abundance of these same elements was also necessarily retained to achieve Earth-like chemistry (Figure 4.10, 4.11). Using the halogen contents and chlorine isotope compositions of chondrites, we show that the Earth's accretionary feedstock was dominated by enstatite chondrites (EC). While the ECs retained much of their C, N, and halogens during metamorphism, the ordinary chondrites (OC) were effectively 'washed-out' facilitated by the presence of water (Figure 4.10, 4.11). Consequently, these results show that chondrites manifest the geochemical, as opposed to cosmochemical, processing of their most-labile elements during the earliest stages of thermal metamorphism (petrologic type ~ 3.2) which in part explains the long-standing ambiguity regarding nebular condensation phases for the halogens. The accretion and metamorphism of meteorite parent bodies resulted in the efficient transfer of labile elements to crustal reservoirs susceptible to collisional erosion. We construct a Monte Carlo simulation depicting this process using our measured data as inputs which show that OC-like materials cannot dominate the Earth, consistent with the fact that ECs are the only meteorite group with identical H, C, N, and Cl isotope compositions to the Earth.

Introduction

As the chondritic meteorites are the last vestiges of material formed after the birth of the Sun 4.6 billion years ago (Bouvier and Wadhwa, 2010), the chemical processing of these

materials throughout accretion dictated the chemistry of the planets and determined whether the water reservoirs in which life evolved, were habitable. All life depends on the availability of liquid water such that the water contents of meteorites have been a primary consideration towards creating habitable terrestrial planets; however, a similarly important group of elements are the halogens (F, Cl, Br, and I).

The halogens are an enigmatic group of bio-essential (Crockford, 2009; McCall et al., 2014), yet toxic elements at high concentrations (Flury and Papritz, 1993; Fuge, 2019; Knauth, 2005; Pavelka, 2004). This problem we term 'halogen poisoning' is particularly pressing for the Earth as its precursors are the non-carbonaceous (NC) ordinary and enstatite chondrites (OCs, ECs)(Dauphas et al., 2014; Warren, 2011) which without an effective mechanism to significantly deplete their halogens, would have imparted high salt contents (Rubin and Choi, 2009) into the asteroids that formed the Earth (Javoy et al., 2010). Excepting F, all other halogens are highly hydrophilic and thus are concentrated in water reservoirs of planets (Sharp and Draper, 2013). These affinities are important in terms of habitability, as while some organisms such as halophytes are capable of surviving in hypersaline environments (Flowers and Colmer, 2008), most photosynthetic organisms are severely hindered by salinity stress (Knauth, 2005; Shetty et al., 2019).

While the chemical compositions of chondrites are well constrained for nearly the entire periodic table (Kallemeyn and Wasson, 1981; Kallemeyn and Wasson, 1986; Wasson and Kalleymeyn, 1988), the variability in highly volatile and bio-essential elements, H, C, N, and the halogens (Crockford, 2009; McCall et al., 2014) are not similarly well-understood owing to their susceptible to contamination (Brearley and Jones, 2018; Grady and Wright, 2003). Although these limitations are not insurmountable given their abundances in

reasonably well-preserved samples (i.e., H, (Piani et al., 2020)), a paucity of research on the halogen geochemistry of chondrites has nonetheless occurred (Brearley and Jones, 2018). Despite the considerable skepticism involved in detangling the terrestrial alteration of meteorite 'finds' (Clay et al., 2017), these concerns have often disregarded peculiar, yet demonstrably primary features such as impact melt and soluble phases (El Goresy et al., 2017) that are more ambiguous in terms of their halogen contents than the evident organically-derived iodine-excesses in many Antarctic Meteorites (Dreibus and Wänke, 1983).

Although meteorite 'falls' are undoubtably more pristine; their halogen contents are nonetheless wide-ranging and disagreed upon (Clay et al., 2017; Dreibus et al., 1979). This issue has recently arisen with discrepant Cl and Br data between Clay et al. 2017, and Palme & Zipfel, 2021 that are difficult to reconcile as most previous studies have measured individual halogens on separate samples, such that it is not possible to detangle the effects of contamination based upon a single halogen measurement. Furthermore, a critical analysis of the available literature data on 'falls' shows a strong bias towards highly metamorphosed chondrites (on average petrologic type > 5) which are often associated with shock and impact melt features (Rubin, 1985; Ruzicka et al., 2015).

Despite these disagreements, the material that accreted to Earth is unequivocally comprised of NC chondrites and achondrites (Dauphas et al., 2014), such that mechanisms of halogen devolatilization necessarily occurred throughout the accretionary history of these bodies to achieve Earth-like halogen contents from the accepted average chondritic values (Lodders and Fegley, 1998; Wasson and Kalleymeyn, 1988). This problem we term 'halogen poisoning' is particularly pressing for the Earth as its precursors are the NC ordinary and

enstatite chondrites (OCs, ECs)(Dauphas et al., 2014; Warren, 2011) which without an effective mechanism to significantly reduce their halogen inventories, would have imparted high halogen contents (Rubin and Choi, 2009) into the asteroids that formed the Earth. The extant material analogous to the initial chemistries of Earth's accretionary materials are the chondrites which manifest the processing of volatile-rich nebular material (petrologic type 3.0 – 3.9*) to volatile-poor asteroidal material (type >4) from thermal metamorphism (Van Schmus and Wood, 1967; Vernazza et al., 2014). The cosmochemical context of this early processing is enigmatic, as NC chondrites are millions of years younger than their more extensively processed achondritic counterparts (Hellmann et al., 2019; Kleine et al., 2009; Spitzer et al., 2020), of which their initially chondritic materials have since been lost.

This lost material reflects the fact that meteorites are the preserved residues from planetary accretion (Marrocchi et al., 2021) thought to represent bodies ranging between 100 to >300 km diameter (Blackburn et al., 2017; Chapman, 1976; McCoy et al., 2006) that are unlikely to be preserved in the inner solar system (Burkhardt et al., 2021). The small sizes of these bodies (as opposed to embryo-sized accretionary components) during processing was likely integral in changing their chemical and isotopic compositions via evaporation ultimately inherited by the Earth (Tang and Young, 2020; Young et al., 2019). When such meteorite bodies accreted early (~ <1.5 Myrs after CAIs) with abundant short-lived radionuclides like ^{26}Al, they experienced melting and differentiation (Wilson et al., 2010) representing meteorite bodies sampling iron meteorite cores, achondritic mantles, and chondritic crusts (Elkins-Tanton, 2012; Elkins-Tanton et al., 2011b; Maurel et al., 2020). The volatile contents and isotope compositions of iron meteorites show that significant open-system degassing of planetesimals occurred throughout accretion (Gargano and Sharp, 2019;

Hirschmann et al., 2021); however, as the precursor materials to the ancient differentiated bodies does not exist in meteorite collections the connection between chondrites and these bodies remains tenuous.

To test the idea that chondrites experienced halogen-loss throughout metamorphism resulting in halogen-poor planets, we measured the halogen contents and chlorine isotope compositions of wide groupings of NC chondrites and achondrites to estimate the halogen inventories of chondritic asteroids at differing extents of metamorphism and determine the source of salt to Earth.

[*]*Petrologic type from 3-6 describes increasing extents of thermal metamorphism manifested by the rocks derived from different regions of the asteroidal body they are derived from.*

[**]*Chondrites are comprised of >80% chondrules.*

Discussion

We find that the halogen contents of our measured Antarctic meteorites are similiar to observed falls (Figure 4.1), and that the halogen contents and chlorine isotope compositions of NCCs are very sensitive to petrologic type and insensitive to differences between sub-types (Fig. 4.2)(Tables 4.1 – 4.4). When compared to the contaminated Antarctic meteorites measured by (Langenauer and Krähenbühl, 1993a), and excluding soluble iodine contents, our measured data are indistinguishable from the accepted literature data (Figure 4.3).

Dreibus	F (ppm)	Cl (ppm)	Br (ppm)	I (ppm)
OCs (n = 10)(Avg type = 5.5)	11.7±4.2	117±48.3	0.295±0.19	0.062±0.036
ECs (n = 1-3)(Avg type = 4)	64	581±160	3.13±0.50	0.315±0.191
Gargano				
OC Falls (SBC)(n = 13)	19.8±10.5	115±37	0.122±0.142	0.064±0.055
Falls (sum)(Avg type = 4.8)	20.3±10.8	203±86	0.396±0.333	0.126±0.223
OC Finds (SBC)(n = 20)	15.5±6.3	143±102	0.260±0.320	0.052±0.054
Falls (sum)(Avg type = 4.2)	23.4±12.8	244±220	0.368±0.369	0.107±0.116
EC Finds (SBC)(n = 7)	47.2±16.7	159±81	0.233±0.129	0.069±0.050
Finds (sum)(Avg type = 4.3)	67.2±23.4	345±316	0.560±0.490	0.400±0.540

Figure 4.1: Halogen data presented in this work in comparison to Dreibus et al (1979).

Table 4.1: Halogen contents and δ37Cl values vs. SMOC of ordinary chondrites.

Sample	Sub-Type	Petrologic Type	WSC_ppm_F	WSC_ppm_Cl	WSC_ppm_Br	WSC_ppm_I	SBC_ppm_F	SBC_ppm_Cl	SBC_ppm_Br	SBC_ppm_I	$\delta^{37}Cl_{WSC}$	$\delta^{37}Cl_{SBC}$	sum_ppm_F	sum_ppm_Cl	sum_ppm_Br	sum_ppm_I
MET 96503	L	3.1	23.8	445.0	0.319	0.028	23.2	475.2	0.283	0.001	-3.55	-4.52	47.0	920.249	0.601	0.029
DOM 10344	LL	3.4	19.3	192.4	0.092	0.108	21.0	218.7	0.252	0.140	-4.62	-4.48	40.2	411.263	0.344	0.247
GRO 06054	L	3.6	18.1	60.2	0.477	0.015	22.8	85.3	0.261	0.046	-3.40	-1.90	40.8	145.592	0.738	0.060
DOM 10490	LL	3.2	17.3	428.8	0.089	0.197	20.8	238.1	0.136	0.088	-2.73	-2.52	38.0	666.986	0.225	0.286
LAR 12034	LL	3.8	16.7	34.0	0.040	0.196	17.8	168.0	0.443	0.188			36.4	205.996	0.487	0.407
MET 01182	H	3.8	15.3	209.35	0.103	0.057	17.5	218.3	0.311	0.058	0.34	-0.06	32.7	427.710	0.414	0.115
QUE 99018	H	4	11.9	141.5	0.046	0.014	15.9	166.5	0.210	0.020	-4.14	-3.43	27.8	308.114	0.256	0.034
GRO 95552	LL	4	11.4	101.8	0.012	0.027	11.0	54.3	0.031	0.020	0.47	1.38	22.4	156.178	0.042	0.047
WSG 95300	H	3.3	10.7	22.6	0.126	0.005	17.6	196.9	0.201	0.013	-1.15	-1.16	28.3	219.628	0.327	0.019
QUE 97028	LL	5	7.1	31.0	0.007	0.031	4.2	68.2	0.036	0.036	1.19	1.16	11.3	99.269	0.043	0.067
PRE 95401	L	3.4	2.8	166.9	0.455	0.070	24.9	121.1	0.306	0.091	-2.42	-1.27	27.8	294.687	0.779	0.163
ALH 84086	L	4	0.6	15.9	0.053	0.018	18.4	140.8	0.094	0.020	-3.46	-3.22	19.0	157.271	0.149	0.039
ALH 84069	H	5		15.2	0.019	0.028	4.1	111.3	0.023	0.023	2.08	2.19	4.0	126.604	0.042	0.051
ALH 85033	L	4		17.4	0.039	0.009	13.1	78.6	0.316	0.010	0.66	0.59	13.1	96.187	0.355	0.019
BTN 00304	L	6		13.8	0.006	0.008	8.3	59.1	0.012	0.009	2.63	1.81	8.3	72.963	0.018	0.017
DAV 92302	LL	3.6		32.6	0.072	0.032	19.3	174.6	1.183	0.077	-2.84	-3.80	19.3	207.324	1.255	0.109
DOM 10005	L	6		22.3	0.009	0.007	11.6	47.3	0.012	0.020	1.22	0.66	11.6	69.691	0.021	0.027
MIL 09004	L	5		18.2	0.049	0.002	15.9	29.9	0.045	0.009			15.8	48.209	0.094	0.011
QUE 93030	H	3.6		24.1	0.123	0.181	17.2	164.8	1.030	0.149	-2.87	-4.17	17.1	187.695	1.147	0.320
TIL 82405	H	6		17.1	0.013	0.054	5.4	47.0	0.024	0.023	1.78	2.54	5.4	64.260	0.037	0.077
Chergach	H	5			0.009	0.008	11.8	74.4	0.018	0.016		1.80	11.8		0.027	0.024
Parnallee	LL	3.6		182.1	0.582	0.017	25.9	180.2	0.475	0.110	-1.60	-4.02	25.8	385.248	1.130	0.129
Tuxtuac	LL	5		54.6	0.381	0.010	14.8	106.2	0.019	0.035	-0.35	0.60	14.7	168.478	0.453	0.047
Avanhandava	H	4		44.8	0.148	0.008	18.7	115.0	0.052	0.048		2.07	18.6	183.750	0.278	0.060
Leedy	L	6		55.1	0.440	0.015	43.7	156.6	0.261	0.055		1.69	43.7	223.028	0.790	0.073
Bjurbole	L	4		86.4	0.259	0.502	16.5	143.6	0.135	0.220		-1.10	16.4	248.087	0.448	0.826
Kilabo	LL	6		49.8	0.293	0.006	24.3	88.3	0.154	0.079		-0.61	24.3	143.885	0.481	0.086
Dhajala	H	3.8		45.4	0.243	0.005	9.8	106.2	0.282	0.048		1.11	9.8	156.628	0.551	0.053
Marilia	H	4		97.1	0.207	0.020	34.1	159.7	0.127	0.092		-1.40	34.0	292.439	0.410	0.119
Nuevo Mercurrio	H	5.5		36.4	0.037	0.005	9.9	54.9	0.014	0.029		0.40	9.8	104.580	0.064	0.036
Chelyabisnk	LL	5			0.017	0.009	112.5	89.1	0.005	0.018			112.4		0.025	0.028
Chelyabinsk	LL	5					15.7	131.2	0.030	0.055						
Portales	H	5	1.2	30.1	0.063	0.005	12.2	87.1	0.020	0.028		0.49	13.5	121.513	0.092	0.034

Table 4.2: Halogen contents and δ37Cl values vs. SMOC of enstatite chondrites.

Sample	Sub-Type	Petrologic Type	WSC_ppm_F	WSC_ppm_Cl	WSC_ppm_Br	WSC_ppm_I	SBC_ppm_F	SBC_ppm_Cl	SBC_ppm_Br	SBC_ppm_I	$\delta^{37}Cl_{WSC}$	$\delta^{37}Cl_{SBC}$	sum_ppm_F	sum_ppm_Cl	sum_ppm_Br	sum_ppm_I
ALH 81021	EL	6	15.8	221.221	0.229	0.318	36.1	73.984	0.175	0.057		1.7	52.5	303.416	0.412	0.387
TIL 91714	EL	5	20.3	690.702	0.474	0.125	33.2	300.704	0.351	0.067		0.52	53.5	991.635	0.825	0.192
MAC 88136	EL	3	32.3	279.594	0.064	1.324	77.7	184.72	0.209	0.173	1.02	1.32	112.4	484.714	0.277	1.593
EET 96135	EH	4.5	9.8	26.953	0.036	0.029	44.9	88.285	0.065	0.024	2.23	8.5	54.8	115.622	0.101	0.053
DOM 14021	EH	3	27.6	771.947	1.127	0.137	58.8	220.568	0.417	0.056	-0.3	0.13	86.5	994.297	1.546	0.194
MAC 02747	EL	4	19.9	106.594	0.16	0.211	30.4	134.18	0.304	0.073	2.3	2.15	51.2	245.106	0.47	0.292
EET 96299	EH	4.5	9.7	91.824	0.175	0.052	49.2	109.881	0.111	0.032	-2.85	8.6	59.1	202.834	0.288	0.084

Table 4.3: Leachable salt contents of ordinary and enstatite chondrites.

Sample	Sub-Type	Petrologic Type	ppm_Rb	ppm_Sr	ppm_Na	ppm_K	ppm_Mg	ppm_Ca	ppm_Ti	ppm_Fe
MET 96503	L	3.1								
DOM 10344	LL	3.4								
GRO 06054	L	3.6								
DOM 10490	LL	3.2	0.011	0.013	1151.921	4.744	304.534	18.225	0.005	1.806
LAR 12034	LL	3.8								
MET 01182	H	3.8								
QUE 99018	H	4	0.035	0.012	269.416	5.142	224.535	10.891	0.002	0.006
GRO 95552	LL	4								
WSG 95300	H	3.3	0.112	0.002	892.853	72.054	11.627	0.800	0.003	0.042
QUE 97028	LL	5	0.008	0.015	157.271	2.748	414.421	18.895	0.001	0.311
PRE 95401	L	3.4								
ALH 84086	L	4								
ALH 84069	H	5	0.018	0.004	199.130	1.948	28.164	4.034	0.002	0.044
ALH 85033	L	4								
BTN 00304	L	6	0.008	0.004	128.417	0.951	25.195	2.876	0.007	0.082
DAV 92302	LL	3.6								
DOM 10005	L	6								
MIL 09004	L	5								
QUE 93030	H	3.6	0.003	0.005	178.262	1.053	22.710	3.896	0.008	0.274
TIL 82405	H	6	0.008	0.015	540.961		367.182	9.179	0.001	21.690
ALH 81021	EL	6	0.024	0.055	123.004	2.904	21.686	331.739	0.003	0.05
TIL 91714	EL	5	0.017	0.191	133.236	2.44	18.705	1006.376	0.006	0.559
MAC 88136	EL	3	0.181	0.263	402.391	33.12	377.565	524.154	0.009	2.476
EET 96135	EH	4.5	0.004	0.639	193.244	0.743	414.643	281.885	0.016	19.517
DOM 14021	EH	3	0.023	0.159	294.419	6.071	144.33	269.643	0.012	5.791
MAC 02747	EL	4	0.16	0.223	326.854	37.922	265.354	473.925	0.009	1.711
EET 96299	EH	4.5	0.007	0.761	208.884	1.187	412.419	327.316	0.014	11.424

Table 4.4: Halogen contents and δ37Cl values vs. SMOC of achondrites.

Sample	Type	SBC_ppm_F	SBC_ppm_Cl	SBC_ppm_Br	SBC_ppm_I	$\delta^{37}Cl_{SMOC}$	sum_ppm_F	sum_ppm_Cl	sum_ppm_Br	sum_ppm_I
Norton County	Aubrite	7.138	2.6	0.007	0.012					
Pena Blanca	Aubrite	24.396	65.87	0.024	0.017	3.7	28.18	79.31	0.03	0.02
NWA 8551	Ureilite	22.832	72.648	0.118	0.082	-0.4				
NWA 8456	Lodranite	26.016	189.204	0.15	0.13	0.6				
NWA 7904	Brachinite	20.393	58.266	0.06	0.061	-1.3				
NWA 8547	Ureilite	19.232	146.082	0.258	0.694	-0.5				

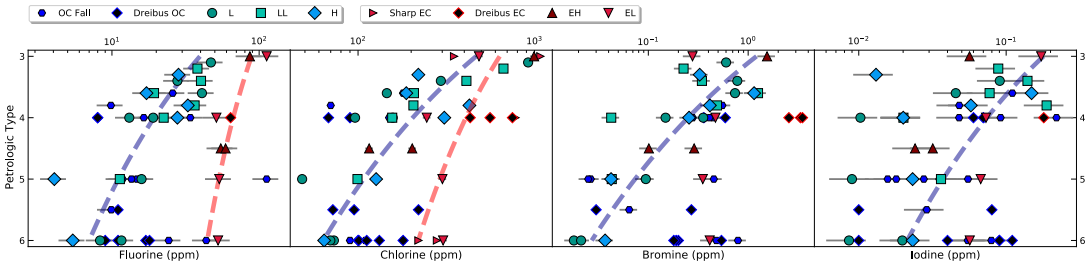

Figure 4.2: Halogen contents (WSC + SBC, except I) vs. petrologic type of ordinary and enstatite chondrites. Regression lines are best fit through all data with exception to Dreibus OC (Dreibus et al., 1979) and petrologic type 6 OC falls suspected to contain impact melt. OC R^2 (F, Cl, Br and I) are 0.64, 0.66, 0.66, 0.46, respectively. EC R^2 (F and Cl) are 0.72 and 0.32, respectively.

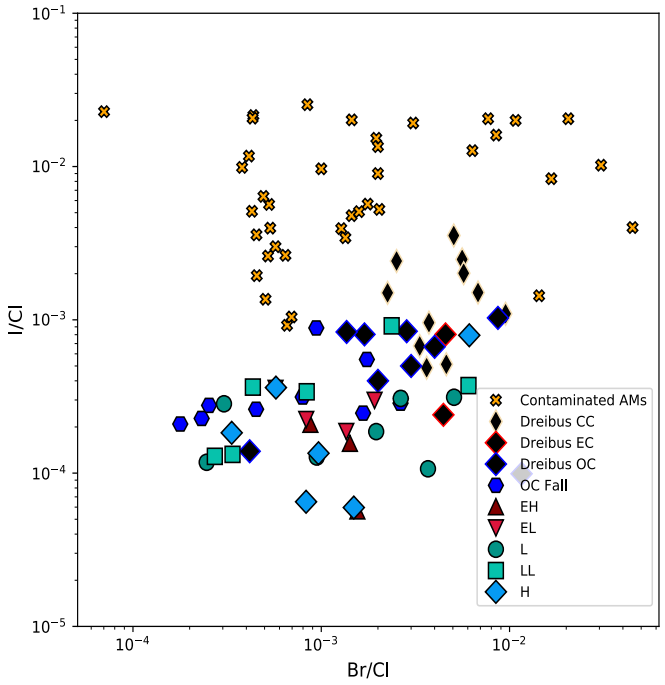

Figure 4.3: Total Br/Cl vs. I/Cl. Iodine contents are only insoluble. Contaminated AMs from (Cheng et al., 2020; Langenauer and Krähenbühl, 1993a; Langenauer and Krähenbühl, 1993b)

Owing to the water-solubility of the halides and the occurrence of water-ice in their matrices (Lewis and Jones, 2016; Lewis and Jones, 2019), OCs show stark F and Cl depletions during early-stage metamorphism from type 3.0 to 4. In comparison, the anhydrous ECs (Brearley and Jones, 2018; Brearley and Krot, 2013) and achondrites (Keil, 2010) depict similar extents of Cl-loss yet retain significantly higher fluorine contents in excess to many type 6 OCs. While the idea of 'washing out' halogens with aqueous fluids could feasibly significantly deplete halogen contents, this process cannot significantly fractionate Cl isotope compositions by the >7‰ observed in this data set (Barnes and Sharp, 2017) and is only applicable to the OCs. Instead, we favor the idea that evaporative Cl-loss

would result in concomitant increases in $\delta^{37}Cl$ values as seen for other volatile elements (Hellmann et al., 2021).

Evaporative loss of halogens from OCs and ECs is consistent with wide ranges of $\delta^{37}Cl$ values from -5 to +2, 0 to +7‰, respectively, increasing with decreasing Cl contents (Fig. 4.4). Low $\delta^{37}Cl$ values (~ -5‰) have been measured in a variety of planetary materials including iron meteorites (Gargano and Sharp, 2019), Martian meteorites (Shearer et al., 2017), and Parnallee (LL3.6)(Sharp et al., 2013), and is thought to represent the initial $\delta^{37}Cl$ value of the inner solar system (Fig. 4.5). These low values, however, are not retained in any other chondrite group.

This could be explained by the higher ambient metamorphic conditions of the ECs (Zhang et al., 1995), and that CC matrices are processed and volatile-depleted (Bland et al., 2005). It is also feasible that chondrule-forming processes contributed excess light volatile-element isotopes into chondrules (Koefoed et al., 2020; Nie et al., 2021), although it is unclear as to why these low $\delta^{37}Cl$-bearing chondrules would only be preserved in OCs. This could be explained if a majority of halogens are cited in chondrule mesostasis which is rapidly decomposed in the earliest stages of metamorphism as this component often contains up to 4wt% Cl (Bridges et al., 1997; Grossman et al., 2002; Grossman and Brearley, 2005; Piani et al., 2016) which further serves to explain the stark halogen depletion occuring from type 3.0 to 4. As several Cl-rich chondrules in type 3 ECs demonstrably depict evaporative processes (Mercer and Jones, 2010), it is also feasible that these isotopically primitive components are simply not preserved, or conversely, are difficult to isolate from the exotic halogen-bearing mineralogy of the ECs (Rubin and Choi, 2009).

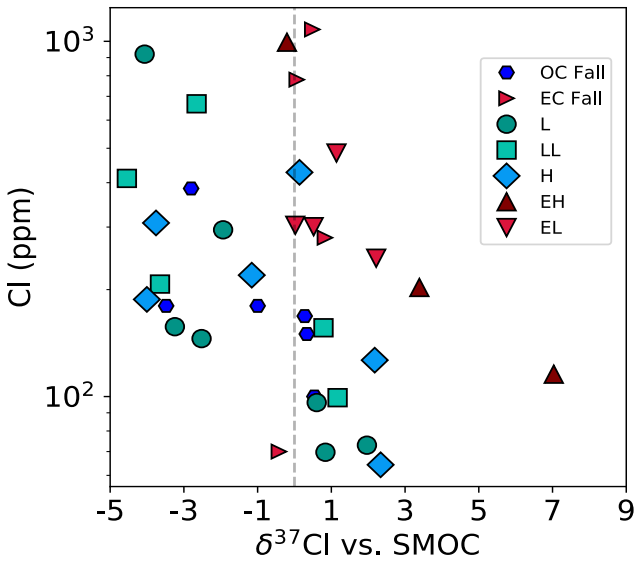

Figure 4.4: $\delta^{37}Cl_{SBC+WSC}$ vs. $[Cl]_{SBC+WSC}$ of NCCs data includes (Sharp et al., 2013).

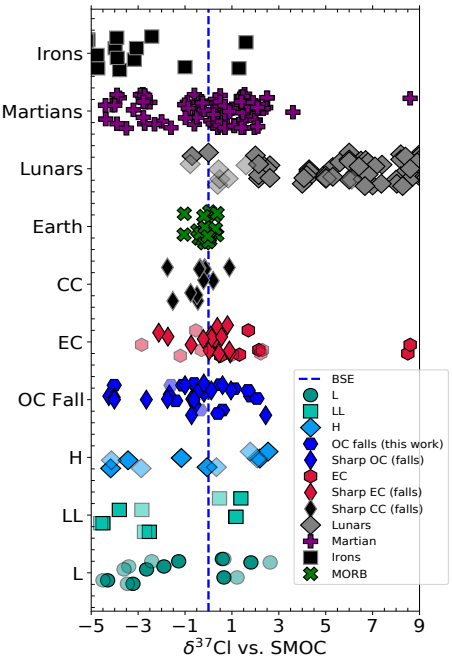

Figure 4.5: $\delta^{37}Cl$ values of planetary materials. Insoluble $\delta^{37}Cl$ values are solid, soluble $\delta^{37}Cl$ values are faded. Data sources include (Gargano and Sharp, 2019; Gargano et al., 2020; Sharp et al., 2013; Sharp et al., 2010; Shearer et al., 2014; Shearer et al., 2017)

Despite the difficulties in relating the thermal history of OCs and ECs, the large range of halogen contents and $\delta^{37}Cl$ values in both NCC groups is readily explained by evaporation of chondritic materials throughout metamorphism. Both NCCs and achondrites exhibit concomitant loss of F and Cl that generally parallels the trend depicted by lunar pyroclastic glasses (Saal and Hauri, 2021). Evidently the extent, or style (Gargano et al., 2021) of evaporation was not as extreme on meteorite parent bodies when compared to the Moon, depicted by the limited range of achondrite bulk-rock $\delta^{37}Cl$ values from -1.3 to +3.7 in contrast to the wide-range of lunar materials from 0 to >30‰ (Fig. 4.5); however, localized conditions necessarily allowed for similarly prolific Cl isotope fractionation on the ~525 km diameter 4Vesta with $\delta^{37}Cl$ values in apatite up to 40‰ (Barrett et al., 2019).

Although body size clearly affects the efficiency of the myriad of volatile loss processes occuring on early solar system bodies (Elkins-Tanton, 2012; Elkins-Tanton et al., 2011b; McCoy et al., 2006), the Cl and F contents of BSE, HEDs, and lunar materials depict the preferential loss of Cl >> F (Fig 4.6) that is not manifested in the chondrite suite nor the achondrites and may have been inherited by their accretionary components (Young et al., 2019). As the outer ~5 km shells of meteorite bodies dissipate heat faster than can be gained from underlying sources (Ghosh and McSween Jr, 1998), it can be expected that cold crustal reservoirs potentially acted as sinks for underlying degassing volatiles. Following this rationale further, chondritic crusts could contain excess internally derived volatiles from their parent bodies deposited locally within the crust – consistent with the occurrence of halite in chondritic breccias (Chan et al., 2018). Asteroidal crustal reservoirs, however, are widely recognized to be susceptible to loss during accretion (Allibert et al., 2021; Boujibar et al.,

2015; Carter et al., 2018), such that crustal erosion in addition to evaporation likely explains further extents of halogen depletions throughout the growth of meteorite parent bodies.

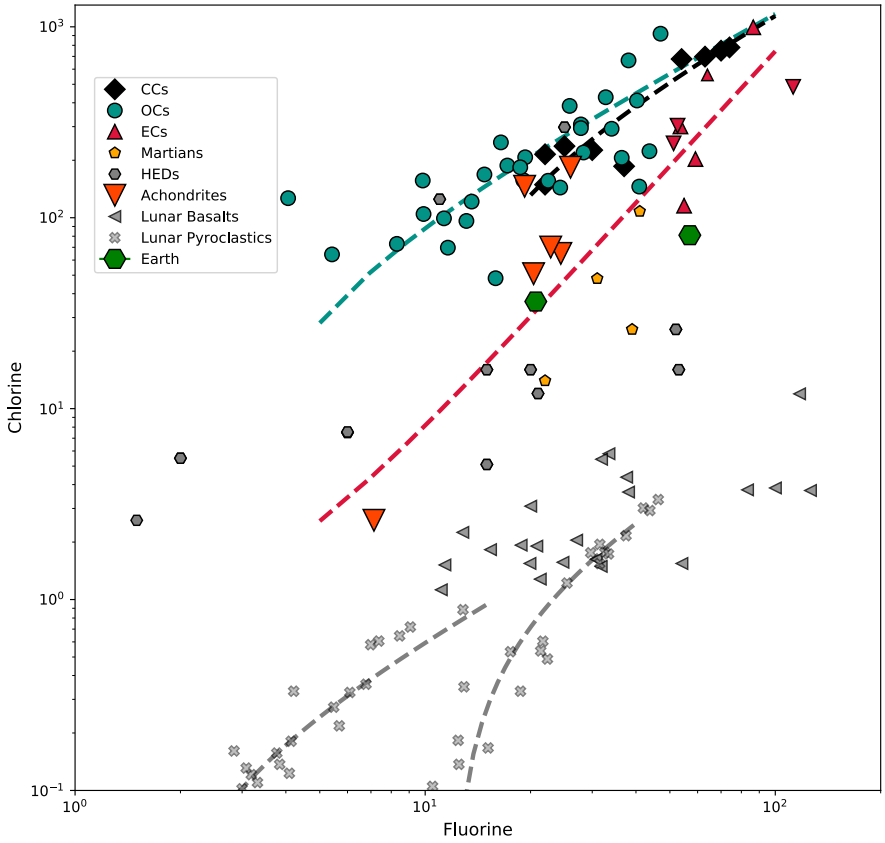

Figure 4.6: Total F and Cl contents of planetary materials. Teal, black, red, and grey dashed lines are regressions through all OC, CC, EC+achondrites and PGB data, respectively. CC data from Dreibus et al. (1979). PGB data from Saal et al. (2020). HED and Martian data (Shergotty and EETA 79001 A, B, C) from Dreibus et al. (1985). Earth estimates are from Lodders and Fegley (1998), and Guo and Korenaga (2021).

This general idea is consistent with the high Cl contents of several HEDs and achondrites relative to the degassing trends exhibited by ECs and achondrites. We suspect these Cl-enrichments are analogous to the Stannern trend exhibited by the HEDs (Stannern and Molteno are enriched in Cl > F, (Dreibus and Wanke, 1985)) – likely produced via interactions with partial melts, crustal contamination (Barrat et al., 2007; Crossley et al., 2018), and the incorporation of internally derived vapors (Sarafian et al., 2017). Subsequent loss of such Cl-rich crustal reservoirs serves as a parsimonious explanation for the progressive Cl >> F depletion throughout planetary accretion. This idea is further consistent with the Mg/Si ratio of the Earth – which requires erosion of Si-rich crusts on EC asteroids (Boujibar et al., 2015), and has been previously proposed as a significant mechanism to deplete Cl from planetary bodies (Sharp and Draper, 2013). Similar to the necessity of isotope fractionation on small bodies (Tang and Young, 2020; Young et al., 2019) – collisional erosion was also most efficient while bodies remained small (McCoy et al., 2006).

As follows we construct a Monte Carlo simulation depicting the changes in the halogen contents of meteorite bodies occuring via collisional erosion. As no large differences are seen between chondrite sub-types (i.e., L vs. LL vs. H), we assume that the halogen inventories of OC and EC-like chondritic asteroids can be estimated by changes in the halogen contents of OCs and ECs as a function of petrologic type. Further, as achondrites fall within the degassing trends depicted by the NC chondrites, we also include these bodies such that our model is representative of both minimally metamorphosed chondrite parent bodies, as well as partially differentiated achondrite bodies with small portions of chondritic crusts.

Our mass balance equation is as follows:

$$[X]_{Final} = \frac{[X]_{Body} - [X]_{Crust} + [X]_{Crust} * X + (1 - X)(1 - Y)[X]_{Crust}}{X + (1 - X)(1 - Y)}$$

Where X is the fraction of total [X] (F, Cl) in the mantle of the body before erosion, and Y is the fraction of crust that is lost. We apply this model to two separate asteroidal populations comprised of OC and EC material. We allow the fluorine contents of the initial bodies to range between 5 to 20, and 5 to 40 ppm, respectively, for the OC and EC populations. These values are chosen to limit the simulated bodies to those with <= 30% chondritic crust (Boujibar et al., 2015; Vernazza et al., 2014)(calculated by mass balance between the mantle and crust end-members). Similarly, we limit the model solutions to those with bodies with >60% of total fluorine in mantles ($[X]_{Body}$) to depict these mass balance constraints.

We then calculate the Cl contents of those bodies based upon the F/Cl ratios of OC and EC materials separately. This allows the 'creation' of initial bodies that fall along the lines depicted by increasingly F-Cl-poor planetary materials either on the OC and EC populations (initial bodies would plot on the teal and red lines on Figure 4.6). We then allow for the [F, Cl] contents to range between the minimum and maximum values of each respective group with a suprachondritic enrichment of approximately 100% to represent crustal enrichment of halogens. In the case of the OC and EC populations, this results in ranges of [F, Cl] of [5-100, 100-1000], and [40-200, 200-1500], respectively ($[X]_{Crust}$). Figure 4.7 depicts these model results.

Figure 4.8 shows the average F and Cl contents of the bodies and crusts for the EC and OC-like simulations that best-fit the BSE estimates from L&K and G&K (Guo and Korenaga, 2021; Lodders and Fegley, 1998). Although we do not favor one estimate over another, given the recent understanding that the transition zone is a large fluorine reservoir (Roberge et al., 2015) – the L&F F value should be taken as a minimum. The model results

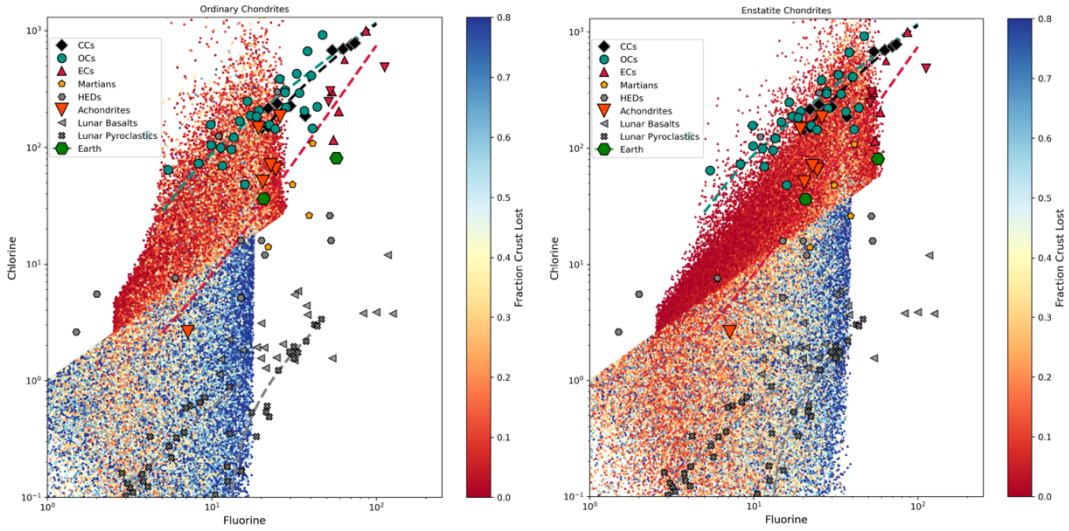

Figure 4.7: Monte Carlo simulation of collisional erosion from OC and EC-like bodies. Color bar is the fraction of crust lost. Round series are OC-like simulations, whereas triangle are EC-like simulations.

cannot reproduce the BSE from the G&K estimate sourced from OC-like bodies. Using the L&F estimate, the OC-population only produces BSE-like bodies from unreasonably high mantle [Cl] contents of 173±13.8 ppm which far exceeds the measured type 6 OCs (~70 ppm) which presumably represents the mantle maximum (i.e., a partially differentiated body's mantle should always contain less volatiles than the most metamorphosed chondritic precursor materials). Similarly, the OC population cannot reproduce Shergotty-like bodies.

In contrast, the EC-like materials readily produce BSE-like bodies with Cl contents consistent with the measured achondrites and type 6 ECs (LF: 62.0±23.7, GK: 106.5±7.7). This idea is consistent with the relatively lower amount of crustal erosion required for the EC-like simulations (LK: 8.5±7.6%, GK: 6.4±8.6% vs. LK (OC-bodies): 17.3±15.0%) which agree with the extent of erosion necessary obtaining Earth-like Si/Mg ratios from ECs

(Boujibar et al., 2015). Thus, these data and model results indicate that the salt contents of the BSE are best explained by ECs.

In conclusion, the Earth was necessarily accreted from NC chondrite material that experienced salt-loss throughout metamorphism by a continuum of devolatilization processes including, fluid 'wash-out', vaporization, and collisional erosion. The individual contributions of these processes are currently not possible to disentangle, however, the secular trend of decreasing volatile contents with increasing metamorphism is reflected in both chondrites and achondrites and suggests a logical 'volatile-loss' kinship between these materials. The markedly dissimilar F contents of the metamorphosed OCs relative to the BSE suggests that EC-like materials dominated the Earth's accretionary feedstock.

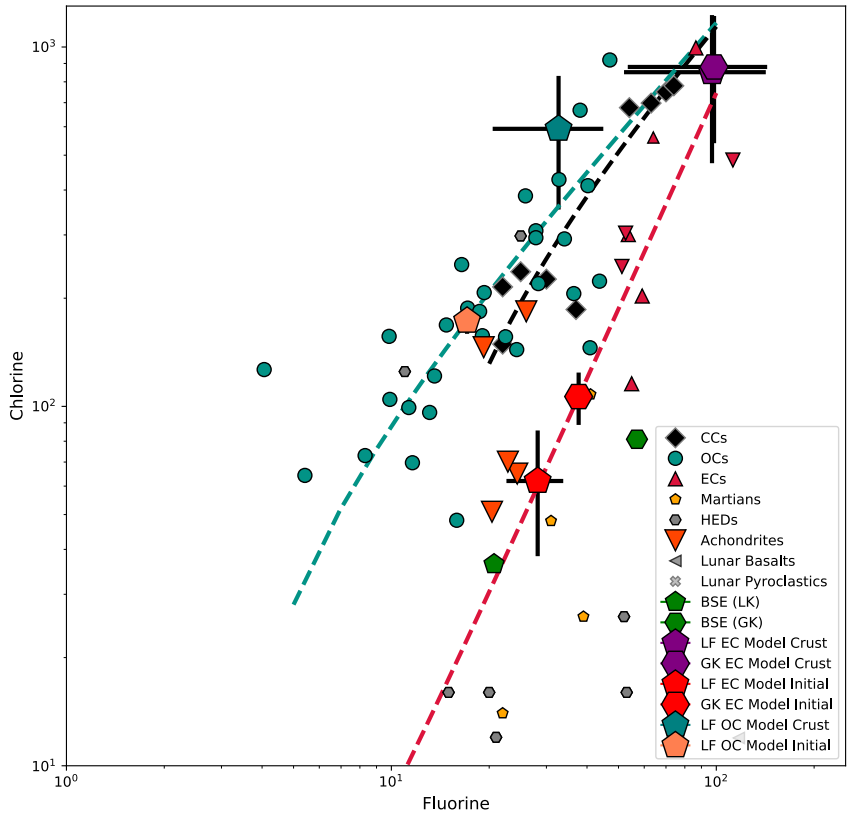

Figure 4.8: F vs. Cl with model results from Monte Carlo simulations.

Supplemental information

Supplemental Figures

Figures 4.9 and 4.10 are shown to simply show the relationships with other highly volatile bio-essential element systems in chondrites (Grady et al., 1986; Grady et al., 1983; Hashizume and Sugiura, 1995).

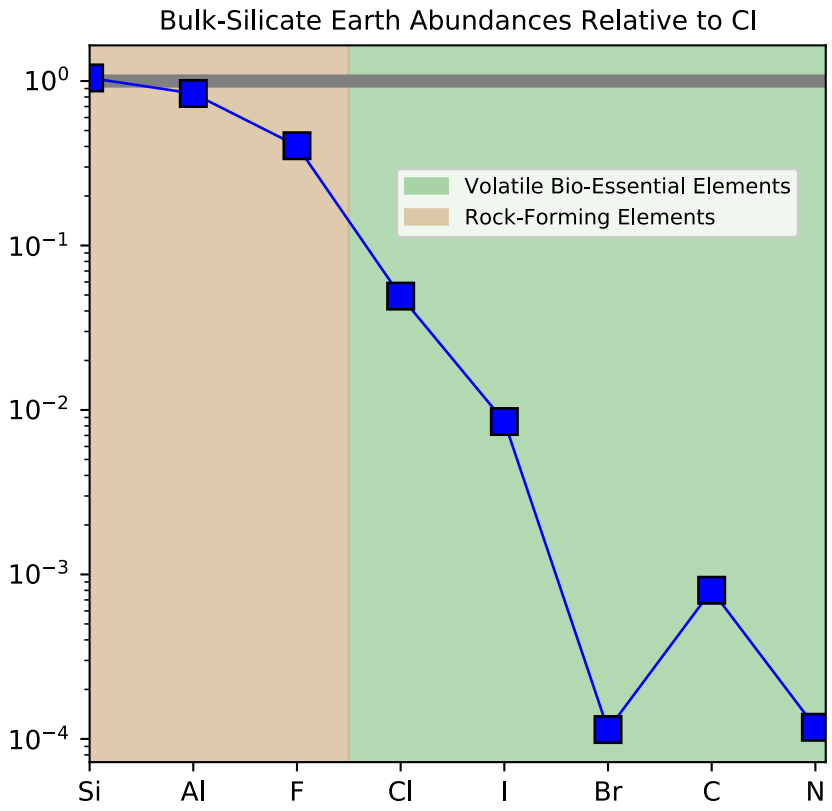

Figure 4.9: Selected elemental abundances in the bulk-Silicate earth relative to CI chondrites. This figure depicts the similarly extensive depletions of highly-volatile and bio-essential elements. Data from (Lodders and Fegley, 1998)

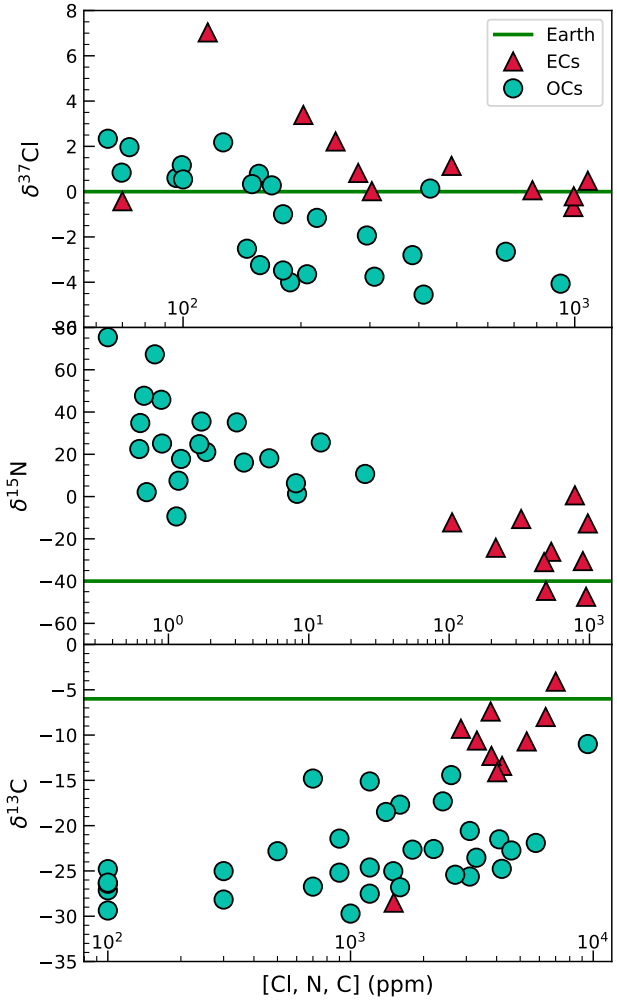

Figure 4.10: Cl, N, C contents vs. Cl, N and C isotope compositions. Chlorine data from this work and Sharp et al. (2013). N and C data from Grady et al. (1986, 1982, 2003) and Hashizume & Sugiura (1995). Horizontal green line indicates estimates for the bulk-Earth's Cl, N and C isotope compositions of 0, ~-40 (Mysen, 2019), and -6‰, respectively.

Literature Disagreement

The available literature halogen abundances of chondrites are wide-ranging due to differences in samples and analytical procedures including spectroscopy, neutron activation and pyrolysis (Allen Jr and Clark, 1977; Clark et al., 1967; Dreibus et al., 1979; Garrison et al., 2000; Goles et al., 1967; Greenland and Lovering, 1965; Kallemeyn and Wasson, 1981). Disagreements are thought to result from contamination, both in Antarctic meteorites (Dreibus et al., 1979; Dreibus and Wänke, 1983; Heumann et al., 1987; Heumann et al., 1990; Kato et al., 2000; Shinonaga et al., 1994), as well as for terrestrial falls and finds (Clay et al., 2017), and are further complicated by significant heterogeneity between samples and a large water-soluble chloride component (20-50% of total Cl)(Brearley and Jones, 2018). Heterogeneity is likely associated with the lability of the halogens and are thought to be significantly heterogenous on the scales of ~1 g for CI chondrites (Barrat et al., 2012; Marrocchi et al., 2021). Thus, the inadvertent use of typically low-mass samples (i.e., (<7 mg) Clay et al., 2017) has potentially further confounded representative halogen contents of chondrites.

While falls are certainly the most pristine samples, there remains the problem of incomplete data sets measured in the same sample chips. This issue is further compounded since while falls are certainly the most well-preserved, insufficient samples and masses are readily available to characterize differences between sub-types and petrologic types. This is particularly important as thermal metamorphism of chondrites has been shown to result in extensive volatile loss (Tandon and Wasson, 1968) and isotope fractionation (Creech and Moynier, 2019; Moynier et al., 2007a), although this idea has not yet been tested for the halogens.

In fact, careful analysis of the available literature data shows a bias towards high petrologic type samples with the OCs measured in Dreibus et al., (1979) averaging 5.5, Reed et al., (1964, 1966) 5.6, Goles et al., (1962, 1967) 5.4, Sharp et al., (2013) 5.0. The comparisons of OC data to those of ECs are more fraught as much of the available data for ECs are derived from unequilibrated low petrologic type samples such as Qingzhen (EH3)(Kallemeyn and Wasson, 1986). As the data presented here (see Figures 4.2 and 4.3) clearly show that the halogen contents of chondrites are sensitive to petrologic type, and further, that our measured Antarctic meteorites are not evidently contaminated (Figure 4.4, 4.17), the historical literature debates will not be elaborated upon.

I suspect that much of the disagreement regarding the halogen contents of chondrites have centered around non-representative comparisons (i.e., differences in petrologic type) and oversimplifications (i.e., susceptibility of contamination relative to petrologic type and peculiar, yet primary chemical features such as impact melt) which have inadvertently created a biased perspective on the halogen inventories of chondrites towards those of highly thermally metamorphosed, and thereby extensively volatile-depleted samples. Further, due to many studies measuring a single halogen (i.e, F, or Br), it is difficult to reconcile whether the source of this variability results from contamination or features such as impact melt. The only data including the entire suite of halogens in reasonably well-preserved samples have been generated by Dreibus et al. (Figure 4.1)(Dreibus et al., 1979; Dreibus and Wanke, 1985; Dreibus and Wänke, 1983; Dreibus et al., 1986), and thus are the only comparisons made.

Although recent halogen data has been generated by Clay et al. (2017), these data do not include fluorine contents and additionally, I suspect that the small sample sizes (all <7 mg) make the comparisons to our data (large bulk-rock samples > ~1g) difficult as no other

data measured by any other method agree with these data and has been recently addressed (Palme and Zipfel, 2021). I do not use these data as well as several other literature sources as most data were generated from independent methods for individual halogen measurements on different samples and where the same samples were measured, they were performed on different sample chips (Brearley and Jones, 2018). Given the expected heterogeneity in halogen contents, and the fact that the presence of these features cannot be reconciled as individual halogens were measured on separate samples, I suggest these comparisons are not representative.

In response to these historical difficulties, this work was designed specifically to test the question of the extent of halogen contamination of chondrite 'finds' as well as perform the first study to measure a broad group of samples from all available sub-types and petrologic types for their full suite of soluble and insoluble halogens. It is important to note that the sample request criteria for the Antarctic samples specifically requested interior chips, free from fusion crust and obvious patches/veins containing alteration features which was confirmed upon visual inspection. Similarly, large sample masses were processed (approximately 2 grams of OC material and 1 gram of EC material) to limit the effects of heterogeneity, as well as maximize the primary component of the chondrites relative to any contaminants if present. As follows I discuss the 'Antarctic Meteorite Paradigm' which has been a prevalent discussion point regarding the halogen contents of chondrites, as it is generally thought that they are irreconcilably contaminated with halogens.

The Antarctic Meteorite Paradigm

The Antarctic meteorite paradigm is presented in several publications and generally follows that Antarctic meteorites are extensively contaminated with halogens due to

interactions with organohalides emitted by phytoplankton blooms (CH_3I) and/or sea spray (Dreibus and Wänke, 1983; Heumann et al., 1987; Heumann et al., 1990; Kato et al., 2000; Langenauer and Krähenbühl, 1993b; Noll et al., 2003; Shinonaga et al., 1994). Dreibus and Wanke (1986) first proposed the idea that iodine overabundances in Antarctic meteorites were related to aerosol interactions with CH_3I in achondrites. Langenauer and Krahenbuhl (1993) concluded similar findings and proposed that the halogen contaminants were largely contained in first few millimeters of the surface of type 5 and 6 OCs, although additionally suggested a sea spray contaminant contributed excess F, Cl and Br contents.

It is important to note that the two processes of sea spray and organohalide emissions manifest in starkly different chemical trends. Organohalide emissions are only significant for I >> Br (Carpenter et al., 2003), and seawater, while rich in Cl (19,400 ppm) and Br (70 ppm), is F (~1.5 ppm) and I-poor (~0.05 ppm). Thus, if an argument is to be made to contaminate the full suite of halogen contents, it necessarily invokes a sea spray derived Cl & Br contaminant, an aerosol derived CH_3I contaminant, as well as a poorly defined fluorine-rich contaminant which cannot be feasibly sourced from the ocean. Furthermore, sea spray derived contaminants necessarily occur alongside other soluble elements in seawater (i.e., Na, K, Ca) which should overprint any primary leachable chemical features present in chondrites. With these inconsistencies in mind, I suspect that the weathering profiles observed by Langenauer and Krahenbuhl (1993) at least for the least likely elements to be contaminated such as F, result from the in-situ mobilization of labile elements from the chemical instability of meteoritic components in the oxidizing environment of Earth.

Several ideas regarding halogen contamination in Antarctic meteorites can be tested in our data set due to the fact that contaminants are likely isolated to water-soluble phases

(Brearley and Jones, 2018). First, samples collected close to the coastline would more readily interact with sea spray derived halogens which would serve to increase their water-soluble halogen contents, as well as drive their $\delta^{37}Cl_{WSC}$ towards seawater (0‰). These trends are not observed in our data, with F, Cl, Br, and I content and $\delta^{37}Cl_{WSC}$ values independent of distance collected inland (Fig. 4.11-4.14). The retention of low $\delta^{37}Cl$ (~ -5‰) values in both water-soluble and insoluble chloride in several samples necessarily argues by mass balance that a majority of measured chloride is not derived from seawater. This idea is further supported by the limited Cl isotope data from McMurdo dry valley lakes with $\delta^{37}Cl$ values from -1 to 0.5‰ (Berry Lyons et al., 1999), and from Antarctic sea ice with $\delta^{37}Cl$ values from -1.1 to 0.4‰ (Vallelonga et al., 2021), as well as dry valley soils from -2.1 to 0.56‰ (Bao et al., 2008).

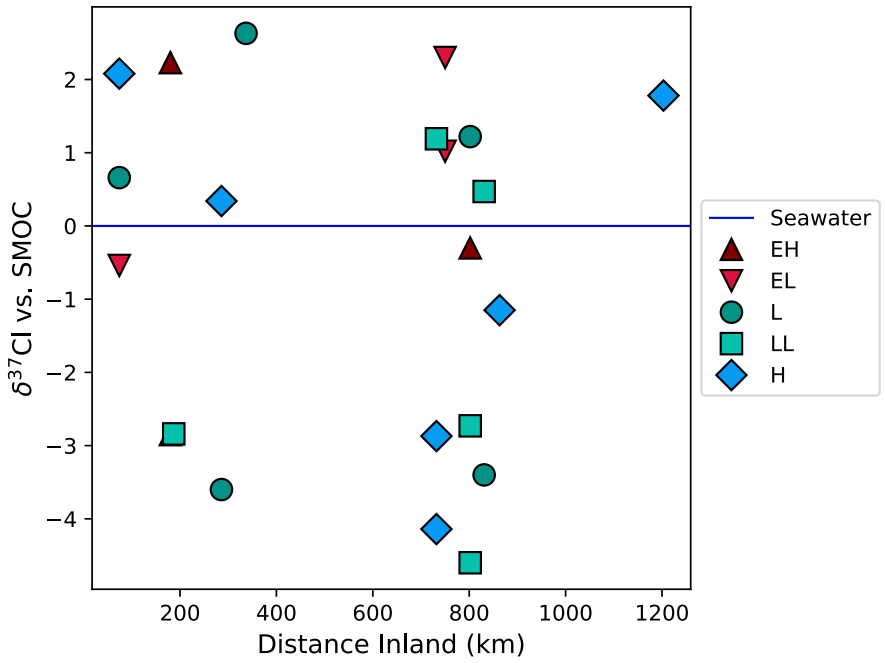

Figure 4.11: Distance inland (Km) vs. $\delta^{37}Cl_{WSC}$ vs. SMOC.

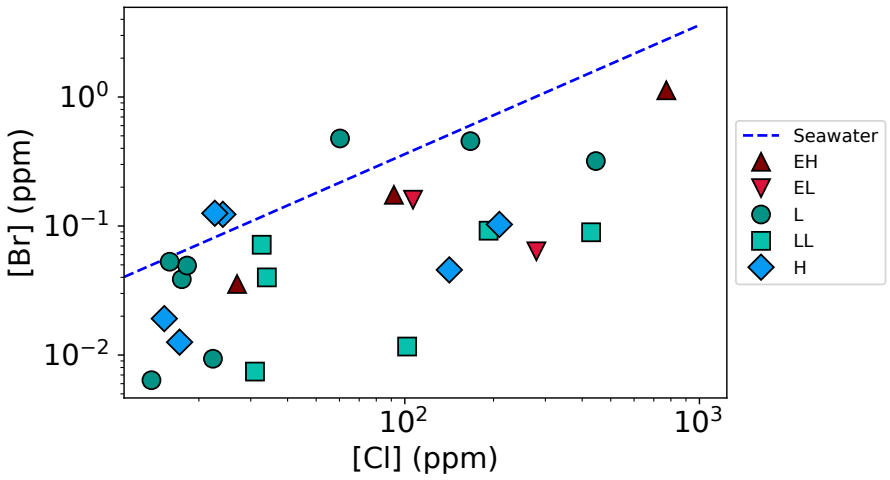

Figure 4.12: Leachable (WSC) Cl vs. Br contents (ppm).

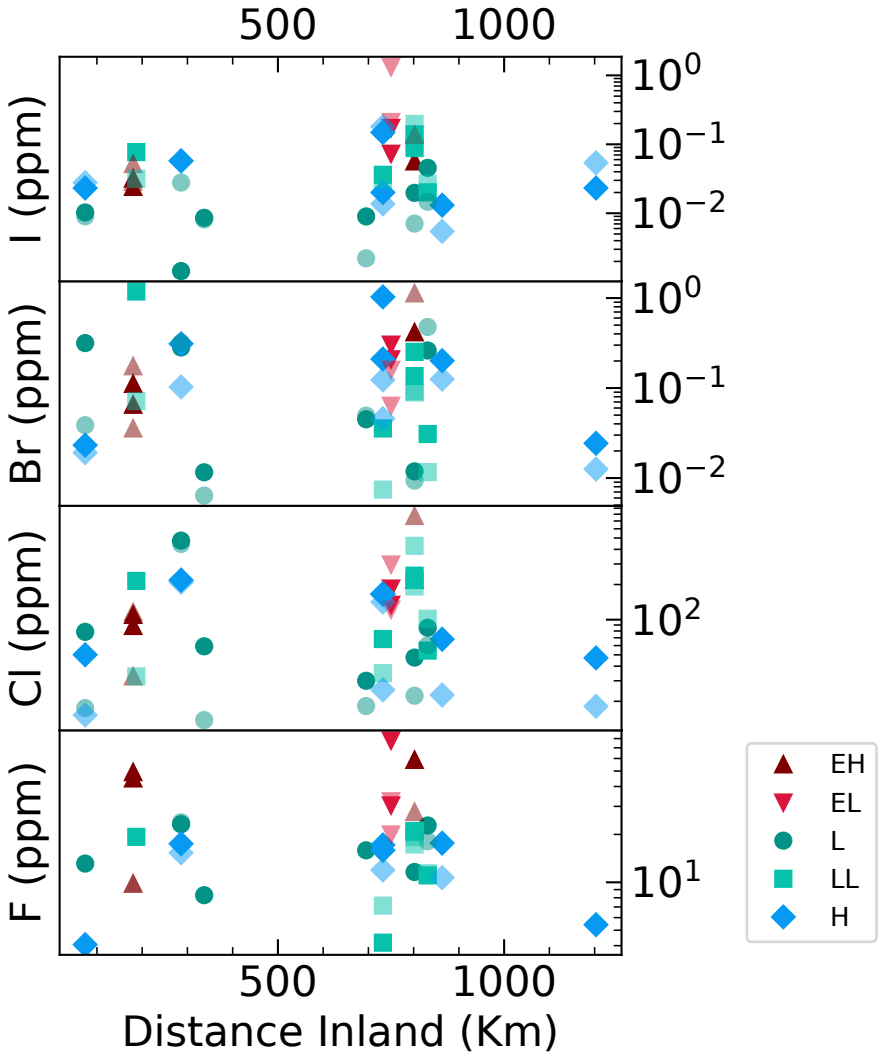

Figure 4.13: Distance inland (km) vs halogen contents. Bold symbols are structurally-bound halogens. Faded symbols are water-soluble halogens.

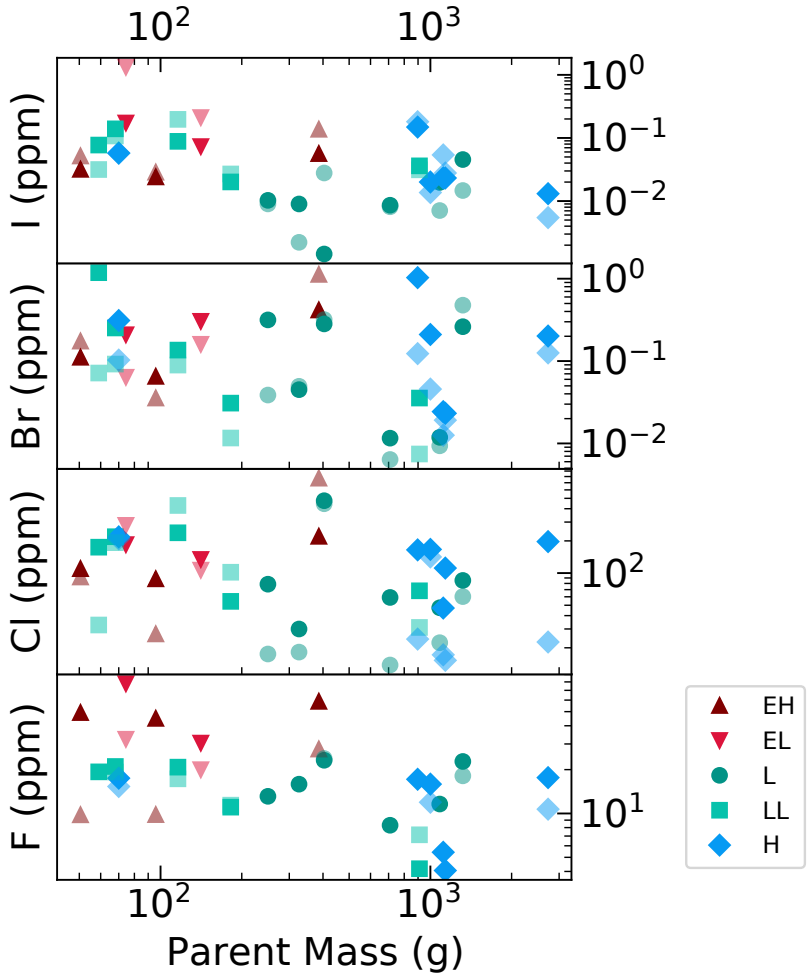

Figure 4.14: Parent mass (g) vs. halogen contents. Bold symbols are structurally-bound halogens. Faded symbols are water-soluble halogens.

The water-soluble halogen contents are also not directly related to leachable Na, K, Ca, Rb, or Sr contents (Figure 4.15), and in fact, the markedly higher leachable Ca and Sr content of the ECs is consistent with the retention of soluble oldhamite (Defouilloy et al., 2016) and suggests that the primary leachable components in these rocks have not been overprinted or washed out via terrestrial alteration. The potential for limited fluid mobility in Antarctica is unsurprising, as ambient air temperatures are rarely above -15 °C (Fig. 4.16)(Schultz, 1986), and the halogen contents of Antarctic snow are exceptionally low with Cl, Br and I contents ranging from 0.3-40, 0.002-0.14, and $3x10^{-7}$-$1.8x10^{-3}$ ppm, respectively, with Cl and Br concentrations > 8 and 0.014 ppm, respectively only found near the coast (Heumann et al., 1987).

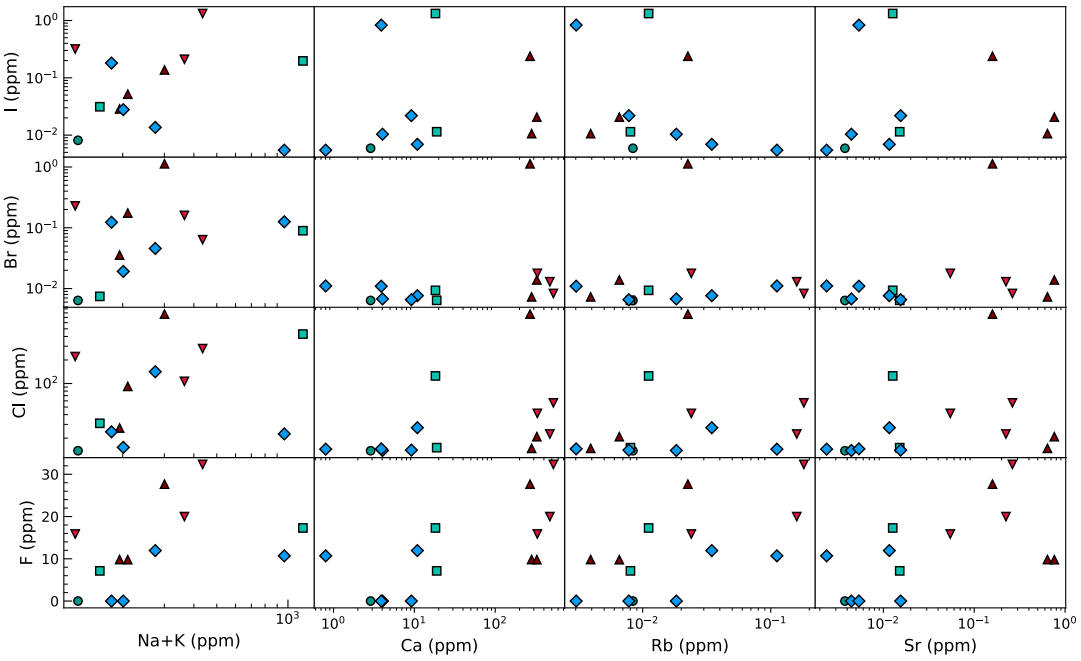

Figure 4.15: water-soluble halogen contents vs. leachable Na+K, Ca, Rb, and Sr contents (ppm).

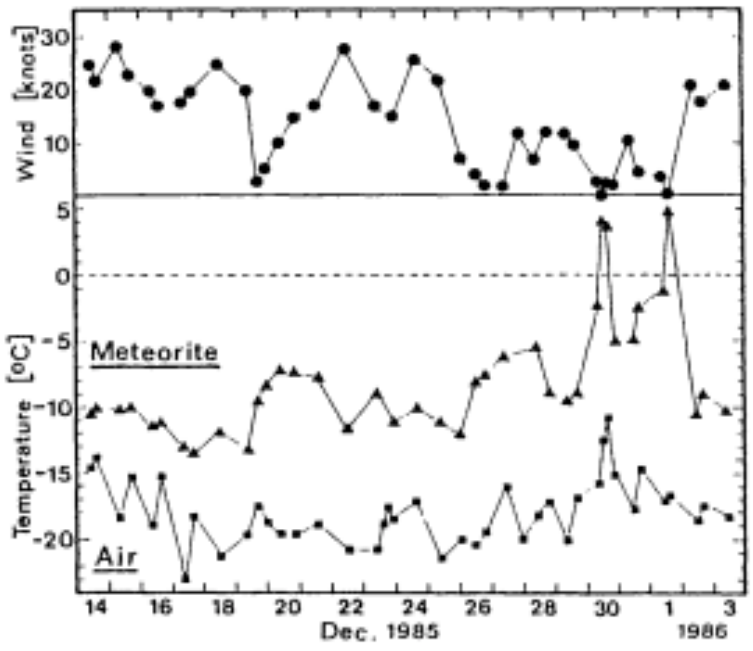

Figure 4.16: Temperature over time for a meteorite specimen in Antarctica (Schultz, 1986).

In summary, the Antarctic Meteorite Paradigm is commonly cited without context as to its relevance and prevalence in meteorite collections (i.e., Clay et al. 2017), as even chondrites under museum storage conditions continue to manifest weathering features (Lee and Bland, 2004). Although it is apparent that surfaces of rusty rocks are contaminated with iodine (Figure 4.18), we stress that not all chondrites measured in such works (Dreibus and Wänke, 1983; Garrison et al., 2000; Heumann et al., 1987; Shinonaga et al., 1994) are similarly contaminated with F, Cl and Br. Furthermore, the sole use of highly metamorphosed samples to establish these paradigms (i.e., type 5 and 6 OCs)(Langenauer and Krähenbühl, 1993a) inadvertently leads to the idea that contamination was ubiquitous and extensive – despite the fact that the primary halogen contents of these materials are inherently exceptionally low as seen in Figure 4.2. Comparatively volatile-rich low

petrologic type samples would require a far more extensive contaminant to overprint their primary chemistries and would likely be evident in excesses in soluble iodine contents.

Using this rationale our highest quality data are derived from low petrologic type samples with large primary inventories of halogens. Although we cannot quantify the extent of contamination for these samples, evidently the contamination has not overprinted the primary feature of decreasing halogen contents with increasing extents of thermal metamorphism. Thus, given the fact that our samples retain primary halogen contents consistent with observed falls (Figures 4.1, 4.2) with isotopic compositions inconsistent with that of seawater (Fig. 4.11, we lean towards the fact that iodine abundances in contaminated samples are exceptionally high (1-10 ppm) which is in stark contrast to the accepted iodine abundances in chondrites (Figure 4.17).

The high iodine contents of contaminated Antarctic meteorites from (Langenauer and Krähenbühl, 1993a) are clearly observed relative to the data presented in this work (Figure 4.18). While nearly all samples plot tightly on top of chondrite falls, the high soluble I/Cl ratio of which I suspect reflects iodine contamination of MAC 88136 is evident in this space (explained in the following section). The similarity in $\delta^{37}Cl$ values in soluble and insoluble fractions provides further evidence for the fact that a majority of measured chloride is not derived from seawater. Although several samples exhibit high water-soluble I, followed by Cl contents, which suggests that despite no obvious criterion for the extent of contamination – an overabundance of these components relative to the petrologic type of the samples are indicative of some degree of contamination. Due to the absence of quantitative contamination criteria, I exclude the water-soluble iodine contents of Antarctic chondrites (except those depicted in Figure 4.17), and water-soluble Cl contents in two enstatite chondrites (TIL

91714, ALH 81021). It is important to note that despite the high soluble iodine contents of the most evidently contaminated sample MAC 88136, is not similarly enriched in F, Cl and Br; indicative of the fact that the iodine enrichments in Antarctic meteorites do not occur similarly alongside other the halogens as the contaminant is likely derived from CH_3I (Dreibus and Wänke, 1983).

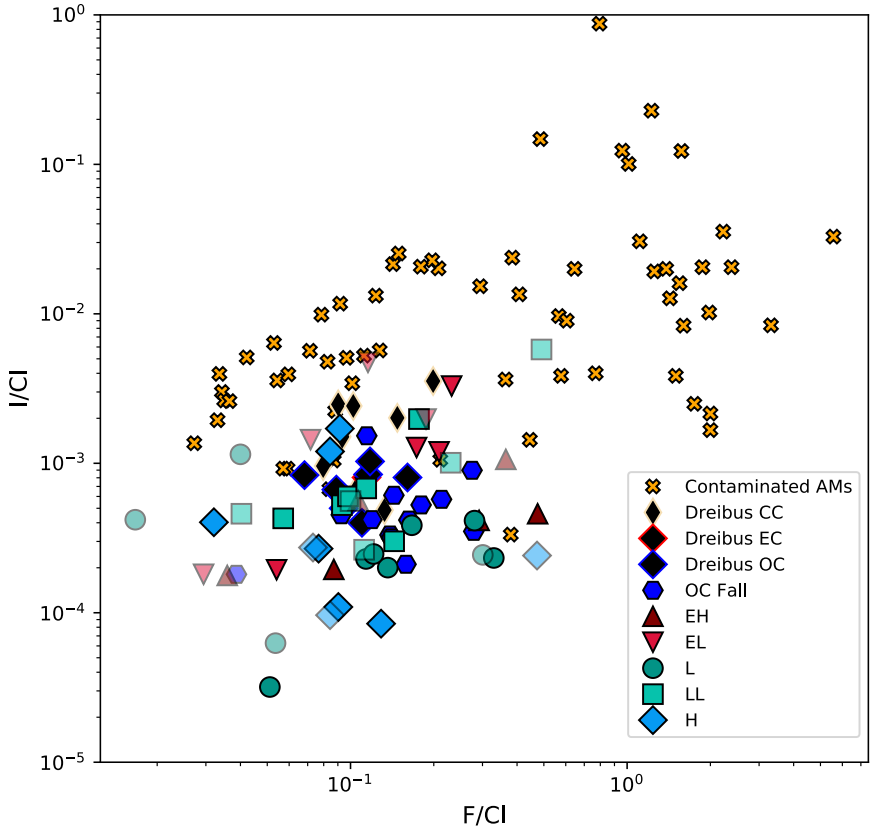

Figure 4.17: F/Cl (ppm) vs. I/Cl (ppm) of chondrites and contaminated Antarctic chondrites from Langenauer and Krahenbuhl (1993). Bold symbols are SBC+WSC ratios, faded symbols are WSC ratios.

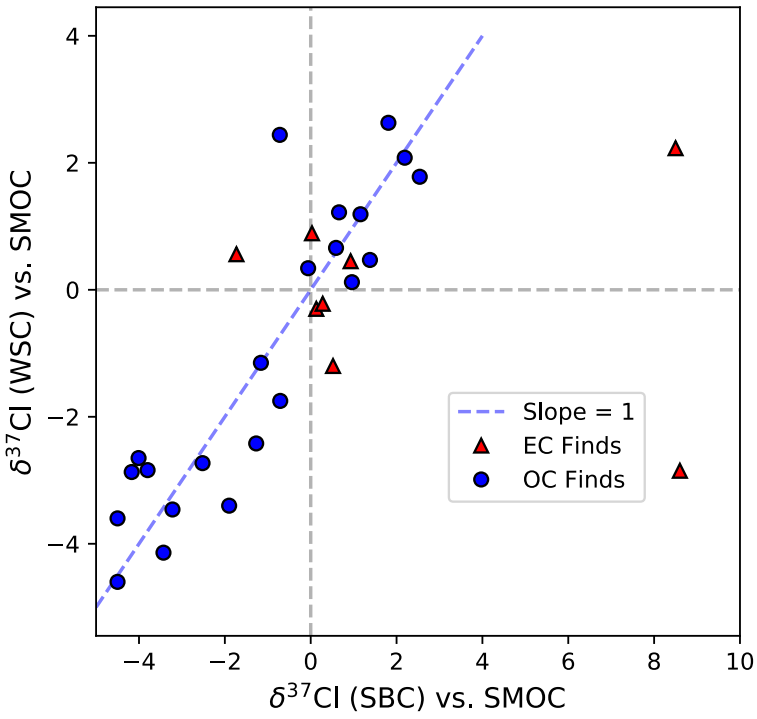

Figure 4.18: δ^{37}Cl (SBC) vs. δ^{37}Cl (WSC) of chondrites.

The halogen contents of NC chondrites

L Chondrites: 7 samples of L chondrites were measured (petrologic type, weathering grade): MET 96503 (3.1, B), PRE 95401 (3.4, A/B), GRO 06054 (3.6, A), ALH 84086 (4.0, A/B), ALH 85033 (4/5, A), BTN 00304 (6, A), and DOM 10005 (6, A/B). Their average total F, Cl, Br and insoluble I contents (ppm, n = 7, average petrologic type = 4.4) are as follows: 23.0 ± 14.3, 226 ± 291, 0.34 ± 0.32, and 0.026 ± 0.029 (0.046 ± 0.050 insoluble + soluble). Their δ^{37}Cl values range from -4.5 to 2.6‰.

LL Chondrites: 6 samples of LL chondrites were measured: DOM 10490 (3.2, B), DOM 10344 (3.4, B), DAV 92302 (3.6, B), LAR 12034 (3.8, A/B), GRO 95552 (4, A), and QUE 97028 (5, A). Their average total F, Cl, Br and I contents (ppm, n = 6, average

petrologic type = 3.8) are as follows 28.0 ± 11.9, 291 ± 212, 0.40 ± 0.45, and 0.092 ± 0.063 (0.193 ± 0.142 insoluble + soluble). Their $\delta^{37}Cl$ values range from -4.6 to 1.4‰.

H Chondrites: 6 samples of H chondrites were measured: WSG 95300 (3.3, A/B), QUE 93030 (3.6, B/C), MET 01182 (3.8, A/B), QUE 99018 (4, A/B), ALH 84069 (5, A), and TIL 82405 (6, B). Their average total F, Cl, Br and I contents (ppm, n = 6, average petrologic type = 4.3) are as follows 19.3 ± 12.4, 222 ± 130, 0.37 ± 0.41, and 0.048 ± 0.052 (0.103 ± 0.112 insoluble + soluble). Their $\delta^{37}Cl$ values range from -4.2 to 2.5‰.

E Chondrites: 3 samples of EH and 4 samples of EL chondrites were measured: DOM 14021 (EH3, A), EET 96135 (EH4/5, B), EET 96299 (EH4/5, B), MAC 88136 (EL3, A), MAC 02747 (EL4, B/C), TIL 91714 (EL5, C), and ALH 81021 (EL6, C). Two EL samples TIL 91714 and ALH 81021 were chosen out of necessity to include the high petrologic type EL chondrites and contained unusually high WSC Cl and I contents, and thus only the insoluble halogens and $\delta^{37}Cl$ values are depicted for these samples.

MAC 88136 contains an exceptionally high soluble I content of 1.3 ppm that suggests a large contaminant component in the soluble fraction for this sample. The insoluble I content, however, is not unusual for a type 3 EC at 0.173 ppm (the average I content of ECs from Dreibus et al. 1986 is 0.315 ppm), which suggest that despite the contaminant being present in the water-soluble fraction, it has not overprinted the presumably largely primary insoluble iodine contents. This rock is known to contain an exotic mineral assemblage including presolar grains, and also contains a variety of demonstrably primary soluble F-Cl phases (El Goresy et al., 2017) such that it is expected to have high halogen contents; however, the Mn-Cr systematics in this rock have also been suggested to have been effected by weathering (Hopp et al., 2021). Thus, whether MAC 88136 is overwhelmingly

contaminated, or rather, retains an exotic halogen geochemistry cannot be unambiguously determined at this time.

As most ECs cluster with $\delta^{37}Cl$ values around 0‰ – this isotope system is not ideal to probe potential halogen contamination, although the retention of high $\delta^{37}Cl$ values up to +8.6‰ similarly depicts that a majority of chloride is not derived from seawater. EET 96135 and EET 96299 (suspected pairings) both contain high $\delta^{37}Cl_{SBC}$ values of 8.5 and 8.6‰, respectively, although with different $\delta^{37}Cl_{WSC}$ values of 2.2 and -2.9‰, respectively. These two samples contain comparable $[Cl]_{SBC}$ of 88 and 110 ppm, albeit with different $[Cl]_{WSC}$ of 27 and 92 ppm, respectively. The lower $[Cl]_{WSC}$ and higher $\delta^{37}Cl_{WSC}$ values are likely related to vaporization effects, whereby the vapor component of EET 96135 was evaporated to a further extent than its pairing EET 96299. This general idea is further supported by the anomalously high $\delta^{41}K$ values around -0.3‰ of EET 96135 (Zhao et al., 2020).

Ordinary chondrite falls: Approximately 12 OC falls including 4 LLs, 6 Hs and 2 Ls with an average petrologic type of 4.8 were measured. Their average total F, Cl, Br and I contents are as follows: 28.0 ± 28.5, 203 ± 87, 0.40 ± 0.33, and 0.064 ± 0.054 (0.126 ± 0.223 insoluble + soluble). Their $\delta^{37}Cl_{SBC}$ values range from -4.0 to 2.1‰. Several of these samples contain impact melt such as Chelyabinsk (Badyukov et al., 2015) with high F and Br contents which are discussed in later sections. These data are largely indistinguishable to the measured Antarctic meteorites (Figure 4.2), although are limited to high petrologic types.

Water soluble halogens and the source of Cl in NC chondrites

Water-soluble components are inherent properties of chondritic meteorites as their isotope values are demonstrably primary for Cl and S isotopes (Defouilloy et al., 2016) and thus, cannot be excluded from their bulk compositions. We find similar proportions of water-

soluble chloride in our Antarctic meteorites (~30-50%) to both observed falls and finds, although water-soluble fluoride contents are most significant to low petrologic type chondrites. This result suggests that water-soluble fluoride phases are only retained in unequilibrated chondrites and are quickly lost/partitioned into insoluble phases as metamorphism progresses. Evidently metamorphism effectively mobilized the labile halogens from chondritic components, locally depositing them within the rock itself. Recrystallization of vapor/fluid-derived components could also serve as a mechanism to mix soluble and insoluble isotopic reservoirs. This idea is consistent with similarities in $\delta^{37}Cl_{WSC}$ and $\delta^{37}Cl_{SBC}$ values (Figure 4.18). Following this rationale further, this idea of prolific mobilization of labile elements leads to the possibility of halogen-enrichments in the lowest petrologic types (i.e., vapor/fluid incorporation from different regions of the parent body).

Regarding the source of halogens, I suspect that a significant halogen component in NC chondrites is *originally* cited within chondrule glass and mesostasis which can contain large Cl contents up to 4.6 wt% (Bridges et al., 1997; Grossman and Brearley, 2005; Piani et al., 2016). In a canonical model of condensation of solids from a gas of solar composition, it is thought that the halogens would either condense primarily as apatite or sodalite (Lodders, 2003; Rubin and Choi, 2009), however, neither of these phases are primary in NC chondrites (Brearley and Jones, 2018). Evidently halogen-bearing phases in chondrites have been processed even in the lowest petrologic type samples (i.e., Semarkona LL3.00)(Grossman and Brearley, 2005), and Qingzhen (EH3)(Goresy et al., 1988; Mercer and Jones, 2010)), and further, halogen-bearing components are necessarily lost as metamorphism progresses resulting in halogen depletions with increasing petrologic type (Figures 4.2, 4.3).

This long-standing inconsistency can be explained if the original Cl-bearing components are not preserved due to their rapid decomposition from minimal extents of metamorphism (i.e., mesostasis alteration such as in the OCs (Grossman and Brearley, 2005), mesostasis evaporation as in the ECs (Mercer and Jones, 2010)). Later thermal processing and aqueous/anhydrous metasomatism of the unstable Cl-bearing glasses and other Cl-bearing phases would manifest by changes in the halogen-bearing mineralogy (i.e., apatite formation in OCs (Jones et al., 2014), and djerfisherite decomposition in ECs (Goresy et al., 1988)).

It is important to note that although type 3 chondrites are considered unequilibrated, they have been significantly heated for millions of years with 3.7-3.8 OCs retaining peak temperatures of around 600 ºC (McCoy et al., 1991). Given the volatility and lability of the halogens, it is feasible that primary halogen-bearing phases have simply not been preserved – consistent with the wide ranging 5-15 Myr I-Xe ages of ECs (Hopp et al., 2016), as well as the I-Xe ages in OCs (Bernatowicz et al., 1988). Furthermore, given the fact that it is evident that primary soluble halogen-bearing components exists within both OCs and ECs, it is necessarily stated that inadequate sample preparation and preservation procedures (i.e., sectioning & polishing with water, storage of sections outside of desiccators, etc.) have undoubtably contributed to the difficulty in observing these phases (Gargano and Sharp, 2019).

The idea that the primary halogen-bearing phases are no longer present is also consistent with the abundance of alteration features present within even in the most primitive type 3.00 OCs (Semarkona LL3.00)(Grossman and Brearley, 2005; Lewis and Jones, 2019); as well as the ubiquitous presence of ‘bleached’ chondrules (leached of alkalis and Al) in

nearly all petrologic type OCs (Grossman et al., 2000). These general metasomatic processes for the OCs are discussed in detail by (Lewis et al., 2022) and are thought to have occurred similarly in all ordinary chondrite parent bodies over a short period of 2-3 Myrs. It generally follows: 1) matrix-bound ices are released during the earliest stages of metamorphism (type 3.0-3.2)(T <260 °C), 2) fluids dissolve Na-Cl-rich mesostasis glass increasing chondrule porosity and efficiency of fluid infiltration, 3) brief introductions of halogen and alkali-rich fluids transport labile elements in the formation of secondary apatite.

In summary, the heterogeneity in mesostasis halogen contents, as well as the chemical and thermal instability of halogen-rich components (Grossman and Brearley, 2005; Libourel, 2021) likely explains the occurrence of water-soluble halogens and significant depletions of the halogens throughout metamorphism which require the loss of halogen-bearing components. This would explain why only the lowest petrologic type OCs with extant primary mesostasis and/or the retention of Cl originally cited within mesostasis retain the low δ^{37}Cl values (~ -5‰); however, the systematically higher δ^{37}Cl values of ECs are likely in part related to their higher ambient metamorphic conditions (Zhang et al., 1995), or evaporation (as opposed to leaching in the case of OCs) of their Cl-rich chondrule glass (Mercer and Jones, 2010).

The chlorine isotope systematics of NC chondrites: evaporation and reservoir effects

Despite ambiguities regarding the low initial δ^{37}Cl values of the NC chondrites, the >7‰ range in δ^{37}Cl values from both the OCs, and ECs necessitates an evaporative mechanism of isotope fractionation. While shock effects are pervasive in many chondrites (Rubin, 2004), this study was not designed to be sensitive to this question, and the isotopic effects of impact vaporization are incompletely understood (Boynton et al., 1976; Epstein

and Taylor, 1970; Housley, 1979; Housley et al., 1974). Impact induced vaporization is thought to result in the formation of vugs and vapor deposited phases in OCs (Benedix et al., 2008; Olsen, 1981). I suspect that impact induced evaporation results in analogous isotopic effects to thermal evaporation (i.e., isotopic fractionation resulting from the mass loss of evaporated material, albeit at different α values (Day et al., 2020a)), and likely in part explains the high $\delta^{37}Cl$ and $\delta^{41}K$ values of EET 96135 and 96299 (a pairing), as well as the high $\delta^{37}Cl$ values measured in Chelyabinsk (LL5) apatite up to +7‰ (Taylor et al., 2014). Further discussion on these processes is covered in the following section.

Assuming analogous behavior between thermal and shock induced evaporation, if evaporation occurred in the most extreme conditions with large effective $\alpha_{Kinetic}$ values, and with relatively light isotopologues such as HCl, large ranges in $\delta^{37}Cl$ values would result from minimal extents of evaporation (Gargano et al., 2021)(Figure 4.4). The largest range of $\delta^{37}Cl$ values (0 to >30‰) measured in lunar materials likely depict such extreme kinetic evaporation (i.e., $F_{Remaining} < 0.1$ & $\alpha_{Kinetic} = \sqrt{M_1/M_2}$)(Gargano et al., 2021). In contrast, the <7‰ range in chondrites reflects a more modest system with either effective α values closer to unity, limited extents of Cl evaporation, and/or in addition to the contribution from reservoir effects (Gargano et al., 2021).

Regarding reservoir effects, it is important to note that bulk-rock measurements represent an integrated average of all Cl-bearing components, with the measured $\delta^{37}Cl$ value reflecting that of the dominant components. Thus, given the inherent heterogeneity of chondrites, as well as the high concentration of the Cl-reservoir in distinct phases (i.e., chondrule mesostasis), reservoir effects are undoubtably important in terms of relating the bulk-rock $\delta^{37}Cl$ values to the evaporative history of the individual components. Following

the rationale that chondrules are significant Cl-bearing components, these reservoir effects can be exemplified by the Na-Cl-rich mesostasis which occurs in both OCs and ECs.

A detailed study of chondrules from Qingzhen (EH3) show evaporative loss of NaCl from chondrule mesostasis with marked Cl-depletions on chondrule rims (Mercer and Jones, 2010; Mercer et al., 2011). These authors find that within a single chondrule, mesostasis Cl contents can range from <1-4wt%, which, if reflective of evaporative extent, would suggest that >70% of the Cl in the mesostasis has been evaporated. If this evaporation were not inhibited by diffusion rate, and occurred under ideal vacuum conditions, it would result in the residual Cl having a higher δ^{37}Cl value of ~16‰ from a presumed initial -5‰. As chondrites are assemblages of multiple generations of chondrules (Brearley and Jones, 1998), despite the presence of these potentially high δ^{37}Cl-bearing chondrules, this component has inherently been depleted in Cl such that the measured bulk-rock isotope values are more representative of the components which retained their Cl.

For example, assuming a simple system comprised of two chondrules with identical initial δ^{37}Cl values and [Cl], and with only a single chondrule experiencing the evaporative event, integrating these two components together would result in a bulk δ^{37}Cl value of -0.2‰, even though a chondrule with a δ^{37}Cl value of 16‰ was measured. This issue is likely even more significant than this simple example shows as deviations from ideality (i.e., well mixed chondrule melt that is batch evaporating) would ultimately result in less extreme variations in δ^{37}Cl values (i.e., a poorly mixed evaporated chondrule rim could potentially be significantly isotopically fractionated by evaporation with minimal effect on the remaining Cl in the chondrule core). As NC chondrites are dominated by chondrules (~70-90% by volume), the reservoir effects of volatile element isotope fractionation from these

components feasibly controls the bulk-rock isotope values of chondrites in at least for the elements that are concentrated in chondrules (Brearley, 1996; Brearley and Jones, 1998). This schematic understanding likely explains the range of $\delta^{41}K$ values in chondrules from -9.5 to 17.8‰ (Koefoed et al., 2020; O'D and Grossman, 2005), that are seemingly related to chondrule size (Koefoed et al., 2020) and may be analogous to the model of oxygen isotope exchange in chondrules (Bridges et al., 1998). Further specifying these processes is difficult as it is suspected that the original source (and thereby the phase depicting the isotopic fractionation mechanism) is no longer preserved.

Outstanding and enigmatic features of halogen geochemistry in chondrites

The OCs and ECs manifest starkly different halogen contents and halogen-bearing mineral assemblages throughout metamorphism. Rubin & Choi 2009 suggest that due to exceptionally reducing conditions of the EC formation region, the halogens could efficiently condense metal-halides (i.e. MgF_2, $FeCl_2$, $FeBr_2$, MgI_2), whereas in more oxidizing environments (i.e., of the OCs) halogens largely remained in the gas phase. A similar understanding is attributed to the occurrence of the atypical lithophile element sulfides in ECs (i.e., CaS, Mn-Na-sulfides, etc.)(Ebel, 2006; El Goresy et al., 2017). Although ECs are evidently F, Cl, and S-rich relative to OCs in terms of bulk-rock volatile contents (roughly enriched by a factor of 2)(Lodders and Fegley, 1998), both ECs and CCs contain similarly Na-Cl-rich chondrule glass and mesostasis with up to 4.6 wt% Cl (Bridges et al., 1997; Goresy et al., 1988; Piani et al., 2016; Rubin and Choi, 2009).

OCs manifest several cryptic metasomatic features which, due to the idea that OCs contained low primary halogen contents have been suggested to reflect the contribution from extraneous components (i.e., as HCl-clathrate suggested by Sharp et al. 2013). These features

are often associated with Fe-alkali-halogen metasomatism (**FAHM**) that is well documented in the CV chondrites (Brearley and Krot, 2013), which, coincidentally, also contain nearly identical halogen contents to the OCs (Figure 4.6). Tieschitz (H3.6) exhibits an extreme manifestation of FAHM by an abundance of "White Matrix" and extremely F-Cl rich altered chondrule mesostasis (enriched by factors of 2-56, and 5-47, respectively), resulting from an influx of a halogen-bearing aqueous fluids that leached, and subsequently deposited halogens within the parent body (Hutchison et al., 1998).

Owing to the widespread redistribution of the high halogen contents of type 3.0 to 3.9 OCs (Fig. 4.2), the source of the metasomatic fluids are readily derived from inside the parent body – sourced from the decomposition of chondrule glass and mesostasis (Jones et al., 2014; Lewis and Jones, 2016; Lewis and Jones, 2019; Lewis et al., 2022). Several measurements on OC chondrule glass and mesostasis depict large ranges in F and Cl contents from <1 to 807, and <1 to 2,700 ppm, respectively (Grossman et al., 2002; Shimizu et al., 2021); although, I suspect that the measurements of Shimizu et al. (2021) are underestimating fluorine contents as the F/Cl ratios range between 0.01 and 0.02, relative to the average of type 3-4 OCs of 0.11 (sum) to 0.13 (insoluble). Conversely, an unidentified F-rich and Cl-poor phase may be present.

Thus, in context to the presence of water in OC matrix, the high F-Cl contents and chemical susceptibility of chondrule glass - the metasomatic features in OCs are explained by the wide-spread mobility of saline fluids on the OC parent body during early metamorphism which is supported by the 1-2 orders of magnitude halogen loss from type 3 to 6 (Fig. 4.2). This idea is consistent with the apatite formation model of Jones et al, whereby phosphide

present in metals is oxidized alongside the mobilization of halogens in the formation of apatite in OCs (Jones et al., 2014; Lewis and Jones, 2016; Lewis et al., 2022).

In contrast to the aqueous metasomatic system of the OCs, ECs were likely anhydrous and instead controlled by S-F-Cl-alkali-bearing metasomatic mediums. ECs contain a myriad of exotic minerals with high halogen contents including fluor-richterite (F-rich amphibole)(Olsen et al., 1973; Rubin, 1983), fluorphlogopite (F-rich mica)(Lin and Kimura, 1998), lawrencite ($FeCl_2$)(Keil, 1968), and djerfisherite (K-Cl-rich sulfide)(Lin and Goresy, 2002). The origin of these minerals is attributed to the local environment of the EC region characterized by high C/O ratios, very low oxygen and high sulfur fugacities, (Ebel, 2011; Grossman et al., 2008; Rubin and Choi, 2009), as well as high F, Cl and N fugacities (El Goresy et al., 2017; Lin et al., 2011). Several authors have attempted to constrain the origin of these phases as nebular condensates (Clay et al., 2014; Ebel, 2011; Ebel, 2006; Lin and El Goresy, 2002), however, the underlying rationale that an abundance of volatile-rich fluids/vapors capable of forming these components as metasomatic phases would not exist (i.e., Clay et al., 2014 in the case for djerfisherite) is inconsistent with several observations.

First, djerfisherite commonly exhibits the 'Qingzhen reaction' whereby djerfisherite decomposes to porous troilite (Goresy et al., 1988) releasing excess Zn, Cl and K. Second, the occurrence of 'mysterite' in the impact melt EH4 Abee (comprised of 90 wt% carbon with 2-4 orders of magnitude of volatile excesses for Sb, Ag, Zn, Hg, and Br (38 ppm) relative to CI chondrites)(Ganapathy and Larimer, 1980; Higuchi et al., 1977) suggests an abundance of potentially metasomatic vapors. Similar features have been observed in the OC Supuhee (H6) with high Br contents at 6.6 ppm (Higuchi et al., 1977). While these authors discuss this enigmatic component as a condensate, it is more easily explained as an

impact/thermally induced evaporative feature, which, as many ECs are suspected to be impact melts (Rubin and Scott, 1997; Weisberg and Kimura, 2012) logically follows that an abundance of vapors would have been present during the thermal metamorphism of ECs.

Similarly, the fact that mysterite is largely comprised of carbon is remarkably similar to the thermal decomposition profile of the EH4 Indarch (Muenow et al., 1992), such that it is also conceivable that this feature could simply represent the vapors derived from the heating of EC material at temperatures > 1,000 ºC which subsequently mobilized a variety of volatile-metals (Pokrovski et al., 2013) in the halogen-rich vapor. Further, given the exotic assemblages of graphite and sinoite with F-Cl-rich lawrencite in ECs (El Goresy et al., 2017), the decomposition of these assemblages are expected to produce a Si-C-N-S-halogen-rich vapor phase. Thermal decomposition of sinoite has been previously attributed to variations in the $\delta^{15}N$ values in ECs (Russell et al., 1995). If these processes occurred very early on the parent bodies with extant short-lived radionuclides (i.e., ^{36}Cl), or conversely, represent fractional distillates, vapor-sourced components could be easily assumed to be condensates due to exotic isotope values (i.e., very low $\delta^{30}Si$ and $\delta^{15}N$ values) despite representing distillation features.

Lastly, several features that cannot be isolated from shock effects also manifest with distinct halogen contents and potentially explain several outstanding ambiguities in our data set. The Br contents of mysterite are exceptionally high and has evidently pervasively permeated throughout Abee with exceptionally high Br contents (2.5-3.5 ppm)(Dreibus et al., 1979) relative to the average of 0.56 ppm in the samples measured in this work. Similarly, Figure 4.2 shows that although the OCs in general depict well-defined depletion trends going up petrologic type, several type 5/6 samples are often enriched in Br >> I ≈ Cl ≈ F. A

similarly pervasive incorporation of vaporized Br explains the stark Br-enrichments in several OCs which also occur alongside enrichments in F, Cl, and I. This idea is likely analogous with the initial observations for the significance of volatile enrichments in several NC chondrites (Laul et al., 1973) that were later attributed to mysterite (Ganapathy and Larimer, 1980; Higuchi et al., 1977).

While I suspect that impact melt also imparts high fluorine contents, as several OCs with known impact melt (Rubin, 2004) contain high F contents relative to their petrologic type (i.e., type 5/6 OCs Leedey [F = 44, Br = 0.79 (ppm)], Kilabo [24, 0.48], and Chelyabinsk [(112,16) (0.005, 0.03)]), it is unclear as to the distinction between the presence of impact melt relative to the incorporation of volatiles derived from impact vaporization. Complicating matters further, while halogen enrichments are seemingly indicative of shock processes, this is not always consistent. In fact, several samples contain high Br contents without high F contents, and the high Br contents occur in both the soluble, and insoluble fractions which suggests some degree of post-depositional recrystallization. Thus, although not all chondrites show evidence for excess halogens that are easily explained by the pervasiveness of thermal/impact sourced vapors – this mechanism clearly contributes to halogen heterogeneity and is most evident in the halogen-poor high petrologic type chondrites which exhibit nearly 100x enrichments in Br contents relative to the presumed 'normal' type 6 OCs (Figure 4.2) and are coincidentally the majority of samples in which the historical literature data have measured.

5. SECULAR CHANGES IN PALEOSALINITY: HALOGEN GEOCHEMISTRY OF MARINE SEDIMENTS & METHOD DEVELOPMENT OF HALOGEN GEOCHEMICAL AND ISOTOPIC TECHNIQUES

Abstract

This work presents advancements in the understanding of halogen geochemistry of marine sediments. Although the initial framework was to simply address paleosalinity utilizing marine cherts and carbonates, the halogen geochemistry of marine sediments implicates diagenesis, oxygenation, and are undoubtably complicated by biochemical mechanisms capable of sourcing large amounts of oxidized halogen species in the ocean retained in marine carbonates.

In terms of marine cherts, we find that their fluid inclusions contain Br/Cl ratios consistent with seawater (Figure 5.5), and Br/I ratios consistent with I-Sr-rich dolomitized fluids (Figure 5.4). Enigmatic relationships with bulk-rock chert $\delta^{18}O$ values and fluid-inclusion bound Cl and Br contents (Figure 5.5) complicates the simple idea that cherts record seawater-derived fluid inclusions (Burgess et al., 2020), and may be in part explained by saline evaporative fluids acting as diagenetic mediums (Moore, 1989). Phanerozoic (n = 49) and Precambrian (n = 32) cherts retain similar halogen contents (F, Cl, Br, and I) of 4.0 ± 8.2, 8.5 ± 10.0, 0.043 ± 0.056, and 0.025 ± 0.054 ppm, and 6.0 ± 9.4, 6.5 ± 7.4, 0.053 ± 0.070, and 0.0044 ± 0.0045 ppm, respectively. While the long-term record of cherts reflects

minimal change in the Br/Cl and I/Cl ratio of the ocean over time, these ratios evidently become more variable in the Phanerozoic (Figure 5.8), likely reflective of organic matter sequestration; however, I caution to overinterpret these relationships given the likely association with diagenesis.

In terms of marine carbonates, we find that carbonates do not exhibit simple halogen partitioning from seawater and are instead largely reflective of the biochemistry of the biomineralizing organism comprising the carbonate sediments. *Corraline* Red Algae (2.1 and 4.0 ppm Br and I) and *Siderastrea* coral (5.0 and 4.3 ppm Br and I) contain exceptionally high Br and I contents which are likely reflective of high abundances of bromoperoxidase enzymes within these biomineralizing organisms (Isupov et al., 2000; Sheffield et al., 1992; Wever et al., 2018) which evidently produce the oxidized species bromate and iodate compatible in the carbonate structure (Midgley et al., 2021). Similar halogenases are widespread in marine organisms (Barnum, 2020) such as phytoplankton (Kuhlisch et al., 2021; Sheyn et al., 2016) such that it is difficult to detangle the presence of biomineralizing organisms (i.e., *Siderastrea* coral) vs. an abundance source of oxidized halogen species potentially resulting from massive phytoplankton die-offs during carbon isotope excursions. Furthermore, although chlorine may be similarly effected by biochemistry (Barnum, 2020), the marked difference in the abiotic partitioning behavior of F and Cl between aragonite and calcite (Kitano and Okumura, 1973; Kitano et al., 1975; Okumura et al., 1983) make this behavior difficult to further specify without detailed mineralogical determinations.

Despite these ambiguities, Triassic dolomites contain markedly different halogen contents with far higher Cl and Br contents up to 230 and 3.1 ppm, respectively, and are effectively ‘washed-out’ of their iodine contents during dolomitization (Figure 5.16)(Wang et

al., 2020). In comparison the Cl, Br, and I contents of well-preserved Mississippian (n = 22, 14.0 ± 7.1, 0.521 ± 0.230, and 1.22 ± 0.63 ppm, respectively) and Tonian (n = 23, 42.1 ± 38.7, 0.252 ± 0.210, 1.66 ± 1.98 ppm, respectively) carbonates reflect the fact that the halogen contents cannot be explained by diagenesis. Consistent with the interpretations of the I/Ca record (Lu et al., 2010; Wörndle et al., 2019), we suggest that similar relationships with I/Cl and Br/Cl ratios reflect an abundance of oxidized halogen species in the environment of carbonate deposition; however, suspect that these relationships are largely caused by an abundance of halogenases-bearing organisms as opposed to simple oxygenation which readily explains the concomitant increases in I/Cl and Br/Cl during carbon isotope excursions despite the fact that the Mississippian suite is also reflective of euxinic conditions (Cheng et al., 2020).

Preface

Motivation

Throughout the development of the methods to measure the halogen contents of planetary materials, I became interested in the historical problem of paleosalinity (Holland, 2003; Knauth, 2005; Rubey, 1951). This long-standing question is difficult to address as the methodology of measuring the full suite of halogen contents was not available when this work started and the marine rocks which retain chemical signatures from ancient seawater are poorly understood in terms of primary vs. secondary (i.e., diagenetic) features. Although the halogens have been traditionally viewed as conversative elements throughout Earth's history (Rubey, 1951) – their seemingly ubiquitous biochemical utility (Barnum, 2020) points towards an unexplored field of halogen biogeochemistry (Channer et al., 1997). Although the initial scope of this work was to broadly test the question of whether the ocean

has experienced a secular decrease in salinity (Knauth, 1998; Knauth, 2005), the findings demonstrate significant, yet ambiguous biochemical and diagenetic effects.

The initial lithologies, cherts, were chosen as they persist throughout much of the geologic record and are thought to be more chemically resistant to diagenesis. Previous work by Sharp et al. (2007) in testing whether the Cl isotope composition of the ocean had changed throughout time had measured a broad array of cherts, finding significant Cl contents, albeit invariant $\delta^{37}Cl$ values (Sharp et al., 2007). Based on this idea, I suspected that cherts also housed the full suite of halogen elements as fluid inclusions that had been observed previously in quartz (Channer et al., 1997; De Ronde et al., 1997; Marty et al., 2018). Similarly, literature sources indicated that halogens may be incorporated as primary constituents in marine carbonates (Carpenter, 1969; Kitano and Okumura, 1973; Kitano et al., 1975; Okumura et al., 1986; Williams and Harriss, 1970), and it was also becoming widely-recognized that the iodine contents of marine carbonates could be qualitative proxies for the presence of oxygenated waters as only the oxidized form of iodine, iodate (IO_3^-) was capable of entering the carbonate structure (Hardisty et al., 2014; Lu et al., 2010).

Upon further investigation into the topic of halogen redox proxies however, it became apparent that kinetic effects had been largely overshadowed and the halogen contents of carbonates may be more representative of biochemical processes (Butler et al., 1981; Chance et al., 2014; Edwards and Truesdale, 1997). In fact, the biochemical utilization of the halogens is nearly ubiquitous (Barnum, 2020) that in some species, such as macroalgae (Küpper et al., 2008) – represent a geochemically significant reservoir of Br and I (Channer et al., 1997; Sharp and Draper, 2013), and also contain the biochemical mechanisms to form a wide array of oxidized halogen species. As shown later in this work, the chemical species

bromate (BrO_3^-) is compatible in the carbonate structure (Midgley et al., 2021) which does not have a feasible abiotic mechanism capable of producing significant quantities of this species in the ocean.

The biochemical utilization of halogens results from a group of enzymes called halogenases (specifically haloperoxidases) which oxidize halides to hypohalous acids (Agarwal et al., 2017). The evolution of halogenases are thought to have increased the flux of halogens to the stratosphere (Barnum, 2020) as cyanobacteria, phytoplankton and seaweeds are all recognized to release hypohalous acids in seawater, which can react with organic matter to produce volatile halocarbons (Wever and van der Horst, 2013). Consequently, it is apparent that several mechanisms can produce oxidized halogen species, however, it is difficult to unambiguously delineate them from one another.

For example, it was found that phytoplankton can release significant quantities of halogenated organic matter metabolites following cell lysis (Kuhlisch et al., 2021; Sheyn et al., 2016) – which if performed on a large enough scale, such as during large carbon isotope excursions, could feasibly result in the abundance of oxidized halogen species such as bromate that could be incorporated into carbonates (Midgley et al., 2021). However, the carbonate skeletons of some marine organisms (i.e., Red Algae) also independently reflect the high abundances of halogenases enzymes (Carter et al., 2002; Isupov et al., 2000) which result in exceptionally high Br and I contents (given the increasing difficulty of oxidizing low atomic mass halogens, halogen-specific peroxidases such as bromoperoxidase are capable of oxidizing both Br and I (Barnum, 2020)).

Thus, halogenases contribute to the production of oxidized halogen species in the ocean and the release of halocarbons to the atmosphere; and as such, these abundant

biochemical mechanisms undoubtably contribute to the halogen geochemistry of the ocean, atmosphere, and marine sediments which are currently being utilized as an abiotic redox proxy (Hardisty et al., 2014; Lu et al., 2010). As follows I broadly present the problem of paleosalinity and investigate the halogen geochemistry of marine cherts and carbonates.

Introduction & Background

The Earth is the only known terrestrial planet with abundant liquid water and extant life. The source of Earth's water, and the development of the appropriate physiochemical conditions which allowed for life to evolve, however, are still long-standing questions. One of these conditions is thought to be the abundances of halogens (F, Cl, Br, I), which are generally hydrophilic and are nearly entirely partitioned into seawater and organics (Gargano and Sharp, 2019; Knauth, 2005; Sharp and Draper, 2013). Halogens are bio-essential elements (Brown et al., 2018; McCall et al., 2014; Venturi et al., 2000), however, the overabundance of these same elements is toxic to lifeforms, and the loss of halogens during planetary accretion may have been limited the salinity of the ocean (Gargano and Sharp, 2019; Sharp and Draper, 2013).

Although abundant liquid water suitable for life exists on the surface of the Earth today, the earliest ocean was likely distinct, sourced from internally derived volatiles which accumulated throughout geologic time (Holland, 2003; Holland, 2005; Rubey, 1951; Schilling et al., 1978). The accumulation of Cl without an effective sink in evaporites potentially resulted in an ocean with 2x modern salinity (Knauth, 2005). Alongside these high salinities are also high estimated paleotemperatures in the Archean from between 55-85 °C (Knauth and Lowe, 2003; Marin-Carbonne et al., 2012). Together, the high temperatures and salinity of the Archean ocean may well have limited O_2 solubility (Knauth, 2005),

resulting in conditions which would be unsuitable for most marine organisms or in the least, dramatically reduce photosynthetic efficiencies thus increasing the duration of Earth's anoxia.

The evolution of Earth's ocean from the Archean is poorly constrained (Knauth, 1998). Evaporites consisting of salts such as NaCl are the ideal lithology to reconstruct paleosalinity and are the only effective sink for Cl, however, the evaporite record is incomplete and poorly preserved from the Precambrian (Knauth, 1998; Knauth, 2005). Whilst the poor preservation of evaporites is easily explained by their inherent solubility, their formational environments (highly evaporative restricted water basins capable of exchanging with the open ocean) were also limited until long-lived continental cratons grew in the late Paleoproterozoic (Hay et al., 2001; Knauth, 2005). Consequently, geochemically relevant (i.e., significant reservoir of Cl removed from the ocean) evaporite formation may have only started by ~2.5 Ga (Knauth, 1998), which can be expected to have increased the volumes of evaporites, which by ~0.7 Ga, are thought to have accumulated significantly enough to result in a decrease in ocean salinity (Hay et al., 2006; Hay et al., 2001)(Figure 5.1).

It is important to note that although some amount of evaporites may have formed in the Precambrian, the relative volumes that could have been preserved is limited by the amount of exposed land surface capable of forming the restricted basins whereby evaporites form which have likely generally increased throughout time (Babel and Schreiber, 2014; Korenaga, 2018). Throughout the Phanerozoic in particular, the percent of continental area covered by water has increased from around 65 to 95% (Hay et al., 2006), likely contributing to the preservation of evaporites and consequently, removal of Cl from the ocean. Evaporite

basins begin to be efficiently preserved in the Phanerozoic where ocean salinity decreased substantially from around 55 to 35 g/L (Figure 4.1)(Hardie, 1996; Hay et al., 2006; Holland, 2005; Lowenstein et al., 2001). Few attempts have been made to reconstruct ocean salinity beyond the Phanerozoic given the scarcity of well-preserved evaporites; however, comparatively chemically resistant rocks, such as cherts and carbonates may retain primary halogen contents of the seawater they were derived from.

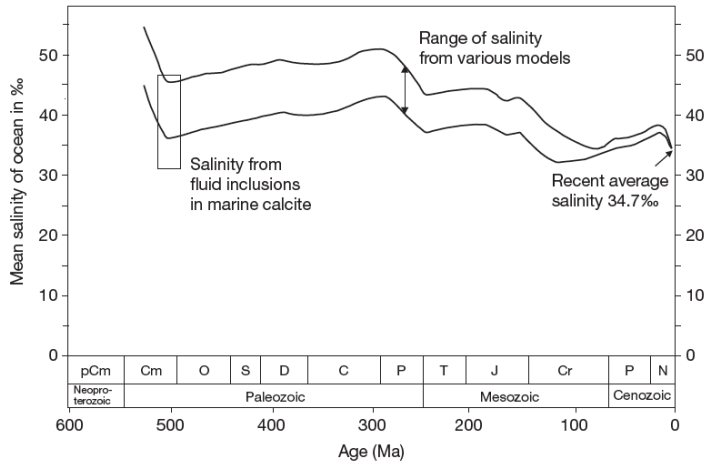

Figure 5.1: Reconstructed seawater salinity in the Phanerozoic (Hay et al. 2006, Babel and Schreiber, 2014).

Background systematics: applications for paleosalinity and oxygenation

Chlorine and bromine are the most appropriate analogues for paleosalinity, and halite sequestration is the most effective means in which Cl can be removed from the ocean (Hay et al., 2006; Hay et al., 2001). Halite crystallization results in an increasingly concentrated bittern brine containing excess Br that is not incorporated into the halite structure until the latest stages of crystallization (Eggenkamp et al., 2019). Assuming a semi-open system, halite crystallization without the incorporation of the Br-rich bittern brine will result in a progressive depletion of Cl > Br, thereby reducing the Cl/Br ratio of seawater. Conversely,

wholesale closed system evaporite formation will result in no changes in the Cl/Br ratio of the ocean.

In terms of the application to oxygenation, the partitioning of iodine into carbonates is strongly dependent on speciation and presumably applies to the other halogens (i.e., Cl and Br)(Feng and Redfern, 2018; Midgley et al., 2021). Coincidentally, the time periods where evaporites could feasibly begin to be substantially preserved (~ 2.5 and 0.7 Ga) also correspond to punctuated oxygenation events which correspond to increased iodine contents of carbonates (Figure 5.2)(Hardisty et al., 2014) resulting from photosynthetic organisms overwhelming the capacity of oxygen sinks (Farquhar et al., 2000). Thus, the halogen contents of marine sediments may be sensitive to both oxygenation, and salinity.

Sample Suites

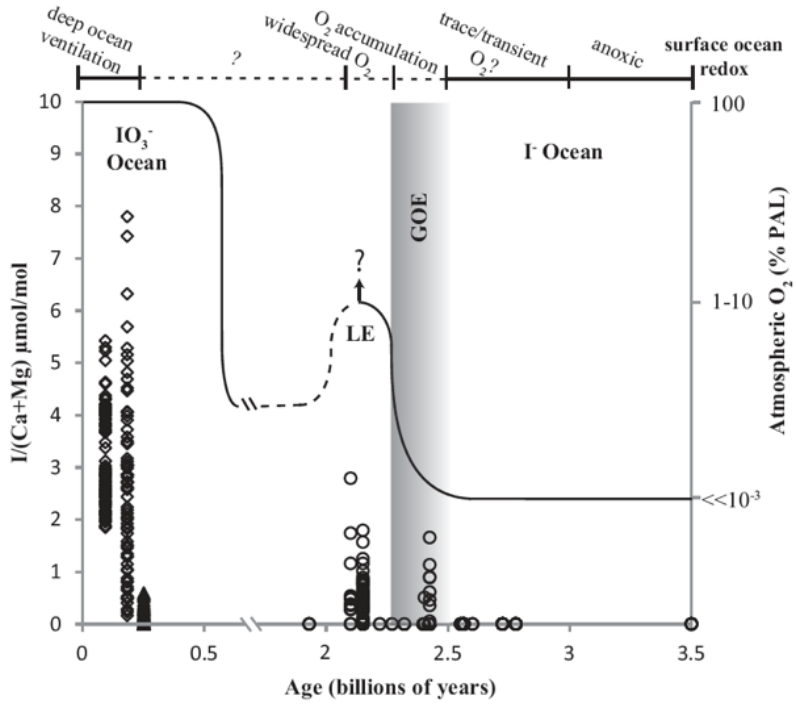

Figure 5.2: Iodine contents of marine carbonates over time (Hardistry et al. 2014).

The largest sample suite utilized in this work include Phanerozoic and Precambrian collections of cherts and carbonates from the career collection of Paul Knauth (Knauth, 1998; Knauth, 2005; Knauth and Epstein, 1976; Knauth and Lowe, 1978; Knauth and Lowe, 2003) currently housed at the University of New Mexico, Center for Stable Isotopes. Additional chert and carbonate samples were gathered from Maya Elrick encompassing the Phanerozoic, as well as a well characterized Mississippian carbonate sequence depicting a shift to euxinic conditions and a large carbon isotope excursion (Cheng et al., 2020). An additional well characterized Tonian carbonate sequence crossing through a large carbon isotope excursion during a period of increased ocean oxygenation was gathered from Galen Haverson (Halverson et al., 2018; Wörndle et al., 2019). A small sample suite of marine carbonates from pre- and post-Messinian Salinity Crisis (Garcia-Castellanos et al., 2009) was requested from Marco Brandano at the University of Rome. The data for these sample suites are shown in Tables 5.1-5.4.

Table 5.1: Leachable chemistries of cherts (Knauth and Epstein, 1976; Knauth and Lowe, 1978).

Sample	Age (Myrs)	ppm_F	ppm_Cl	ppm_Br	ppm_I	ppm_Sr	ppm_Ca	ppm_Na	ppm_Mg	ppm_K	$\delta^{18}O$ vs. SMOW
K233	15	1.2	4.58	0.0244	0.0123	0.19	16.57	42.74	0.8	0.55	20.785
K234	15	7.0	1.23	0.0275	0.2514	0.41	11.2	30.54	2.29	1.83	19.306
K235	15	1.6	1.09	0.0307	0.2664	0.49	15.38	36.21	3.23	1.27	23.981
K235	20		0.33	0.0185	0.0817						23.981
K259	75	1.3	5.88	0.0326	0.0023	0.03	6.3	16.74	9.32	3.94	19.823
K70	80	41.9	8.46	0.0443	0.0228						27.108
K410	100		2.05	0.0256	0.0023						
K15	230	3.1	4.1	0.0153	0.0057	0.19	22.15	36.25	1.25	0.33	27.54
K252	245		4.74	0.0150	0.0030						23.7
K248	250		9.7	0.0709	0.0044						17.304
K28	250		27.05	0.0890	0.0060						29.357
K28	250	1.4	31.3	0.1614	0.0196	0.04	12.86	55.27	14.58	8.08	29.357
K14	270		6.58	0.0610	0.0050						
K209	290		6.07	0.0130	0.0020						38.9
K62	295		5.84	0.0270	0.0380						31.29
K51	304		3.83	0.0310	0.0080						
K60	310		3.97	0.0220	0.0060						
K10	310		6.08	0.0280	0.0090						
K22	310	2.5	3.17	0.0406	0.1292	0.04	7.05	36.53	0.62	0.95	31.717
K41	310	1.2	4.76	0.0395	0.0168	0.21	14.49	36.14	3.4	4.61	31.44
K24	330	3.2	18.16	0.0751	0.0527	0.08	19.69	33.35	41.97	1.65	29.731
K121	330	3.6	15.06	0.0375	0.0057	0.03	9.48	25.79	1.9	6.39	28.789
K138	340		10.78	0.0450	0.0070						31.288
K12	340		3.47	0.0140	0.0050						29.22
K138	340		13.07	0.0460	0.0070						31.288
K171	340	2.2	45.28	0.1514	0.0433	0.07	10.8	64.2	1.43	2.51	32.827
K128	340	2.8	6.76	0.0258	0.0185	0.05	8.82	40.85	0.61	1.76	29.415
K120	340	4.8	7.17	0.0215	0.0137	0.05	8.28	36.02	0.5	4.78	29.199
K8	340	0.6	12.11	0.0549	0.0057	0.03	6.36	10.23	15.12	3.66	28.456
K167	345	1.3	2.89	0.0188	0.0018	0.04	11.41	11.5	2.15	0.9	34.146
C19	348	3.4	9.18	0.0364	0.0376						
K130	350		4.19	0.0190	0.0150						
K169	355	0.4	3.22	0.0152	0.0050	0.07	10.49	32.58	0.38	3.18	30.352
K105	360		2.55	0.0170	0.0020						
K111	370	0.4	0.88	0.0086	0.0018	0.02	6.63	13.22	3.65	0.54	29.141
K243	420		1.12	0.0150	0.0020						26.9
K243	420		1.1	0.0160	0.0020						
K139	420	1.8	10.09	0.0329	0.0215	0.04	8.84	48.41	3.39	6.77	29.712
K76	440		2.55	0.0110	0.0060						29.765
K76	440		4.42	0.0170	0.0050						29.765
K260	460	2.0	3.65	0.0202	0.0170	0.37	12.3	25.82	5.14	11.15	16.497
K81	465		5.72	0.0250	0.0060						26.103
K93	475		3.78	0.0180	0.0020						24.54
K6	480		14.82	0.0590	0.0010						25.136
K85	480	5.0	3.46	0.0154	0.0194	0.04	7.29	29.81	0.25	1.28	26.164
K244	485		3.87	0.0160	0.0010						26.9
K221	500	2.3	44.91	0.3627	0.0015	0.01	5.2	15.33	19.71	2.73	26.411
K3	505		17.98	0.0580	0.0030						25.825
K161	541	0.5	2.51	0.0134	0.0014	0.02	4.22	12.61	1.37	0.46	23.258
K907	742	4.5	3.66	0.0408	0.0038						30
K1011	750	1.1	7.69	0.0370	0.0121						
K1008	750		2.74	0.0171	0.0039						
Bitter Springs	800		28.76	0.2110	0.0050						
Bitter Springs	800		23.97	0.1370	0.0030						
Skillogalee Chert	800		4.03	0.0130	0.0040						
K736	1100	21.7	2.29	0.0254	0.0017						
K734	1100		11.78	0.1719	0.0043						
K31	1200		10.47	0.0914	0.0046						29.037
K34	1225		13.27	0.0640	0.0010						30.662
K32	1250		10.7	0.0650	0.0040						29.5
K191	1300		4.49	0.0320	0.0050						
K188	1300		5.85	0.0420	0.0010						19.1
K188	1300		5.79	0.0300	0.0010						19.1
K522	1800	1	1.54	0.0141	0.0027						21.8
K547	1800	27.5	20.74	0.3153	0.0219						24.6
K579	1800		1.2	0.0115	0.0032						17
K555	1800	2.1	4.46	0.0460	0.0034						23.7
K501	1800		19.91	0.1317	0.0154						23.1
K507	2300	2.1	3.9	0.0319	0.0064						26
SAF-210-42	3000		1.77	0.0183	0.0076						
K384	3000	1.3	2.59	0.0198	0.0021						
SAF-210-43	3000		3.15	0.0251	0.0021						
K595	3250	1.5	0.74	0.0089	0.0015						20
K604	3250		1.16	0.0110	0.0067						21.7
K1091	3250		0.66	0.0084	0.0034						
K611	3250	2.2	1.11	0.0072	0.0013						17.9
K1103	3300		2.59	0.0258	0.0020						19.6
K589	3400		2.51	0.0104	0.0022						19.8
K1057	3460	0.4	1.29	0.0047	0.0020						15.6
Komati River	3500		1.89	0.0070	0.0010						

Komati River	3500		2.01	0.0070	0.0010						
K1078		1.5	0.92	0.0061	0.0075						14
C20		2.5	1.05	0.0119	0.0632						
K709		6.1	5	0.0314	0.0207						
K627			7.86	0.0302	0.0028						15
K945			3.47	0.0260	0.0017						14.57
CR8			3.72	0.0240	0.0103						
K626		12.2	2.12	0.0072	0.0008						16.1
K615			0.8	0.0060	0.0013						19.6
K594			4.05	0.0189	0.0013						20.8
K949			1.61	0.0071	0.0014						14.21
K434			7.84	0.0277	0.0009						
K309			74.59	0.3145	0.0012						

Table 5.2: Halogen contents and O, C and Cl isotope compositions of Mississippian carbonates. Oxygen and carbon isotope data from Cheng et al. (2020).

Sample	Stratigraphic Position	ppm_F	ppm_Cl	ppm_Br	ppm_I	$\delta^{18}O$ vs. SMOW	$\delta^{13}C$ vs. PDB	$\delta^{37}Cl$ vs. SMOC
m3.3	3.3	33.358	18.409	0.248	0.536		0.3	0.3
m13.4	13.4	47.406	10.293	0.218	0.385		1	-0.67
m19	19	56.757	11.221	0.235	0.671	-3.48	1.75	-0.52
m28	28	66.167	19.353	0.325	1.425	-5.12	2.24	0.20
m39.5	39.5	55.307	12.701	0.285	0.642	-5.94	2.24	
m46	46	32.452	20.857	0.44	0.735	-5.13	2.93	
m54	54	63.911	11.291	0.831	1.307	-8.21	2.4	
m62.5	62.5	123.546	26.192	0.472	0.945	-4.84	2.76	
m70	70	87.145	15.116	0.45	1.032	-4.62	3.96	0.42
m75.3	75.3	54.481	13.37	1.09	2.367	-3.29	4.97	
m80	80	49.723	12.891	0.467	1.176	-3.02	6.18	0.6
m83.5	83.5	125.068	9.626	0.513	2.085	-3.35	6.67	0.8
m89	89	184.277	14.425	0.881	2.816	-2.94	7.04	0.7
m99	99	291.774	16.975	0.43	0.637	-3.04	5.78	
m105	105	145.278	11.259	0.665	1.532	-2.6	5.3	1.50
m113.1	113.1	116.957	36	0.578	1.49	-4.26	4.52	1.54
m119.4	119.4		7.436	0.751	1.965	-3.23	5.05	
m122	122	88.579	4.973	0.455	0.936	-3.32	5.39	1.47
m152.5	152.5	206.071	7.336	0.396	0.812	-3.93	6.61	2.1
m166	166	88.634	10.819	0.544	1.398	-3.44	6.8	
m207	207	126.011	6.44	0.406	0.676	-2.73	5.85	
m252	252	72.911	10.168	0.773	1.241		1.97	0.66

Table 5.3: Halogen contents and O, C and Cl isotope compositions of Tonian carbonates. Oxygen and carbon isotope data from Worndle et al. (2019).

Sample	Stratigraphic Position	ppm_F	ppm_Cl	ppm_Br	ppm_I	$\delta^{18}O$ vs. SMOW	$\delta^{13}C$ vs. PDB	$\delta^{37}Cl$ vs. SMOC
G0.7	0.7	58.342	90.432	0.38	0.659	-8.42	-0.47	0.64
G20.8	20.8	169.79	22.882	0.077	0.775	-7.86	-1.28	
G42.4	42.4	285.244	13.148	0.074	0.276	-8.08	-1.34	
G64.2	64.2	77.319	25.565	0.128	0.456	-8.07	-0.61	
G85.3	85.3	41.001	42.379	0.179	0.148	-7.9	-0.13	1.0
G105.7	105.7	25.871	29.911	0.141	0.179	-7.61	-0.33	0.63
G121.3	121.3	23.473	93.248	0.348	0.158	-7.94	-0.08	0.33
G137.5	137.5	57.082	22.926	0.119	0.315	-7.77	-0.23	
G157.6	157.6	23.548	11.442	0.048	0.188	-7.95	0.08	
G183.9	183.9	200.153	17.155	0.105	0.651	-7.05	-2.49	
G217.5	217.5	26.034	29.335	0.125	0.444	-6.43	-2.2	1.6
G226.1	226.1	62.005	38.838	0.242	1.586	-6.11	-1.99	
G243.6	243.6	87.179	35.762	0.239	2.13	-5.98	-2.53	
G258.9	258.9	289.231	19.336	0.146	2.715	-6.2	-1.38	
G268.8	268.8	293.934	58.816	0.431	2.686	-5.45	-1.33	-0.23
G290.6	290.6	148.797	10.352	0.163	2.885	-5.71	-2.38	
G304.8	304.8	548.435	48.607	0.356	8.15	-3.45	-2.34	
G314.9	314.9	313.918	32.087	0.358	5.757	-4.4	-2.05	0.39
G321.9	321.9	250.839	17.405	0.219	3.589	-3.62	-0.42	
G334.6	334.6	81.187	28.062	0.21	1.251	-6.95	2.31	0.6
G340.2	340.2	136.836	176.174	0.954	1.456	-0.83	4.5	-0.51
G341.9	341.9	125.169	11.399	0.127	0.665	-4.81	2.58	

Table 5.4: Halogen contents of modern carbonates,

Sample	Location	ppm_Cl	ppm_Br	ppm_I
Porite Coral	Phoenix Islands	148.679	0.521	2.259
Tridacnda (bivalve)	Phoenis Islands	53.415	0.354	0.37
Coral	Bahamas	292.728	4.962	4.289
Coral	Bahamas	101.741	0.685	2.147
Corraline Red Algae	Bahamas	18.929	2.071	4.044

Sample Preparation

The sample preparation techniques developed throughout this work were developed to maximize the number of samples that were capable of being processed given the breadth of the study question. Given the large number of samples necessary to encompass significant portions of geologic time – it was infeasible to process large amounts of cherts and carbonates by the same techniques used for planetary materials. Given the presumed occurrence of fluid inclusions in cherts, it was suspected that leaching of chert powders was a viable extraction technique. This method was successful in obtaining adequate halogen concentrations to measure the full suite of halogen elements. The procedures for cherts are as follows:

1) Homogenous >20g chips of chert are selected that are free of obvious cracks/veins and are coarsely crushed to 0.5 – 1 mm grain size and loaded into 50 mL centrifuge tubes.
2) Coarsely crushed cherts are then repeatedly washed in DI water 10x and dried in aluminum weigh boats.
3) Approximately 10 grams of coarsely crushed chert is then finely powdered and loaded into a 50 mL centrifuge tube and 20 mL of DI water is added.
4) Fine chert powders are leached for 24 hours, and the leachate solution is centrifuged.

Experiments were also performed in attempting to extract halogens from carbonates via acid digestion. Although this technique was found to be effective, and is used in the

analyses of the iodine contents of carbonates (Lu et al., 2010) – the required masses of carbonates for Cl and Br determinations results in a highly concentrated carbonate solution that is unsuitable for ICPMS as it clogs the inlet (see following section about method development for more information). As such, pyrohydrolysis was utilized for carbonates. The procedures for carbonates were as follows:

1) Homogenous >10g chips of carbonate are selected that are free of obvious cracks/veins as finely crushed.
2) Carbonate powders are loaded into 50 mL centrifuge tubes and approximately 10-30 mL of 15-30% H_2O_2 solution was added daily to remove organics. Some carbonates were particularly reactive, such that lower concentrations of H_2O_2 were necessarily utilized in initial cleaning stages. Carbonate powders are cleaned in this manner for 4 weeks at approximately 60 ºC.
3) After the removal of organics, carbonate powders are then rinsed in DI water 5x to remove excess peroxide and any residual fluid inclusion/contaminant bound halogens and subsequently dried in aluminum weigh boats.
4) Approximately 0.5 to 2 grams of cleaned carbonate powders were weighed and packed inside of quartz tubes and melted via pyrohydrolysis.

Halogen Contents of Marine Sediments: Cherts

The application of halogen geochemistry to marine sediments remains poorly understood (Burgess et al., 2020; Goldsmith, 2007). As most marine sediments are recrystallized at some point during lithification (Paul Knauth, 1992), our measurements cannot be assumed to represent unaltered seawater chemistries, and instead, are undoubtably affected by secondary processes effecting pore waters (Worden, 1996). Despite this

complexity, we assume that even if their chemistries are more so related to pore waters, then the chemistries of such pore waters are nevertheless related to the initial seawater the marine cherts are derived from.

Chert is microcrystalline quartz that is extant across much of the geologic record (Knauth, 1998; Knauth, 2005; Knauth and Epstein, 1976; Knauth and Lowe, 1978; Knauth and Lowe, 2003). These rocks record significant changes in the physiochemical conditions of the ocean, with a presumed secular decrease in ocean temperatures recorded in oxygen isotope compositions (Knauth and Epstein, 1976; Knauth and Lowe, 1978; Knauth and Lowe, 2003), as well as biochemical changes in the silica cycle whereby across the Archean and Proterozoic – silica deposition was controlled largely by abiotic reactions, whereas Phanerozoic cherts record the biochemical precipitation of SiO_2 (i.e., diatoms, radiolarian, etc)(Maliva et al., 2005). Thus, despite the formational environments of cherts being widely-varied, their petrogenesis is associated with silica precipitation and recrystallization (Knauth, 1994; Paul Knauth, 1992). Whilst these distinctions are not directly tested in this work, it is important to note that Precambrian and Phanerozoic cherts are not directly analogous to each other and add an additional layer of complexity in interpreting the long-term record.

Several studies have used the halogen contents of fluid inclusions within microcrystalline cherts to describe the physiochemical conditions of Earth's ancient ocean (Burgess et al., 2020; De Ronde et al., 1997; Goldsmith, 2007; Marty et al., 2018). Precambrian quartz hosted fluid inclusions have been measured to indicate seawater [Cl] of 10-100x of modern values interpreted as representing a more saline Archean ocean (De Ronde et al., 1997; Weiershäuser and Spooner, 2005). Other works show disparate results, with largely invariant halogen ratios throughout time (Burgess et al., 2020; Marty et al.,

2018). These ambiguous trends likely result from the complex diagenetic petrogenesis of pore fluids and the decomposition of I >> Br-rich organics (Goldsmith, 2007) that are difficult to reconcile solely in terms of halogen measurements. In response to the difficulties of these previous works, in addition to the chosen leaching method – the Phanerozoic chert measurements presented as follows were also measured for their leachable salt contents (i.e., Na, Ca, etc.).

The leachable chemistries alongside the halogen contents are plotted in Figures 5.3 and 5.4. Several overarching trends can be observed in this dataset with Cl and Br most coherently corresponding with K, Na, Mg, and Sr contents. The leachable fluorine and iodine contents of cherts are more difficult to interpret, likely resulting from a complex confluence of carbonate dissolution and reprecipitation, as well as organic decomposition within pore fluids (Rude and Aller, 1991; Windom, 1971). These relationships are unsurprising, as the occurrence of salts in sedimentary formation waters is expected (Worden, 1996) – explaining the relationships with K and Na contents, however, the relationship with Mg and Sr contents are likely associated with carbonate dissolution (Windom, 1971).

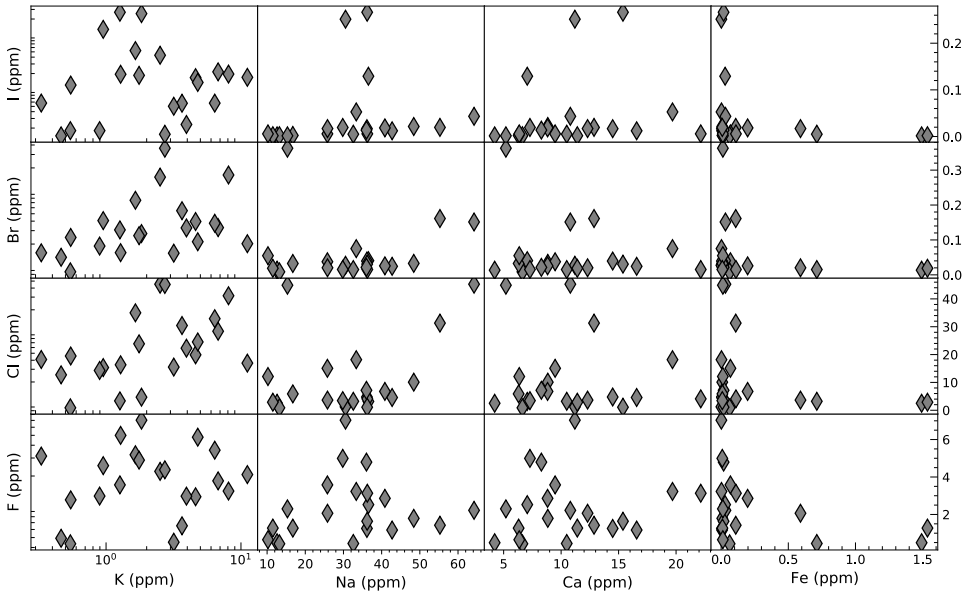

Figure 5.3: Leachable chemistry (K, Na, Ca, and Fe vs. halogens) of Phanerozoic cherts.

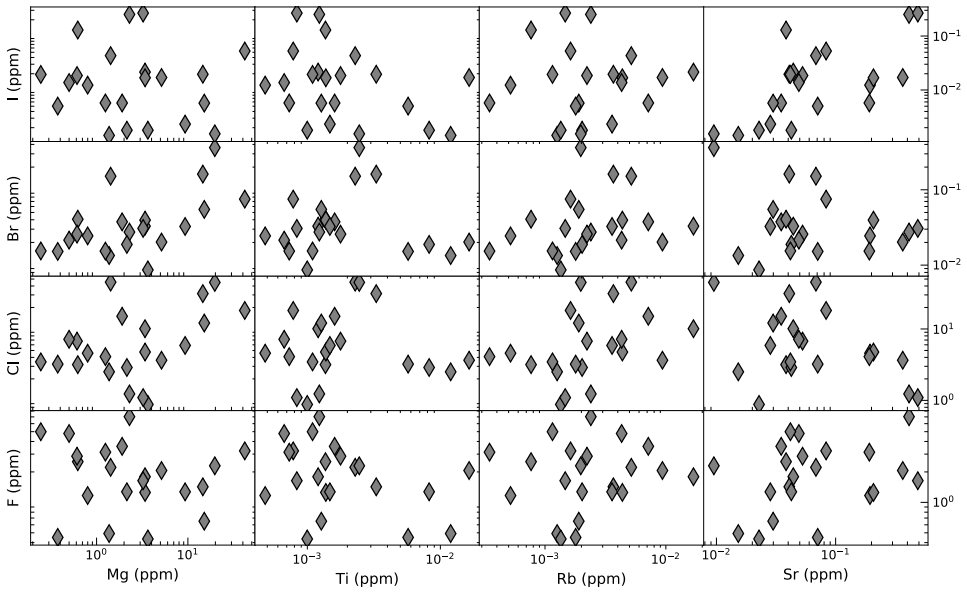

Figure 5.4: Leachable chemistry (Mg, Ti, Rb, and Sr vs. halogens) of Phanerozoic cherts.

When the halogen contents of cherts are compared to their oxygen isotope compositions, a relationship with $\delta^{18}O$ values and Cl and Br contents is apparent (Figure 5.5). This relationship could be explained by the occurrence of evaporites or evaporated seawater providing high $\delta^{18}O$ value and high Cl and Br contents in the pore/formation waters in which the cherts obtained their fluid inclusions. This idea is consistent with the Cl/Br ratios of cherts, that fall parallel to the seawater line (Figure 5.6). Conversely, these trends could also be explained by mixtures of Cl-Br poor and low $\delta^{18}O$ meteoric waters, and Cl-Br rich and high $\delta^{18}O$ waters. It is important to note that the oxygen isotope compositions for these samples do not reflect the fluid inclusions, but rather the bulk-rock, although the relationship with bulk-rock $\delta^{18}O$ and fluid-inclusion Cl-Br content is suspect in terms of the diagenetic history of chert.

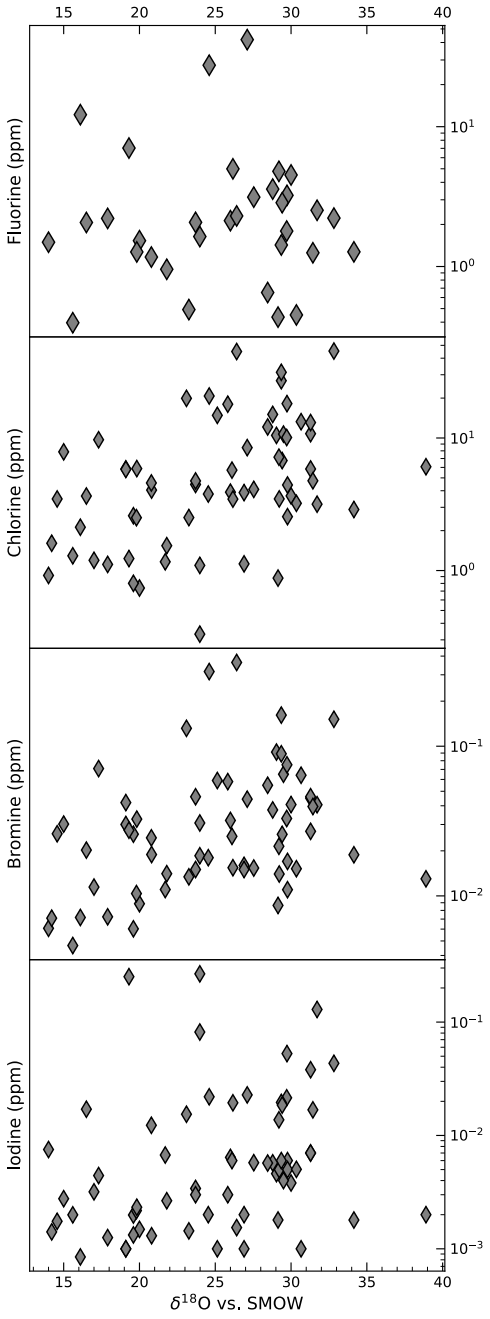

Figure 5.5: $\delta^{18}O$ vs. SMOW vs. halogen contents of Phanerozoic cherts (Knauth and Epstein, 1976).

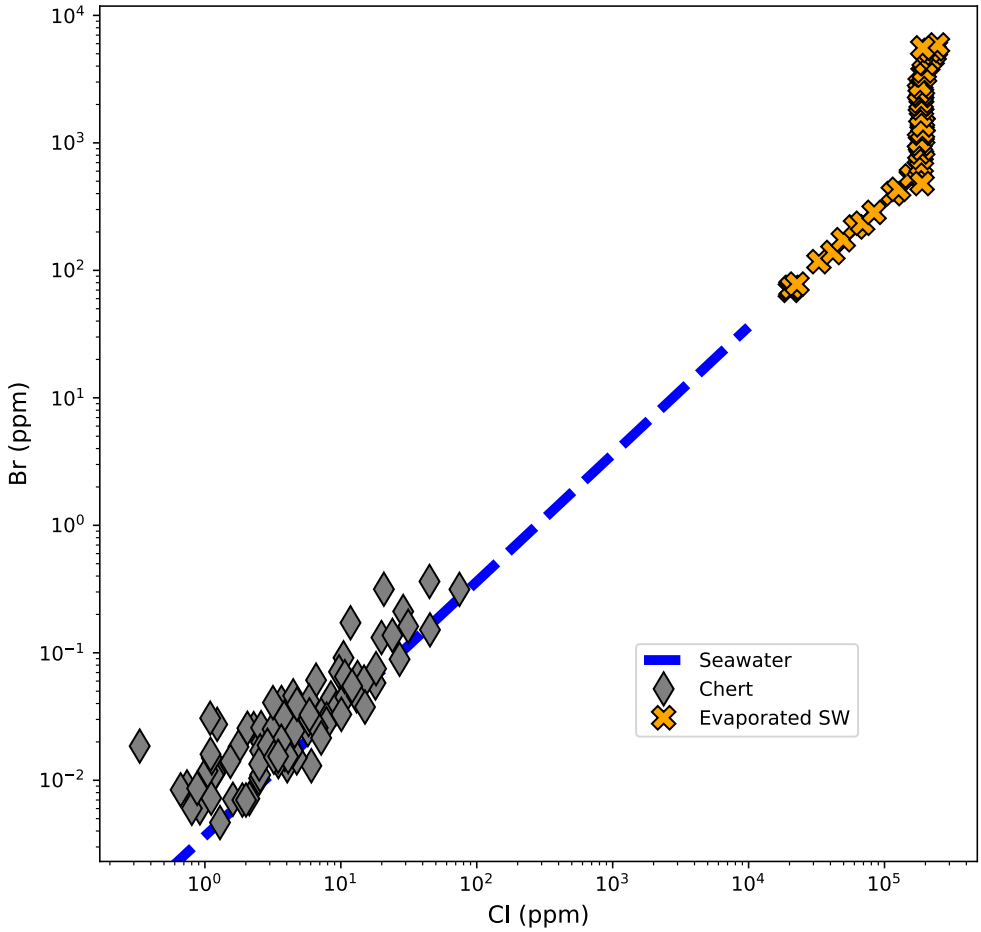

Figure 5.6: Cl vs. Br contents of marine cherts, and evaporated seawater (McCaffrey et al., 1987).

As the marine cherts analyzed in this data set were chosen simply for temporal range - our data is not sensitive to the wide array of questions regarding the effects of diagenesis and different formational environments of cherts. In fact, the Br/Cl ratios of cherts are largely invariant to the wide range of environments and time periods they represent, and instead; seemingly retain the Br/Cl ratios of pore waters during lithification that remained largely unchanged. These results are consistent with the idea that fluid inclusions within cherts record the halogen ratio of seawater they are derived from (Burgess et al., 2020; Goldsmith, 2007). Although the iodine contents of cherts are likely complicated by the occurrence of organics, and/or I-rich carbonate dissolution these data can also be utilized to explore if long-term changes are present.

Figures 5.7 and 5.8 show the halogen contents and ratios of cherts throughout time. These data are in agreement with other works which suggest that the halogen ratios of chert/quartz hosted fluid inclusions has remained similar throughout time (Burgess et al., 2020; Goldsmith, 2007). Despite seemingly invariant halogen ratios – the halogen contents of cherts conflict with the general idea that ocean salinity has decreased throughout time (i.e., Knauth, 2005). Instead, these data would suggest that the idea of a 10-100x more saline Archean ocean reflects separate processes (De Ronde et al., 1997; Weiershäuser and Spooner, 2005) as the oldest cherts measured contain lower Cl and Br contents than cherts throughout the Phanerozoic. Given the relationship with the Cl-Br contents and $\delta^{18}O$ values of Phanerozoic cherts, this could be interpreted to reflect a less-saline diagenetic fluid for Precambrian cherts, although insufficient data and inadequate stratigraphic context for the measured samples makes this idea difficult to further interrogate.

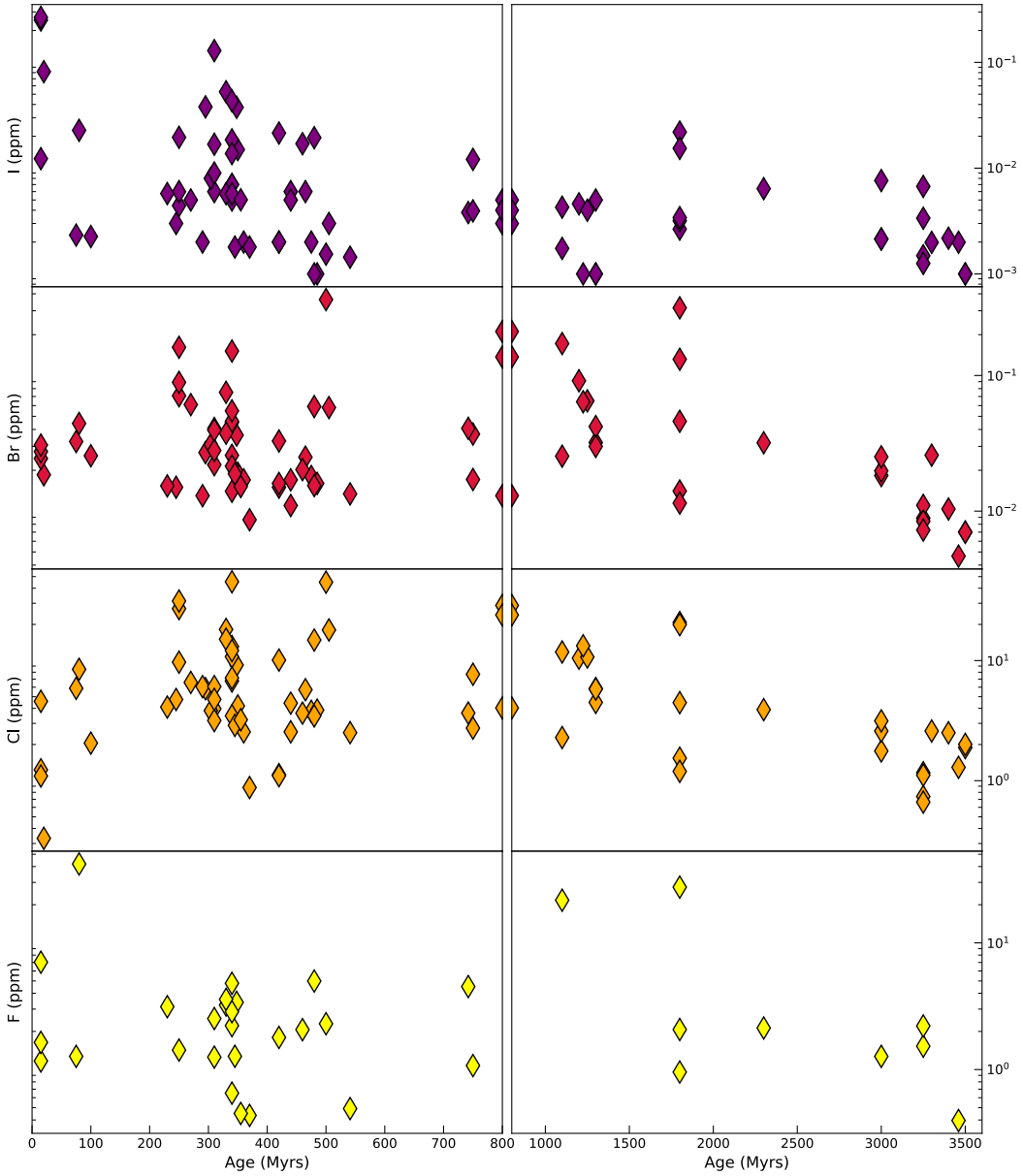

Figure 5.7: Age vs. halogen contents of cherts (Knauth and Epstein, 1976).

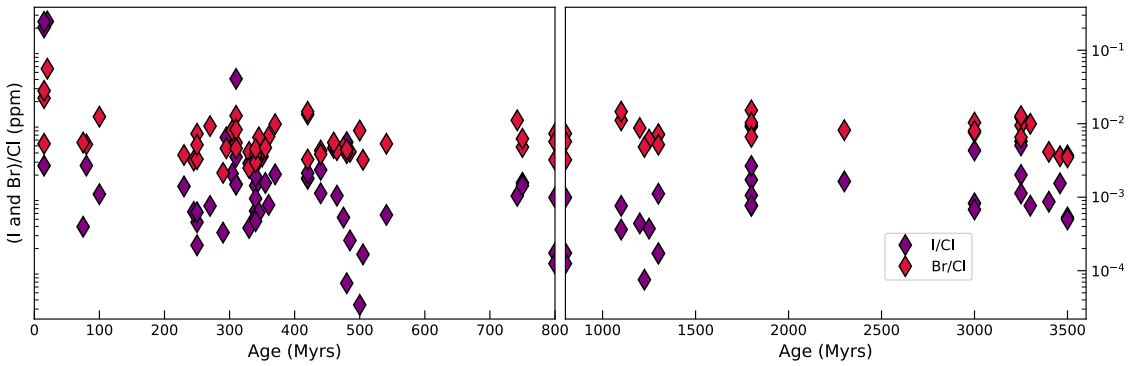

Figure 5.8: I/Cl (purple) and Br/Cl (red) of cherts throughout time. Ages from (Knauth and Epstein, 1976).

In summary, although these data depict more complex processes than envisioned during the initial study design – the invariant halogen ratios suggest that the ratios of these elements in the ocean have not significantly changed throughout time. This idea is consistent with the fact that evaporites are easily eroded and changes in the Cl/Br ratio of the ocean would only occur if evaporites failed to incorporate the Br-rich late-stage brine (McCaffrey et al., 1987). In contrast, if evaporite sequestration largely occurred in a closed system – the Br/Cl ratio of the ocean would remain unchanged. Thus, the framework of utilizing Br/Cl ratios as a proxy for Cl >> Br sequestration may be fundamentally flawed if a majority of evaporite sequestration occurred in a closed system and further complicated by the sequestration of organic Br (Channer et al., 1997; Leri et al., 2014).

Halogen Contents of Marine Sediments: Carbonates

Although marine cherts are far more well preserved in the rock record (Marin-Carbonne et al., 2012; Paul Knauth, 1992), marine carbonates provide an additional means of testing the idea of secular changes in paleosalinity. In the initial stages of this work, it was found that halide-carbonate partitioning experiments had previously been performed by a variety of workers and was generally larger in aragonite than calcite (Kitano and Okumura,

1973; Kitano et al., 1975; Okumura et al., 1983; Okumura et al., 1986). If this partitioning behavior adequately described the incorporation of the halogens into marine carbonates, then well-preserved carbonates could be expected to contain halogens in quantifiable proportions from the water they are derived from. This idealistic idea, however, fails to match the apparent partitioning behavior of the halogens in carbonates. The wide-array of marine carbonates measured in this work are plotted relative to the experimentally determined partition coefficients in Figure 5.9 – which shows that these partitioning data do not adequately describe the halogen contents of carbonates. Instead, I suspect that biochemistry/redox conditions strongly contribute to variations in halogen contents of carbonates.

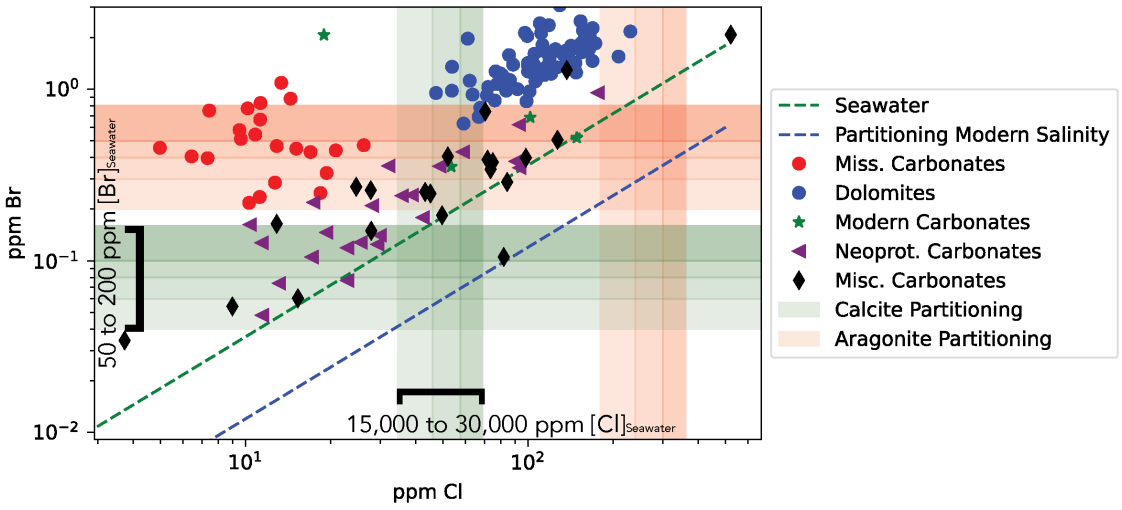

Figure 5.9: Cl vs. Br (ppm) contents of ancient marine carbonates. Partition data for Cl from (Kitano et al., 1975) and Br (Cheng et al., 2020; Okumura et al., 1986). Faded green and red bars are the calcite and aragonite partition fields, respectively, showing the theoretical Cl and Br content of carbonates formed from waters containing 15,000 to 30,000 ppm [Cl], and 50 to 200 ppm [Br], respectively. Dolomite data from Wang et al. (2020).

This complexity is consistent with the understanding of iodine partitioning – which has been shown to only enter the carbonate structure as iodate, as opposed to iodide (Lu et al., 2010). As such, the iodine contents of marine carbonates are currently utilized as a proxy for ocean oxygenation (Feng and Redfern, 2018; Hardisty et al., 2014; Liss et al., 1973; Podder et al., 2017; Wörndle et al., 2019). A similar mechanism may explain the stark Br enrichments of several modern and ancient marine carbonates and is further consistent with clear trends in Br/Cl and I/Cl values (Figure 5.13). The modern carbonate data indicate a biochemical effect whereby the skeletons of *Corraline* Red Algae and *Siderastrea* Coral retain very high Br contents (Table 5.4). This idea is consistent in the identification of the Br-specific haloperoxidase enzyme in such organisms (Carter et al., 2002; Isupov et al., 2000), which evidently locally produces bromate that can be incorporated into the carbonate structure (Midgley et al., 2021). Thus, the confluence of salinity, redox, and biochemical proxies emerge in the development of halogen geochemistry in marine carbonates.

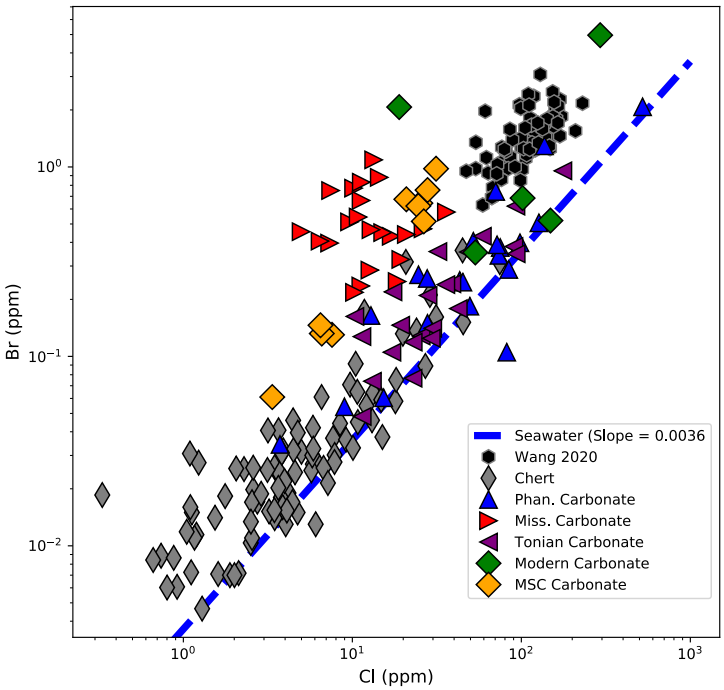

Figure 5.10: Cl vs. Br contents of marine sediments.

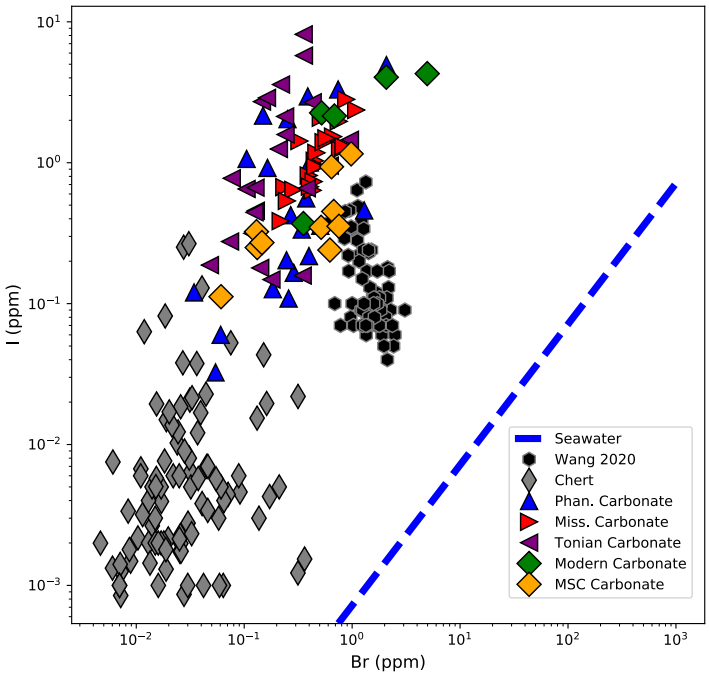

Figure 5.11: Br vs. I contents of marine sediments.

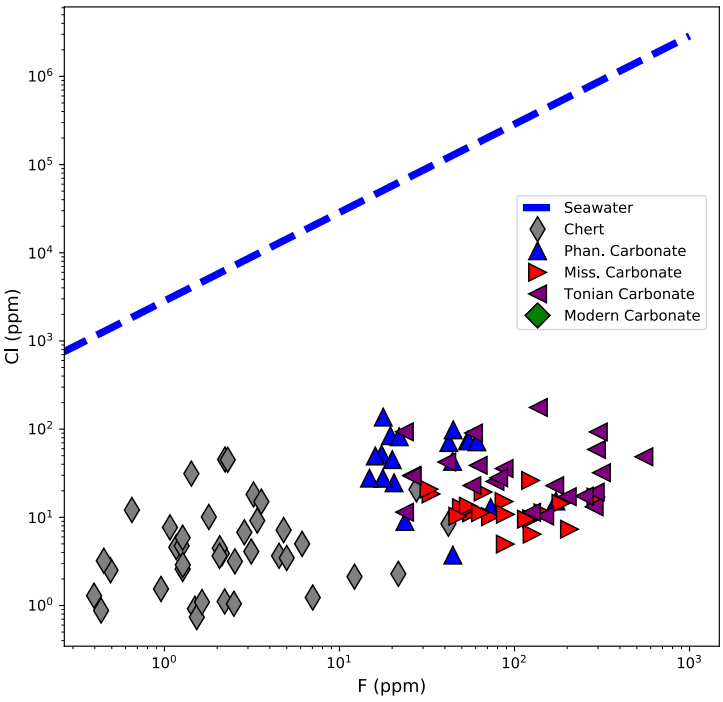

Figure 5.12: F vs. Cl contents of marine carbonates.

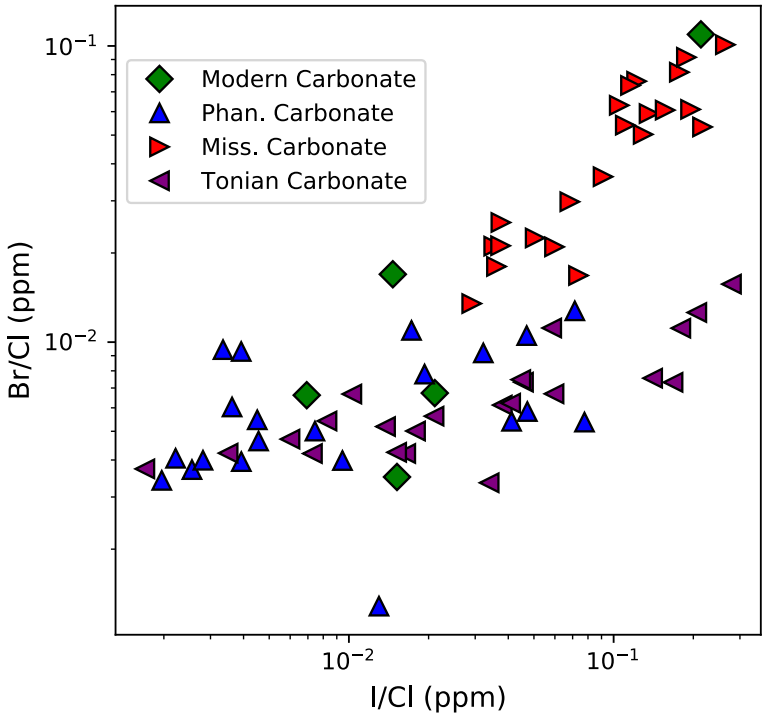

Figure 5.13: I/Cl vs. Br/Cl of marine carbonates.

Despite the cumulative contributions from variations in salinity, redox conditions, and most significantly – biochemistry, I begin by presenting the halogen contents of marine carbonates in context with the previously discussed cherts (Figures 5.10 to 5.13). Marine carbonates from a variety of localities and time periods reflect stark enrichments in F, Br, and I relative to the seawater slope line. In terms of F, this element is recognized to be preferentially incorporated into the carbonate structure of aragonite >> calcite (Carpenter, 1969; Kitano and Okumura, 1973; Rude and Aller, 1991), such that ranges in fluorine contents likely reflects differences in mineralogy. In contrast, Br and I contents are independent from F, such that Br and I enrichments are likely minimally effected by mineralogical variations and are more likely to reflect redox/biochemical conditions.

Figure 5.14 shows the Cl and Br contents of all carbonate suites measured and their regression lines. Figure 5.15 shows the Br/Cl and I/Cl ratios of all sediments and their respective regression lines. Several overarching trends are apparent:

1) The Br/Cl slope of marine carbonates typically parallels seawater. Phanerozoic and Tonian carbonates fall along the seawater slope, whereas the Messinian and Triassic (Wang et al., 2018) carbonates are enriched in Br relative to seawater. Mississippian carbonates retain markedly high Br/Cl ratios most akin to *Corraline* Red Algae (Figure 5.13).
2) Dolomites are markedly Cl and Br-rich ranging between 50 - 230, and 0.63 – 3.1 ppm, respectively (Wang et al., 2020), whereas the average Cl and Br contents of Mississippian and Tonian carbonates are 14.0 ± 7.06, 0.52 ± 0.23, and 42.1 ± 38.72, 0.25 ± 0.21 ppm, respectively.

3) Br/Cl and I/Cl values are directly related in several carbonate suites – with Tonian and Mississippian carbonates retaining the most robust regressions, whereas Triassic dolomites retain no significant relationships reflective of an effective diagenetic overprint with saline fluids (Figure 5.15).

4) Marine cherts fall at the base of trends present in Figure 5.15, indicating a potential overarching relationship with diagenetic fluids between cherts and carbonates.

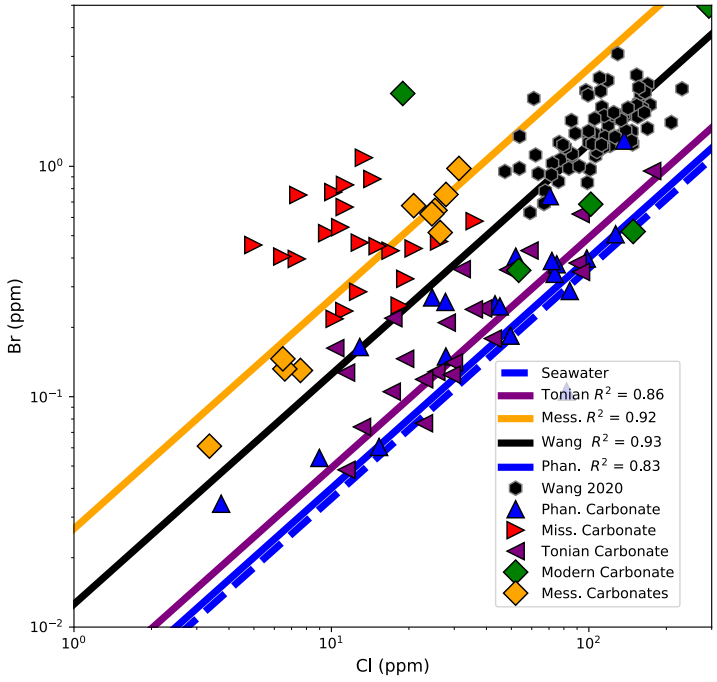

Figure 5.14: Cl and Br contents of marine carbonates.

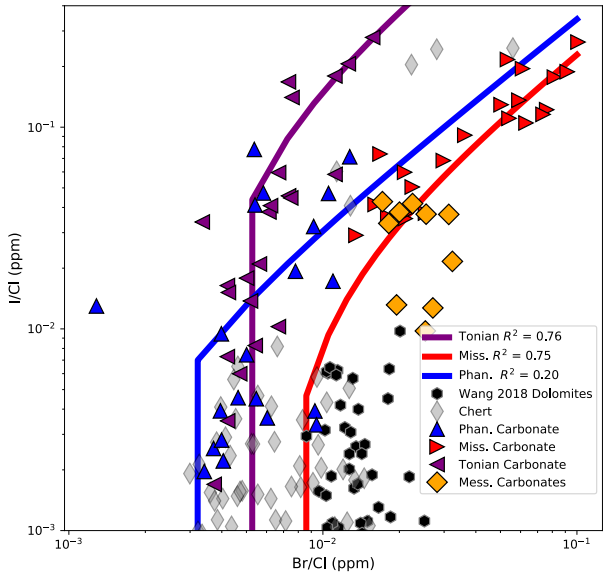

Figure 5.15: Br/Cl and I/Cl of cherts and carbonates.

Although this study was not designed to test the question of diagenesis on the halogen contents of marine carbonates, Wang et al., (2018) measured increasingly dolomitized carbonates for their Cl, Br and I contents which are halogen-rich relative to the presented carbonate measurements. These data can be used to interrogate the effects of dolomitization and diagenesis on halogen contents and several diagenetic indicators such as Sr and Mn. Figure 5.16 shows the effects of increasing dolomitization on halogen contents resulting in marked increases in Br and Mn contents, moderate increases in Cl contents – and rapid loss of iodine and Sr. It is important to note that Br/Cl ratios of such carbonates are independent of dolomitization extent, such that diagenesis resulted in constant Br/Cl ratios. Evidently the diagenetic fluid that altered the carbonate suite from Wang et al. (2020) was saline and would have become I-Sr-rich after dolomitization. A similar fluid source may explain the relationship between I and Sr contents of marine cherts (Figure 5.4), and is consistent with the idea that dolomitization has strong controls on seawater and pore water chemistry (Holland, 2003; Holland, 2005).

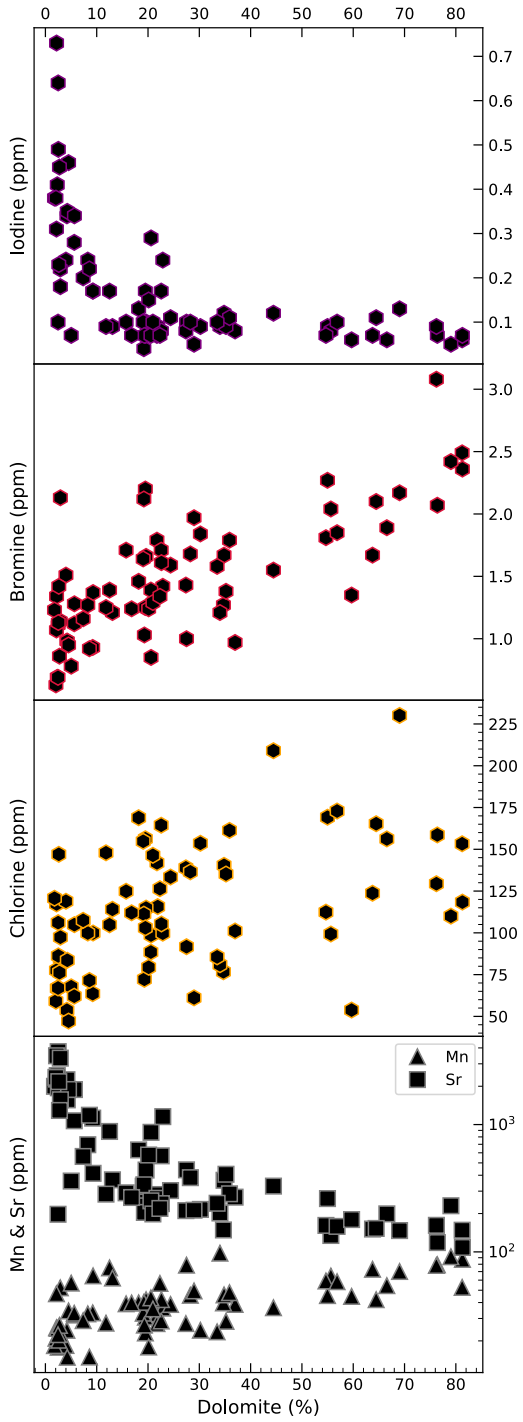

Figure 5.16: Dolomite content of Triassic carbonates relative to Mn, Cl, Br, and I contents (Wang et al., 2020).

The effects or extent thereof of diagenesis on the halogen contents of the Tonian and Mississippian suites is difficult to further specify. Figure 5.17 depicts the halogen contents of all carbonate suites relative to Sr and Mn contents. Although mineralogical and trace element partitioning variability likely further complicates relating these samples suites solely by their Mn-Sr contents. Figure 5.18 normalizes the halogen, Mn, and Fe contents relative to Ca contents as diagenesis results in a net Ca-loss and metal partitioning into carbonates are likely to reflect changes in trace element partitioning behaviors (Sánchez-Román et al., 2014; Temmam et al., 2000). Figure 5.19 normalizes the same elements relative to Cl as I suspect that Cl is similarly strongly controlled by mineralogical variations akin to fluorine (Carpenter, 1969). Several overarching trends are present:

1) Figure 5.17 shows that the Tonian and Mississippian carbonate suites retain high I content reflective of minimal extents of dolomitization. Enigmatically, the Tonian carbonate suite reflects inverse relationships with Sr and Br contents which suggests a mineralogical variation controlling Sr contents coincident with environmental changes attributed to increased Br partitioning into carbonates.
2) Figure 5.18 depicts that Br/Ca and I/Ca ratios are correlated with (Mn, Fe)/Ca ratios – potentially resulting from microbially induced Fe-rich carbonate precipitation (Sánchez-Román et al., 2014) and/or physiochemical conditions which increase the partitioning of metals into carbonates such as decreasing [Cl] (Temmam et al., 2000).
3) Figure 5.19 shows that Br/Cl and I/Cl ratios are the most well-defined halogen ratios and show comparatively stronger relationships to (Mn, Fe)/Cl (Figure 5.19)

than (Mn, Fe)/Ca (Figure 5.18). This suggests that the incorporation mechanisms for Br and I are similar and poorly related to mineralogical variability – consistent with the empirical (Lu et al., 2010) and theoretical (Midgley et al., 2021) partitioning behaviors of these elements. Further, the well-defined (Mn, Fe)/Cl vs. Br/Cl relationships suggest that Cl is an effective normalization factor in terms of relating the halogen contents of carbonates relative to other systems that are strongly affected by changes in carbonate mineralogy.

4) The (Fe, Mn)/Ca vs. Br/Cl relationship may be associated with the high Fe and Zn contents associated with organic bromine (Leri et al., 2010).

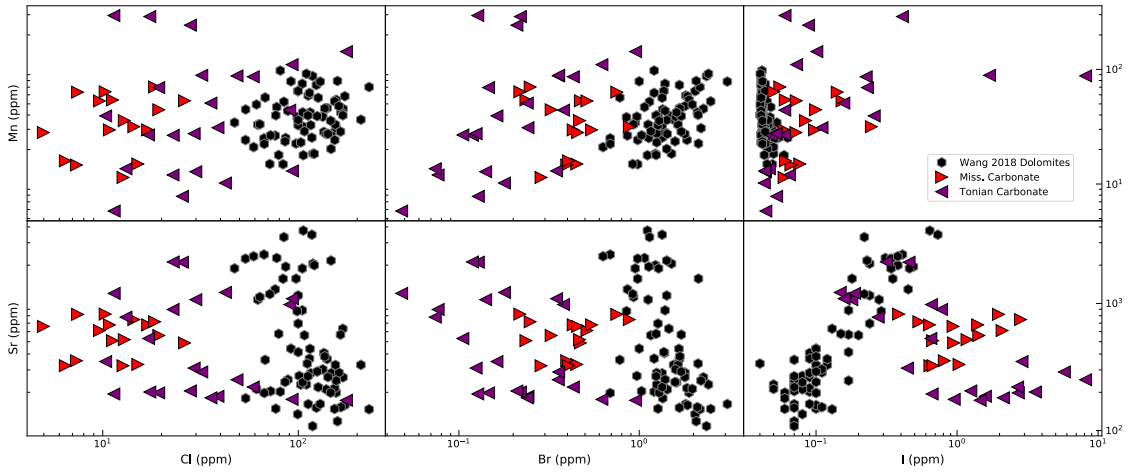

Figure 5.17: Cl, Br and I contents of marine carbonates relative to Sr and Mn (Cheng et al., 2020; Wörndle et al., 2019). Dolomite data from (Wang et al., 2020)

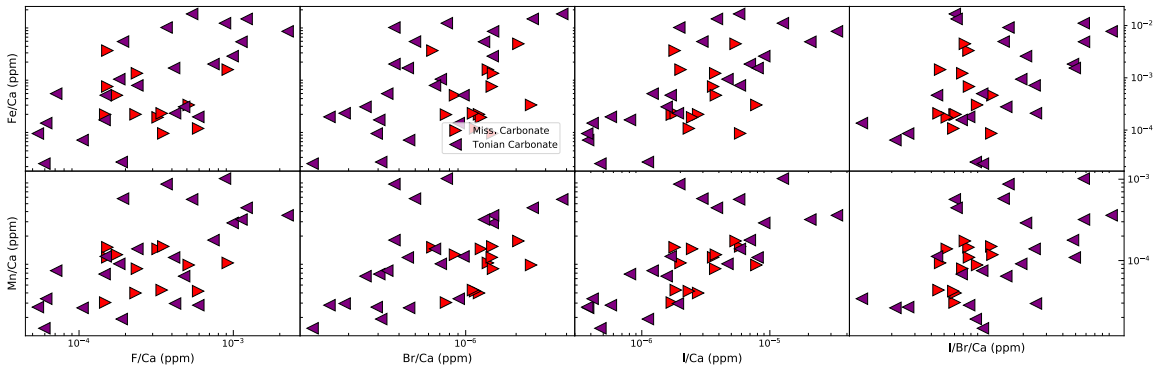

Figure 5.18: Halogen/Ca ratios vs. Mn/Ca, Sr/Ca (Cheng et al., 2020; Wörndle et al., 2019).

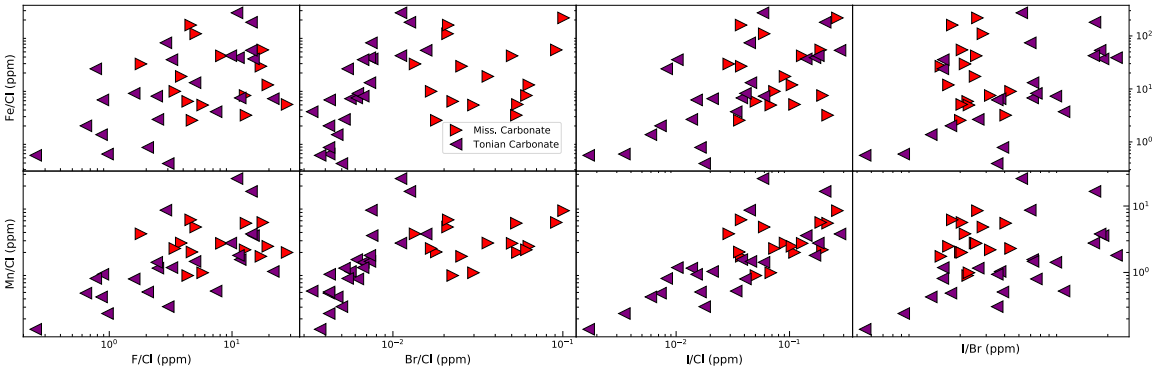

Figure 5.19: Halogen/Cl ratios vs. Mn/Cl, Fe/Cl (Cheng et al., 2020; Wörndle et al., 2019).

Despite these ambiguities, the halogen geochemistry of Tonian and Mississippian carbonates cannot be entirely explained by diagenesis. Evidently the partitioning behavior of the halogens is controlled by several separate factors (i.e., F vs. I) and does not simply represent the halogen content of the seawater they are derived from. This complex behavior is further exemplified by Messinian carbonates which relate to a period of rapid evaporite formation from the Mediterranean Sea (referred to as the Messinian Salinity Crisis, MSC)(Garcia-Castellanos et al., 2009)(Figure 5.20).

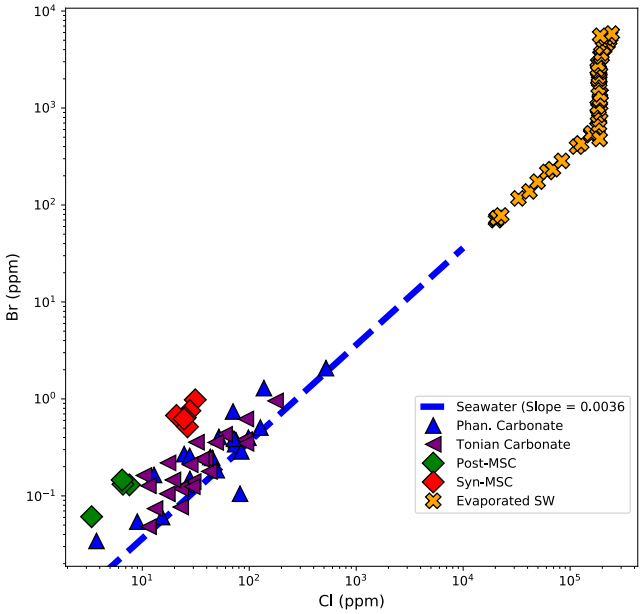

Figure 5.20: Cl vs. Br contents of marine carbonates, and evaporated seawater (McCaffrey et al., 1987).

The 'syn-MSC' carbonates represent carbonates formed in highly saline waters during an intense evaporative event, with 'post-MSC' carbonates reflecting less saline waters after the Messinian Salinity Crisis ended. Figure 5.20 shows that the Cl and Br contents of syn-MSC are Cl-Br-rich, whereas post-MSC carbonates are Cl-Br-poor. Whilst these results suggest that the halogen contents of marine carbonates are qualitatively indicative of the salinity, or in the least, indicative of changing facies conditions consequently related to

increased salinity of their host waters, this is an incomplete explanation. Both the syn and post-MSC are aragonitic carbonate sediments, although the syn-MSC carbonates contain abundant coralline Red Algae (Marco Brandano pers. comm.). Given the bromoperoxidase activity in coralline Red Algae (Isupov et al., 2000; Sheffield et al., 1992; Wever et al., 2018), it is difficult to reconcile whether the Cl-Br-rich carbonates of the syn-MSC are reflective of higher salinity conditions, or rather, from an increased partitioning of Cl & Br influenced by the halogenases activity of the biomineralizing organism.

Given these evident biogeochemical relationships that overprint the expected trends with increased salinity that cannot be adequately tested at this time, I focus on interpreting the temporal relationships Br/Cl and I/Cl record of the Tonian and Mississippian carbonate suites. If a similar rationale is applied to Br as for I (Lu et al., 2010), in so far that the only viable species capable of being incorporated into the structure are oxidized (i.e., iodate and bromate)(Midgley et al., 2021) – then the Br contents of carbonates are necessarily reflective of the processes which produce the oxidized Br-species which I suspect is associated with haloperoxidase activity in the surrounding environment. Following this rationale further, if the mechanism of Br incorporation into marine carbonates is inherently associated with biochemistry, then these processes may be apparent during periods of punctuated biological productivity.

Carbon isotope excursions are generally thought to represent time periods in which massive sequestrations of organic matter resulted in increases in the $\delta^{13}C$ values of the ocean and thereby marine carbonates (Saltzman et al., 2012). To test this general idea, we measured two well-characterized sample suites from environments indicative of changing redox potentials and similarly large carbon isotope excursions from the Mississipian and Tonian. A

detailed overview of these sequences can be found in (Halverson et al., 2018; Wörndle et al., 2019) for the Tonian, and (Cheng et al., 2020) for the Mississippian.

The Tonian carbonate suite is significant as marine algae and macroalgae are recognized to have high concentrations of halogenases (Barnum, 2020; Butler and Sandy, 2009; Küpper et al., 2008), and are thought to have 'emerged' in a tight time interval ~ 650 Myrs ago between the Sturtian and Cryogenian 'Snowball Earth' events. (Brocks et al., 2017). This time interval is thought to represent an environmental shift from the dominant primary producers of cyanobacteria, to one of planktonic algae which would serve as a far more efficient means of energy transport across the food web (Irwin et al., 2006; Knoll, 2014; Planavsky et al., 2010) – and potentially facilitating the evolution of eukaryotic life (Brocks et al., 2017; Falkowski et al., 2004; Johnston et al., 2012). The Mississippian sample suite is significant as it has well resolved variations in $\delta^{238}U$ and $\delta^{13}C$ values indicative of expanded euxinic & low-oxygen conditions (Cheng et al., 2020). These two data sets will broadly test the idea that the halogen contents of marine carbonates are more reflective of biochemical processes as opposed to simple redox.

Figures 5.21 and 5.22 depicts the halogen ratios, $\delta^{18}O$, and $\delta^{13}C$ values of the Mississippian and Tonian carbonate suites. Across the individual stratigraphic columns, F/Cl, Br/Cl, and I/Cl ratios are generally related at the same time periods. As fluorine is the most sensitive halogen to changes in mineralogy (i.e., carbonates are becoming more aragonitic), this suggest that the environmental changes attributed to increases in the Br/Cl and I/Cl ratios also occur concomitant with mineralogical changes. These environmental changes attributed to changing carbonate mineralogy and F/Cl, ratios, however, also occur alongside processes which contributed high I/Cl values in the carbonates.

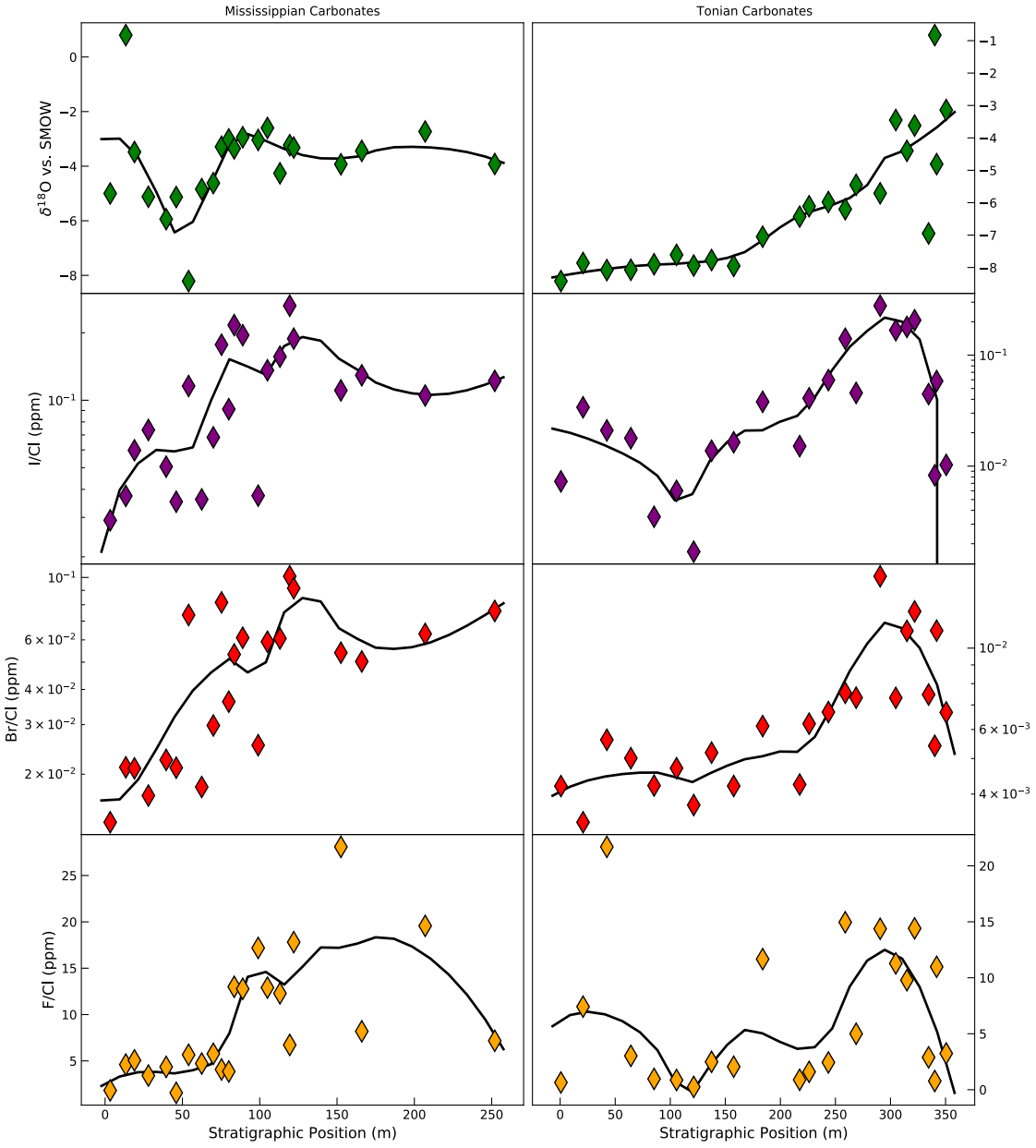

Figure 5.21: Halogen ratios and oxygen isotope compositions of Mississippian and Tonian carbonates (left and right) (Cheng et al., 2020; Wörndle et al., 2019). Regression line is a 2nd order LOWESS.

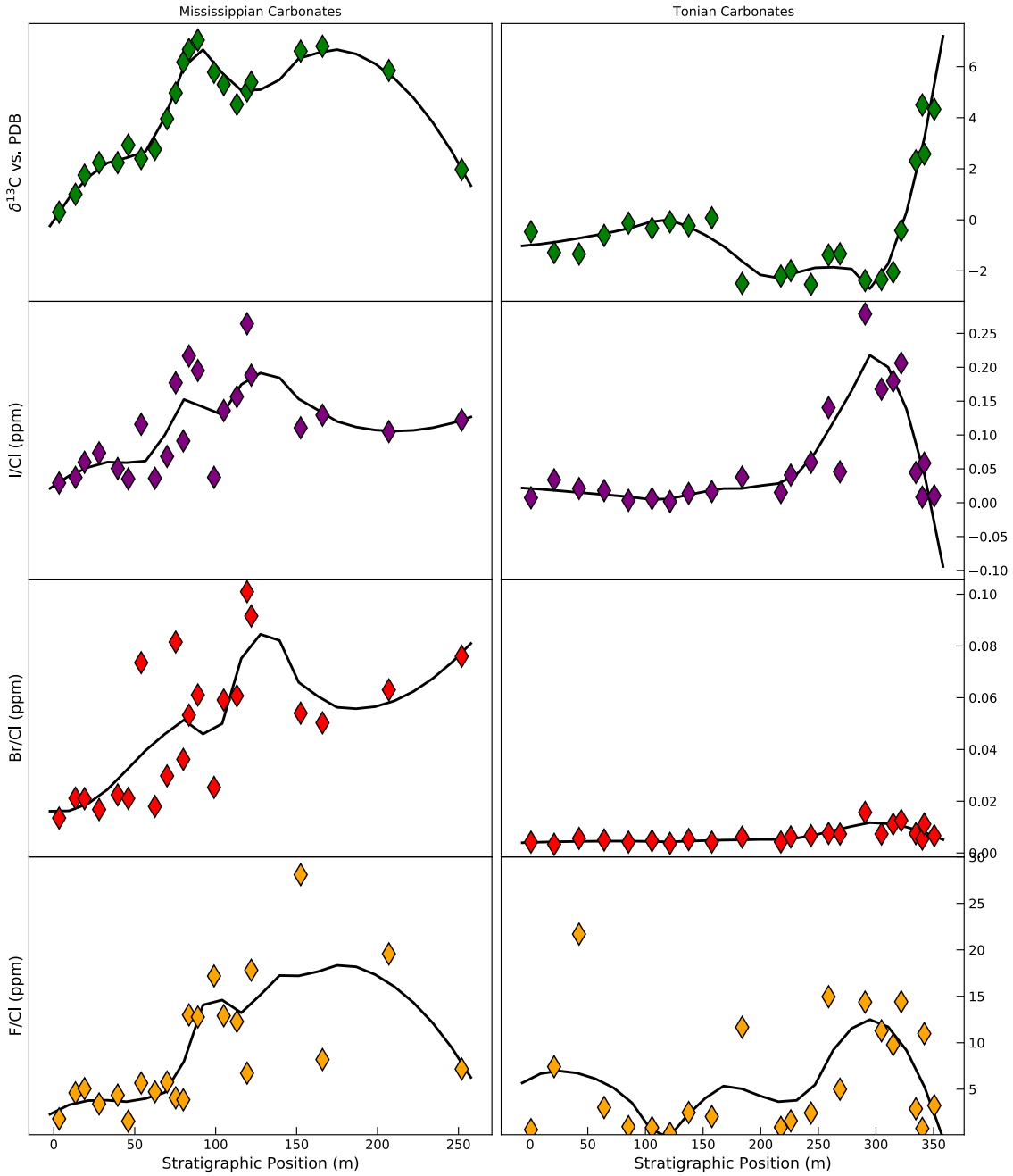

Figure 5.22: Halogen ratios and carbon isotope compositions of Mississippian and Tonian carbonates (left, right) (Cheng et al., 2020; Wörndle et al., 2019). Regression line is a 2nd order LOWESS.

These data show that both carbonate suites reflect highly variable, albeit similarly high halogen contents for F, Cl, Br, and I during the carbon isotope excursions despite the fact that the Mississippian suite reflects oxygen-poor waters which should function to eliminate, or in the least diminish the apparent magnitude of the iodide-iodate redox proxy (Lu et al., 2010). This inconsistency suggest that the iodine contents of carbonates does not simply represent the oxygen content of seawater and is more likely to reflect processes associated with punctuated periods of productivity.

Are the halogen contents of marine carbonates reflective of redox or biochemical processes?

Assuming analogous behavior of Br to the iodate partitioning into carbonates, these data suggests that these changing environments also have a mechanism capable of producing bromate which can enter the carbonate structure (Midgley et al., 2021). One such mechanism can be readily cited within arguably the most important group of organisms in Earth's history – phytoplankton (Falkowski et al., 2004). Algal blooms are a critically important source of biomass for the marine food web and significantly contribute to the carbon cycle (Harris, 1994; Holligan et al., 1993). Algal blooms, however, rapidly 'collapse' – influenced by the depletion of essential nutrients (Huppert et al., 2002), or viral infection (Fuhrman, 1999; Wilhelm and Suttle, 1999), and thus are expected to contribute significant masses of organic matter to produce large carbon isotope excursions in the geologic record (Vincent et al., 2021).

Recent works have indicated that the collapse of algal blooms may result from lytic viral infections, leading to the large releases of algal biomass to the dissolved organic matter (DOM) pool (Kuhlisch et al., 2021). This process termed the 'viral-shunt' (Fuhrman, 1999; Wilhelm and Suttle, 1999) can result in the remodeling of metabolic pathways (Kuhlisch et

al., 2021; Vincent et al., 2021), to further facilitate organic matter sequestration (Guidi et al., 2016; Weinbauer, 2004). Vincent et al., 2021 show that the demise of algal blooms by viral infection and cell lysis can increase inorganic and organic production and thereby potentially carbon sequestration by factors of 2 to 4.5.

Algal cell death via viral infection occurs by the accumulation of reactive oxygen species such as H_2O_2 (Sheyn et al., 2016). Many organisms contain the necessary enzymes to produce antioxidants to scavenge reactive oxygen species, however, cell infection leads to remodeling of metabolic pathways to facilitate infection (Kuhlisch et al., 2021; Sheyn et al., 2016), and thereby cell death by the accumulation of reactive species without the production of antioxidants. The formation of halogenated metabolites in algal blooms occurs by the haloperoxidase enzyme which functions to oxidize halides (i.e., Cl^-, Br^-) by H_2O_2 (Cros et al., 2022; Küpper et al., 2008; Küpper and Carrano, 2019; Ludewig et al., 2020; Murphy et al., 2000). As cells lyse their organic matter – metabolites are released into the water which are rapidly consumed by microbial consumers. Careful study of the lysed metabolites reveals an abundance of reactive halogenated metabolites (i.e., Cl_xI, Cl_x, Br_xCl_y)(Kuhlisch et al., 2021), which could feasibly act as precursor and/or intermediate species capable of forming oxidized halogen species.

In summary, this speculative idea serves as an explanation for the occurrence of high I and Br contents of the measured Mississippian carbonates formed in low-oxygen conditions concomitant with a carbon isotope excursion. Although abiotic oxidation of iodide to iodate is expected, it is not feasible to envision an abiotic mechanism capable of contributing large abundances of bromate in seawater. Massive phytoplankton die offs could be expected to result in the abundance of reactive halogenated metabolites, thereby producing the oxidized

species iodate and bromate, despite the fact that localized waters are oxygen-poor. Thus, the halogen geochemistry of marine carbonates in at least for I and Br is evidently dominated by the biochemistry in the biomineralizing organisms themselves, and potentially reflective of the widespread occurrence of halogenated metabolites and halogenated organic matter that can be oxidized into forms compatible in the carbonate structure such as bromate (Midgley et al., 2021) and iodate (Lu et al., 2010). Although these biochemical processes are likely to similarly effect Cl contents, the large difference in abiotic mineral partitioning behavior for F and Cl in calcite and aragonite (Kitano and Okumura, 1973; Kitano et al., 1975; Okumura et al., 1983) makes this idea difficult to further specify.

A similar idea may explain the $\delta^{37}Cl$ values of marine carbonates (Figure 5.23). Presumably if a highly oxidized form of Cl was entering the carbonate structure as would be

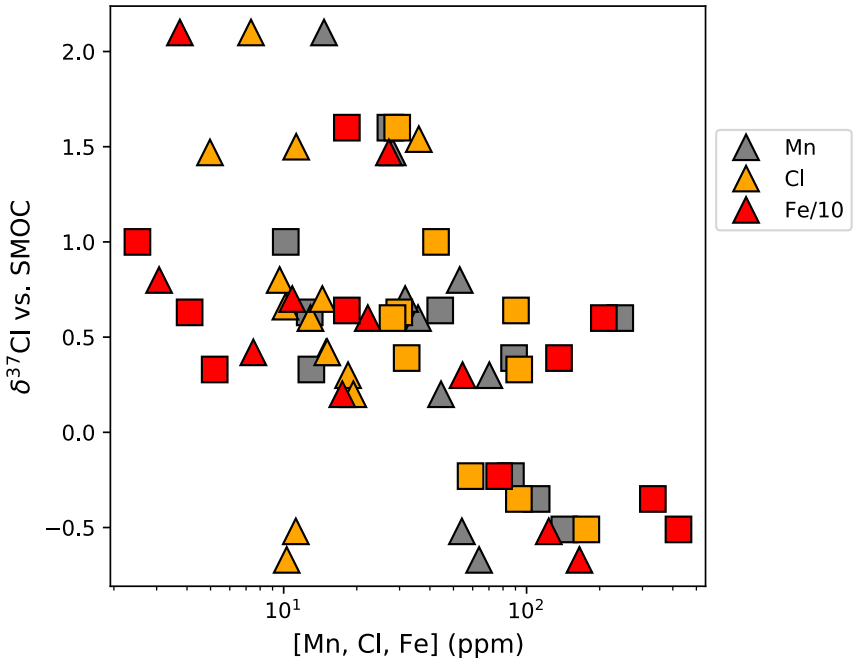

Figure 5.23: Mn, Cl, and Fe contents vs. $\delta^{37}Cl$ values. Mississippian suite are triangles, Tonian suite is squares (Cheng et al., 2020; Wörndle et al., 2019).

predicted from say, chlorate, it would be expected to be significantly isotopically fractionated (Urey, 1947) with respect to seawater which has maintained a near constant $\delta^{37}Cl$ value of ~ 0‰ (Eggenkamp et al., 2019). The modest ~2.5‰ range in $\delta^{37}Cl$ values suggests that either multiple incorporation mechanisms are being measured (i.e., an inorganic seawater component with $\delta^{37}Cl$ of ~ 0‰, and an organic component with unknown $\delta^{37}Cl$ values), or that the a majority of measured chloride is incorporated via a kinetic mechanism akin to Mg isotopes (Hippler et al., 2009).

Method Development of halogen geochemical techniques

Preface

The measurement and extraction of the full suite of halogens (F, Cl, Br, I) from geological materials is analytically difficult due to their ease for contamination, the necessity of multiple analytical methods, as well as unique extraction techniques. The extraction of many elements out of silicate material typically requires the use of halogen-bearing acids such as mixtures of HF-HCl-HNO_3 which are capable of fully dissolving silicates and metals for quantitative chemical measurements. Thus, acid digestion cannot be used to determine halogen contents. In this work I characterize the technique of pyrohydrolysis in terms of the quantitative extraction of the full suite of halogen elements from geological materials and advances in the Cl isotope measurements of trace Cl contents of extremely volatile-poor extraterrestrial lunar materials. This work also discusses halogen measurement techniques by way of Inductively Coupled Plasma Mass Spectrometry (ICPMS) and Ion Chromatography (IC). These techniques have been utilized in characterizing the halogen geochemistry of planetary materials in previous chapters. In this chapter we include a brief presentation and

discussion of this method applied to ancient marine sediments to address a simple long-standing question of paleosalinity of Earth's oceans.

Method Developments

Pyrohydrolysis

Pyrohydrolysis involves the melting of silicate material with an oxy-propane torch in a stream of water vapor with devolatilized compounds collected in a downstream condensing column. This technique presents a number of difficulties in terms of limiting the contribution of halogen 'blanks' and maximizing the halogen-yield. Samples prepared by this method for continuous flow Cl isotope measurements often contain between 5-15 ug of Cl such that trace contaminants can completely overprint the primary halogen contents in measured materials. In contrast, dual-inlet measurements utilize ~ 1000 ug Cl for a single analysis such that contamination is less of a concern for Cl-rich samples, or when ample sample masses are available. It is important to note that the concentration of halogens in sample solutions is a function of both sample mass and condensed solution volume. Small samples can be quickly processed to achieve low volume solutions; however, larger samples are often diluted in large volumes of solution from the duration required to ensure complete melting.

It is recognized that quantitative halogen extraction via pyrohydrolysis is made easier using V_2O_5; however, this reagent contributes variably high halogen-blanks (Jaime Barnes 2019, pers comm.). Furthermore, particularly Cl-poor materials often require >1 grams of material for quality analyses, such that the necessary amount of V_2O_5 (1:1) and thereby the blank it contributes becomes progressively more problematic in halogen-poor materials. Although it has been shown that partial Cl-extraction via pyrohydrolysis results in artificially

low $\delta^{37}Cl$ values by around -1‰, this issue is considered comparatively less important in terms of obtaining the highest-quality primary measurement in particularly Cl-poor materials.

While the use of V_2O_5 may be necessary for lithologies with higher melting temperatures such as peridotites (Jaime Barnes 2019, pers comm.) – a vast majority of planetary materials measured in this works are basalts that are easily melted. Thus, to characterize the halogen extraction from basaltic lithologies – two USGS standards BCR-2 and BHVO-2 were measured without the use of V_2O_5. Relative to Kendrick et al., 2018 these two standards yielded (F, Cl, Br, I), BCR-2: 77±4% (366.1 ppm F), 95±1.4% (101.1 ppm Cl), 88±22% (0.169 ppm Br), 67±23% (0.04 ppm I), and BHV-2: 74±4% (312.4 ppm F), 99±6% (101.6 ppm Cl), 107±15% (0.277 ppm Br), 71±22% (0.05 ppm I)(Kendrick et al., 2018). Thus, pyrohydrolysis of basalts without the use of V_2O_5 results in quantitative halogen yields.

Halogen Measurement Techniques and Matrix Effect Corrections

The halogen measurement techniques utilized in this work include ICPMS (Element2 at Johnson Space Center) and IC (ThermoFisher ICS 1000 with a AS9-HC column at The University of New Mexico). A vast majority of samples measured in this work contain trace halogen abundances such that both instruments were needed to characterize the full suite of halogen contents. IC is used in measuring fluorine abundances, although has high detection limits for Cl such that for samples such as lunars - ICPMS was necessarily utilized. Conversely, due to the high ionization potential of fluorine - the trace F concentrations in pyrolysis solutions of planetary materials (~ 1 ppm) makes ICPMS unable to measure F contents, although with a far lower detection limit for Cl. Thus, ICPMS is utilized for Cl

determinations when sample solutions are too Cl-poor to be measured by IC, however, presents with a significant matrix

effect that decreases Cl and Br counts by approximately 40% (Figure 5.24). Attempts were made to concentrate solutions by heating, however, this led to extensive loss of Br and I and should not be performed. Instead, it is necessary to account for expected yield from samples masses and control the final volume of condensed solutions appropriately to achieve adequate sample concentrations.

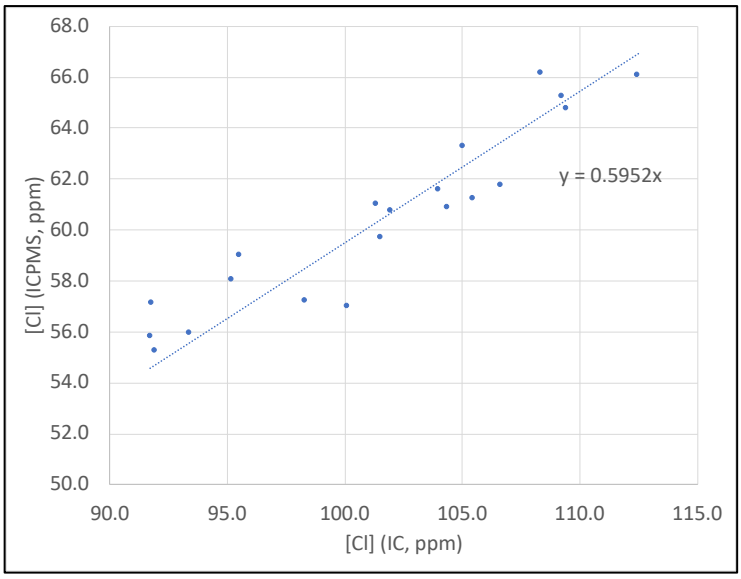

Figure 5.24: Chlorine contents measured by IC and ICPMS indicating the Cl matrix effect.

4- and 5-point calibration curves were utilized for IC and ICPMS, respectively.

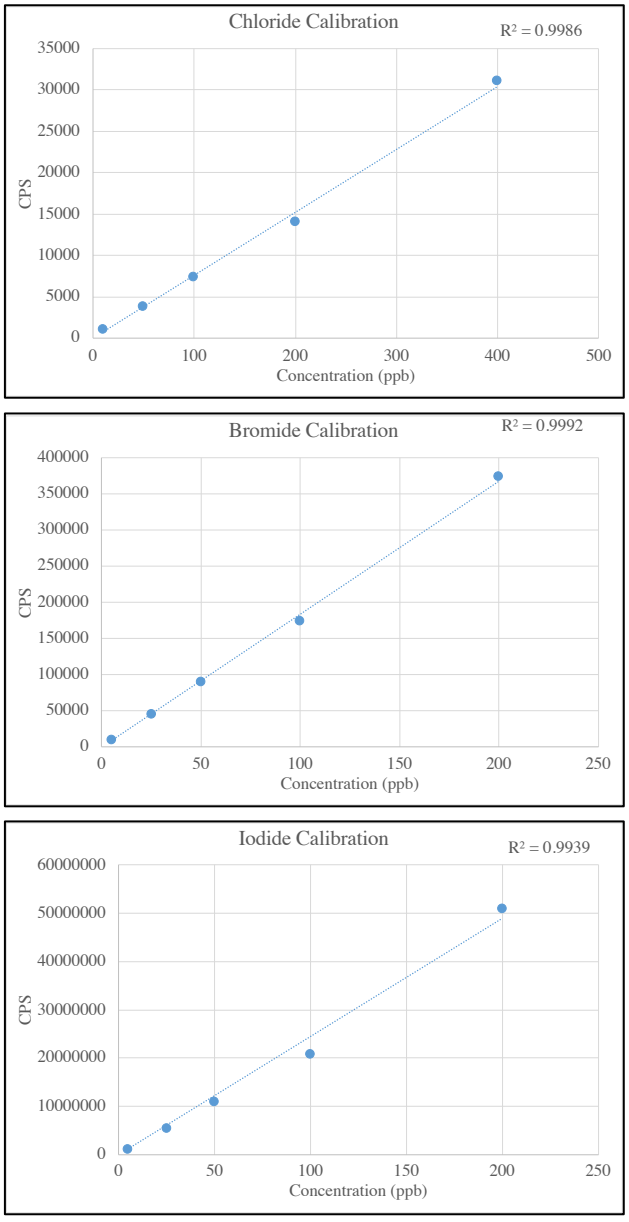

Figure 5.25: Cl (top), Br (middle), and I (bottom) calibration curves for ICPMS.

ICPMS (ppb): Cl: 400, 200, 100, 50, 10, Br & I: 200, 100, 50, 25, 5 (Figure 5.25). Average 1

	I	Cl	Br
RF Power	1100-1200		
Sample Uptake Rate (ul/min)	100-125		
Plasma Gas Flow (l/min)	16.0		
Auxiliary Gas Flow (l/min)	0.80		
Nebulizer Gas Flow (l/min)	1.0-1.1		
Nebulizer	PFA microconcentric nebulizer		
Spray Chamber	Cyclonic Quartz		
Sampler cone	Nickel 1.1 mm aperture diameter		
Skimmer Cone	Aluminum 0.8 mm aperture diameter		
Torch Position	Optimized daily		
Guard Electrode	Yes		
Resolution	Low	Medium	Medium
Number of scans	8	8	8
Number of acquisition points	50	50	50
Acquisition window	100	125	125
Search window	100	100	100
Integration window	20	50	50
Dwell time (sample/ms)	50	25	25

Figure 5.26: Instrument conditions for halogen measurements by ICPMS.

sigma standard deviation on these concentrations were 2.2, 11.4, and 1.14%, respectively. Operating conditions for the ICPMS can be seen in Figure 5.26. Iodine is measured as mass 127 in low resolution mode, Bromine as 79 in medium resolution, and chlorine as 35 in medium resolution.

Method Development of acid-digestion of marine carbonates

Acid-digestion is currently utilized in measuring trace iodide abundances in marine carbonates. As pyrohydrolysis is a very consumable and labor-intensive methodology, we attempted to measure the full suite of halogen contents of carbonates by nitric acid digestion. We found that the high sample mass required for adequate Cl-concentration in sample solutions contributed excess dissolved carbonate in solution that was gradually deposited on the ICPMS inlet that decayed signal strengths throughout the analytical session. Thus, to

measure the full suite of halogen contents of marine carbonates – pyrohydrolysis was determined to be necessary.

Continuous-Flow Chlorine Isotope Measurements

The technique utilized to measure chlorine isotope compositions is Isotope Ratio Mass Spectrometry (IRMS). A Delta^{PLUS}XL equipped with faraday cups for masses 50 and 52 utilizing CH_3Cl as an analyte was utilized. As stated previously, the primary objective of this work was to lower the necessary sample sizes to measure chlorine isotope compositions of Cl-poor planetary materials. Although dual-inlet provides the most high-precision analyses capable of being utilized for natural waters, apatite, and halite – this method requires approximately 1,000 ug of Cl. For example, effectively all lunar materials measured contain <100 ug/g Cl, such that to measure their $\delta^{37}Cl$ values by dual-inlet would require an infeasible amount of material. Continuous-flow, however, presents with difficulties due to size-dependent correction effects (Figure 5.27) and the necessary use of particularly 'sticky' organic gases such as CH_3Cl and CH_3I. These difficulties can be alleviated by several practices:

1) Instrument conditioning by the flow of He and reference gas into the source for at least 60-120 minutes followed by zero-enrichment determination of reference gas vs reference gas to ensure stability.
2) The initial measurements of at least 5 seawater (SMOC) standards comprising the full range of possible unknown sample sizes. A minimum of 20 minutes between every sample is necessary to prevent the introduction of CH_3I into the source. The introduction of CH_3I contributes to variable $\delta^{37}Cl$ values and cannot be remedied during the analytical session.

3) Following sample analyses, the 'reverse-flow' of He through the GC column removing excess CH_3I for at least 20-30 minutes at 120 ºC. Longer analytical sessions achieve more reproducible data if the duration of reverse flow is increased to 30 minutes. Attention is needed to ensure that He flow through the waste trap is continuous throughout long analytical sessions. The introduction of CH_3I into the source most often occurred alongside undetected 'clogs' in the waste trap that limited the efficiency of removing CH_3I from the GC column even if the duration of reverse-flow was adequate. A qualitative 'bubbler' can be used by placing the venting capillary in a vessel of water to indicate when the flow is limited.
4) Standard bracketing between every 3-5 samples. It is common for the calibration curve to shift towards higher isotope values by <1‰ during long analytical sessions. When standard bracketing shows a shift in the calibration curve, a new curve is necessarily constructed unless the remaining samples match the size of remaining standards. The behavior and timing of this shift depends strongly on instrument conditions and overall stability. It is best to ensure instrument stability by repeated measurements of seawater standards of differing chlorine contents.

A well characterized size-dependent calibration curve correction is the most important factor in obtaining high-quality chlorine isotope data by continuous flow. This correction is made by ensuring a constant reference gas area to compare to the standard and sample gases. As signal drift is common during initial instrument conditioning – this is the reasoning behind the prolonged conditioning time before every analytical session. It is

critical to ensure that the standard calibration curve encompasses the entire range of possible unknowns as smaller sample sizes require larger corrections (Figure 5.27).

The standards used in this work include a CH_3Cl reference gas, seawater (Standard Mean Ocean Chloride (SMOC)) and an in-house serpentinite standard EL-O5-14. This

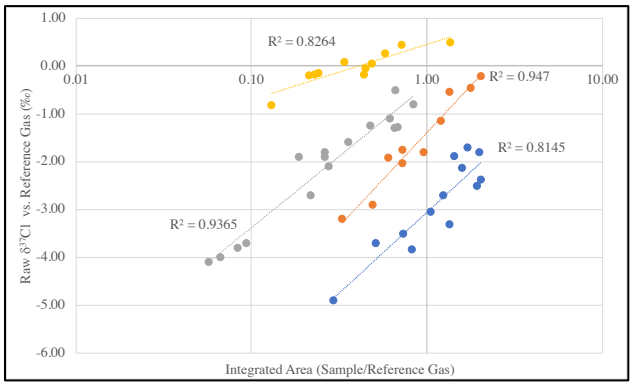

Figure 5.27: Size-dependent chlorine isotope calibration curves of seawater standards from separate analytical sessions.

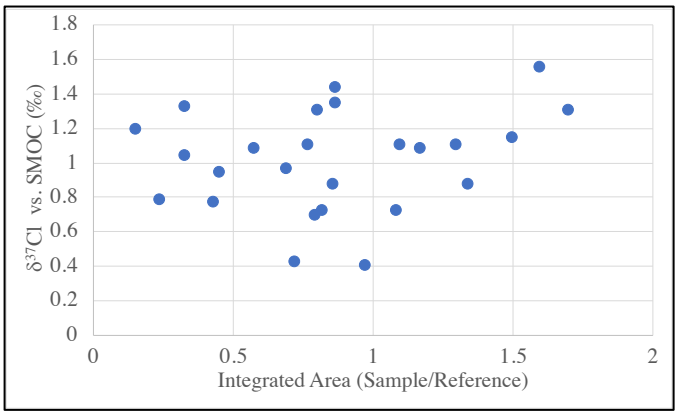

Figure 5.28: Chlorine isotope reproducibility of EL-05-14 in house standard.

serpentinite standard has been characterized by (Barnes et al., 2006) to have a $\delta^{37}Cl$ value of 0.84±0.25‰. Repeated measurements of EL-05-14 (n=25) throughout this work results in an average $\delta^{37}Cl$ value of 1.0±0.30‰, within error of previous measurements (Figure 5.28).

Sample Preparation Procedures

Many samples measured in this work were measured for both water-soluble (WSC) and structurally-bound chloride (SBC). Water-soluble chloride fractions were obtained by leaching powdered rock samples in DI water overnight, whereas SBC fractions were obtained by pyrohydrolysis of dried powders. Both fractions were measured by IC, ICPMS and IRMS for halogen contents and chlorine isotope compositions. By utilizing the known [Cl] from sample solutions determined by IC/ICPMS, a known amount of chloride was removed from residual sample solutions and converted into CH_3Cl. This procedure is as follows:

1) Solutions are reacted with 2-5 mL of HNO_3 overnight to degas sulfur. Solutions suspected to contain excess sulfur can be qualitatively tested by removing a small amount of solution and adding $AgNO_3$ resulting in the formation of a black precipitate.
2) Once sulfur is ensured to have been completely removed, 1 mL of 0.4 M $AgNO_3$ is added to sample solutions in a light-proof laminar flow hood overnight. The reaction of the sample solution with silver nitrate results in the formation of cloudy AgCl. In the presence of light, AgCl can decompose such that all following procedures must ensure minimal light exposure.
3) Solutions containing AgCl are then filtered. Following precipitation overnight, AgCl precipitates have deposited on the bottom of the beaker. The AgCl deposits are most-easily carried back in suspension by ‘stirring’ the beakers by hand before their introduction into a 10 mL filter funnel. Whilst pouring the solution and

precipitates, the beaker is rinsed with a 5% HNO_3 solution to completely remove precipitated AgCl.

a. The filters currently used are GVS cellulose acetate membrane filters (25 mm diameter, 0.22 um pore size) as Whatman GF/F microfiber filters contain a large Cl-blank that is unsuitable for trace Cl-analyses.

4) AgCl-bearing filters are then dried, folded, and packed in 8 mm pyrex tubes. Aluminum foil is used to identify sample tubes and protect AgCl from light. Tubes are then evacuated to <5 millibars and injected with 10 uL of CH_3I. CH_3I is subsequently frozen out by way of liquid nitrogen, and the tube is flame-sealed.
5) Sealed tubes are then reacted at 80 C for 48 hours in the conversion of AgCl to CH_3Cl. It is critical that the temperature of this reaction does not exceed 80 degrees, as it will decompose AgI to I_2 which can be seen by a vivid purple gas in the sample tube.

Continuous-flow chlorine isotope measurements

Improvements were made to the micro-Cl extraction line throughout this work. The purpose of the line is to concentrate the analyte gas (CH_3Cl) and purify it from CH_3I. These steps are performed as follows:

1) Sample tube is scored using a glass-cutting tool and placed into a tube-cracker that is purged with He for a minimum of 5 minutes.
2) Sample tubes are cracked in a 30 mL/min He flow and concentrated for 3 minutes into a liquid nitrogen (LN_2) trap while the instrument run begins. Prolonged exposure of the liquid nitrogen trap leads to a gradual reduction in yield and should be avoided.

3) Immediately following the final reference gas peak, the first LN_2 is heated up with hot water to ensure the entire parcel of gas is released into the GC column at the same time. The GC column is an 8mm pyrex U-trap that is packed with HayesepQ 80/100 mesh held by quartz wool and housed in an oven. Sample gas is passed through the GC column held at 80 degrees, and upon exiting the GC column, a small 'sniffer' capillary is used to detect when CH_3Cl has passed through the GC column. Once the CH_3Cl peak has ended, the flow is reversed back through the GC column and the oven temperature is increased to 120 degrees. The period of 'reverse-flow' necessarily lasts for 20-30 minutes to ensure complete removal of CH_3I from the GC column.

References

Agarwal, V. et al., 2017. Enzymatic halogenation and dehalogenation reactions: pervasive and mechanistically diverse. Chemical reviews, 117(8): 5619-5674.

Allen Jr, R.O., Clark, P.J., 1977. Fluorine in meteorites. Geochimica et Cosmochimica Acta, 41(5): 581-585.

Allibert, L., Charnoz, S., Siebert, J., Jacobson, S.A., Raymond, S.N., 2021. Quantitative estimates of impact induced crustal erosion during accretion and its influence on the Sm/Nd ratio of the Earth. Icarus, 363: 114412.

Amelin, Y., Krot, A., 2007. Pb isotopic age of the Allende chondrules. Meteoritics & Planetary Science, 42(7-8): 1321-1335.

Antonelli, M.A. et al., 2014. Early inner solar system origin for anomalous sulfur isotopes in differentiated protoplanets. Proceedings of the National Academy of Sciences, 111(50): 17749-17754.

Arnold, T. et al., 2010. Measurement of zinc stable isotope ratios in biogeochemical matrices by double-spike MC-ICPMS and determination of the isotope ratio pool available for plants from soil. Analytical and bioanalytical chemistry, 398(7-8): 3115-3125.

Asphaug, E., Agnor, C.B., Williams, Q., 2006. Hit-and-run planetary collisions. Nature, 439(7073): 155.

Asphaug, E., Jutzi, M., Movshovitz, N., 2011. Chondrule formation during planetesimal accretion. Earth and Planetary Science Letters, 308(3-4): 369-379.

Babel, M., Schreiber, B., 2014. 9.17-Geochemistry of evaporites and evolution of seawater. Treatise on geochemistry: 483-560.

Badyukov, D., Raitala, J., Kostama, P., Ignatiev, A., 2015. Chelyabinsk meteorite: Shock metamorphism, black veins and impact melt dikes, and the Hugoniot. Petrology, 23(2): 103-115.
Balcone-Boissard, H., Villemant, B., Boudon, G., 2010. Behavior of halogens during the degassing of felsic magmas. Geochemistry, Geophysics, Geosystems, 11(9).
Bali, E., Hartley, M., Halldórsson, S., Gudfinnsson, G., Jakobsson, S., 2018. Melt inclusion constraints on volatile systematics and degassing history of the 2014–2015 Holuhraun eruption, Iceland. Contributions to Mineralogy and Petrology, 173(2): 1-21.
Bao, H., Barnes, J.D., Sharp, Z.D., Marchant, D.R., 2008. Two chloride sources in soils of the McMurdo Dry Valleys, Antarctica. Journal of Geophysical Research: Atmospheres, 113(D3).
Barnes, J., Selverstone, J., Sharp, Z., 2006. Chlorine isotope chemistry of serpentinites from Elba, Italy, as an indicator of fluid source and subsequent tectonic history. Geochemistry, Geophysics, Geosystems, 7(8).
Barnes, J.D., Sharp, Z.D., 2006. A chlorine isotope study of DSDP/ODP serpentinized ultramafic rocks: Insights into the serpentinization process. Chemical Geology, 228(4): 246-265.
Barnes, J.D., Sharp, Z.D., 2017. Chlorine isotope geochemistry. Reviews in Mineralogy and Geochemistry, 82(1): 345-378.
Barnes, J.J., Franchi, I.A., McCubbin, F.M., Anand, M., 2019. Multiple reservoirs of volatiles in the Moon revealed by the isotopic composition of chlorine in lunar basalts. Geochimica et Cosmochimica Acta, 266: 144-162.
Barnes, J.J. et al., 2016a. An asteroidal origin for water in the Moon. Nature communications, 7: 11684.
Barnes, J.J. et al., 2014. The origin of water in the primitive Moon as revealed by the lunar highlands samples. Earth and Planetary Science Letters, 390: 244-252.
Barnes, J.J. et al., 2016b. Early degassing of lunar urKREEP by crust-breaching impact(s). Earth and Planetary Science Letters, 447: 84-94.
Barnum, T.P., 2020. Discoveries in the Biology of Oxidized Chlorine, UC Berkeley.
Barrat, J.-A. et al., 2007. The Stannern trend eucrites: Contamination of main group eucritic magmas by crustal partial melts. Geochimica et Cosmochimica Acta, 71(16): 4108-4124.
Barrat, J.-A. et al., 2012. Geochemistry of CI chondrites: Major and trace elements, and Cu and Zn isotopes. Geochimica et Cosmochimica Acta, 83: 79-92.
Barrett, T. et al., 2019. Investigating magmatic processes in the early Solar System using the Cl isotopic systematics of eucrites. Geochimica et Cosmochimica Acta, 266: 582-597.
Beaty, D., Albee, A., 1978. Comparative petrology and possible genetic relations among the Apollo 11 basalts, Lunar and Planetary Science Conference Proceedings, pp. 359-463.
Benedix, G. et al., 2008. The formation and chronology of the PAT 91501 impact-melt L chondrite with vesicle–metal–sulfide assemblages. Geochimica et Cosmochimica Acta, 72(9): 2417-2428.
Benedix, G., McCoy, T.J., Keil, K., Love, S., 2000. A petrologic study of the IAB iron meteorites: Constraints on the formation of the IAB-Winonaite parent body. Meteoritics & Planetary Science, 35(6): 1127-1141.

Bernatowicz, T., Podosek, F., Swindle, T., Honda, M., 1988. I-Xe systematics in LL chondrites. Geochimica et Cosmochimica Acta, 52(5): 1113-1121.
Berry Lyons, W., Frape, S.K., Welch, K.A., 1999. History of McMurdo Dry Valley lakes, Antarctica, from stable chlorine isotope data. Geology, 27(6): 527-530.
Blackburn, T., Alexander, C.M.D., Carlson, R., Elkins-Tanton, L.T., 2017. The accretion and impact history of the ordinary chondrite parent bodies. Geochimica et Cosmochimica Acta, 200: 201-217.
Bombardieri, D.J., Norman, M.D., Kamenetsky, V.S., Danyushevsky, L.V., 2005. Major element and primary sulfur concentrations in Apollo 12 mare basalts: The view from melt inclusions. Meteoritics & Planetary Science, 40(5): 679-693.
Boss, A.P., 1998. Temperatures in protoplanetary disks. Annual Reviews of Earth and Planetary Science, 26: 26-53.
Bottke, W.F., Nesvorný, D., Grimm, R.E., Morbidelli, A., O'brien, D.P., 2006. Iron meteorites as remnants of planetesimals formed in the terrestrial planet region. Nature, 439(7078): 821-824.
Boujibar, A., Andrault, D., Bolfan-Casanova, N., Bouhifd, M.A., Monteux, J., 2015. Cosmochemical fractionation by collisional erosion during the Earth's accretion. Nature communications, 6(1): 1-7.
Bouvier, A., Wadhwa, M., 2010. The age of the Solar System redefined by the oldest Pb–Pb age of a meteoritic inclusion. Nature geoscience, 3(9): 637-641.
Boyce, J. et al., 2018. Chlorine isotopes in the low-Ti basalts, and the early loss of volatiles from the Earth-Moon system. Earth and Planetary Science Letters, 500: 205-214.
Boyce, J.W. et al., 2015. The chlorine isotope fingerprint of the lunar magma ocean. Science Advances, 1(8).
Boynton, W.V., Chou, C.-L., Bild, R., Baedecker, P., Wasson, J., 1976. Element distribution in size fractions of Apollo-16 soils: Evidence for element mobility during regolith processes. Earth and Planetary Science Letters, 29(1): 21-33.
Brearley, A., 1996. Nature of matrix in unequilibrated chondrites and its possible relationship to chondrules, Chondrules and the protoplanetary disk, pp. 137-151.
Brearley, A., Jones, R.H., 1998. Chondritic Meteorites. In: Papike, J.J. (Ed.), Planetary Materials. Mineralogical Society of America, Washington, D.C., pp. 3.01-3.370.
Brearley, A.J., 2006. The action of water. Meteorites and the early solar system II, 943: 587-624.
Brearley, A.J., Jones, R.H., 2018. Halogens in chondritic meteorites, The Role of Halogens in Terrestrial and Extraterrestrial Geochemical Processes. Springer, pp. 871-958.
Brearley, A.J., Krot, A.N., 2013. Metasomatism in the early solar system: The record from chondritic meteorites, Metasomatism and the chemical transformation of rock. Springer, pp. 659-789.
Brett, R. et al., 1971. Apollo 12 igneous rocks 12004, 12008, 12009, and 12022: A mineralogical and petrological study, Lunar and Planetary Science Conference Proceedings, pp. 301.
Bridges, J., Alexander, C.O.D., Hutchison, R., Franchi, I., Pillinger, C., 1997. Sodium-, chlorine-rich mesostases in Chainpur (LL3) and Parnallee (LL3) chondrules. Meteoritics & Planetary Science, 32(4): 555-565.

Bridges, J.C., Franchi, I.A., Hutchison, R., Sexton, A.S., Pillinger, C.T., 1998. Correlated mineralogy, chemical compositions, oxygen isotopic compositions and size of chondrules. Earth and Planetary Science Letters, 155(3-4): 183-196.
Britt, D.T., Consolmagno, G., 2003. Stony meteorite porosities and densities: A review of the data through 2001. Meteoritics & Planetary Science, 38(8): 1161-1180.
Brocks, J.J. et al., 2017. The rise of algae in Cryogenian oceans and the emergence of animals. Nature, 548(7669): 578-581.
Brown, K.L., Hudson, B.G., Voziyan, P.A., 2018. Halogens are key cofactors in building of collagen IV scaffolds outside the cell. Current opinion in nephrology and hypertension, 27(3): 171-175.
Buchwald, V.F., 1975. Handbook of iron meteorites.
Buchwald, V.F., Clarke, R.S., 1989. Corrosion of Fe-Ni alloys by Cl-containing akaganéite (beta-FeOOH): The Antarctic meteorite case. American mineralogist, 74: 656-667.
Budde, G. et al., 2016. Molybdenum isotopic evidence for the origin of chondrules and a distinct genetic heritage of carbonaceous and non-carbonaceous meteorites. Earth and Planetary Science Letters, 454: 293-303.
Burgess, R. et al., 2020. Archean to Paleoproterozoic seawater halogen ratios recorded by fluid inclusions in chert and hydrothermal quartz. American Mineralogist: Journal of Earth and Planetary Materials, 105(9): 1317-1325.
Burkhardt, C. et al., 2008. Hf–W mineral isochron for Ca,Al-rich inclusions: Age of the solar system and the timing of core formation in planetesimals. Geochimica et Cosmochimica Acta, 72(24): 6177-6197.
Burkhardt, C. et al., 2011. Molybdenum isotope anomalies in meteorites: constraints on solar nebula evolution and origin of the Earth. Earth and Planetary Science Letters, 312(3-4): 390-400.
Burkhardt, C. et al., 2021. Terrestrial planet formation from lost inner solar system material. Science advances, 7(52): eabj7601.
Butler, A., Sandy, M., 2009. Mechanistic considerations of halogenating enzymes. Nature, 460(7257): 848-854.
Butler, E.C., Smith, J.D., Fisher, N.S., 1981. Influence of phytoplankton on iodine speciation in seawater. Limnology and Oceanography, 26(2): 382-386.
Campbell, A.J., Humayun, M., 2005. Compositions of group IVB iron meteorites and their parent melt. Geochimica et Cosmochimica Acta, 69(19): 4733-4744.
Canfield, D.E., Raiswell, R., Westrich, J.T., Reaves, C.M., Berner, R.A., 1986. The use of chromium reduction in the analysis of reduced inorganic sulfur in sediments and shales. Chemical geology, 54(1-2): 149-155.
Canup, R.M., Visscher, C., Salmon, J., Fegley Jr, B., 2015. Lunar volatile depletion due to incomplete accretion within an impact-generated disk. Nature Geosci, 8(12): 918-921.
Carpenter, L., Liss, P., Penkett, S., 2003. Marine organohalogens in the atmosphere over the Atlantic and Southern Oceans. Journal of Geophysical Research: Atmospheres, 108(D9).
Carpenter, R., 1969. Factors controlling the marine geochemistry of fluorine. Geochimica et Cosmochimica Acta, 33(10): 1153-1167.
Carter, J.N., Beatty, K.E., Simpson, M.T., Butler, A., 2002. Reactivity of recombinant and mutant vanadium bromoperoxidase from the red alga Corallina officinalis. Journal of inorganic biochemistry, 91(1): 59-69.

Carter, P.J., Leinhardt, Z.M., Elliott, T., Stewart, S.T., Walter, M.J., 2018. Collisional stripping of planetary crusts. Earth and Planetary Science Letters, 484: 276-286.
Cassidy, M., Manga, M., Cashman, K., Bachmann, O., 2018. Controls on explosive-effusive volcanic eruption styles. Nature communications, 9(1): 1-16.
Chan, Q.H. et al., 2018. Organic matter in extraterrestrial water-bearing salt crystals. Science advances, 4(1): eaao3521.
Chance, R., Baker, A.R., Carpenter, L., Jickells, T.D., 2014. The distribution of iodide at the sea surface. Environmental Science: Processes & Impacts, 16(8): 1841-1859.
Channer, D.D., De Ronde, C., Spooner, E., 1997. The Cl− Br− I− composition of∼ 3.23 Ga modified seawater: implications for the geological evolution of ocean halide chemistry. Earth and Planetary Science Letters, 150(3-4): 325-335.
Chapman, C.R., 1976. Asteroids as meteorite parent-bodies: The astronomical perspective. Geochimica et Cosmochimica Acta, 40(7): 701-719.
Charnoz, S. et al., 2021. Tidal pull of the Earth strips the proto-Moon of its volatiles. Icarus, 364: 114451.
Chen, H., Savage, P.S., Teng, F.-Z., Helz, R.T., Moynier, F., 2013. Zinc isotope fractionation during magmatic differentiation and the isotopic composition of the bulk Earth. Earth and Planetary Science Letters, 369: 34-42.
Chen, Y. et al., 2015. Water, fluorine, and sulfur concentrations in the lunar mantle. Earth and Planetary Science Letters, 427: 37-46.
Cheng, K., Elrick, M., Romaniello, S.J., 2020. Early Mississippian ocean anoxia triggered organic carbon burial and late Paleozoic cooling: Evidence from uranium isotopes recorded in marine limestone. Geology, 48(4): 363-367.
Chou, C.L., Shaw, D., Crocket, J., 1983. Siderophile trace elements in the Earth's oceanic crust and upper mantle. Journal of Geophysical Research: Solid Earth, 88(S02).
Clark, R., Rowe, M., Ganapathy, R., Kuroda, P., 1967. Iodine, uranium and tellurium contents in meteorites. Geochimica et Cosmochimica Acta, 31(10): 1605-1613.
Clauser, C., 1992. Permeability of crystalline rocks. Eos, Transactions American Geophysical Union, 73(21): 233-238.
Clay, P.L. et al., 2017. Halogens in chondritic meteorites and terrestrial accretion. Nature, 551(7682): 614.
Clay, P.L., O'Driscoll, B., Upton, B.G., Busemann, H., 2014. Characteristics of djerfisherite from fluid-rich, metasomatized alkaline intrusive environments and anhydrous enstatite chondrites and achondrites. American Mineralogist, 99(8-9): 1683-1693.
Creech, J., Moynier, F., 2019. Tin and zinc stable isotope characterisation of chondrites and implications for early Solar System evolution. Chemical Geology, 511: 81-90.
Crockford, S.J., 2009. Evolutionary roots of iodine and thyroid hormones in cell–cell signaling. Integrative and comparative biology, 49(2): 155-166.
Cros, A., Alfaro-Espinoza, G., De Maria, A., Wirth, N.T., Nikel, P.I., 2022. Synthetic metabolism for biohalogenation. Current opinion in biotechnology, 74: 180-193.
Crossley, S. et al., 2018. Experimental insights into Stannern-trend eucrite petrogenesis. Meteoritics & Planetary Science, 53(10): 2122-2137.
Dauphas, N., Burkhardt, C., Warren, P.H., Fang-Zhen, T., 2014. Geochemical arguments for an Earth-like Moon-forming impactor. Phil. Trans. R. Soc. A, 372(2024): 20130244.
Davis, F.A., Humayun, M., Hirschmann, M.M., Cooper, R.S., 2013. Experimentally determined mineral/melt partitioning of first-row transition elements (FRTE) during

partial melting of peridotite at 3 GPa. Geochimica et Cosmochimica Acta, 104: 232-260.
Day, J. et al., 2020a. Moderately volatile element behaviour at high temperature determined from nuclear detonation. Geochemical Perspectives Letters, 13: 54-60.
Day, J.M., Moynier, F., 2014. Evaporative fractionation of volatile stable isotopes and their bearing on the origin of the Moon. Philosophical Transactions of the Royal Society of London A: Mathematical, Physical and Engineering Sciences, 372: 26.
Day, J.M., Moynier, F., Shearer, C.K., 2017a. Late-stage magmatic outgassing from a volatile-depleted Moon. Proceedings of the National Academy of Sciences, 114(36): 9547-9551.
Day, J.M., Sossi, P.A., Shearer, C.K., Moynier, F., 2019. Volatile distributions in and on the Moon revealed by Cu and Fe isotopes in the 'Rusty Rock'66095. Geochimica et Cosmochimica Acta, 266: 131-143.
Day, J.M., van Kooten, E.M., Hofmann, B.A., Moynier, F., 2020b. Mare basalt meteorites, magnesian-suite rocks and KREEP reveal loss of zinc during and after lunar formation. Earth and Planetary Science Letters, 531: 115998.
Day, J.M.D., Moynier, F., Shearer, C.K., 2017b. Late-stage magmatic outgassing from a volatile-depleted Moon. Proceedings of the National Academy of Sciences, 114: 9547-9551.
de Moor, J.M. et al., 2013. Sulfur degassing at Erta Ale (Ethiopia) and Masaya (Nicaragua) volcanoes: Implications for degassing processes and oxygen fugacities of basaltic systems. Geochemistry, Geophysics, Geosystems, 14(10): 4076-4108.
De Ronde, C.E., deR Channer, D.M., Faure, K., Bray, C.J., Spooner, E.T., 1997. Fluid chemistry of Archean seafloor hydrothermal vents: Implications for the composition of circa 3.2 Ga seawater. Geochimica et Cosmochimica Acta, 61(19): 4025-4042.
Defouilloy, C., Cartigny, P., Assayag, N., Moynier, F., Barrat, J.-A., 2016. High-precision sulfur isotope composition of enstatite meteorites and implications of the formation and evolution of their parent bodies. Geochimica et Cosmochimica Acta, 172: 393-409.
Dhaliwal, J.K., Day, J.M., Moynier, F., 2018. Volatile element loss during planetary magma ocean phases. Icarus, 300: 249-260.
Ding, S., Hough, T., Dasgupta, R., 2018. New high pressure experiments on sulfide saturation of high-FeO∗ basalts with variable TiO2 contents–Implications for the sulfur inventory of the lunar interior. Geochimica et Cosmochimica Acta, 222: 319-339.
Dobrică, E., Brearley, A., 2020. Amorphous silicates in the matrix of Semarkona: The first evidence for the localized preservation of pristine matrix materials in the most unequilibrated ordinary chondrites. Meteoritics & Planetary Science, 55(3): 649-668.
Dottin III, J.W., Farquhar, J., Labidi, J., 2018. Multiple sulfur isotopic composition of main group pallasites support genetic links to IIIAB iron meteorites. Geochimica et Cosmochimica Acta, 224: 276-281.
Dreibus, G., Spettel, B., Wänke, H., 1979. Halogens in meteorites and their primordial abundances. In: Ahrens, L.H. (Ed.), Origin and Distribution of the Elements. Pergamon, Oxford, pp. 33-38.
Dreibus, G., Wanke, H., 1985. Mars, a volatile-rich planet. Meteoritics, 20: 367-381.
Dreibus, G., Wänke, H., 1983. Halogens in Antarctic meteorites. Meteoritics, 18: 291.

Dreibus, G., Wänke, H., Schultz, L., 1986. Mysterious iodine-overabundance in Antarctic meteorites, Lunar and Planetary Inst. International Workshop on Antarctic Meteorites.
Ebel, D., 2011. Equilibrium condensation from chondritic porous IDP enriched vapor: Implications for Mercury and enstatite chondrite origins. Planetary and Space Science, 59(15): 1888-1894.
Ebel, D.S., 2006. Condensation of rocky material in astrophysical environments. Meteorites and the early solar system II, 1: 253-277.
Edwards, A., Truesdale, V., 1997. Regeneration of inorganic iodine species in Loch Etive, a natural leaky incubator. Estuarine, Coastal and Shelf Science, 45(3): 357-366.
Eggenkamp, H., 2014. The geochemistry of stable chlorine and bromine isotopes. Springer.
Eggenkamp, H. et al., 2019. The bromine and chlorine isotope composition of primary halite deposits and their significance for the secular isotope composition of seawater. Geochimica et Cosmochimica Acta, 264: 13-29.
El Goresy, A. et al., 2017. Origin of EL3 chondrites: Evidence for variable C/O ratios during their course of formation—A state of the art scrutiny. Meteoritics & Planetary Science, 52(5): 781-806.
El Goresy, A. et al., 1973. Zinc, lead, chlorine and FeOOH-bearing assemblages in the Apollo 16 sample 66095: Origin by impact of a comet or a carbonaceous chondrite? Earth and Planetary Science Letters, 18: 411-419.
Elkins-Tanton, L.T., 2012. Magma oceans in the inner solar system. Annual Review of Earth and Planetary Sciences, 40: 113-139.
Elkins-Tanton, L.T., Burgess, S., Yin, Q.-Z., 2011a. The lunar magma ocean: Reconciling the solidification process with lunar petrology and geochronology. Earth and Planetary Science Letters, 304(3–4): 326-336.
Elkins-Tanton, L.T., Grove, T.L., 2011. Water (hydrogen) in the lunar mantle: Results from petrology and magma ocean modeling. Earth and Planetary Science Letters, 307: 173–179.
Elkins-Tanton, L.T., Weiss, B.P., Zuber, M.T., 2011b. Chondrites as samples of differentiated planetesimals. Earth and Planetary Science Letters, 305(1-2): 1-10.
Epstein, S., Taylor, J.H.P., 1970. The concentration and isotopic composition of hydrogen, oxygen, and silicon in Apollo 11 lunar rocks and minerals. Proc. Lunar Sci. Conf. 2, Suppl.1: 1085-1096.
Faircloth, S., Anand, M., Franchi, I., Zhao, X., Russell, S., 2020. Multiple sulfur isotopic reservoirs in the Moon and implications for the evolution of planetary interiors.
Falkowski, P.G. et al., 2004. The evolution of modern eukaryotic phytoplankton. science, 305(5682): 354-360.
Farquhar, J., Bao, H., Thiemens, M., 2000. Atmospheric influence of Earth's earliest sulfur cycle. Science, 289(5480): 756-758.
Farrington, O.C., 1915. Meteorites: Their Structure, Composition, and Terrestrial Relations.
Feng, X., Redfern, S.A., 2018. Iodate in calcite, aragonite and vaterite CaCO3: Insights from first-principles calculations and implications for the I/Ca geochemical proxy. Geochimica et Cosmochimica Acta, 236: 351-360.
Flowers, T.J., Colmer, T.D., 2008. Salinity tolerance in halophytes. New Phytologist, 179(4): 945-963.

Flury, M., Papritz, A., 1993. Bromide in the natural environment: occurrence and toxicity. Journal of Environmental Quality, 22(4): 747-758.
Fortin, M.-A., Watson, E.B., Stern, R., 2017. The isotope mass effect on chlorine diffusion in dacite melt, with implications for fractionation during bubble growth. Earth and Planetary Science Letters, 480: 15-24.
Fuchs, L.H., 1966. Djerfisherite, alkali copper-iron sulfide: a new mineral from enstatite chondrites. Science, 153(3732): 166-167.
Fuge, R., 2019. Fluorine in the environment, a review of its sources and geochemistry. Applied Geochemistry, 100: 393-406.
Fuhrman, J.A., 1999. Marine viruses and their biogeochemical and ecological effects. Nature, 399(6736): 541-548.
Ganapathy, R., Larimer, J., 1980. A meteoritic component rich in volatile elements: its characterization and implications. Science, 207(4426): 57-59.
Gao, X., Thiemens, M.H., 1991. Systematic study of sulfur isotopic composition in iron meteorites and the occurrence of excess 33S and 36S. Geochimica et Cosmochimica Acta, 55(9): 2671-2679.
Gao, X., Thiemens, M.H., 1993a. Isotopic composition and concentration of sulfur in carbonaceous chondrites. Geochimica et Cosmochimica Acta, 57(13): 3159-3169.
Gao, X., Thiemens, M.H., 1993b. Variations of the isotopic composition of sulfur in enstatite and ordinary chondrites. Geochimica et Cosmochimica Acta, 57(13): 3171-3176.
Garcia-Castellanos, D. et al., 2009. Catastrophic flood of the Mediterranean after the Messinian salinity crisis. Nature, 462(7274): 778-781.
Gargano, A., Sharp, Z., 2019. The chlorine isotope composition of iron meteorites: Evidence for the Cl isotope composition of the solar nebula and implications for extensive devolatilization during planet formation. Meteoritics & Planetary Science, 54(7): 1619-1631.
Gargano, A. et al., 2020. The Cl isotope composition and halogen contents of Apollo-return samples. Proceedings of the National Academy of Sciences, 117(38): 23418-23425.
Gargano, A.M. et al., 2021. The Zn, S, and Cl isotope compositions of mare basalts: implications for the effects of eruption style and pressure on volatile element stable isotope fractionation on the Moon. American Mineralogist: Journal of Earth and Planetary Materials.
Garrison, D., Hamlin, S., Bogard, D., 2000. Chlorine abundances in meteorites. Meteoritics & Planetary Science, 35(2): 419-429.
Gauthier, P.J., Sigmarsson, O., Gouhier, M., Haddadi, B., Moune, S., 2016. Elevated gas flux and trace metal degassing from the 2014–2015 fissure eruption at the Bárðarbunga volcanic system, Iceland. Journal of Geophysical Research: Solid Earth, 121(3): 1610-1630.
Ghosh, A., McSween Jr, H.Y., 1998. A thermal model for the differentiation of asteroid 4 Vesta, based on radiogenic heating. Icarus, 134(2): 187-206.
Ghosh, A., Weidenschilling, S., McSween Jr, H., Rubin, A., 2006. Asteroidal heating and thermal stratification of the asteroid belt. Meteorites and the early solar system II: 555-566.
Godon, A. et al., 2004. A cross-calibration of chlorine isotopic measurements and suitability of seawater as the international reference material. Chemical Geology, 207(1-2): 1-12.

Goldsmith, S.L., 2007. Tracing the Evolution of the Iodine Biogeochemical Cycle. The University of Manchester (United Kingdom).
Goldstein, J., Scott, E., Chabot, N., 2009. Iron meteorites: Crystallization, thermal history, parent bodies, and origin. Chemie der Erde-Geochemistry, 69(4): 293-325.
Goles, G.G., Greenland, L.P., Jérome, D.Y., 1967. Abundances of chlorine, bromine and iodine in meteorites. Geochimica et Cosmochimica Acta, 31(10): 1771-1787.
Goresy, A.E., Yabuki, H., Ehlers, K., Woolum, D., Pernicka, E., 1988. Qingzhen and Yamato-691: A tentative alphabet for the EH chondrites.
Grady, M.M., Wright, I.P., 2003. Elemental and isotopic abundances of carbon and nitrogen in meteorites. Space Science Reviews, 106(1): 231-248.
Grady, M.M., Wright, I.P., Carr, L.P., Pillinger, C.T., 1986. COMPOSITIONAL DIFFERENCES IN ENSTATITE CHONDRITES BASED ON CARBON AND NITROGEN STABLE ISOTOPE MEASUREMENTS. Geochimica Et Cosmochimica Acta, 50(12): 2799-2813.
Grady, M.M., Wright, I.P., Fallick, A.E., Pillinger, C.T., 1983. The stable isotopic composition of carbon, nitrogen and hydrogen in some Yamato meteorites. Nagata, T. Proceedings/8th symposium on Antarctic meteorites. Memoirs of National Institute of Polar Research. Special Issue, 30: 292-305.
Green, D., Ringwood, A., Hibberson, W., Ware, N., 1975. Experimental petrology of Apollo 17 mare basalts, Lunar and Planetary Science Conference Proceedings, pp. 871-893.
Greenland, L., Lovering, J.F., 1965. MINOR AND TRACE ELEMENT ABUNDANCES IN CHONDRITIC METEORITES. Geochimica Et Cosmochimica Acta, 29(8): 821-+.
Grimm, R.E., McSween Jr, H.Y., 1989. Water and the thermal evolution of carbonaceous chondrite parent bodies. Icarus, 82(2): 244-280.
Grossman, J.N., ALEXANDER, C.M.O.D., Wang, J., Brearley, A.J., 2000. Bleached chondrules: Evidence for widespread aqueous processes on the parent asteroids of ordinary chondrites. Meteoritics & Planetary Science, 35(3): 467-486.
Grossman, J.N., Alexanders, C.M.O.D., Wang, J., Brearley, A.J., 2002. Zoned chondrules in Semarkona: Evidence for high-and low-temperature processing. Meteoritics & Planetary Science, 37(1): 49-73.
Grossman, J.N., Brearley, A.J., 2005. The onset of metamorphism in ordinary and carbonaceous chondrites. Meteoritics & Planetary Science, 40(1): 87-122.
Grossman, L., Beckett, J.R., Fedkin, A.V., Simon, S.B., Ciesla, F.J., 2008. Redox conditions in the solar nebula: Observational, experimental, and theoretical constraints. Reviews in Mineralogy and Geochemistry, 68(1): 93-140.
Guidi, L. et al., 2016. Plankton networks driving carbon export in the oligotrophic ocean. Nature, 532(7600): 465-470.
Guo, M., Korenaga, J., 2021. A halogen budget of the bulk silicate Earth points to a history of early halogen degassing followed by net regassing. Proceedings of the National Academy of Sciences, 118(51).
Haack, H., McCoy, T.J., 2003. Iron and stony-iron meteorites. Treatise on geochemistry, 1: 711.
Halliday, A.N., Kleine, T., 2006. Meteorites and the timing, mechanisms, and conditions of terrestrial planet accretion and early differentiation. Meteorites and the early solar system II: 775-801.

Halverson, G.P., Kunzmann, M., Strauss, J.V., Maloof, A.C., 2018. The Tonian-Cryogenian transition in Northeastern Svalbard. Precambrian Research, 319: 79-95.
Hardie, L.A., 1996. Secular variation in seawater chemistry: An explanation for the coupled secular variation in the mineralogies of marine limestones and potash evaporites over the past 600 my. Geology, 24(3): 279-283.
Hardisty, D.S. et al., 2014. An iodine record of Paleoproterozoic surface ocean oxygenation. Geology, 42(7): 619-622.
Harris, R., 1994. Zooplankton grazing on the coccolithophore Emiliania huxleyi and its role in inorganic carbon flux. Marine Biology, 119(3): 431-439.
Hashizume, K., Sugiura, N., 1995. Nitrogen isotopes in bulk ordinary chondrites. Geochimica et cosmochimica acta, 59(19): 4057-4069.
Hauri, E.H., Saal, A.E., Rutherford, M.J., Van Orman, J.A., 2015. Water in the Moon's interior: Truth and consequences. Earth and Planetary Science Letters, 409: 252-264.
Hauri, E.H., Weinreich, T., Saal, A.E., Rutherford, M.C., Van Orman, J.A., 2011. High pre-eruptive water contents preserved in lunar melt inclusions. Science, 333(6039): 213-215.
Hay, W.W. et al., 2006. Evaporites and the salinity of the ocean during the Phanerozoic: Implications for climate, ocean circulation and life. Palaeogeography, Palaeoclimatology, Palaeoecology, 240(1-2): 3-46.
Hay, W.W., Wold, C.N., Söding, E., Floegel, S., 2001. Evolution of sediment fluxes and ocean salinity, Geologic modeling and simulation. Springer, pp. 153-167.
Head, J.W., Wilson, L., 2017. Generation, ascent and eruption of magma on the Moon: New insights into source depths, magma supply, intrusions and effusive/explosive eruptions (Part 2: Predicted emplacement processes and observations). Icarus, 283: 176-223.
Hellmann, J.L. et al., 2021. Tellurium isotope cosmochemistry: Implications for volatile fractionation in chondrite parent bodies and origin of the late veneer. Geochimica et Cosmochimica Acta, 309: 313-328.
Hellmann, J.L., Kruijer, T.S., Van Orman, J.A., Metzler, K., Kleine, T., 2019. Hf-W chronology of ordinary chondrites. Geochimica et Cosmochimica Acta, 258: 290-309.
Herzog, G., Moynier, F., Albarède, F., Berezhnoy, A., 2009. Isotopic and elemental abundances of copper and zinc in lunar samples, Zagami, Pele's hairs, and a terrestrial basalt. Geochimica et Cosmochimica Acta, 73(19): 5884-5904.
Hess, P.C., Parmentier, E., 1995. A model for the thermal and chemical evolution of the Moon's interior: Implications for the onset of mare volcanism. Earth and Planetary Science Letters, 134(3-4): 501-514.
Heumann, K., Gall, M., Weiss, H., 1987. Geochemical investigations to explain iodine-overabundances in Antarctic meteorites. Geochimica et Cosmochimica Acta, 51(9): 2541-2547.
Heumann, K., Neubauer, J., Reifenhäuser, W., 1990. Iodine overabundances measured in the surface layers of an Antarctic stony and iron meteorite. Geochimica et Cosmochimica Acta, 54(9): 2503-2506.
Hiesinger, H., Head, J., Wolf, U., Jaumann, R., Neukum, G., 2011. Ages and stratigraphy of lunar mare basalts: A synthesis. Recent advances and current research issues in lunar stratigraphy, 477: 1-51.

Higuchi, H., Ganapathy, R., Morgan, J.W., Anders, E., 1977. “Mysterite”: a late condensate from the solar nebula. Geochimica et Cosmochimica Acta, 41(7): 843-852.
Hippler, D., Buhl, D., Witbaard, R., Richter, D.K., Immenhauser, A., 2009. Towards a better understanding of magnesium-isotope ratios from marine skeletal carbonates. Geochimica et Cosmochimica Acta, 73(20): 6134-6146.
Hirschmann, M.M., Bergin, E.A., Blake, G.A., Ciesla, F.J., Li, J., 2021. Early volatile depletion on planetesimals inferred from C–S systematics of iron meteorite parent bodies. Proceedings of the National Academy of Sciences, 118(13).
Holland, H., 2003. The geologic history of seawater. Treatise on Geochemistry, 6: 625.
Holland, H.D., 2005. Sea level, sediments and the composition of seawater. American Journal of Science, 305(3): 220-239.
Holligan, P.M. et al., 1993. A biogeochemical study of the coccolithophore, Emiliania huxleyi, in the North Atlantic. Global biogeochemical cycles, 7(4): 879-900.
Hopp, J. et al., 2021. 53Mn-53Cr systematics of sphalerite in enstatite chondrites. Geochimica et cosmochimica acta, 310: 79-94.
Hopp, J., Trieloff, M., Ott, U., 2016. I–Xe ages of enstatite chondrites. Geochimica et Cosmochimica Acta, 174: 196-210.
Housley, R., 1979. A model for chemical and isotopic fractionation in the lunar regolith by impact vaporization, Lunar and Planetary Science Conference Proceedings, pp. 1673-1683.
Housley, R., Cirlin, E., Paton, N., Goldberg, I., 1974. Solar wind and micrometeorite alteration of the lunar regolith, Lunar and Planetary Science Conference Proceedings, pp. 2623-2642.
Hunter, R.H., Taylor, L.A., 1982. Rust and schreibersite in Apollo 16 highland rocks: manifestations of volatile-element mobility. Lunar and Planetary Science Conference Proceedings, 12: 253-259.
Huppert, A., Blasius, B., Stone, L., 2002. A model of phytoplankton blooms. The American Naturalist, 159(2): 156-171.
Huss, G.R., Rubin, A.E., Grossman, J.N., 2006. Thermal metamorphism in chondrites. Meteorites and the early solar system II, 943: 567-586.
Hutchison, R., ALEXANDER, C.M.D., Bridges, J.C., 1998. Elemental redistribution in Tieschitz and the origin of white matrix. Meteoritics & Planetary Science, 33(5): 1169-1179.
Irwin, A.J., Finkel, Z.V., Schofield, O.M., Falkowski, P.G., 2006. Scaling-up from nutrient physiology to the size-structure of phytoplankton communities. Journal of plankton research, 28(5): 459-471.
Isupov, M.N. et al., 2000. Crystal structure of dodecameric vanadium-dependent bromoperoxidase from the red algae Corallina officinalis. Journal of molecular biology, 299(4): 1035-1049.
Jambon, A., Déruelle, B., Dreibus, G., Pineau, F., 1995. Chlorine and bromine abundance in MORB: the contrasting behaviour of the Mid-Atlantic Ridge and East Pacific Rise and implications for chlorine geodynamic cycle. Chemical Geology, 126(2): 101-117.
Javoy, M. et al., 2010. The chemical composition of the Earth: Enstatite chondrite models. Earth and Planetary Science Letters, 293(3-4): 259-268.
Johnston, D. et al., 2012. Late Ediacaran redox stability and metazoan evolution. Earth and Planetary Science Letters, 335: 25-35.

Jolliff, B.L., Wieczorek, M.A., Shearer, C.K., Neal, C.R., 2018. New views of the Moon, 60. Walter de Gruyter GmbH & Co KG.
Jones, R.H. et al., 2014. Phosphate minerals in LL chondrites: A record of the action of fluids during metamorphism on ordinary chondrite parent bodies. Geochimica et Cosmochimica Acta, 132: 120-140.
Kallemeyn, G.W., Wasson, J.T., 1981. The compositional classification of chondrites; I, The carbonaceous chondrite groups. Geochimica et Cosmochimica Acta, 45(7): 1217-1230.
Kallemeyn, G.W., Wasson, J.T., 1986. Compositions of enstatite (EH3, EH4, 5 and EL6) chondrites: Implications regarding their formation. Geochimica et Cosmochimica Acta, 50(10): 2153-2164.
Kato, C., Moynier, F., 2017. Gallium isotopic evidence for extensive volatile loss from the Moon during its formation. Science advances, 3(7): e1700571.
Kato, C., Moynier, F., Valdes, M.C., Dhaliwal, J.K., Day, J.M., 2015. Extensive volatile loss during formation and differentiation of the Moon. Nature communications, 6: 7617.
Kato, F., Ozaki, H., Ebihara, M., 2000. Distribution of halogens in an Antarctic ordinary chondrite, Y-74014 (H6). Antarctic Meteorite Research, 13: 121.
Kaufmann, R., Long, A., Bentley, H., Davis, S., 1984. Natural chlorine isotope variations. Nature, 309: 338-340.
Keil, K., 1968. Mineralogical and chemical relationships among enstatite chondrites. Journal of Geophysical Research, 73(22): 6945-6976.
Keil, K., 2010. Enstatite achondrite meteorites (aubrites) and the histories of their asteroidal parent bodies. Geochemistry, 70(4): 295-317.
Keil, K., Haack, H., Scott, E., 1994. Catastrophic fragmentation of asteroids: Evidence from meteorites. Planetary and Space Science, 42(12): 1109-1122.
Kelly, W.R., Larimer, J.W., 1977. Chemical fractionations in meteorites—VIII. Iron meteorites and the cosmochemical history of the metal phase. Geochimica et Cosmochimica Acta, 41(1): 93-111.
Kendrick, M.A., D'Andres, J., Holden, P., Ireland, T., 2018. Halogens (F, Cl, Br, I) in thirteen USGS, GSJ and NIST international rock and glass reference materials. Geostandards and Geoanalytical Research, 42(4): 499-511.
Kendrick, M.A., Kamenetsky, V.S., Phillips, D., Honda, M., 2012. Halogen systematics (Cl, Br, I) in mid-ocean ridge basalts: a Macquarie Island case study. Geochimica et Cosmochimica Acta, 81: 82-93.
Kesson, S., 1975. Mare basalt petrogenesis, Origins of Mare Basalts and their Implications for Lunar Evolution, pp. 81.
Kimura, M. et al., 2005. Thermal history of the enstatite chondrites from silica polymorphs. Meteoritics & Planetary Science, 40(6): 855-868.
Kitano, Y., Okumura, M., 1973. Coprecipitation of fluoride with calcium carbonate. Geochemical Journal, 7(1): 37-49.
Kitano, Y., Okumura, M., Idogaki, M., 1975. Incorporation of sodium, chloride and sulfate with calcium carbonate. Geochemical Journal, 9(2): 75-84.
Kleine, T., Matthes, M., Nimmo, F., Leya, I., 2018. Silver Isotopic Evidence for Impact-Driven Volatile Loss from Differentiated Asteroids, Lunar and Planetary Science Conference.

Kleine, T., Mezger, K., Palme, H., Scherer, E., Münker, C., 2005. Early core formation in asteroids and late accretion of chondrite parent bodies: Evidence from 182 Hf-182 W in CAIs, metal-rich chondrites, and iron meteorites. Geochimica et Cosmochimica Acta, 69(24): 5805-5818.
Kleine, T. et al., 2009. Hf–W chronology of the accretion and early evolution of asteroids and terrestrial planets. Geochimica et Cosmochimica Acta, 73(17): 5150-5188.
Knauth, L.P., 1994. Petrogenesis of chert. Reviews in Mineralogy and Geochemistry, 29(1): 233-258.
Knauth, L.P., 1998. Salinity history of the Earth's early ocean. Nature, 395(6702): 554.
Knauth, L.P., 2005. Temperature and salinity history of the Precambrian ocean: implications for the course of microbial evolution, Geobiology: Objectives, concepts, perspectives. Elsevier, pp. 53-69.
Knauth, L.P., Epstein, S., 1976. Hydrogen and oxygen isotope ratios in nodular and bedded cherts. Geochimica et Cosmochimica Acta., 40: 1095-1108.
Knauth, L.P., Lowe, D.R., 1978. Oxygen isotope geochemistry of cherts from the Onverwacht Group (3.4 billion years), Transvaal, South Africa, with implications for secular variations in the isotopic composition of cherts. Earth and Planetary Science Letters, 41: 209-222.
Knauth, L.P., Lowe, D.R., 2003. High Archean climatic temperature inferred from oxygen isotope geochemistry of cherts in the 3.5 Ga Swaziland Supergroup, South Africa. Geological Society of America Bulletin, 115(5): 566-580.
Knoll, A.H., 2014. Paleobiological perspectives on early eukaryotic evolution. Cold Spring Harbor Perspectives in Biology, 6(1): a016121.
Koefoed, P. et al., 2020. Potassium isotope systematics of the LL4 chondrite Hamlet: Implications for chondrule formation and alteration. Meteoritics & Planetary Science, 55(8).
Korenaga, J., 2018. Crustal evolution and mantle dynamics through Earth history. Philosophical Transactions of the Royal Society A: Mathematical, Physical and Engineering Sciences, 376(2132): 20170408.
Krot, A., Keil, K., Scott, E., Goodrich, C., Weisberg, M., 2014. Classification of meteorites and their genetic relationships. Meteorites and cosmochemical processes: 1-63.
Kruijer, T.S., Burkhardt, C., Budde, G., Kleine, T., 2017. Age of Jupiter inferred from the distinct genetics and formation times of meteorites. Proceedings of the National Academy of Sciences, 114(26): 6712-6716.
Kruijer, T.S., Kleine, T., Borg, L.E., 2020. The great isotopic dichotomy of the early Solar System. Nature Astronomy, 4(1): 32-40.
Kuhlisch, C. et al., 2021. Viral infection of algal blooms leaves a unique metabolic footprint on the dissolved organic matter in the ocean. Science advances, 7(25): eabf4680.
Küpper, F.C. et al., 2008. Iodide accumulation provides kelp with an inorganic antioxidant impacting atmospheric chemistry. Proceedings of the National Academy of Sciences, 105(19): 6954-6958.
Küpper, F.C., Carrano, C.J., 2019. Key aspects of the iodine metabolism in brown algae: a brief critical review. Metallomics, 11(4): 756-764.
Kuwahara, H. et al., 2017. High Pressure Experiments on Metal-Silicate Partitioning of Chlorine in A Magma Ocean: Implications for Terrestrial Chlorine Depletion. Geochemistry, Geophysics, Geosystems.

Labidi, J., Cartigny, P., 2016. Negligible sulfur isotope fractionation during partial melting: Evidence from Garrett transform fault basalts, implications for the late-veneer and the hadean matte. Earth and Planetary Science Letters, 451: 196-207.
Labidi, J., Cartigny, P., Moreira, M., 2013. Non-chondritic sulphur isotope composition of the terrestrial mantle. Nature, 501(7466): 208-211.
Labidi, J., Farquhar, J., Alexander, C.O.D., Eldridge, D., Oduro, H., 2017. Mass independent sulfur isotope signatures in CMs: Implications for sulfur chemistry in the early solar system. Geochimica et Cosmochimica Acta, 196: 326-350.
Langenauer, M., Krähenbühl, U., 1993a. Depth-profiles and surface enrichment of the halogens in four Antarctic H5 chondrites and in two non-Antarctic chondrites. Meteoritics, 28(1): 98-104.
Langenauer, M., Krähenbühl, U., 1993b. Halogen contamination in Antarctic H5 and H6 chondrites and relation to sites of recovery. Earth and Planetary Science Letters, 120(3-4): 431-442.
Laul, J., Ganapathy, R., Anders, E., Morgan, J.W., 1973. Chemical fractionations in meteorites—VI. Accretion temperatures of H-, LL-and E-chondrites, from abundance of volatile trace elements. Geochimica et Cosmochimica Acta, 37(2): 329-357.
Lee, M.R., Bland, P.A., 2004. Mechanisms of weathering of meteorites recovered from hot and cold deserts and the formation of phyllosilicates. Geochimica et Cosmochimica Acta, 68(4): 893-916.
Leri, A.C. et al., 2010. Natural organobromine in marine sediments: new evidence of biogeochemical Br cycling. Global Biogeochemical Cycles, 24(4).
Leri, A.C., Mayer, L.M., Thornton, K.R., Ravel, B., 2014. Bromination of marine particulate organic matter through oxidative mechanisms. Geochimica et Cosmochimica Acta, 142: 53-63.
Lewis, J.A., Jones, R.H., 2016. Phosphate and feldspar mineralogy of equilibrated L chondrites: The record of metasomatism during metamorphism in ordinary chondrite parent bodies. Meteoritics & Planetary Science, 51(10): 1886-1913.
Lewis, J.A., Jones, R.H., 2019. Primary feldspar in the Semarkona LL 3.00 chondrite: Constraints on chondrule formation and secondary alteration. Meteoritics & Planetary Science, 54(1): 72-89.
Lewis, J.A., Jones, R.H., Brearley, A.J., 2022. Plagioclase alteration and equilibration in ordinary chondrites: Metasomatism during thermal metamorphism. Geochimica et Cosmochimica Acta, 316: 201-229.
Libourel, G., 2021. Extraterrestrial Glasses. Encyclopedia of Glass Science, Technology, History, and Culture, 2: 801-813.
Lin, Y., El Goresy, A., 2002. A comparative study of opaque phases in Qingzhen (EH3) and MacAlpine Hills 88136 (EL3): Representatives of EH and EL parent bodies. Meteoritics & Planetary Science, 37(4): 577-599.
Lin, Y. et al., 2011. Earliest solid condensates consisting of the assemblage oldhamite, sinoite, graphite and excess 36S in lawrencite from Almahata Sitta MS-17 EL3 chondrite, Workshop on Formation of the First Solids in the solar system, Abstract.
Lin, Y., Goresy, A.E., 2002. A comparative study of opaque phases in Qingzhen (EH3) and MacAlpine Hills 88136 (EL3): Representatives of EH and EL parent bodies. Meteoritics & Planetary Science, 37(4): 577-599.

Lin, Y., Kimura, M., 1998. Petrographic and mineralogical study of new EH melt rocks and a new enstatite chondrite grouplet. Meteoritics & Planetary Science, 33(3): 501-511.
Liss, P., Herring, J., Goldberg, E., 1973. The Iodide/Iodàte System in Seawater as a Possible Measure of Redox Potential. Nature Physical Science, 242(120): 108.
Lock, S.J., Bermingham, K.R., Parai, R., Boyet, M., 2020. Geochemical constraints on the origin of the Moon and preservation of ancient terrestrial heterogeneities. Space Science Reviews, 216(6): 1-46.
Lock, S.J. et al., 2018. The origin of the Moon within a terrestrial synestia. Journal of Geophysical Research: Planets, 123(4): 910-951.
Lodders, K., 2003. Solar system abundances and condensation temperatures of the elements. Astrophysical Journal, 591: 1220-1247.
Lodders, K., Fegley, B., Jr., 1998. The Planetary Scientist's Companion. Oxford Univeristy Press, Oxford, 371 pp.
Longhi, J., 1992. Experimental petrology and petrogenesis of mare volcanics. Geochimica et Cosmochimica Acta, 56(6): 2235-2251.
Longhi, J., Walker, D., Hays, J.F., 1972. Petrography and crystallization history of basalts 14310 and 14072, Lunar and Planetary Science Conference Proceedings, pp. 131.
Lowenstein, T.K., Timofeeff, M.N., Brennan, S.T., Hardie, L.A., Demicco, R.V., 2001. Oscillations in Phanerozoic seawater chemistry: Evidence from fluid inclusions. Science, 294(5544): 1086-1088.
Lu, Z., Jenkyns, H.C., Rickaby, E.M., 2010. Iodine to calcium ratios in marine carbonate as a paleo-redox proxy during oceanic anoxic events. Geology, 38: 1107–1110.
Lucas, M.P. et al., 2020. Evidence for early fragmentation-reassembly of ordinary chondrite (H, L, and LL) parent bodies from REE-in-two-pyroxene thermometry. Geochimica et Cosmochimica Acta, 290: 366-390.
Ludewig, H. et al., 2020. Halogenases: structures and functions. Current Opinion in Structural Biology, 65: 51-60.
Ma, C., Liu, Y., 2019. Discovery of a zinc-rich mineral on the surface of lunar orange pyroclastic beads. American Mineralogist: Journal of Earth and Planetary Materials, 104(3): 447-452.
Maliva, R.G., Knoll, A.H., Simonson, B.M., 2005. Secular change in the Precambrian silica cycle: insights from chert petrology. Geological Society of America Bulletin, 117(7-8): 835-845.
Marin-Carbonne, J., Chaussidon, M., Robert, F., 2012. Micrometer-scale chemical and isotopic criteria (O and Si) on the origin and history of Precambrian cherts: implications for paleo-temperature reconstructions. Geochimica et Cosmochimica Acta, 92: 129-147.
Marini, L., Moretti, R., Accornero, M., 2011. Sulfur isotopes in magmatic-hydrothermal systems, melts, and magmas. Reviews in Mineralogy and Geochemistry, 73(1): 423-492.
Markowski, A., Quitté, G., Halliday, A.N., Kleine, T., 2006. Tungsten isotopic compositions of iron meteorites: Chronological constraints vs. cosmogenic effects. Earth and Planetary Science Letters, 242(1–2): 1-15.
Marks, N.E., Borg, L.E., Shearer, C.K., Cassata, W.S., 2019. Geochronology of an Apollo 16 clast provides evidence for a basin-forming impact 4.3 billion years ago. Journal of Geophysical Research: Planets, 124: 2465-2481.

Marrocchi, Y., Delbo, M., Gounelle, M., 2021. The astrophysical context of collision processes in meteorites. Wiley Online Library.
Marshall, R.R., Keil, K., 1965. Polymineralic inclusions in the Odessa iron meteorite. Icarus, 4(5-6): 461-479.
Marty, B., Avice, G., Bekaert, D.V., Broadley, M.W., 2018. Salinity of the Archaean oceans from analysis of fluid inclusions in quartz. Comptes Rendus Geoscience, 350(4): 154-163.
Mason, B., 1962. Meteorites. John Wiley & Sons, Inc. New York, New York.: 274.
Maurel, C. et al., 2020. Meteorite evidence for partial differentiation and protracted accretion of planetesimals. Science advances, 6(30): eaba1303.
McCaffrey, M., Lazar, B., Holland, H., 1987. The evaporation path of seawater and the coprecipitation of Br (super-) and K (super+) with halite. Journal of Sedimentary Research, 57(5): 928-937.
McCall, A.S. et al., 2014. Bromine is an essential trace element for assembly of collagen IV scaffolds in tissue development and architecture. Cell, 157(6): 1380-1392.
McCoy, T.J., Mittlefehldt, D.W., Wilson, L., 2006. Asteroid differentiation. Meteorites and the early solar system II.
McCoy, T.J., Scott, E.R., Jones, R.H., Keil, K., Taylor, G.J., 1991. Composition of chondrule silicates in LL3-5 chondrites and implications for their nebular history and parent body metamorphism. Geochimica et Cosmochimica Acta, 55(2): 601-619.
McCubbin, F., Barnes, J., 2020a. Chlorine-Isotopic Analysis of Apatite in an Olivine-Hosted Melt Inclusion in Magnesian-Suite Troctolite 76535: Further Evidence of a KREEP-Rich Parental Magma? LPI(2326): 2415.
McCubbin, F.M., Barnes, J.J., 2020b. The chlorine-isotopic composition of lunar KREEP from magnesian-suite troctolite 76535. American Mineralogist: Journal of Earth and Planetary Materials, 105(8): 1270-1274.
McCubbin, F.M. et al., 2015. Magmatic volatiles (H, C, N, F, S, Cl) in the lunar mantle, crust, and regolith: Abundances, distributions, processes, and reservoirs. American Mineralogist, 100(8-9): 1668-1707.
McKay, D.S., Wentworth, S.J., 1993. Grain surface features of Apollo 17 orange and black glasses. Lunar and Planetary Science Conference, 24: 961-962.
Mercer, J.A., Jones, R.H., 2010. Origin of chlorine in the mesostasis of Qingzhen (EH3) chondrules. Annual Meteoritical Society Meeting, 73: 5268.pdf.
Mercer, J.A., Sharp, Z.D., Jones, R.H., 2011. The chlorine isotope composition of chondrites. Lunar and Planetary Science Conference, 42: 2463.pdf.
Midgley, S., Fleitmann, D., Grau-Crespo, R., 2021. Bromate incorporation in calcite and aragonite.
Moore, C.H., 1989. Carbonate diagenesis and porosity. Elsevier.
Moore, W.B., Simon, J.I., Webb, A.A.G., 2017. Heat-pipe planets. Earth and Planetary Science Letters, 474: 13-19.
Morbidelli, A., Lunine, J.I., O'Brien, D.P., Raymond, S.N., Walsh, K.J., 2012. Building terrestrial planets. Annual Review of Earth and Planetary Sciences, 40: 251-275.
Morgan, J., Walker, R., Brandon, A., Horan, M., 2001. Siderophile elements in Earth's upper mantle and lunar breccias: data synthesis suggests manifestations of the same late influx. Meteoritics & Planetary Science, 36(9): 1257-1275.

Moynier, F., Albarède, F., Herzog, G., 2006. Isotopic composition of zinc, copper, and iron in lunar samples. Geochimica et Cosmochimica Acta, 70(24): 6103-6117.
Moynier, F. et al., 2010. Volatilization induced by impacts recorded in Zn isotope composition of ureilites. Chemical Geology, 276(3-4): 374-379.
Moynier, F., Blichert-Toft, J., Telouk, P., Luck, J.-M., Albarède, F., 2007a. Comparative stable isotope geochemistry of Ni, Cu, Zn, and Fe in chondrites and iron meteorites. Geochimica et Cosmochimica Acta, 71: 4365-4379.
Moynier, F., Blichert-Toft, J., Telouk, P., Luck, J.-M., Albarède, F., 2007b. Comparative stable isotope geochemistry of Ni, Cu, Zn, and Fe in chondrites and iron meteorites. Geochimica et Cosmochimica Acta, 71(17): 4365-4379.
Muenow, D.W., Keil, K., Wilson, L., 1992. HIGH-TEMPERATURE MASS-SPECTROMETRIC DEGASSING OF ENSTATITE CHONDRITES - IMPLICATIONS FOR PYROCLASTIC VOLCANISM ON THE AUBRITE PARENT BODY. Geochimica Et Cosmochimica Acta, 56(12): 4267-4280.
Murphy, C.D., Moore, R.M., White, R.L., 2000. Peroxidases from marine microalgae. Journal of Applied Phycology, 12(3): 507-513.
Mysen, B., 2019. Nitrogen in the Earth: abundance and transport. Progress in Earth and Planetary Science, 6(1): 1-15.
Neal, C.R., Taylor, L.A., 1992. Petrogenesis of mare basalts: A record of lunar volcanism. Geochimica et Cosmochimica Acta, 56(6): 2177-2211.
Newcombe, M. et al., 2019. Effects of pH2O, pH2 and fO2 on the diffusion of H-bearing species in lunar basaltic liquid and an iron-free basaltic analog at 1 atm. Geochimica et Cosmochimica Acta, 259: 316-343.
Newcombe, M. et al., 2017. Solubility of water in lunar basalt at low pH2O. Geochimica et Cosmochimica Acta, 200: 330-352.
Ni, P., Zhang, Y., Chen, S., Gagnon, J., 2019. A melt inclusion study on volatile abundances in the lunar mantle. Geochimica et Cosmochimica Acta, 249: 17-41.
Nie, N.X. et al., 2021. Imprint of chondrule formation on the K and Rb isotopic compositions of carbonaceous meteorites. Science advances, 7(49): eabl3929.
Nie, N.X., Dauphas, N., 2019. Vapor drainage in the protolunar disk as the cause for the depletion in volatile elements of the Moon. The Astrophysical Journal Letters, 884(2): L48.
Noble, D.C., Smith, V.C., Peck, L.C., 1967. Loss of halogens from crystallized and glassy silicic volcanic rocks. Geochimica et Cosmochimica Acta, 31(2): 215-223.
Noll, K. et al., 2003. Detection of terrestrial fluorine by proton induced gamma emission (PIGE): A rapid quantification for Antarctic meteorites. Meteoritics & Planetary Science, 38(5): 759-765.
O'D, C.M., Grossman, J.N., 2005. Alkali elemental and potassium isotopic compositions of Semarkona chondrules. Meteoritics & Planetary Science, 40(4): 541-556.
Okumura, M., Kitano, Y., Idogaki, M., 1983. Incorporation of fluoride ions into calcite—Effect of organic materials and magnesium ions in a parent solution. Geochemical Journal, 17(5): 257-263.
Okumura, M., Kitano, Y., Idogaki, M., 1986. Behavior of bromide ions during the formation of calcium carbonate. Marine Chemistry, 19(2): 109-120.
Olsen, E., 1981. Vugs in ordinary chondrites. Meteoritics, 16(1): 45-59.

Olsen, E., Huebner, J.S., Douglas, J., Plant, A., 1973. Meteoritic amphiboles. American Mineralogist: Journal of Earth and Planetary Materials, 58(9-10): 869-872.
Palme, H., Zipfel, J., 2021. The composition of CI chondrites and their contents of chlorine and bromine: Results from instrumental neutron activation analysis. Meteoritics & Planetary Science.
Paniello, R.C., Day, J.M., Moynier, F., 2012. Zinc isotopic evidence for the origin of the Moon. Nature, 490(7420): 376.
Paul Knauth, L., 1992. Origin and diagenesis of cherts: an isotopic perspective, Isotopic signatures and sedimentary records. Springer, pp. 123-152.
Pavelka, S., 2004. Metabolism of bromide and its interference with the metabolism of iodine. Physiological research, 53: S81-90.
Piani, L., Marrocchi, Y., Libourel, G., Tissandier, L., 2016. Magmatic sulfides in the porphyritic chondrules of EH enstatite chondrites. Geochimica et Cosmochimica Acta, 195: 84-99.
Piani, L. et al., 2020. Earth's water may have been inherited from material similar to enstatite chondrite meteorites. Science, 369(6507): 1110-1113.
Planavsky, N.J. et al., 2010. The evolution of the marine phosphate reservoir. Nature, 467(7319): 1088-1090.
Podder, J. et al., 2017. Iodate in calcite and vaterite: Insights from synchrotron X-ray absorption spectroscopy and first-principles calculations. Geochimica et Cosmochimica Acta, 198: 218-228.
Pokrovski, G.S., Borisova, A.Y., Bychkov, A.Y., 2013. Speciation and transport of metals and metalloids in geological vapors. Reviews in Mineralogy and Geochemistry, 76(1): 165-218.
Poole, G.M., Rehkämper, M., Coles, B.J., Goldberg, T., Smith, C.L., 2017. Nucleosynthetic molybdenum isotope anomalies in iron meteorites–new evidence for thermal processing of solar nebula material. Earth and Planetary Science Letters, 473: 215-226.
Potts, N.J., Barnes, J.J., Tartèse, R., Franchi, I.A., Anand, M., 2018. Chlorine isotopic compositions of apatite in Apollo 14 rocks: Evidence for widespread vapor-phase metasomatism on the lunar nearside∼ 4 billion years ago. Geochimica et Cosmochimica Acta, 230: 46-59.
Potts, N.J., Bromiley, G.D., Brooker, R.A., 2021. An experimental investigation of F, Cl and H2O mineral-melt partitioning in a reduced, model lunar system. Geochimica et Cosmochimica Acta, 294: 232-254.
Potts, N.J. et al., 2016. Characterization of mesostasis regions in lunar basalts: Understanding late-stage melt evolution and its influence on apatite formation. Meteoritics & Planetary Science, 51(9): 1555-1575.
Pringle, E.A., Moynier, F., 2017. Rubidium isotopic composition of the Earth, meteorites, and the Moon: Evidence for the origin of volatile loss during planetary accretion. Earth and Planetary Science Letters, 473: 62-70.
Qin, L., Dauphas, N., Wadhwa, M., Masarik, J., Janney, P.E., 2008. Rapid accretion and differentiation of iron meteorite parent bodies inferred from 182Hf–182W chronometry and thermal modeling. Earth and Planetary Science Letters, 273(1–2): 94-104.

Rai, V.K., Jackson, T.L., Thiemens, M.H., 2005. Photochemical mass-independent sulfur isotopes in achondritic meteorites. Science, 309(5737): 1062-1065.
Rasmussen, K.L., Malvin, D.J., Buchwald, V.F., Wasson, J.T., 1984. Compositional trends and cooling rates of group IVB iron meteorites. Geochimica et Cosmochimica Acta, 48(4): 805-813.
Reed, G.W., Jovanovic, S., 1973. Fluorine in lunar samples: implications concerning lunar fluorapatite. Geochimica et Cosmochimica Acta, 37: 1457-1462.
Reed, G.W.J., Jovanovic, S., 1970. Halogens, mercury, lithium and osmium in Apollo 11 samples. Proceedings of the Apollo 11 Lunar Science Conference, 2: 1487-1492.
Rees, C., Thode, H., 1974. Sulfur concentrations and isotope ratios in Apollo 16 and 17 samples, Lunar and Planetary Science Conference Proceedings, pp. 1963-1973.
Renggli, C., King, P., Henley, R., Norman, M., 2017. Volcanic gas composition, metal dispersion and deposition during explosive volcanic eruptions on the Moon. Geochimica et Cosmochimica Acta, 206: 296-311.
Renggli, C.J., Klemme, S., 2020. Experimental constraints on metal transport in fumarolic gases. Journal of Volcanology and Geothermal Research, 400: 106929.
Renggli, C.J., Klemme, S., 2021. Experimental investigation of Apollo 16 “Rusty Rock” alteration by a lunar fumarolic gas. Journal of Geophysical Research: Planets, 126(2): e2020JE006609.
Richet, P., Bottinga, Y., Javoy, M., 1977. A review of hydrogen, carbon, nitrogen, oxygen, sulphur, and chlorine stable isotope fractionation among gaseous molecules. Annual Review of Earth and Planetary Science, 5: 65-110.
Roberge, M. et al., 2015. Is the transition zone a deep reservoir for fluorine? Earth and Planetary Science Letters, 429: 25-32.
Robinson, K.L. et al., 2016. Water in evolved lunar rocks: Evidence for multiple reservoirs. Geochimica et Cosmochimica Acta, 188: 244-260.
Rubey, W.W., 1951. Geologic history of seawater. Geological Society of America Bulletin, 62: 1111-1147.
Rubin, A.E., 1983. The Adhi Kot breccia and implications for the origin of chondrules and silica-rich clasts in enstatite chondrites. Earth and Planetary Science Letters, 64(2): 201-212.
Rubin, A.E., 1985. Impact melt products of chondritic material. Reviews of Geophysics, 23(3): 277-300.
Rubin, A.E., 2004. Postshock annealing and postannealing shock in equilibrated ordinary chondrites: Implications for the thermal and shock histories of chondritic asteroids. Geochimica et Cosmochimica Acta, 68(3): 673-689.
Rubin, A.E., 2018. Carbonaceous and noncarbonaceous iron meteorites: Differences in chemical, physical, and collective properties. Meteoritics & Planetary Science.
Rubin, A.E., Choi, B.-G., 2009. Origin of halogens and nitrogen in enstatite chondrites. Earth, Moon, and Planets, 105(1): 41-53.
Rubin, A.E., Scott, W.R., 1997. Abee and related EH chondrite impact-melt breccias. Geochimica et Cosmochimica Acta, 61(2): 425-435.
Rude, P.D., Aller, R.C., 1991. Fluorine mobility during early diagenesis of carbonate sediment: An indicator of mineral transformations. Geochimica et Cosmochimica Acta, 55(9): 2491-2509.

Russell, S., Lee, M., Arden, J., Pillinger, C., 1995. The isotopic composition and origins of silicon nitride from ordinary and enstatite chondrites. Meteoritics, 30(4): 399-404.
Rutherford, M.J., Head, J.W., Saal, A.E., Hauri, E., Wilson, L., 2017. Model for the origin, ascent, and eruption of lunar picritic magmas. American Mineralogist, 102(10): 2045-2053.
Ruzicka, A., Hugo, R., Hutson, M., 2015. Deformation and thermal histories of ordinary chondrites: Evidence for post-deformation annealing and syn-metamorphic shock. Geochimica et Cosmochimica Acta, 163: 219-233.
Saal, A.E., Hauri, E.H., 2021. Large sulfur isotope fractionation in lunar volcanic glasses reveals the magmatic differentiation and degassing of the Moon. Science Advances, 7(9): eabe4641.
Saal, A.E. et al., 2008. Volatile content of lunar volcanic glasses and the presence of water in the Moon's interior. Nature, 454(7201): 192-195.
Saal, A.E., Hauri, E.H., Van Orman, J.A., Rutherford, M.A., 2013. Hydrogen isotopes in lunar volcanic glasses and melt inclusions reveal a carbonaceous chondrite heritage. Science, 340: 1317-1320.
Saltzman, M., Thomas, E., Gradstein, F., 2012. Carbon isotope stratigraphy. The geologic time scale, 1: 207-232.
Sánchez-Román, M. et al., 2014. Microbial mediated formation of Fe-carbonate minerals under extreme acidic conditions. Scientific Reports, 4(1): 1-7.
Sarafian, A.R., John, T., Roszjar, J., Whitehouse, M.J., 2017. Chlorine and hydrogen degassing in Vesta's magma ocean. Earth and Planetary Science Letters, 459: 311-319.
Sato, M., 1976. Oxygen fugacity and other thermochemical parameters of Apollo 17 high-Ti basalts and their implications on the reduction mechanism, Lunar and planetary science conference proceedings, pp. 1323-1344.
Schauble, E.A., Rossman, G.R., Taylor, H.P., 2003. Theoretical estimates of equilibrium chlorine-isotope fractionations. Geochimica et Cosmochimica Acta, 67: 3267-3281.
Scheinberg, A., Fu, R., Elkins-Tanton, L., Weiss, B., 2015. Asteroid differentiation: Melting and large-scale structure. University of Arizona Press Tucson, AZ, pp. 533-552.
Schilling, J.-G., Unni, C., Bender, M., 1978. Origin of chlorine and bromine in the oceans. Nature, 273(5664): 631.
Schultz, L., 1986. Allende in Antarctia: Temperatures in Antarctic Meteorites. Meteoritics, 21: 505.
Scott, E.D., 1972. Chemical fractionation in iron meteorites and its interpretation. Geochimica et Cosmochimica Acta, 36(11): 1205-1236.
Scott, E.R., 1979. Origin of anomalous iron meteorites. Mineral. Mag, 43: 415-421.
Scott, E.R.D., Wasson, J.T., 1975. Classification and properties of iron meteorites. Reviews of Geophysics, 13(4): 527-546.
Selverstone, J., Sharp, Z.D., 2011. Chlorine isotope evidence for multicomponent mantle metasomatism in the Ivrea Zone Earth and Planetary Science Letters, 310: 429-440.
Sharp, Z. et al., 2013. The chlorine isotope composition of chondrites and Earth. Geochimica et Cosmochimica Acta, 107: 189-204.
Sharp, Z.D. et al., 2007. Chlorine isotope homogeneity of the mantle, crust and carbonaceous chondrites. Nature, 446: 1062-1065.

Sharp, Z.D., Draper, D.S., 2013. The chlorine abundance of Earth: Implications for a habitable planet. Earth and Planetary Science Letters, 369-370: 71-77.
Sharp, Z.D., Shearer, C.K., McKeegan, K.D., Barnes, J.D., Wang, Y.Q., 2010. The Chlorine Isotope Composition of the Moon and Implications for an Anhydrous Mantle. Science, 329(5995): 1050-1053.
Sharp, Z.D., Williams, J., Shearer, C.K., Agee, C.B., McKeegan, K.D., 2016. The chlorine isotope composition of Martian meteorites 2. Implications for the early solar system and the formation of Mars. Meteoritics and Planetary Sciences, doi: 10/1111/maps.12591: 16 pp.
Shearer, C., Papike, J., 1993. Basaltic magmatism on the Moon: A perspective from volcanic picritic glass beads. Geochimica et Cosmochimica Acta, 57(19): 4785-4812.
Shearer, C. et al., 2014. Chlorine distribution and its isotopic composition in "rusty rock" 66095. Implications for volatile element enrichments of "rusty rock" and lunar soils, origin of "rusty" alteration, and volatile element behavior on the Moon. Geochimica et Cosmochimica Acta, 139: 411-433.
Shearer, C.K., Elardo, S.M., Petro, N.E., Borg, L.E., McCubbin, F.M., 2015. Origin of the lunar highlands Mg-suite: An integrated petrology, geochemistry, chronology, and remote sensing perspective. American Mineralogist, 100(1): 294-325.
Shearer, C.K. et al., 2006. Thermal and Magmatic Evolution of the Moon. Reviews in Mineralogy and Geochemistry, 60: 365-518.
Shearer, C.K. et al., 2017. Distinct Chlorine Isotopic Reservoirs on Mars.: Implications for character, extent and relative timing of crustal interaction with mantle-derived magmas, evolution of the martian atmosphere, and the building blocks of an early Mars. Geochimica et Cosmochimica Acta.
Shearer, C.K., Papike, J.J., 2005. Early crustal building processes on the moon: Models for the petrogenesis of the magnesian suite. Geochimica et Cosmochimica Acta, 69(13): 3445-3461.
Shearer, C.K., Papike, J.J., Simon, S.B., Shimizu, N., 1989. An ion microprobe study of the intra-crystalline behavior of REE and selected trace elements in pyroxene from mare basalts with different cooling and crystallization histories. Geochimica et Cosmochimica Acta, 53: 1041-1054.
Sheffield, D., Harry, T., Smith, A., Rogers, L., 1992. Purification and characterization of the vanadium bromoperoxidase from the macroalga Corallina officinalis. Phytochemistry, 32(1): 21-26.
Shetty, P., Gitau, M.M., Maróti, G., 2019. Salinity stress responses and adaptation mechanisms in eukaryotic green microalgae. Cells, 8(12): 1657.
Sheyn, U., Rosenwasser, S., Ben-Dor, S., Porat, Z., Vardi, A., 2016. Modulation of host ROS metabolism is essential for viral infection of a bloom-forming coccolithophore in the ocean. The ISME journal, 10(7): 1742-1754.
Shimizu, K. et al., 2021. Highly volatile element (H, C, F, Cl, S) abundances and H isotopic compositions in chondrules from carbonaceous and ordinary chondrites. Geochimica et Cosmochimica Acta, 301: 230-258.
Shinonaga, T., Endo, K., Ebihara, M., Heumann, K., Nakahara, H., 1994. Weathering of Antarctic meteorites investigated from contents of Fe3+, chlorine, and iodine. Geochimica et Cosmochimica Acta, 58(17): 3735-3740.

Sigmarsson, O., Moune, S., Gauthier, P.-J., 2020. Fractional degassing of S, Cl and F from basalt magma in the Bárðarbunga rift zone, Iceland. Bulletin of Volcanology, 82(7): 1-8.
Snyder, G., Borg, L., Nyquist, L., Taylor, L., 2000. Chronology and isotopic constraints on lunar evolution. Origin of the Earth and Moon: 361-395.
Snyder, G.A., Taylor, L.A., Neal, C.R., 1992. A chemical model for generating the sources of mare basalts: Combined equilibrium and fractional crystallization of the lunar magmasphere. Geochimica et Cosmochimica Acta, 56(10): 3809-3823.
Sossi, P.A., Fegley Jr, B., 2018. Thermodynamics of element volatility and its application to planetary processes. Reviews in Mineralogy and Geochemistry, 84(1): 393-459.
Sossi, P.A., Nebel, O., O'Neill, H.S.C., Moynier, F., 2018. Zinc isotope composition of the Earth and its behaviour during planetary accretion. Chemical Geology, 477: 73-84.
Spitzer, F. et al., 2020. Isotopic evolution of the inner Solar System inferred from molybdenum isotopes in meteorites. The Astrophysical Journal Letters, 898(1): L2.
Steenstra, E. et al., 2018. Evidence for a sulfur-undersaturated lunar interior from the solubility of sulfur in lunar melts and sulfide-silicate partitioning of siderophile elements. Geochimica et Cosmochimica Acta, 231: 130-156.
Tandon, S., Wasson, J.T., 1968. Gallium, germanium, indium and iridium variations in a suite of L-group chondrites. Geochimica et Cosmochimica Acta, 32(10): 1087-1109.
Tang, H., Young, E., 2020. Evaporation from the Lunar Magma Ocean Was Not the Mechanism for Fractionation of the Moon's Moderately Volatile Elements. The Planetary Science Journal, 1(2): 49.
Taylor, L. et al., 2014. Metamorphism in the Chelyabinsk meteorite, Lunar and Planetary Science Conference, pp. 2346.
Temmam, M., Paquette, J., Vali, H., 2000. Mn and Zn incorporation into calcite as a function of chloride aqueous concentration. Geochimica et cosmochimica acta, 64(14): 2417-2430.
Treiman, A.H. et al., 2014. Phosphate-halogen metasomatism of lunar granulite 79215: Impact-induced fractionation of volatiles and incompatible elements. American Mineralogist, 99: 1860-1870.
Urey, H.C., 1947. The thermodynamic properties of isotopic substances. Journal of the Chemical Society (Resumed): 562-581.
Vallelonga, P. et al., 2021. Concentration and isotopic composition of bromine and chlorine in Antarctic sea ice. Geochimica et Cosmochimica Acta, 293: 18-27.
van Kan Parker, M., Mason, P.R., Van Westrenen, W., 2011. Trace element partitioning between ilmenite, armalcolite and anhydrous silicate melt: Implications for the formation of lunar high-Ti mare basalts. Geochimica et Cosmochimica Acta, 75(15): 4179-4193.
van Kooten, E.M., Moynier, F., Day, J.M., 2020. Evidence for transient atmospheres during eruptive outgassing on the Moon. The Planetary Science Journal, 1(3): 67.
Van Schmus, W., Wood, J.A., 1967. A chemical-petrologic classification for the chondritic meteorites. Geochimica et Cosmochimica Acta, 31(5): 747-765.
Venturi, S., Donati, F.M., Venturi, A., Venturi, M., 2000. Environmental iodine deficiency: A challenge to the evolution of terrestrial life? Thyroid, 10(8): 727-729.
Vernazza, P. et al., 2014. Multiple and fast: The accretion of ordinary chondrite parent bodies. The Astrophysical Journal, 791(2): 120.

Vincent, F. et al., 2021. Viral infection switches the balance between bacterial and eukaryotic recyclers of organic matter during algal blooms.
Vollstaedt, H., Mezger, K., Leya, I., 2020. The selenium isotope composition of lunar rocks: Implications for the formation of the Moon and its volatile loss. Earth and Planetary Science Letters, 542: 116289.
Voshage, H., Feldmann, H., 1979. Investigations on cosmic-ray-produced nuclides in iron meteorites, 3. Exposure ages, meteoroid sizes and sample depths determined by mass spectrometric analyses of potassium and rare gases. Earth and Planetary Science Letters, 45(2): 293-308.
Wadhwa, M. et al., 2007. From dust to planetesimals: implications for the solar protoplanetary disk from short-lived radionuclides. Protostars and planets V: 835-848.
Walker, D., Kirkpatrick, R., Longhi, J., Hays, J., 1976. Crystallization history of lunar picritic basalt sample 12002: Phase-equilibria and cooling-rate studies. Geological Society of America Bulletin, 87(5): 646-656.
Walker, D., Longhi, J., Hays, J.F., 1972. Experimental petrology and origin of Fra Mauro rocks and soil, Lunar and Planetary Science Conference Proceedings, pp. 797.
Walker, R.J., Horan, M.F., Shearer, C.K., Papike, J.J., 2004. Low abundances of highly siderophile elements in the lunar mantle: evidence for prolonged late accretion. Earth and Planetary Science Letters, 224(3–4): 399-413.
Wang, L., Hu, W., Wang, X., Cao, J., Yao, S., 2020. Halogens (Cl, Br, and I) geochemistry in Middle Triassic carbonates: Implications for salinity and diagenetic alteration of I/(Ca+ Mg) ratios. Chemical Geology, 533: 119444.
Wang, L.-X., Marks, M.A., Keller, J., Markl, G., 2014. Halogen variations in alkaline rocks from the Upper Rhine Graben (SW Germany): Insights into F, Cl and Br behavior during magmatic processes. Chemical Geology, 380: 133-144.
Wang, Y., Hsu, W., Guan, Y., 2019. An extremely heavy chlorine reservoir in the Moon: Insights from the apatite in lunar meteorites. Scientific reports, 9(1): 1-8.
Wang, Z.-Z. et al., 2017. Zinc isotope fractionation during mantle melting and constraints on the Zn isotope composition of Earth's upper mantle. Geochimica et Cosmochimica Acta, 198: 151-167.
Warren, P.H., 2011. Stable-isotopic anomalies and the accretionary assemblage of the Earth and Mars: A subordinate role for carbonaceous chondrites. Earth and Planetary Science Letters, 311(1–2): 93-100.
Warren, P.H., Wasson, J.T., 1979. The origin of KREEP. Reviews of Geophysics, 17: 73-88.
Wasson, J.T., 1990. Ungrouped iron meteorites in Antarctica: Origin of anomalously high abundance. Science, 249(4971): 900-902.
Wasson, J.T., Huber, H., 2006. Compositional trends among IID irons; their possible formation from the P-rich lower magma in a two-layer core. Geochimica et Cosmochimica Acta, 70(24): 6153-6167.
Wasson, J.T., Huber, H., Malvin, D.J., 2007. Formation of IIAB iron meteorites. Geochimica et Cosmochimica Acta, 71(3): 760-781.
Wasson, J.T., Kallemeyn, G.W., 2002. the IAB iron-meteorite complex: A group, five subgroups, numerous grouplets, closely related, mainly formed by crystal segregation in rapidly cooling melts. Geochimica et Cosmochimica Acta, 66(13): 2445-2473.

Wasson, J.T., Kalleymeyn, G.W., 1988. Compositions of chondrites. Philosophical Transactions of the Royal Society of London, A325: 535-544.
Wasson, J.T., Matsunami, Y., Rubin, A.E., 2006. Silica and pyroxene in IVA irons; possible formation of the IVA magma by impact melting and reduction of L-LL-chondrite materials followed by crystallization and cooling. Geochimica et Cosmochimica Acta, 70(12): 3149-3172.
Wasson, J.T., Willis, J., Wai, C.M., Kracher, A., 1980. Origin of iron meteorite groups IAB and IIICD. Zeitschrift für Naturforschung A, 35(8): 781-795.
Webster, J., Kinzler, R., Mathez, E., 1999. Chloride and water solubility in basalt and andesite melts and implications for magmatic degassing. Geochimica et Cosmochimica Acta, 63(5): 729-738.
Weiershäuser, L., Spooner, E., 2005. Seafloor hydrothermal fluids, Ben Nevis area, Abitibi greenstone belt: implications for Archean (~ 2.7 Ga) seawater properties. Precambrian Research, 138(1-2): 89-123.
Weinbauer, M.G., 2004. Ecology of prokaryotic viruses. FEMS microbiology reviews, 28(2): 127-181.
Weisberg, M.K., Kimura, M., 2012. The unequilibrated enstatite chondrites. Geochemistry, 72(2): 101-115.
Wever, R., Krenn, B.E., Renirie, R., 2018. Marine vanadium-dependent haloperoxidases, their isolation, characterization, and application. Methods in enzymology, 605: 141-201.
Wever, R., van der Horst, M.A., 2013. The role of vanadium haloperoxidases in the formation of volatile brominated compounds and their impact on the environment. Dalton Transactions, 42(33): 11778-11786.
Wieczorek, M.A. et al., 2013. The crust of the Moon as seen by GRAIL. Science, 339(6120): 671-675.
Wilhelm, S.W., Suttle, C.A., 1999. Viruses and nutrient cycles in the sea: viruses play critical roles in the structure and function of aquatic food webs. Bioscience, 49(10): 781-788.
Williams, H.H., Harriss, R.C., 1970. Chloride and bromide in carbonate rocks in relation to the chemical history of ocean water. Canadian Journal of Earth Sciences, 7(6): 1539-1551.
Williams, J. et al., 2016. The chlorine isotopic composition of Martian meteorites 1: Chlorine isotope composition of Martian mantle and crustal reservoirs and their interactions. Meteoritics & Planetary Science, 51(11): 2092-2110.
Wilson, L., Head, J., 2018. Controls on lunar basaltic volcanic eruption structure and morphology: Gas release patterns in sequential eruption phases. Geophysical Research Letters, 45(12): 5852-5859.
Wilson, L., Head, J.W., 2017a. Eruption of magmatic foams on the Moon: Formation in the waning stages of dike emplacement events as an explanation of “irregular mare patches”. Journal of Volcanology and Geothermal Research, 335: 113-127.
Wilson, L., Head, J.W., 2017b. Generation, ascent and eruption of magma on the Moon: New insights into source depths, magma supply, intrusions and effusive/explosive eruptions (Part 1: Theory). Icarus, 283: 146-175.
Wilson, L., Keil, K., McCOY, T.J., 2010. Pyroclast loss or retention during explosive volcanism on asteroids: Influence of asteroid size and gas content of melt. Meteoritics & Planetary Science, 45(8): 1284-1301.

Windom, H.L., 1971. Fluoride concentration in coastal and estuarine waters of Georgia. Limnology and Oceanography, 16(5): 806-810.
Wing, B.A., Farquhar, J., 2015. Sulfur isotope homogeneity of lunar mare basalts. Geochimica et Cosmochimica Acta, 170: 266-280.
Wood, J.A., 2005. The chondrite types and their origins, Chondrites and the protoplanetary disk, pp. 953.
Wood, J.A., Dickey Jr, J., Marvin, U.B., Powell, B., 1970. Lunar anorthosites and a geophysical model of the moon. Geochimica et Cosmochimica Acta Supplement, 1: 965.
Worden, R.H., 1996. Controls on halogen concentrations in sedimentary formation waters. Mineralogical Magazine, 60(399): 259-274.
Wörndle, S., Crockford, P.W., Kunzmann, M., Bui, T.H., Halverson, G.P., 2019. Linking the Bitter Springs carbon isotope anomaly and early Neoproterozoic oxygenation through I/[Ca+ Mg] ratios. Chemical Geology, 524: 119-135.
Wu, N., Farquhar, J., Dottin III, J.W., Magalhães, N., 2018. Sulfur isotope signatures of eucrites and diogenites. Geochimica et Cosmochimica Acta, 233: 1-13.
Yang, J., Goldstein, J.I., 2006. Metallographic cooling rates of the IIIAB iron meteorites. Geochimica et Cosmochimica Acta, 70(12): 3197-3215.
Yang, J., Goldstein, J.I., Michael, J.R., Kotula, P.G., Scott, E.R.D., 2010. Thermal history and origin of the IVB iron meteorites and their parent body. Geochimica et Cosmochimica Acta, 74(15): 4493-4506.
Yang, J., Goldstein, J.I., Scott, E.R., 2007. Iron meteorite evidence for early formation and catastrophic disruption of protoplanets. Nature, 446(7138): 888.
Young, E. et al., 2019. Near-equilibrium isotope fractionation during planetesimal evaporation. Icarus, 323: 1-15.
Young, E.D., Zhang, K.K., Schubert, G., 2003. Conditions for pore water convection within carbonaceous chondrite parent bodies–implications for planetesimal size and heat production. Earth and Planetary Science Letters, 213(3-4): 249-259.
Zhang, L. et al., 2019. Reassessment of pre-eruptive water content of lunar volcanic glass based on new data of water diffusivity. Earth and Planetary Science Letters, 522: 40-47.
Zhang, Y., Benoit, P.H., Sears, D.W., 1995. The classification and complex thermal history of the enstatite chondrites. Journal of Geophysical Research: Planets, 100(E5): 9417-9438.
Zhao, C. et al., 2020. Potassium isotopic compositions of enstatite meteorites. Meteoritics & Planetary Science, 55(6): 1404-1417.
Zolotov, M.Y., Matsui, T., 2002. Chemical models for volcanic gases on Venus, Lunar and Planetary Science Conference, pp. 1433.
Zolotov, M.Y., Mironenko, M.V., 2007. Hydrogen chloride as a source of acid fluids in parent bodies of chondrites. Lunar and Planetary Science Conference, 38: 2340.pdf.